MONASH UNIVERSITY

DOCTORAL THESIS

On the adhesion dynamics of *Plasmodium falciparum* infected red blood cells

Emma HODGES

Supervisors:

Prof. Ravi JAGADEESHAN

Prof. Brian M COOKE

A thesis submitted in fulfillment of the requirements

for the degree of Doctor of Philosophy

in the

Department of Chemical Engineering and

Department of Microbiology

July 20, 2016

Copyright

Declaration of Authorship

I, Emma HODGES, declare that this thesis titled, "On the adhesion dynamics of *Plasmodium falciparum* infected red blood cells" and the work presented in it are my own. I confirm that:

This thesis contains no material which has been accepted for the award of any other degree or diploma at any university or equivalent institution and that, to the best of my knowledge and belief, this thesis contains no material previously published or written by another person, except where due reference is made in the text of the thesis.

Signed:

_____

Date:

_____

Abstract

Adhesion of malaria parasite-infected red blood cells (iRBCs) to microvascular endothelium is a central event in the pathogenesis of severe *falciparum* malaria. A biophysical approach was taken to study the dynamics of this adhesive process using two different experimental techniques: dual micropipette aspiration and optical tweezers.

A dual micropipette adhesion assay was used to investigate the probability and strength of adhesion between an iRBC and an endothelial cell expressed receptor (CD36) that is important in the pathogenesis of malaria. A novel method was employed to assess the adhesion of individual iRBCs for which the shear elastic modulus was also obtained. This allowed for the first time the determination of the influence of cell rigidity on adhesion. At a constant compression force, an increased cell stiffness resulted in a decreased contact area. However, an increased cell stiffness resulted in an increased adhesion force, at a constant contact area. An optical tweezer assay was also employed to measure adhesion. The advantage of this method is that it provides a means of non-invasively manipulating objects in solution, however there are limitations with respect to the maximum force that can be applied to break the adhesion bonds ($\sim$100pN).

The two experimental methods gave comparable results. The adhesion probability increased with increasing contact time, until approximately 10s where it remained stable at $\sim 40\%$. A model for 2D kinetic adhesion was fitted to obtain a kinetic rate of dissociation, $k_\mathrm{d} = 0.11\pm0.02\mathrm{s}^{-1}$ and $k_\mathrm{d} = 0.089\pm0.025\mathrm{s}^{-1}$ for the micropipette and optical tweezer method respectively. The grouped adhesion constant ($m_r m_l K_A^o$) was found to be 0.086 ± 0.014 using optical tweezers. Increased contact area resulted in an increase in the adhesion strength for both methods. The optical tweezer method further showed an increased contact time correlated to an increased adhesion strength.

A limitation with these experimental techniques is that they are inherently non-equilibrium in nature. Consequently, a Langevin simulation was developed to model the detachment of a bead held in an optical trap, from a membrane to which it is initially bound to explore the use of fluctuation theorems to obtain equilibrium values from non-equilibrium work trajectories. The equilibrium free energy of binding was obtained for various tweezer pulling rates using fluctuation theorems. Further, umbrella sampling was used to obtain the equilibrium probability of detachment for a variety of trap potentials.

Acknowledgements

Contents

List of Figures

List of Tables

Abbreviations

2D	Two dimensional
3D	Three dimensional
AFM	Atomic force microscopy
AIC	Akaike information criterion
APES	3-hydroxy amino-propyl tri-ethoxy silane
BUCS	Binding-unbinding correlation spectroscopy
CCD	Charged coupled device
CHO	Chinese hamster ovary
CR1	Complement receptor 1
CSA	Chrondroitin sulfate A
DF	Degrees of freedom
GDMAT	Gas-driven micropipette aspiration technique
GND	Ground
HCT	Haematocrit
ICAM-1	Intercellular adhesion molecule 1
iRBC	Infected red blood cell
IR	Infrared
IFA	Indirect fluorescence assay
knobs	Electron dense protrusions on surface of iRBC membrane
LED	Light emitting diode
MCHC	Mean corpuscular hemoglobin concentration
MTC	Magnetic twisting cytometry
MP	Micropipette
NA	Numerical aperture
OT	Optical tweezer

PB	Push button
PNG	Papua New Guinea
PBS	Phosphate-buffered saline
P. falciparum	*Plasmodium falciparum*
PfEMP1	*Plasmodium falciparum* erythrocyte membrane protein 1
PSD	Power spectrum density
PWM	Pulse width modulator
QPD	Quadrant photodetector
RBC	Red blood cell
RIFIN	Repetitive interspersed family
SEM	Scanning electron microscope
SLM	Spatial light modulator
STEVOR	Sub-telomeric variable open reading frame
SURFIN	Surface associated interspersed gene family
VSA	Variant surface antigen
VCAM	Vascular cell adhesion molecule

Symbols

A_c	Area of contact	μm^2
B	Bending modulus	mN/m
K	Area expansion modulus	mN/m
P_A	Probability of adhesion	
$[R]$	Concentration of receptor	M
$[L]$	Concentration of ligand	M
$[B]$	Concentration of bound receptor-ligand complex	M
k_f	Kinetic rate forward direction	$\text{M}^{-1}\text{s}^{-1}$
k_r	Kinetic rate reverse direction	s^{-1}
K_a	Equilibrium association constant	M^{-1}
k_r^o	Zero force kinetic rate reverse direction	s^{-1}
K_a^o	Zero force equilibrium association constant	M^{-1}
k	Trap stiffness	pN/μm
p_n	Probability of adhesion with n bonds	
t	Contact time	s^{-1}
m_r	Surface density receptor	molecule/μm
m_l	Surface density ligand	molecule/μm
f	Force opposed	pN
$m_{\min}$	Minimum surface density (either receptor or ligand)	molecule/μm
$m_{\max}$	Maximum surface density (either receptor or ligand)	molecule/μm
N_{bound}	Population of bound cells	
$N_{unbound}$	Population of bound cells	
R	Resistor	kΩ
C	Capacitor	μF
R_p	Radius of micropipette	μm

L_p	Length of tongue	μm
F_p	Force on aspirated RBCS	pN
F_c	Force of compression	pN
F_d	Displacement force	pN
F_A	Force of adhesion	pN
F	Force	pN
r	Radius of contact for RBC	μm
R	Radius of RBC at rest	μm
h	Radius of compressed RBC	μm
D_{minimum}	Minimum diameter of RBC	μm
d_m	Distance trap moved	μm
t_m	Time trap moved	s^{-1}
x	Distance between bead center and focus of laser	μm
W	Normalised work	
$W*$	Normalised work at intersection	
$P_{\mathrm{F}}(W)$	Distribution of work values obtained in forward direction	
$P_{\mathrm{R}}(-W)$	Distribution of negative work values obtained in reverse direction	
U_{M}	Normalised membrane potential	
U_{OT}	Normalised optical tweezer potential	
U	Summed normalised potential	
k_{M}	Normalised membrane spring constant	
k_{OT}	Normalised optical tweezer spring constant	
x_{OT}	Normalised displacement of optical trap minima	
$x_{\mathrm{M}}^{\mathrm{ub}}$	Normalised x position upper bound membrane	
$x_{\mathrm{OT}}^{\mathrm{lb}}$	Normalised x position lower bound of optical trap	
F_{λ_f}	Normalised free energy at final state	
F_{ext}	Normalised external force	
F_{rand}	Normalised random force	
F_{λ_0}	Normalised free energy at initial state	
H_{λ}	Energy of the system at a fixed value of λ	
v_{OT}	Normalised velocity of optical trap	

Z	Partition function	
W_d	Dissipated work	
C	Cumulants	
$H(x)$	Heaviside function	
N_T	Total number of trajectories	
N_A	Number of times attached	
N_D	Number of times detached	
$p_\text{neq}^{\lambda_f}$	Non-equilibrium bead distribution at final state	
p_A	Equilibrium probabilities of bead remaining attached	
p_D	Equilibrium probabilities of bead detachment	
B	General probability	
t_D	Normalised final time	
η_i	Cytoplasmic viscosity	mPa·s
μ	Shear elastic modulus	pN/μm
ΔG	Change in Gibbs free energy	
ΔP	Change hydro-static pressure	pN/μm
ρ_k	Density of knobs	knobs/μm
λ	Wavelength	nm
ν	Data record frequency	Hz
λ	External perturbation parameter	
λ_0	External perturbation parameter (initial state)	
λ_f	External perturbation parameter (final state)	
ϵ_M	Normalised membrane depth	
ϵ_OT	Normalised membrane depth	
ΔF	Normalised free energy difference	
ΔF_anal	Analytical normalised free energy difference	
Δt	Time step	
ζ	Friction coefficient	
Σ_t	Normalised dissipation function	
Δ	Size of histogram bin	

σ_{F}^2	Variance for forward trajectories
σ_{R}^2	Variance for reverse trajectories
$<>$	Mean value
μ_n	Central moment n
χ_{A}	Indicator function of probability attachment
χ_{D}	Indicator function of probability detachment

This thesis is dedicated to my family for all your love and support and to

Callum:

For making me smile even when I'm sad. For making me calm when I am mad and to letting me be crazy with you. You are my good man.

Chapter 1

Introduction

1.1 Cell adhesion

Cellular adhesion plays a pivotal role in many biological processes. Immune response, formation and maintenance of multicellular structures, the transformation of fertilized eggs into embryos are all examples of biological processes which depend crucially on cellular adhesion (Reddi, 1998; Hoffman and Edelman, 1983; Springer et al., 1987). However, changes in cell adhesion can also play a critical part in disease. A growing body of evidence supports the importance of altered cell adhesive properties, for example in the development and progression of cancer (Okegawa et al., 2004). Adhesion also plays a crucial role in the parthenogenesis of malaria.

Malaria is a parasitic disease that is transmitted by female *Anopheles* mosquitoes between human hosts. There are six species of malaria parasites of the genus *Plasmodium* which can infect humans and cause malaria, with *Plasmodium falciparum* resulting in the highest mortality. Although the number of deaths per year has steadily decreased over the past decade, there has been a steady rise in the number of resistant parasites to current anti-malarials, including a relatively new class of anti-malarial drug artemisinin (World Health Organization, 2015; Ashley et al., 2014). This indicates a continued need to understand how the disease affects the human host, in order to discover different means to combat and potentially eradicate this disease.

A critical factor in the unique virulence of *P. falciparum* malaria parasites is their ability to cause the red blood cells (RBCs) that they infect to adhere to microvasculature endothelium. The accumulation of large numbers of parasite-infected red blood cells (iRBCs) within specific organs results in organ dysfunction or failure, a hallmark of infections that lead to serious, life-threatening clinical complications. Of particular relevance to *P. falciparum* is sequestration of iRBCs in the

brain, leading to the development of cerebral malaria (Newbold et al., 1997; Rénia et al., 2012; Mackintosh, Beeson, and Marsh, 2004).

Various different molecules located on the microvasculature endothelium have been identified as receptors to which iRBCs can adhere. Significant research has been conducted into these receptors and ligands that play a role in iRBC sequestration. Some receptors, such as intercellular adhesion molecule-1 (ICAM-1) mediate rolling adhesion of iRBCs, whereas others, such as the glycoprotein CD36, result in firm, stationary adhesion when forming bonds of iRBCs with the parasites exported ligand *Plasmodium falciparum* erythrocyte membrane protein-1 (PfEMP1), located on the surface of the iRBC (Cooke et al., 1994; Nash et al., 1992; Crabb et al., 1997). However, the strength of adhesion between iRBCs and surface-bound receptors on the microvasculature endothelium, and the effect that parameters such as individual RBC rigidity, contact area between the cells, compressive force and contact time have on the probability and force of adhesion, have yet to be fully explored.

1.2   Experimental techniques and models of cell adhesion

Significant progress has been made over the past two decades with respect to experimental biophysics and bioengineering. These advances have enabled direct mechanical probing and manipulation of single cells and molecules in real-time, allowing the imposition and measurement of picoNewton forces and nanometer displacements (Suresh et al., 2005). Such experimental techniques include atomic force microscopy (AFM), optical and magnetic tweezers, and micropipette manipulation. Predominately, the adhesive properties of iRBCs have been probed using AFM (Li et al., 2013), whereas optical tweezers have been used to probe the deformability of iRBCs by attaching and manipulating beads on the surface of iRBCs (Davis et al., 2012; Suresh et al., 2005). Optical tweezers have not yet been applied to the study of the force and probability of parasite iRBC adhesion to endothelial cell receptors.

The past two decades has also seen significant advances with respect to the understanding and modelling of cellular adhesion, in particular 2D kinetics. In particular, 2D kinetics have been explored with respect to biological systems such as T-cell activation (Chesla, Selvaraj, and Zhu, 1998; Zhu, 2000b). The above mentioned experimental techniques allow data to be obtained on the probability of adhesion as a function of contact time. The 2D kinetic model can then be fitted

to the obtained experimental data, allowing kinetic parameters such as on and off rates to be obtained for single cell-cell adhesion events (Chesla, Selvaraj, and Zhu, 1998).

In understanding the mechanisms of *P. falciparum* iRBC adhesion (and therefore, potential new treatments) these kinetic parameters must be understood in order to determine how an iRBC will behave under flow conditions. The kinetic parameters can be used to determine whether or not adhesion will occur, and if it does occur, whether adhesion is fixed, rolling or transient. Although previous studies have modelled general cell-cell adhesion (Korn and Schwarz, 2008), an analogous model with experimentally measured kinetic parameters and flow observations of iRBC adhesion to microvasculature endothelium are not currently available. There are various receptors on the surface of microvasculature endothelial cells to which iRBCs bind, resulting in different forms of adhesion, however this thesis will focus only on CD36 which is known to mediate firm, stationary adhesion.

Altered deformability of the iRBC is known to occur as the parasite matures within. There has been much conjecture on the effect that altered iRBC mechanics have on adhesion. Although studies have shown this deformability helps the iRBCs migrate towards the microvasculature endothelium wall and adhere, there has been little evidence that correlates the actual deformability of an individual cell and its specific adhesive properties.

1.3 Objectives

This thesis will address the gaps in our knowledge of iRBC adhesion to the microvasculature endothelial receptor CD36. The specific objectives of this thesis are:

1. To use recent experimental techniques in conjunction with 2D kinetic models to study the kinetics of iRBC adhesion to CD36. Dual micropipette experiments are used to obtain probability of adhesion data with respect to contact time, and the resulting data are fitted to the kinetic models to obtain on and off rates.

2. To develop a new experimental method that uses micropipette aspiration techniques, in order to study the correlation of cell deformability with microvasculature endothelium adhesion. The combined micropipette methods are used to measure the membrane rigidity of an iRBC, and then using the same iRBC, study its adhesion to CD36 using dual micropipettes.

This allows us to obtain direct evidence of the adhesion of an iRBC with a known rigidity to CD36, and consequently determine the effect that altered rigidity has on contact area and adhesion strength. The effect of other parameters such as contact time, contact force and contact area on the resulting strength of adhesion are also be explored using the micropipette method.

3. To explore the potential of optical tweezers to non-invasively study iRBC adhesion to CD36. These results are compared in terms of both the probability and strength of adhesions to the results obtained using micropipette techniques, and used to determine if there are any limitations in either method that need to be considered when undertaking adhesion assays.

4. To model the detachment of a cell bound to a theoretical membrane with an optical tweezer potential, using a Langevin equation. With this numerical model, explore fluctuation theorems to obtain equilibrium properties such as the free energy of binding or unbinding, as well as the equilibrium probability of adhesion. This potentially paves the way for analysing experimental data that is inherently far from equilibrium and obtaining equilibrium values.

1.4   Thesis outline

This thesis explores measurement techniques and the analysis of cellular adhesion in the context of *P. falciparum* iRBC. Adhesion of *P. falciparum* iRBC is critically important for both the survival of the parasite in the human host, and also plays a central role in the severity of the infection. The dual micropipette method to assess single cell adhesion was expanded upon to allow concurrent measurement of the shear elastic modulus (a measure of membrane rigidity) of the iRBC. This allowed investigation of the correlation between cell rigidity and cellular adhesion. An optical tweezer method was also employed to look at adhesion in a non-invasive way. A limitation of current force spectroscopy experimental methods are that they are inherently non-equilibrium in nature. Consequently, any obtained results are not only a function of the system under study but also the experimental technique, for example the loading rate of an AFM or the velocity of the optical tweezer. Fluctuation theorems can be used to obtain equilibrium values from non-equilbrium work trajectories.Therefore, a Langevin simulation, which theoretically modelled cell detachment using optical tweezers, was used to explore the potential of fluctuation theorems in adhesion experiments.

The structure of this thesis is as follows. Chapter 2 details background information on healthy and diseased red blood cell (RBCs), cellular adhesion and experimental techniques to analyse adhesion. Chapter 3 details the experimental materials and methods used within this thesis. Chapters 4 and 5 describe experimental analysis of cellular adhesion using micropipettes and optical tweezers, respectively. Chapter 6 includes a numerical method approach to studying cellular adhesion using a Langevin equation. Finally, summarising discussion is provided in Chapter 7. Further detail on the contents of the aforementioned chapters is elaborated on in the following sub-sections.

1.4.1 Chapter 2

This chapter provides background on cellular adhesion. Firstly, healthy human RBCs are discussed in order to understand the effect of changes to the RBCs in diseased states. The changes that occur due to infection with the *P. falciparum* parasite is then discussed with particular emphasis to the changed adhesive properties of the iRBC. The physics behind cell adhesion and methods to model the adhesion process are then explored. Following this, experimental methods utilised to measure adhesion are considered, in particular micropipette and optical tweezer methods.

1.4.2 Chapter 3

The materials and methods used throughout this thesis are detailed within this chapter, including a list of all chemicals and reagents. In-vitro culture of *P. falciparum* methods are detailed, followed by the procedures to bind the receptor of interest to prepared glass beads, for further study.

1.4.3 Chapter 4

This chapter contains the results of adhesion studies of iRBCs to CD36 using dual micropipettes. The chapter begins with a brief introduction and then details the experimental setup, including an outline of the method to measure RBC shear elastic modulus. The results of the micropipette method are then presented. First, the probability of adhesion is explored and models fitted to obtain kinetic parameters. Then, the effect that different parameters have on the force of adhesion is discussed. In particular, this method has allowed measurement of cell adhesion force with RBCs of known membrane rigidity, and for the first time shows the effect that membrane rigidity has on the resulting cellular adhesion properties.

1.4.4   Chapter 5

This chapter explores iRBC adhesion using a non-invasive optical tweezer method and compares the adhesion results with those obtained using the more invasive micropipette method. The advantages and limitations of the optical tweezer method is further discussed.

1.4.5   Chapter 6

A numerical method is described for studying adhesion using the Langevin equation, which expands on the optical tweezer method. The formulation of the model is presented, going into detail on fluctuation theorems and the use of the Langevin equation. The models of the potentials used to describe cells in the optical trap and attachment to another cell/membrane are further detailed. The validation of the model source code is presented and the results of the simulation discussed.

1.4.6   Chapter 7

This final chapter summarises the contributions this thesis has made to the study of cellular adhesion, in particular the adhesion of *P. falciparum* iRBCs to microvascular endothelial receptor CD36. It concludes with questions raised by this thesis and provides recommendations for possible future work.

Chapter 2

Background

2.1 The mature human red blood cell

2.1.1 Properties of a healthy RBC

In a resting state, a mature healthy RBC has a biconcave disc shape with an average diameter between 7.2 to 8.4μm, an average maximum width between 2.3 to 2.8μm and a minimum width in the center of the cell between 0.5 to 1.15μm (Fung, 2013), illustrated in Fig. 2.1. However, during its 120 day lifespan, circulating many times throughout the human body, it is exposed to extreme mechanical stress as it repeatedly passes through small capillaries (Diez-Silva et al., 2010), often required to pass through blood vessels 2-3μm in diameter.

The flexible membrane of a RBC and its ability to deform is an essential feature of its biological function. Healthy mature RBCs are deformable and are highly pleomorphic, passing through a broad spectrum of transitional shapes as they circulate through the human body (Surgenor, 1975).

In order to withstand the high mechanical stresses, the RBC has unique mechanical properties that allow it to repeatedly undergo the necessary large deformations to circulate through the body. The ability of the RBC to recover from these deformations, and consequently perform its function of transporting oxygen and carbon dioxide throughout the body, is dependent upon the specific material characteristics of this cell type. These include RBC geometry, cytoplasmic viscosity, and membrane viscoelasticity and rigidity (Skalak et al., 1973; Evans, 1989; Kim, Kim, and Park, 2012).

2.1.2 Mature RBC geometry

Changes in the geometry of an RBC, with respect to size, morphology and surface area to volume ratio, all affect the deformability of the RBC and contribute to clinical symptoms (Mohandas and

Evans, 1994). For example, RBC size is inceased in macrocytic anaemia as a result of vitamin B12 or folate deficiencies (Aslinia, Mazza, and Yale, 2006). In diseases such as sickle cell anemia, hereditary spherocytosis and hereditary elliptocytosis (Mohandas et al., 1980), the morphology of the RBC is altered. In the case of malaria, the surface to area volume ratio of the *P. falciparum* iRBC is reduced due to the presence of the parasite (Nash et al., 1989).

Under normal conditions, the discocyte morphology of the mature and healthy RBC optimises the surface area to volume ratio, allowing the RBC to deform dramatically whilst maintaining a constant surface area and stability (Mohandas and Chasis, 1993; Svetina, 2012). The surface area to volume ratio can be reduced by either an increase in the volume of the cell (so the cell becomes more spherical) or a decrease in the effective surface area. Increased sphericity can be caused by osmotic swelling or by disease states, including malaria. Spherocytic RBCs must increase their surface area in order to deform, which requires a significantly greater force than that needed to deform at a constant surface area (Evans, 1989). The reduction of surface area to volume ratio in *P. falciparum* iRBC increases the force required to deform the cell, which in turn reduces the ability of the iRBC to travel through narrow capilaries throughout the body.

2.1.3   Cytoplasmic viscosity

Cytoplasmic viscosity characterizes the resistance to the rate of deformation. An increase in the cytoplasmic viscosity leads to a reduction in the ability of the RBC to effectively deform. Mature RBCs lack a nucleus and internal organelles, and consequently the major contributing factor to the cytoplasmic viscosity is haemoglobin. As a result, the rheological properties of the normal intracellular fluid of RBCs are dominated by the concentration and physicochemical properties of the hemoglobin content.

The cytoplasmic viscosity (η_i) is ~ 7 mPa·s for a normal RBC with a mean corpuscular hemoglobin concentration (MCHC) of $\sim$32 g/dl. Elastic behavior is negligible. The cytoplasmic viscosity increases non-linearly with increased MCHC; an increase of MCHC to 40 g/dl results in an almost quadruple increase in the cytoplasmic viscosity (Chien, 1987).

Cytoplasmic viscosity can increase in response to changes in the type or concentration of haemoglobin, as occurs in haematological disorders. In malaria, however, cytoplasmic viscosity is altered due to the introduction of the large rigid nucleus and internal organelles of the *P. falciparum* parasite (Chien, 1987).
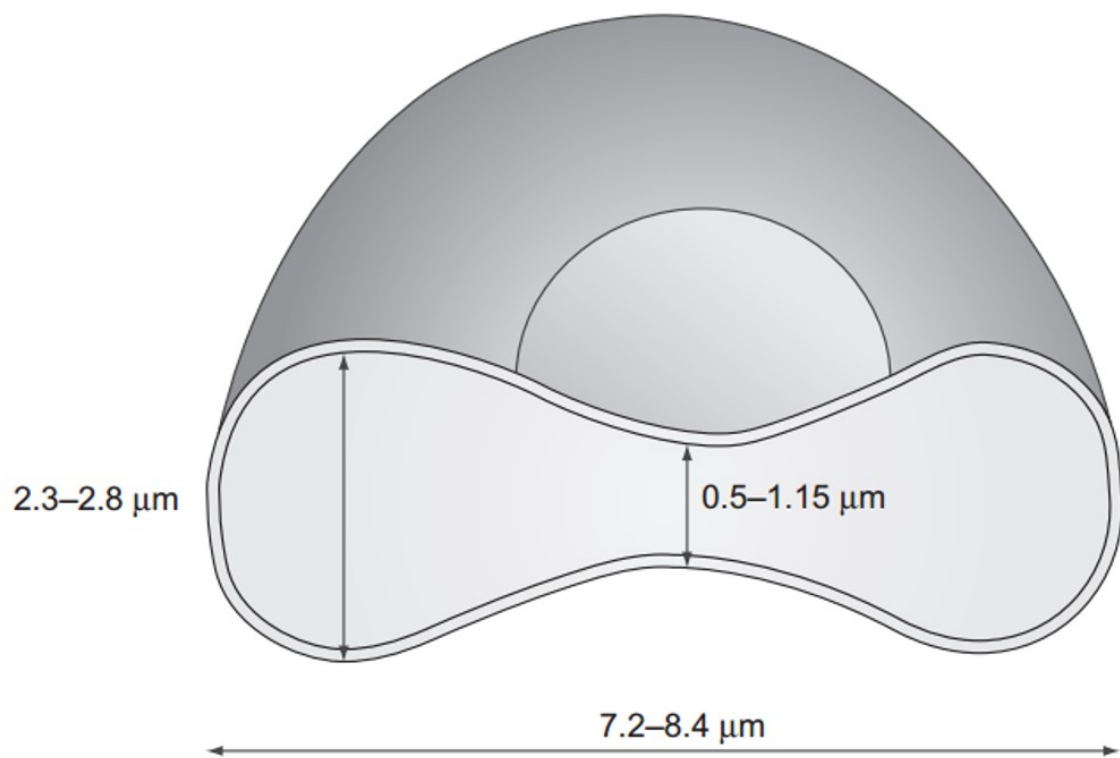
FIGURE 2.1: **Cross-sectional view of a mature healthy RBC at rest.** The average range for dimension of a RBC are shown. The minimum thickness of the RBC is located at the center of cell whilst the maximum is towards the outer edge. (Adapted from Rubenstein, Yin, and Frame, 2015)

2.1.4   RBC membrane material properties

RBC deformability is also regulated by the deformability and viscoelasticity of the RBC membrane. The structure and composition of the RBC membrane has been studied extensively and is well characterised (for reviews see Bennett, 1985; Branton, Cohen, and Tyler, 1981; Mohandas and Evans, 1994). The mature RBC membrane is comprised of a typical plasma membrane, overlying and linked to a well defined spectrin-based structural skeleton. The membrane mass is made up of approximately 52% protein, 40% lipid and 8% carbohydrate.

In order for the membrane to deform normally, the spectrin molecules that make up the skeletal network must be able to undergo conformational rearrangement. If the proximity between the plasma membrane and skeleton is altered or if the associations between or within the spectrin network are changed, the ability of the RBC to deform can be affected.

Deformation of the RBC normally takes place at a constant surface area, as the RBC membrane is highly resistant to area expansion or compression (Lacelle, Evans, and Hochmuth, 1978). Therefore, deformation of the membrane generally only involves extension (shearing) and bending (folding). The RBC membrane behaviour under stress is complex, with the membrane being capable of exhibiting solid, semi-solid and liquid behaviour depending on the magnitude and duration of the applied force (Mohandas and Chasis, 1993).

When subjected to small forces over a short period of time, the RBC membrane acts as an elastic solid. The RBC is able to undergo large elastic extensions with complete recovery to its initial shape when the applied force is removed. However, if the forces are applied for long periods of time, the RBC membrane acts as a semi-solid material and does not completely recover its shape even after applied force is removed. Further, if a large force is applied to the RBC, the membrane undergoes plastic deformation and begins to flow (Evans and La Celle, 1975). This viscoelastic behavior of the RBC membrane is essential for its function *in vivo*. It is therefore useful to characterise the material properties of the RBC, in terms of both its elastic and its viscous properties.

Elastic property of the RBC membrane

The elastic property characterizes the deformability of a material when a force is applied. The elastic properties of a RBC is determined by the RBC membrane cortex structures. Although RBC membrane deformation is highly complex, it can be explained by three fundamental types

TABLE 2.1: **Types of deformation and corresponding typical modulus values for healthy RBCs.** Row 1 shows schematic representation of three main types of deformation of a membrane (adapted from Kim, Kim, and Park, 2012). Row 2 indicates the range of typical moduli values for healthy RBC for the corresponding types of deformation (Kim, Kim, and Park, 2012; Waugh and Evans, 1979; Hochmuth and Waugh, 1987; Evans, 1983; Henon et al., 1999).

	Area expansion	Shear	Bend
Deformation type			
Healthy RBC	K = 300-500 mN/m	μ=2.5μN/m	B= 1.8×10^{-12} dyn/cm
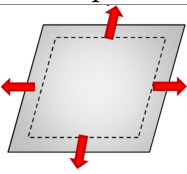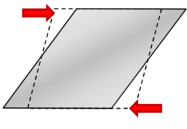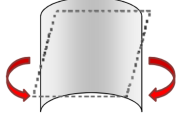
of deformation of the membrane (Kim, Kim, and Park, 2012). Consequently, the RBC membrane elastic property can be characterized by three mechanical moduli: area expansion modulus K, shear modulus μ and bending modulus B. Schematic representation of the types deformation and typical moduli values for healthy RBCs are shown in table. 2.1.

Area expansion membrane deformation

There is a strong resistance to change in the area of the RBC membrane which can be attributed to the lipid bilayer. In cases of surface expansion, for example as a result of osmotic swelling, the area expansion modulus relates the applied tensile force to the corresponding increase in surface area (Chien, 1978).

Shear membrane deformation

The resistance of the RBC membrane to shear deformation is characterised by the membrane shear elastic modulus, μ. The membrane shear elastic modulus provides a measure of force required when RBC undergoes uniaxial deformation at a constant surface area. The resistance of the membrane to shear deformation is primarily attributable to the elasticity of the underlying skeleton scaffold. The lipid bilayer provides negligible resistance to shear due to its fluid nature.

Bending membrane deformation

Membrane bending stiffness can be important in small deformations and in shape changes. Bending of the membrane requires both membrane expansion and compression. The elastic bending modulus, B is a factor of the chemical compositions of the lipids which make up the lipid bilayer of the membrane.

2.2   Experimental methods to measure RBC deformability

There are two broad categories of techniques which measure deformability characteristics of a single cell; those which locally probe sections to deform the cell and those which use mechanical loading of an entire cell. Magnetic twisting cytometry (MTC) is one method that allows measurement of viscoelastic properties of cell components. A portion of cell is deformed by magnetic beads attached onto the surface of RBC. The beads surface is functionalised and therefore when a magnetic field is applied it causes the bead to want to twist and consequently deform the cell (Bao, Suresh, et al., 2003). Another technique used to locally probe sections of the cell is AFM which uses the sharp tip at the end of the cantilever to generate the local deformation (Jena and Hörber, 2002).

Micropipette aspiration and optical tweezers are techniques that can also be used to generate whole cell deformation information. The decreased capability of iRBCs to deform has been extensively examined using micropipette aspiration technique where cell is deformed using negative hydrostatic pressure (Glenister et al., 2002; Suresh et al., 2005). Micropipette aspiration can be used to partially or completely aspirate a single RBC into a glass micropipette. The micropipette diameter can vary from less than 1 μm to 10 μm (Cooke, Stuart, and Nash, 2014).

Optical tweezers can be used to measure deformability of a RBC. One setup is obtained using a technique where beads are attached on either side of the cell; one is held stationary whilst the other is moved with a determined force (Quinn et al., 2010). The area expansion and the shear moduli of RBC membrane can be determined by applying force to three silica beads that are bound to the RBC membrane (Lenormand et al., 2001). Another technique which does not require beads being attached to the RBC was developed by Lyubin et al. (2012). The technique involves holding a red blood cell using two lasers at opposing edges of the cell; holding one laser stationary whilst oscillating the other one using an acousto-optical deflector. This method allows determination of a tangent phase difference parameter which is a measure of the viscoelastic property of the cell under study.

2.3 Alterations to RBC and disease states

2.3.1 Hematological disorders

Hereditary disorders such as spherocytosis, elliptocytosis, ovalocytosis and sickle cell anemia cause altered the deformability of the RBC (for reviews see Iolascon, Perrotta, and Stewart, 2003; Tse and Lux, 1999; Mallouh, 2012; Gallagher, 2005).

Spherocytosis

Spherocytosis is a hereditary RBC disorder that is characterized by an increased sphericity of the RBC. It is characterised by a deficiency or defect in one or more of the proteins that comprise the RBC membrane (Perrotta, Gallagher, and Mohandas, 2008). As a result of the abnormal shape and consquent reduced deformability the RBCs are prematurely trapped and destroyed in the spleen. The clinical severity of this disorder ranges from asymptomatic condition to life-threatening anemia (Iolascon, Avvisati, and Piscopo, 2010).

Elliptocytosis and ovalocytosis

Elliptocytosis and ovalocytosis are a group of disorders that result in elliptical, oval or elongated RBCs which alters the membrane function and reduces red cell deformability. It is caused by mutations in a variety of genes that ultimately affect the RBC cytoskeleton. The majority of patients with elliptocytosis or ovalocytosis are asymptomatic, although some demonstrate hemolytic anemia and splenomegaly (Da Costa et al., 2013; Soderquist and Bagg, 2013; Mohandas et al., 1992; Schofield et al., 1992).

Sickle cell anemia

Sickle cell anemia is a group of blood disorders that affect the molecular structure of haemoglobin and is characterised by the sickle shape of the RBC that occurs under certain conditions. The result of an increase in η_i and consequent decrease in RBC deformability (Chien, 1987; Stuart and Nash, 1990) can lead to clinical complications and organ damage, due to its affect on passage of RBCs through microvasculature.

2.3.2 Diseases that alter RBCs

Obstruction of the microcirculation plays a central role in the pathophysiology of severe malaria. A contributing factor is reduced deformability of the iRBC. The following section goes into greater detail about malaria and the affect the parasite has on iRBC.

2.4 Malaria

2.4.1 Epidemiology of malaria

In 2015, there was an estimated 438 000 malaria deaths worldwide and 3.2 billion people remain at risk of malaria (World Health Organization, 2015). Malaria is a disease caused by an apicomplexan parasite of the genus *Plasmodium*. There are five species of *Plasmodium* that can infect humans: *Plasmodium falciparum*, *Plasmodium vivax*, *Plasmodium malariae*, *Plasmodium ovale* and *Plasmodium knowlesi*. Of these, *P. falciparum* is responsible for the majority of malaria-associated morbidity and mortality worldwide (Petter and Duffy, 2015). Malaria is the third leading cause of death globally after HIV and tuberculosis (Qidwai et al., 2013).

Malaria stemming from the Italian word for 'bad air' has been around for at least 4,000 years. In 2010, analysis of King Tutankhamun's DNA showed he was infected with *P. falciparum* (Hawass et al., 2010). The persistence of the parasite, it's ability to effect evolutionary selection (Qidwai et al., 2013) as well as the increased resistance to current antimalarial treatments (Setiawan and Ministry of Health Republic of Indonesia, 2010) all indicate a paramount need to understand the processes which cause severe malaria in order to develop strategies for the prevention and treatment of severe disease.

2.4.2 Lifecycle of *Plasmodium falciparum*

P. falciparum has a complex lifecycle requiring periods in human and mosquito hosts as shown in Fig. 2.2, where the lifecycle can be divided into three distinct stages: the mosquito, human liver and human blood stage (Greenwood et al., 2008; Tuteja, 2007).

Sporozoites are injected into the skin of a human host by an infected female *Anopheles* mosquito as it takes a blood meal (Frischknecht et al., 2004). The sporozoites travel to the liver and invade
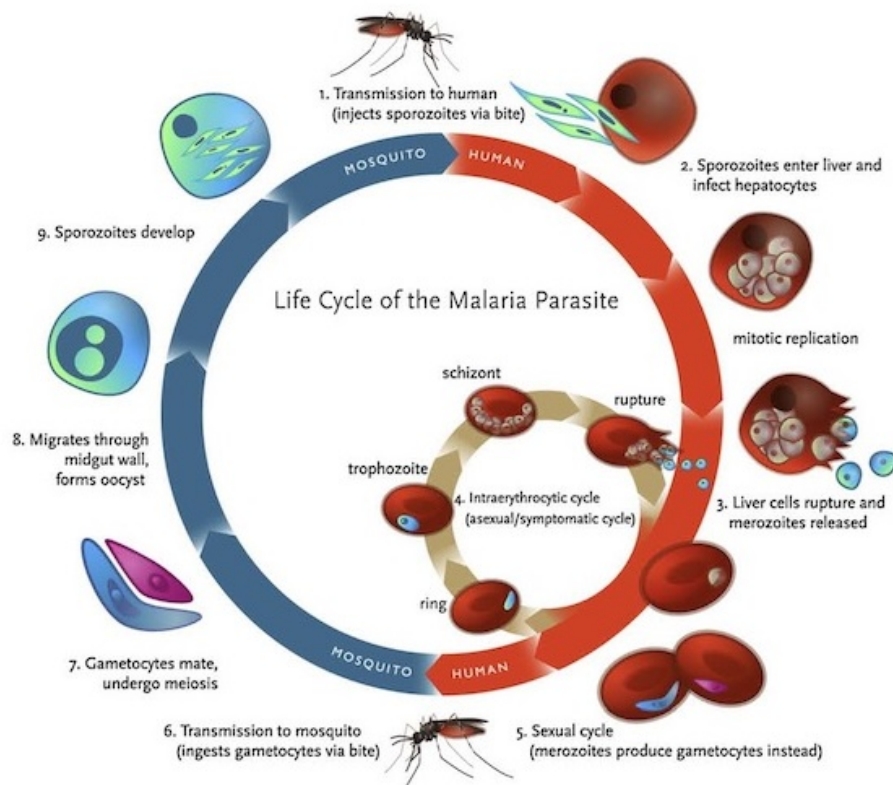
FIGURE 2.2: **Lifecycle of *P. falciparum.*** Sporozoites are injected into the bloodstream of a human host by an infected female *Anopheles* mosquitoes. The sporozoites travel to the liver, invade hepatocytes and replicate. The hepatocytes rupture and mesozoites are released into the blood which initiates the asexual blood stage. A fraction of merozoites form sexual gametocytes which can transmit to an *Anopheles* mosquito and cycle continues. The asexual stage is where the clinical symptoms present. Image taken from Greenwood et al., 2008

hepatocytes within an hour (Trampuz et al., 2003). After several rounds of multiplication and differentiation, the hepatocytes rupture and mesozoites are released into the blood which initiates the asexual blood stage.

Merozoites rapidly invade circulating RBCs. Once within the RBC, the parasite matures over a 48 hr cycle from a ring stage (immature trophozoites), to the mature trophozoite and then the schizont stage (Bannister et al., 2000). The cell then raptures releasing new merozoites which go on to infect other RBC's. A fraction of merozoites form sexual gametocytes in response to specific stimuli of parasite or host origin, which can transmit to an *Anopheles* mosquito when taking a blood meal (Bruce et al., 1990).

Following ingestion by the mosquito, the gametocytes get exposed to specific stimuli that trigger their maturation into gametes. The male and female gametes fuze to form a zygote , which develops into an ookinete and meiotic recombination occurs. The Ookinetes traverse the mid-gut epithelial cell wall and form oocysts. These oocysts rupture to release sporozoites that actively migrate to the salivary glands, where they reside until the mosquito takes a blood meal, which simultaneously delivers sporozoites to the next human host and the cycle continues (Josling and Llinás, 2015).

2.4.3   Pathogenesis of *Plasmodium falciparum*

Severe malaria is a complicated syndrome, with both human host and parasite factors playing a role (Baruch, 1999). Severe malaria is defined as infection causing vital organ dysfunction and/or death. Clinical features of severe malaria are, but not limited to, impaired consciousness, prostration, multiple convulsions, acidotic breathing, acute respiratory distress, acute kidney injury, circulatory collapse or shock, abnormal bleeding and/or clinical jaundice (World Health Organization, 2012). In order to survive in the human host, *P. falciparum* has developed strategies to evade both antimalarial agents as well as the human bodies immune system.

The role of sequestration

The capacity of iRBCs to sequester in the microvasculature of various organs and consequently evade splenic clearance is an important immune evasion strategy of the parasite (Bachmann et al., 2009). However, it is this ability to cytoadhere that significantly contributes to the pathology of the disease (Miller et al., 2002). IRBCs adhere throughout the vasculature, predominately in post

capillary venules leading to an accumulation of iRBCs and resulting in a reduction of oxygen delivery to tissues. In order for iRBCs to be able to adhere, significant modifications to the RBC by the parasite are required.

2.5 Modification of iRBCs

During the blood stage, the parasite modifies the RBC in which it resides resulting in significant changes to the iRBC compared to a healthy RBC (Cooke, Mohandas, and Coppel, 2001). The membrane becomes less flexible, making it difficult for the RBC to pass through the microvasculature. Special pores are created in the RBC membrane by the parasite to enable nutrients, such as carbohydrates, amino acids, and purine bases to be transported into the RBC. Further, some RBC membrane components are modified or digested (Chen, Schlichtherle, and Wahlgren, 2000). Importantly, several parasite-derived proteins are inserted into and protrude out from the RBC membrane, including PfEMP1 which enables the iRBC to cytoadhere to endothelial cells and other intravascular cells (Moxon, Grau, and Craig, 2011; Cooke, Stuart, and Nash, 2014). Further, parasite-derived proteins can cause significant changes to the RBC membrane such as the formation of elctron-dense protrusions (knobs) which aid in the adhesiveness of the iRBC (Waller et al., 1999). A visual comparison between infected red blood cells (iRBCs) and healthy RBCs is shown in Fig. 2.3 (Moxon, Grau, and Craig, 2011).

2.5.1 Altered deformability of iRBCs

Modifications to the membrane and cytoskeleton of the iRBC by the *P. falciparum* parasite leads to dramatic effects on the RBC ability to function as a result of drastic changes to the RBC normal characteristics. As the parasite matures within the cell it increasingly effects the cytoplasmic viscosity, surface area to volume ratio and viscoelasticty of the membrane, all which are important to RBCs rheological properties and consequently its ability to function normally (see section 2.1.1). The presence of the increasingly large, rigid and highly viscous intracellular parasite as it matures, which can occupy up to 90% of the total RBC volume, causes significant alterations in cell shape and deformability. However, changes in the iRBCs membrane due to the parasite also contributes to changed functionality of RBC. Membrane deformability studies have demonstrated that mature iRBC membranes are more rigid than healthy RBCs. This changed deformability is a function
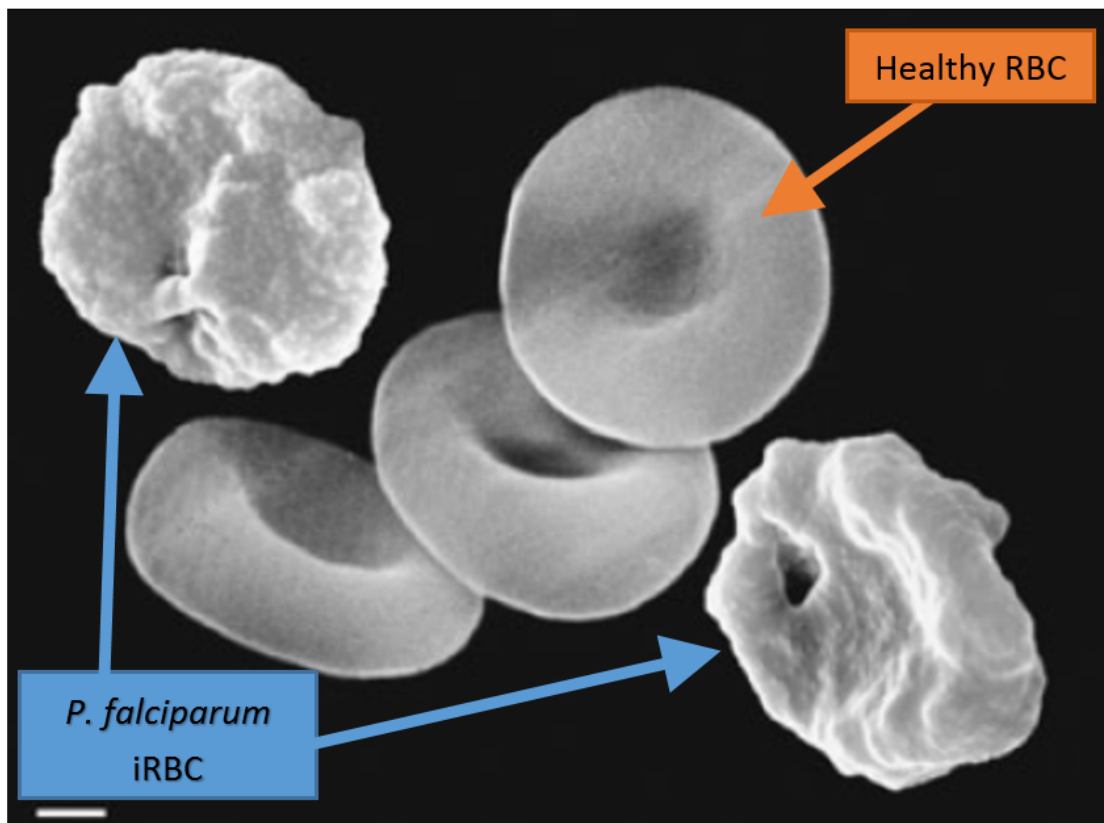
FIGURE 2.3: Scanning electron microscope images of *P. falciparum* iRBCs which show increased sphericity with a rough surface and healthy RBCs (the three middle cells) that show a biconcave structure and a smooth surface (image modified from Moxon, Grau, and Craig, 2011). Scale bar = 1 μm

of not only the parasites developmental stage, with immature ring stage having negligible effect on membrane rigidity, but also the *P. falciparum* strain.

2.5.2 Adhesive properties of iRBCs

Adhesion of iRBCs is mediated by parasite derived ligands expressed on the surface of iRBCs, the majority of adhesive ligands can be attributed to the parasite-derived surface protein family *Plasmodium falciparum* erythrocyte membrane protein 1 (PfEMP1) (Smith, 2014; Baruch, 1999). Other parasite-derived variant surface antigens (VSAs) are expressed on RBC membrane and include repetitive interspersed family (RIFIN), sub-telomeric variable open reading frame (STEVOR) and surface-associated interspersed gene family (SURFIN). These VSAs are antigenically diverse however their importance and role they play in adhesion varies and still to some degree remains unknown (Chan, Fowkes, and Beeson, 2014).

The adhesive properties of iRBCs can be defined based on adhesion of the iRBC to either i). uninfected RBCs (rosetting), ii). other iRBCs (platelet mediated autoagglutination) or iii). endothelial cells lining the vasculature (cytoadherence). Sequestration of iRBCs to vasculsar endothelium is an essential pathological feature of severe malaria. However, the role of rosetting and autoagglutination in pathogensis is still unclear with links to disease severity being found in some studies but not others (Chotivanich et al., 2004; Al-Yaman et al., 1995; Newbold et al., 1997; Rowe et al., 1995; Carlson et al., 1990). Adhesion can also occur between iRBCs to dendritic cells, B cells, monocytes and macrophages to modulate host immune functions (see reviews by Chua et al., 2013).

Rosetting

Rosetting is the spontaneous binding of iRBCs to uninfected RBCs and has been suggested to play a critical role in severe malaria (Helmby et al., 1993). Rosetting was shown to enhance micovascular obstruction under ex-vivo flow conditions (Kaul et al., 1991) and has been linked to severe malaria in African children (Rowe et al., 1995; Carlson et al., 1990).

The potential importance of rosetting in severe malaria could be indicated by evolution favouring the genes for two lethal diseases (thalassemia and sickle cell anemia). In their heterozygous forms these diseases have been implicated in a protection against cerebral malaria. Studies have

shown an impaired ability of thalassemic RBCs and, under certain conditions, hemoglobin S containing RBCs to form rosettes. This impaired ability to form rosettes may hinder sequestration required for cerebral malaria (Carlson et al., 1994; Cockburn et al., 2004).

Rosettes are often formed by *P.falciparum* iRBCs adhering to complement receptor 1 (CR1). Polymorphisms, including thalassemia, which result in CR1 deficiency in RBC are common in malaria endemic regions in PNG and have been shown to confer protection against severe malaria. It has been suggested this protection is due to the reduced ability of rosette formation of iRBCs with the CR1 deficient RBCs (Cockburn et al., 2004).

Recent data suggests that PfEMP1 may not be the only molecule responsible for RBC binding and rosette formation, the ligand which mediates rosetting may be dependent on the blood group of the infected patient. *P.falciparum* utilises PfEMP1 ligand to form rosettes with blood group O RBCs. However, it has recently been proposed that RIFINs are the parasite derived ligands expressed on the iRBC membrane which form rosettes with blood group A RBCs (Goel et al., 2015).

Autoagglutination

Autoagglutination is platelet mediated clumping of iRBCs and is associated with severe malaria (Pain et al., 2001; Mayor et al., 2011; Bull et al., 2000). This adhesive phenomena is distinct from rosetting as it has been shown that rosetting parasites do not necessarily autoagglutinate and vice versa (Roberts et al., 1992). Autoagglutination has been shown to be common in field isolates in Kenyan children and strongly associated with severe malaria (Roberts et al., 2000).

Autoagglutination of iRBCS is mediated by platelets and requires the expression of CD36, a platelet glycoprotein also found on endothelial cells (Pain et al., 2001). PfEMP1 is the parasite derived ligand expressed on surface of RBC membrane that has been implicated in autoagglutination. Interestingly, it was also observed that, autoagglutinates were observed only in cultures with >8% parasitemia, however rosettes were observed even at low levels of parasitaemia (Vigan-Womas et al., 2008).

Cytoadherence

Adherence of the iRBCs to the microvasculature endothelium is a vital component in *P. falciparum* virulence. Sequestration of iRBCs, in particular organs within the human host, results in serious,

life-threatening disease as a result of organ dysfunction or failure. In particular, accumulation of iRBCs in the brain resulting in the development of cerebral malaria (Grau and Craig, 2012).

Cytoadhesion is mediated by specific interaction between receptors on the surface of endothial cells and parasite-derived PfEMP1 expressed on the surface of iRBC (Kraemer and Smith, 2006). Endothelial receptors that have been identified to play a role in iRBC adhesion include, glyco-protein CD36, thrombospondin, intercellular adhesion molecule-1 (ICAM-1) and vascular cell adhesion molecule (VCAM) (Newbold et al., 1997). Platelets are commonly used when studying *P. falciparum* iRBC adhesion as a model for CD36-mediated adhesion. IRBCs have been shown to bind firmly to platelets at shear stresses analogous to those in the microvasculature and to have pH sensitivity consistent with that of CD36-mediated cytoadhesion. Further, binding of IRBC to platelets are largely abolished in the presence of antibodies to CD36 with only a small change to binding in the presence of ICAM-1 antibodies (Cooke and Nash, 1995). Platelet coated surfaces represent a practically simple model for studying malarial cytoadhesion.

PfEMP1 is a family encoded by ~ 60 different *var* genes which, through mutually exclusive transcription, only one PfEMP1 variant is expressed on the surface of the iRBC at a time (Scherf et al., 1998). However, the parasite is able to switch between the *var* gene being expressed every generation, at a switching rate of $\sim 2\%$ per generation, which facilitates parasite immune evasion (Roberts et al., 1992). However, it can also affect binding specificity as specific variants have been shown to interact with different receptors to varying degrees. For example, the VAR2CSA variant interacts with specific receptors on the placenta, chrondroitin sulfate A (CSA) allowing iRBCs expressing the VAR2CSA variant of PfEMP1 to adhere to the placenta (Ndam et al., 2005; Magistrado et al., 2008).

2.6 The physics of cell adhesion

Cell adhesion is an important phenomena. Our immune system relies on this process to recruit leukocytes to inflamed tissue from circulation. Further, in clinical areas, such as stem cell research, adhesion kinetics alter the effectiveness of cell separation devices (Chesla, Selvaraj, and Zhu, 1998). Adhesion can also be a critical parameter in disease progression. As discussed in section 2.5, *P. falciparum* causes the iRBC to become more rigid and cytoadhesive, resulting in impairment of blood flow, leading to severe anaemia, coma and even death (Moxon, Grau, and Craig, 2011).
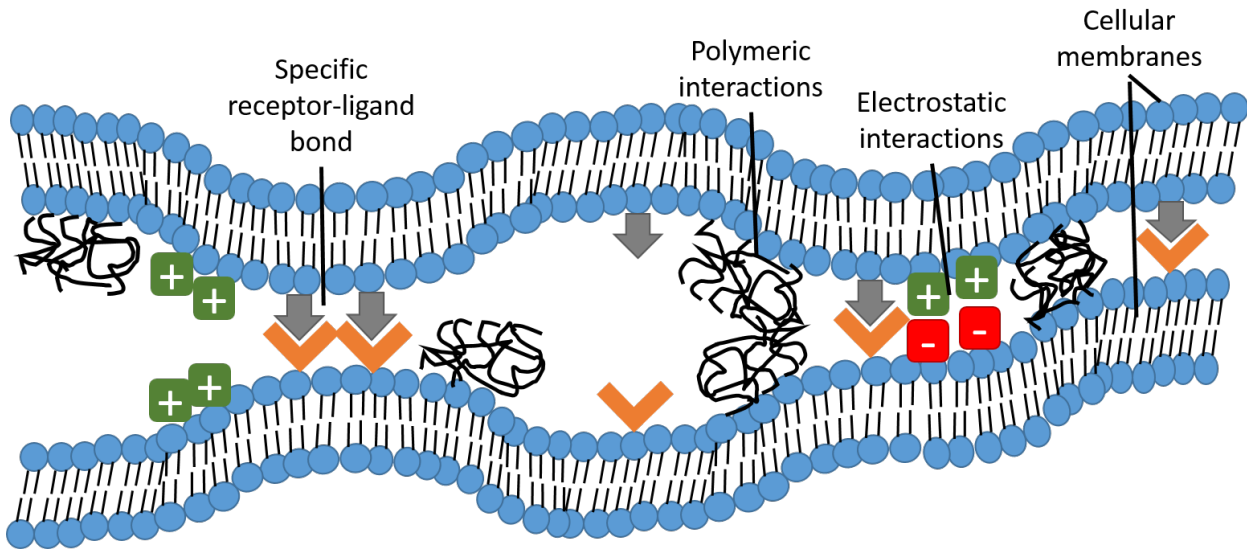
FIGURE 2.4: **Schematic of the interplay between specific and generic interactions during cellular adhesion.** Attractive interactions including specific lock-and-key interactions between receptors and bonds need to compete against generic repulsive forces such as polymeric repulsion due to the glycocalix, undulating forces due to membrane fluctuation and electrostatic repulsion. (schematic adapted from Gönnenwein et al., 2003)

2.6.1 Specific versus generic forces

Cellular adhesion is a complex process controlled by subtle interplay between specific and generic forces. Specific forces are those between a receptor and its conjugate ligand, which can be described using the lock and key principle (Helm, Knoll, and Israelachvili, 1991). Receptor-ligand interactions require topologically and chemically complimentary structures, this allows the specific lock and key interaction to occur (Koshland, 1995). Generic forces involved in adhesion are non-specific and can be attractive as well as repulsive. Examples of generic forces involved in adhesion are: van der Waals, electrostatic, polymeric and thermal fluctuations (Evans, 1995). The brush-like polymer glycocalix layer present on the RBC membrane acts as a repulsive barrier to ensure specificity in spite of the presence of generic adhesive interactions (Lipowsky and Sackmann, 1995).

The lock and key principle

The total adhesion energy of bound cells and consequently the forces required to detach cells is a function of the specific binding energy between each receptor and its conjugate ligand as well as the total number of bonds formed. It should be noted that each specific lock and key bond
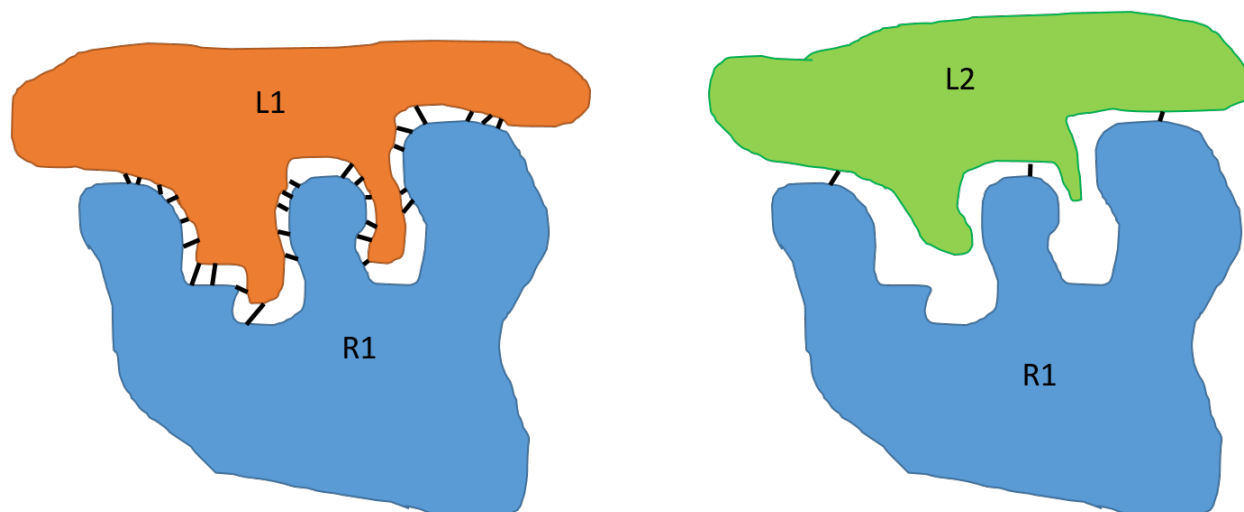
FIGURE 2.5: **Schematic of the lock and key principle.** Two pairs of biomolecules indicate the importance of structural and chemical complementary structures and hence the inherent specificity of receptor-ligand bonds. Only when the two molecules fit well together, indicated by receptor 1 (R1) and ligand 1 (L1) can many weak interactions form resulting in a strongly attached aggregate. However in the case of receptor (R1) binding with ligand 2 (L2) only a few weak interactions can form and so aggregate can easily be dissociated by thermal fluctuations. (schematic adapted from Gönnenwein et al., 2003)

actually relies on the interplay of many individual weak bonds which when working together form the strong receptor-ligand bond. These weak bonds include:

- Van der Waals interactions are a a transient, weak electrical attraction between transient or permanent dipoles. Energies are on order 0.2 to 0.5 $k_B T$. Van der Waals attractions, although transient and weak, can still provide an important component where a "lock and key" fit of the two molecules yields extensive Van der Waals attractions, resulting in significant forces due to the sheer number of interactions.

- Hydrogen bonds form as a result of electrostatic interactions. A hydrogen bond occurs when a hydrogen atom, that is slightly positive due to being covalently bound to a highly electronegative atom, forms a bond to a nearby electronegative atom. The two electronegative atoms share the hydrogen atom. Energies are on order 1 to 2 $k_B T$.

- Hydrophobic interactions occur between non-polar molecules in an aqueous environment, by aggregating together they reduce the energy associated with unfavorable arrangement of water molecules and hence form an attractive force between them. The energies of these interactions depend on serval factors however they are generally stronger than van deer waal interactions or hydrogen bonds.

- Ionic bonds are due to electrostatic interactions between complementary charged ions. Energies are on order 2 to 4 $k_B T$

The specificity of receptor-ligand bonds are a direct result of the fact that these bonds individually are weak and so many bonds have to work together to form a stable bond against thermal fluctuations and other generic forces which cause the bonds to dissociate. It is only when these highly complex structures are structurally and chemically complimentary that sufficient weak interactions can form to result in a strong attachment, the receptor-ligand bond.

Further, these interactions both specific and generic can occur on varying length scales. For reviews on the physics of cell adhesion, and the length scales in play, see Sackmann and Goennenwein, 2006; Lipowsky and Sackmann, 1995.

2.6.2 Modelling adhesion

2.6.3 Modelling adhesion using kinetic theory and the master equation

One method of modelling cell adhesion is by just considering specific receptor-ligand bonds, where a receptor (R) and ligand (L) form a receptor ligand bond (B) with an on rate (k_f) and dissociate with an off rate (k_r) (Zhu, 2000a). The intrinsic kinetics (reaction rates and binding affinity) determine the adhesive events between interacting cells, since the kinetic parameters govern not only how likely and how fast the adhesion occurs but also if an adhesion does occur, how strong the adhesion is and how long it lasts (Li et al., 2015).

As a cell approaches the binding distance between it and another cell, whether adhesion occurs is not only a function of bond length, species concentration and reaction rates, but also a probability function as a consequence of thermal fluctuations at the cellular level. These thermal fluctuations and membrane fluidity work on length scales of the weak interactions and therefore can cause the dissociation of the receptor-ligand bonds (Zhu, 2000a).

In situations where there is a significant number of interacting pairs the stochastic fluctuations are statistically averaged out and a deterministic approach can be taken, this situation often occurs in three-dimensional kinetics where the receptor and/or ligand can move freely in the three dimensions and are not bound to a fluid membrane (see 2.6.4). However, in cases where binding can only occur within a defined area of contact and interactions are infrequent, the stochastic nature of the individual molecules becomes significant, as is the case in two-dimensional kinetics

where both the receptors and ligand are bound to opposing surfaces/membranes (see 2.6.4). This phenomenon is supported by experimental data that show cells undergoing identical experimental conditions do not show an all or nothing binding nature (Zhu, 2000a).

2.6.4 Two-dimensional versus three-dimensional kinetics

Three-dimensional (3D) kinetics is the case where one or more of the molecular species (ligand or receptor) are in solution and consequently are unbounded, therefore able to move in all three spacial dimensions. There are many developed methods and experimental apparatus able to evaluate 3D kinetic rates, such as surface plasmon resonance and radio-immunoassays (Cheung and Konstantopoulos, 2011). However, in the case of adhesion ligands, both receptors and ligands are anchored on their respective cell surfaces, and consequently have restricted movement, this is defined as two-dimensional (2D) kinetics (Zhu, 2000a; McQuarrie, 1963). Unlike 3D kinetics it has really only been in the last decade that experimental methods in conjunction with theory and even simulation, to determine two-dimensional kinetics have been proposed (Zhu, 2000a). The restricted movement due to the fixed surface receptor and ligands results in altered kinetics compared to that of free moving receptors in solution.

2.6.5 Kinetic theory

For simplicity consider a single-step reversible bimolecular interaction which can be described as a reaction that is second order in the forward direction (adhesion of receptor and ligand) and first order in the reverse direction (dissociation of receptor-ligand bond):

$$R + L \underset{k_r}{\overset{k_f}{\rightleftharpoons}} B \tag{2.1}$$

where R, L and B designate the receptor, ligand and bond complex, respectively. k_f and k_r are the respective forward and reverse rate coefficients for this association reaction. The equilibrium association constant K_a is defined as k_f/k_r. The kinetics of this reaction is a function of whether a deterministic approach can be taken or if stochastics comes into play.

3D kinetics

As discussed in section 2.6.4 3D kinetics are considered for cases whether either or both the receptor and ligand are in solution. As thousands of receptors are interacting with thousands of ligands, the molecular fluctuations of individual interactions are averaged out by statistical behaviour and consequently adhesion, described as a reaction detailed in section 2.6.5, can be modeled using a simple deterministic equation:

$$\frac{\mathrm{d}[B]}{\mathrm{d}t} = k_f[R][L] - k_r[B]$$

where the concentrations of the receptor, ligand and bond are designated $[R]$, $[L]$ and $[B]$, respectively with units of molar concentration (M). The forward rate k_f is in units $M^{-1}s^{-1}$ and the reverse rate k_r is in units s^{-1}. The equilibrium association constant K_a is in units M^{-1}.

2D kinetics

The kinetics of receptor-ligand binding in cell-cell interactions is a stochastic process regulated by applied forces and can be modeled using 2D kinetics. This stochastic nature of binding can be described using a probabilistic model. The probabilistic expression of this bimolecular interaction described in section 2.6.5, assuming first order kinetics in dissociation and overall second order in association, is given by the master equation (Zhu, 2000b).

$$\frac{\mathrm{d}p_n}{\mathrm{d}t} = m_r m_l A_c k_f \left(\frac{f}{n}\right) p_{n-1} - \left[m_r m_l A_c k_f \left(\frac{f}{n+1}\right) + n k_r \left(\frac{f}{n}\right)\right] p_n$$
$$+ (n+1) k_r \left(\frac{f}{n+1}\right) p_{n+1} \quad (2.2)$$

The master equation expresses the number of bonds that any adherent cell may have, as a discrete, time-varying, random variable that fluctuates significantly. Here p_n is the probability that adhesion is by n number of bonds, and the surface density of receptors and ligands is given by m_r and m_l respectively. A_c is the contact area (μm^2) and f is an expression of force applied to the system.

A probability vector $(p_0, p_1, p_2..., p_n, ...p_{A_c m_{min}})^T$ is required to describe the state of the system, as any number of bonds between 0 to $A_c m_{min}$ could result in adhesion. m_{min} is the density of either the receptor or ligand, whichever is the smaller of the two. The change in probability with

time t at any n is such that it is affected only by the influxes from and effluxes to its immediate neighbours (i.e. $n \pm 1$), where the first and last term on right hand side of eq. 2.2 represents the influxes and the middle term the effluxes.

In certain situations, constant density assumptions can be used to simplify the master equation (Chesla, Selvaraj, and Zhu, 1998). In the case where either the receptor or ligand density is significantly larger than the other, the former species (in the free state) can be approximated as constant in the contact area. The density of the species which excessively outnumbers the other is designated m_{max} whilst the density of reaction limiting species is designated m_{min}. In this situation the master equation can be simplified and the probability of adhesion takes the form of a binomial distribution (Chesla, Selvaraj, and Zhu, 1998):

$$p_A(t) = 1 - [1 - q(t)]^{-A_c m_{min}} \tag{2.3}$$

where:

$$q(t) = \frac{1 - \exp(-k_r^o t)}{1 + m_{max} K_a^o} \tag{2.4}$$

The probability of adhesion, p_A, is $1 - p_0$ where p_0 is the probability no bonds are formed in contact area A_c (μm^2). Density is in units molecules/μm^{-2}. The zero force (designated with ^{o}) equilibrium association constant K_a^o and reverse kinetic rate k_r^o are in units μm^2 and s^{-1}, respectively. The contact time, t, is in s.

Another case that can be considered is if the number of free receptor and ligands stays approximately constant in the contact area, even during formation of a small number of bonds (Chesla, Selvaraj, and Zhu, 1998). This occurs if the density of the receptors and ligands is significantly greater than the number of bonds that have nonvanishing probabilities. This allows the master equation to be simplified and the resultant analytical solution is given by Equation 2.5.

$$p_n(t) = \frac{\langle n \rangle^n}{n!} \exp\left(-\langle n \rangle\right) \tag{2.5}$$

where $< n >$ is the average number of bonds, given by:

$$< n >= A_c m_r m_l K_a^0 \left[1 - \exp\left(-k_r^0 t\right)\right] \tag{2.6}$$

The probability of an adhesion event is again defined as one minus the probability of having

no adhesion (n=0) and the analytical solution takes the form of a Poisson distribution (Chesla, Selvaraj, and Zhu, 1998):

$$p_A(t) = 1 - \exp\left\{-A_c m_r m_l K_A^o \left[1 - \exp(-k_r^o t)\right]\right\} \qquad (2.7)$$

It should be noted that these analytical derivations look at the kinetics for the case of zero force. However, experimentally there is an inherent force requirement due to the mechanical nature of adhesion assays which force the cells together and apart.

2.6.6 Modelling adhesion using fluctuation theorems

Traditionally adhesion has been modeled at the molecular level using a lock and key system of receptors and ligands. However, cell-cell adhesion involves a number of individual receptor-ligand bonds comprised of many weak interactions as well as generic interactions, both attractive and repulsive, which collectively can be modeled as an energy landscape of binding.

With force spectroscopy, the force to pull or de-bind a single cell can be measured, with the work of de-binding being related to the energy difference between bound and unbound states. This measurement is advantageous in that it uses a single system (say a single cell and substrate) rather than a population assay which may incorporate non-uniformities in the cell population. Force spectroscopy experiments are inherently non-equilibrium in nature and the resulting forces associated with binding/unbinding are a factor of the experimental method, i.e. the loading rates for atomic force microscopy (AFM) or the pulling rates in optical tweezers (OT). These force spectroscopy methods are discussed in more detail in section 2.7. Despite having no variability in terms of cells under investigation when the same cell-cell pair are repeatedly brought into contact, there is significant variability in the outcome of a single pulling event every time the cells are brought into contact with each other in terms of whether adhesion occurs or not when the cells are separated. However these variations in the outcome of single cell-cell adhesion events enable the measurement of energy of binding and associated properties more accurately. This interpretation of data is based upon non-equilibrium fluctuation theorems developed in the 1990s and is particularly suited for experiments of soft systems. Briefly the work required to bind or unbind a pair of cells using force spectroscopy can be biased to obtain the equilibrium free energy

of binding even when procedure was not carried out under equilibrium or quasi-equilibrium conditions.

2.7   Experimental methods

Experimental methods to measure adhesion between cells can be broadly categorised into methods that look at the molecular level, the single cell level or bulk cell assays where a population of cells are investigated. These techniques are discussed further below.

2.7.1   Molecular assays

Molecular assays can be used to analyse binding affinities of adhesion between receptors and ligands i.e. protein-protein interactions. However, this means that it does not take into account the other factors that come in to play with cell adhesion. As discussed in section 2.6.4 generally in molecular assays the receptor and/or ligand is in solution and so is not restricted to a surface, and consequent contact area, unlike in true cell-cell adhesion. Further, in these assays generally only the receptor and ligands are present. Consequently these assays cannot take into account the generic interactions that are also present during cellular adhesion.

Techniques used to measure protein-protein interaction kinetics and obtain binding affinities include: surface plasmon resonance (Karlsson and Fält, 1997; Myszka, 1997), protein affinity chromatography, sedimentation, gel filtration, fluorescence methods, and solid-phase sampling of equilibrium solutions. Review of these methods can be found in (Phizicky and Fields, 1995; Schreiber, 2002; Lakey and Raggett, 1998). Traditionally these methods only focused on obtaining binding affinities however recent advances have focused on expanding these methods to look at binding kinetics and factors that can affect obtained properties such as pH and viscosity (Schreiber, 2002).

2.7.2   Single cell assay

The turn of this century saw pioneering research into single cell adhesion kinetics (Zhu, 2000a). Predominately, single cell techniques focus around a relationship between probability of adhesion from a significant number of trials and the contact time, resulting in information about 2D kinetic rates. By using curve fitting techniques such as least squares method or Monte Carlo fitting,

the simplified analytical solution (eq. 2.5) can be fitted to the obtained experimental results and kinetic information and binding affinities can be obtained.

Techniques that can be used to measure single cell-cell adhesion include micropipette aspiration (Chesla, Selvaraj, and Zhu, 1998; Huang et al., 2004; Hogan et al., 2015; Colbert et al., 2009), optical tweezers (Fällman et al., 2004; Gou et al., 2013; Rinko, Lawrence, and Guilford, 2004), biological force probes (Lower, Tadanier, and Hochella, 2000; Evans, Ritchie, and Merkel, 1995) and atomic force microscopy (Drelich and Mittal, 2005).

More detail of single cell assays using micropipettes and optical tweezers, respectively will be discussed in section 2.7.4 and section 2.7.5.

2.7.3   Bulk cell assays

Bulk cell assays can be used to assess the fraction of adherent cells, and/or the force dependence of the detached fraction of cells, for a population of cells. The techniques can be broadly categorized into two types: static and flow based adhesion assays. Although bulk cell assays, in particular flow assays, can give vital information about adhesion under physiological conditions, the techniques can lose information on a individual cell level.

Static assays

Traditionally in vitro cell adhesion has been most commonly investigated using static assays. An example is the investigation of adhesion *P. falciparum* iRBCs to various receptors expressed on either sub-confluent monolayers of cultured cells or purified, immobilized proteins. The iRBCs suspensions are allowed to settle in Petri dishes with bound receptors adhered to the bottom of the dish. The dishes are then, either continuously or periodically, agitated gently for a period of incubation and non-adherent cells removed by washing. Adherent cells are counted, generally by staining and direct microscopic observation (Cooke et al., 1994).

Static assays are technically simple, inexpensive and a large number of assays can be carried out concurrently. However, it should be noted that adhesion measured under static conditions does not necessarily translate into adhesion under conditions of physiological flow. *P. falciparum* iRBCs have been shown to have markedly different adhesion characteristics when subjected to shear forces (Cooke and Coppel, 1995).

Flow-based adhesion assays

Flow based bulk cell assays include techniques such as the centrifugation assay to enable the measurement of force dependence with respect to binding affinity by using centrifugation to detach less adherent cells with a defined force and time (Piper, Swerlick, and Zhu, 1998). Flow chamber assays which can be used to measure adhesion under physiological conditions, for example mimic the shear forces exerted on adherent cells in the human microvasculature (Cooke et al., 1993; Phiri et al., 2009; Cooke and Coppel, 1995; Kojima et al., 1992). Adhesion under shear flows can be obtained using cone and plate viscometers (Liang et al., 2008; Shankaran and Neelamegham, 2001).

Flow-based adhesion assays have been used extensively to study the adhesive properties of flowing leukocytes in-vitro (Smith, Berg, and Lawrence, 1999). Lawrence and Springer (1991) showed, using an in-vitro flow-based assay, that leukocytes exhibit rolling behaviour on artificial lipid bilayers, a phenomena which has been exploited by numerous research groups to gather specific data from flow-based assays.

By varying parameters such as cell deformability (and therefore associated contact area), media viscosity (to see if it's shear stress or shear rate that regulates rolling) and cell size (to manipulate tether force applied) a greater understanding of the flow characteristics of leukocytes has been developed (Li et al., 2012) (Yago et al., 2004). Information obtained in the form of fractional stop and go times, mean stop and go times as well as stop frequencies lead theorists to believe the leukocytes exhibit a triphasic force-dependant slip-catch-slip bond regime in flow systems. It was further shown, using flow-based assays, that E-selectin-mediated rolling was regulated by wall shear stress rather than wall shear rate and that cell deformation and membrane tether extrusion had no effect on the triphasic force-dependant pattern exhibited by the cells and was not the dominant mechanism underlying flow enhanced rolling (Li et al., 2012).

Furthermore transient tether lifetimes can be used to give information about dissociation rates. Smith, Berg, and Lawrence (1999) calculated forced dissociation rates for a variety of selectin expressing leukocytes. A novel side view flow assay system was developed by Dong and Lei (2000) to look at characteristic binding time, cell rolling velocity and cell-surface contact as a function of changes to shear stress and cell deformability.

Flow-based adhesion assays have been used to study a variety of parameters of *P. falciparum* iRBC such as microfluidics that demonstrated blockages occur when mature iRBCs flow through

microfluidic channels with widths of $2 - 4\mu$m (Shelby et al., 2003). The type of adhesion observed (rolling or fixed) has been found to depend on the receptor, with iRBCs exhibiting fixed adhesion to CD36 however showing rolling behavior on ICAM-1 (Cooke et al., 1994). Further, specific genes have been systematically knocked out to determine the affect absence of proteins coded by the specific genes has on observed adhesion (Cooke et al., 2002).

2.7.4   Micropipette aspiration techniques

Sung, Saldivar, and Phillips (1994) were early pioneers of micropipette aspiration assays to obtain information about adhesive properties of leukocytes, using the method to incrementally induce a pressure driven force until the cell detached from the other cell to give a quantitative determination of strength of adhesion. The technique was expanded further to be used to study single cell adhesion probability to allow measure of forward and reverse kinetic rate constants (Chesla, Selvaraj, and Zhu, 1998) (Zhao et al., 2002) (Fu et al., 2011) (Chesla et al., 2000). Chesla, Selvaraj, and Zhu (1998) explored adhesion kinetics between IgG-coated RBC and CD16A-expressing Chinese hamster ovary (CHO) cells. The major advantage of the micropipette technique is the control afforded to the experimentalist; unlike in bulk flow systems, you can control and measure the contact time, the contact area (by how hard the cells are forced together) as well as the force applied to pull the cells apart for each individual cell. Briefly, the CHO cell and RBC were independently held by apposing pipettes, then using a computer program and piezo translator the RBC was repeatedly driven to the stationary CHO cell, impinged for defined contact time and then retracted at a predetermined rate. In this method the probability of adhesion was determined visually for between 50-200 repeated tests for each pair of cells and situation, the number of adherent events over the number of times cells were brought into contact gave the probability of adhesion.

Single cell adhesion studies using micropipette techniques have also been used to examine adhesion between lymphocytes and endothelial cells (Zhao et al., 2002). Kinetic off rates of integrbin meditated adhesions have been derived using the micropipette technique to study how cell signalling can affect the strength and persistence of the adhesive bonds (Kinoshita et al., 2010).

Fu et al. (2011) employed a gas-driven micropipette aspiration technique (GDMAT) that looked at interactions between neutrophils and tumor cells. In this system, a tumour or endothelial cell was held by stationary pipette and a neutrophil held in by variable pressure pipette, driven by the pressure unit to approach, contact and then withdraw from stationary held cell. A solenoid valve

allowed nearly instantaneous switching from positive to negative pressures. GDMAT allows greater accuracy and the semi-automated work allowed larger data sets to be compiled compared to traditional micropipette systems. Using equation 2.5, Fu et al. (2011) were able to determine on rates (k_f) and off rates (k_r) when using best fit performed by SigmaPlot on obtained experimental data. Unlike traditional micropipette aspiration methods where visualisation was used to determine if an adhesion event took place or not, Fu et al. (2011) used the resulting velocity distribution of the neutrophil to determine if an adhesion event took place. Further, four different states corresponding to four different velocity profiles were determined indicating whether a cell was unattached, had formed a weak tether, had formed adhesion without tether extraction or had formed firm adhesion. It is an important note that adhesion kinetics are assumed to be first order.

2.7.5 Optical Tweezers

Observations of comet tails by Kepler in the 1600s led to one of the earliest recorded speculations that light could be used to manipulate particles by exerting a mechanical force. Although an intriguing novelty, limitations due to the small amount of force produced, especially when compared to the large forces that are generally needed to be overcome, restricted many potential applications. However, in 1969 Arthur Ashkin dramatically changed this perception by realising that small particles only need small forces to enable movement and were therefore a perfect candidate for optical manipulation (Verdeny et al., 2011).

In the 1980s Ashkin used a gradient force to successfully trap a micro-particle using single beam optics, now commonly referred to as the optical tweezer method (OT) (Ashkin et al., 1986). Rapid expansion resulted, potentially due to advantages of the method, as it allows for non invasive trapping and manipulation of a diverse range of objects. It is a powerful tool due to its ability to provide a sterile non invasive tool for manipulation of cells and colloidal particles in the force range of sub-picoNewton (pN) to several hundred pN range with precision of $< 1pN$ (Castelain et al., 2012).

There are two main forces associated with optical trapping; scattering force, which works in the direction of light beam propagation pushing objects along and trapping/gradient force which induces the particle to move towards the focal point of the laser provided that the particle has a refractive index different from that of the medium (LIM, 2006). In an OT system, the laser beam is focused by an objective lens with a high numerical aperture. The numerical aperture must be

high as although this decreases the effective working distance; i.e a numerical aperture of 1.3 has a working distance of approximately 200 μm^2, it increases the gradient force which must be higher than the scattering force in the focal zone if the particle is to be 'trapped'.

The basic setup includes a laser (generally infrared when using biological samples as the higher wavelength is less damaging to the cells), collimator (device that narrows a beam of light), expander (used in optical trapping to expand the incoming beam thus ensuring the full use of the objective aperture, creating maximal optical field gradient and giving the most efficient particle trapping in the focal point) and objective (such as 100x water as this has a high numerical aperture and therefore a resulting larger trapping force). One advancement is the use of spatial light modulators (holographs) which allow the formation of multiple traps from the one laser source (Verdeny et al., 2011). Quadrant photodetectors (QPD) have been used to measure laser beam deflection and therefore the lateral forces the trap exerted on beads, calibrated from the low frequency component of Brownian motion. Piezo electric stages and 2D acousto-optical deflectors have also been used to manipulate positions of stages and traps respectively.

Since the start of this decade optical tweezers have been used to gain knowledge about binding strength and kinetic rates of adhesion events. Litvinov et al. (2002) used optical tweezers to look at rupture forces of various fibrinogen-integrin pairs and how they are effected by the presence of various antagonists. An interesting aspect of their research was by looking at both yield strength as well as probability they were able to discern whether the addition of antagonists or even agonists affected binding by changing the strength of the bonds, or if it changed the likelihood of bonds forming. In their case it was found that addition of these stimulators increased the accessibility (i.e. increased the probability of binding) but the adhesion strength remained relatively constant (i.e yield strength).

Optical tweezers have successfully been used to determine kinetic and thermodynamic unbinding parameters for integrin - fibrinogen complexes (Litvinov et al., 2011). The setup used allowed the duration and magnitude of compressive contact to be controlled as well as the magnitude of the tensile force during rupture, allowing measurement of bond lifetimes. Further to this research Litvinov et al. (2012) described two dimensional kinetics of integrin - fibrinogen interactions by a combined theoretical approach with optical tweezers, named the "binding-unbinding correlation spectroscopy" or "(BUCS)". The methodology uses force free association of the individual cells as well as forced dissociation of the complex to get the kinetic parameters.

Chapter 3

Materials and Methods

3.1 Chemicals and reagants

All chemicals and reagents were purchased from Amersham Pharmacia Australia Pty. Ltd., Amersham Biosciences AB Sweden, AMIRAD Pharmacia Biotech Australia, BDH Chemicals Australia Pty. Ltd., BIO-RAD Laboratories Australia Pty. Ltd., DIFCO Laboratories USA, Invitrogen Australia Pty. Ltd., Life technologies Australia, Vector Laboratories Inc. USA, Sigma-Aldrich Australia Pty. Ltd., Promega Australia Pty. Ltd., ThermoFisher Scientific Australia Pty. Ltd., GL Sciences, Inc. USA, Amresco, Inc. USA, Merck & Co, Inc. Darmstadt Germany, Alfa Aesar, A Johnson Matthey Company, USA, MoBiTech, Germany and MO BIO Laboratories, Inc. USA. All media components were obtained from Oxoid UK Ltd., Life Technologies Australia, Baxter Healthcare Australia Pty. Ltd., Opthalmic Laboratories Australia, Pharmacia and Upjohn Australia Pty. Ltd. and Sigma-Aldrich Pty. Ltd.

3.2 In vitro culture of *Plasmodium falciparum*

The parasite line used in this study was 3D7, a well characterized clone from a clinical isolate (The Netherlands). All culture procedures were carried out in a laminar flow hood at room temperature under aseptic conditions. All media, reagents and culture solutions were either filter sterilised (0.22 μm filter) or autoclaved prior to use.

3.2.1   Culture media

10X RPMI-1640 (Life Technologies) was diluted with sterile water (Baxter Healthcare) to make 1X RPMI-1640 solution with gentamicin sulphate (40 μg/ml) (Pharmacia and Upjohn), N-2-hydroxy-ethypiperazine-NO-2 ethane sulfonic acid (HEPES; 25 mM) (Sigma-Aldrich) and hypoxanthine (200 μM) (Sigma-Aldrich). The pH was adjusted to 6.7 with 2 M NaOH (BDH). 14 mM sodium bicarbonate (0.2%) (Pfizer) was added to make incomplete RPMI. Complete RPMI was further prepared by the addition of AlbuMAX II (0.5%) (Life Technologies). Both incomplete and complete RPMI were stored at 4°C and used within 1 month.

3.2.2   Preparation of Human RBCs for malaria culture

Human RBCs were obtained from the Australian Red Cross blood service and prepared by centrifugation for 5 min at 1649 x g. Packed RBCs were washed once in sterile $1 \times$ PBS (Oxoid) and further centrifuged for another 5 min. Washed RBCs were then resuspended in an equal volume of complete RPMI to approximate 50% haematocrit (HCT) and stored at 4°C for a maximum of one week.

3.2.3   Maintaining in vitro culture of *P. falciparum*

Parasites were maintained under continuous culture in complete RPMI using standard procedure Trager and Jensen, 1976. Culture was maintained at a parasitaemia (percent of parasite infected cells to uninfected cells) between 1-10% in 25 cm^2 flasks containing 300μl of packed RBCs (3% HCT) and 10ml of complete RPMI. and gassed with 1% O_2, 5% CO_2, and 94% N_2 (BOC gases) prior to incubation at 37°C. Depending on the parasitaemia of the parasite cultures, media was either replaced every day (high parasitaemia) or every second day (lower parasitaemia) in order to meet the nutritional requirements of parasites.

3.2.4   Measuring paristemia using Giemsa stain on blood smears

Parasitaemia and stage of maturation of parasites were determined by microscopic observation of Giemsa (BDH)-stained thin blood smears. The smears were fixed with methanol prior to being stained with freshly prepared 10% (w/v) Giemsa solution for 3-5 min. Both the parasitaemia and

the developmental stage (merozoite, ring, trophozoite and schizont) were determined by microscopic examination on a Leica DME microscope (Leica, Germany) using the 100X oil immersion objective lens.

3.2.5 Synchronisation and purfication of *P. falciparum* cultures

Gelatin flotation

During continuous in vitro *P. falciparum* culture, parasites become asynchronous and can potentially loose their adhesive properties through the loss of knob expression on iRBCs surface. In order to keep a knob positive phenotype, cultures were synchronised using gelatin flotation (Waterkeyn, Cowman, and Cooke, 2001). Parasites were cultured to obtain 3% mature stage (trophozoite and schizont) iRBCs. Cultures were pelleted by centrifugation, packed cell volumes were estimated and an equal volume of incomplete RPM1 was added to approximate 50% haematocrit. Two volumes of 1 % (w/v) gelatin suspension was then added to cell suspension, mixed well and incubated for 10-20 min at 37°C in incubator until the separation of RBCs and gelatin containing iRBCs with knobs were observed. Knob positive iRBCs, which float in gelatin and were, therefore in the supernatant layer were collected, washed with incomplete RPM1 and pelleted at 600 x g for 5 min. Knob positive iRBCs were then cultured as described in sec. 3.2.3.

Sorbitol synchronisation

Sorbitol selectively lyses late stage parasites, keeping normal RBCs and ring-stage parasites intact (Lambros and Vanderberg, 1979). Ten volumes of 5% (w/v) sorbitol (Sigma-Aldrich) was added to packed iRBCs and incubated for 10 min at 37°C. Cells were then pelleted using centrifugation at 600 x g for 5 min and washed with incomplete RPMI. Synchronised parasites were cultured as described in sec. 3.2.3. To obtain highly synchronised cultures, they underwent a second round of sorbitol lysis 4-6 hr following the first round of sorbitol lysis.

Percoll gradient purification

Mature (trophozoite and schizont) stage iRBCs were enriched on Percoll Dluzewski et al., 1984. A stock solution of Percoll consisting of 9 parts Percoll (Amersham Biosciences) and 1 part sterile 10X PBS was made. The cells were pelleted at 600 x g for 5 min and were adjusted to 10% HCT

with complete RPMI. 70% (v/v) Percoll in complete RPMI was aliquoted into 10 ml tubes and pre-warmed to 37°C. The same volume of cell suspension was gently layered over the Percoll and the tubes were centrifuged at 1250 x g for 10 min. After centrifugation, mature stage iRBCs were at the Percoll/RPMI interface with ring-stage iRBCs and normal RBCs pelleted at the bottom of the tube. Mature stage iRBCs were placed into a new tube and washed with 1X PBS. Purified mature stage parasites were then ready to be used for subsequent analysis.

Magnet harvest

Magnetic columns, MACS system (Miltenyi Biotec), were used to separate and concentrate mature stage iRBCs from ring-stage iRBCs and normal RBCs. This method takes advantage of the presence of haemozoins, which are magnetic and are produced as a result of Fe (II)-containing haemoglobin breakdown in mature iRBCs. When this method is compared to Percoll gradient purification, it is particularly suitable for molecular and biochemical analysis of the biology of parasites, as it does not affect the viability and morphology of parasites (Spadafora, Gerena, and Kopydlowski, 2011; Karl, Davis, and St Pierre, 2010; Bates et al., 2010). MACS separation columns CS were placed into the vario MACS $^{®}$ magnetic support and equilibrated by adding 30 ml of 1X PBS. Parasite cultures were centrifuged at 600 x g for 5 min, supernatants were discarded and pelleted cells were resuspended in 10 ml of complete RPM1. 10 ml of iRBCs at 18% HCT were loaded on top of the column. A low flow rate was used to pass the culture through the column (4-6 drops per 10 sec). Columns were then washed using 30 ml of prewarmed (37°C) incomplete RPM1 at medium flow rate (10 drops per 10 sec). Columns were removed form the magnetic field and mature iRBCs were eluted using 30 ml of pre-warmed (37°C) complete RPM1.

3.2.6   Cryopreservation and thawing of *P. falciparum* cultures

Cryopreservation

Cryopreservation of parasites was performed under sterile conditions. Cultures containing a high percentage of ring-stage parasites were prepared and pelleted at 600 x g for 5 min. Cell pellets were then resuspended in two pellet volumes of freezing solution (28% (w/v) glycerol (BDH), 3% (w/v) D-sorbitol, 0.65% (w/v) NaCl), the suspension was transferred to cryovials (Thermofisher Scientific). Cryovials were then immediately placed into liquid nitrogen and stored until required.

Thawing

Cryovials of *P. falciparum* stabilates were removed from liquid nitrogen storage and placed in 37°C incubator until stabilates were thawed completely (approximately 5 min). IRBCs were rehydrated under sterile conditions, 0.2 ml of thawing solution 1 (12% (w/v) NaCl) was added in a dropwise manner per each ml of stabilate. This was followed by slowly adding 5 ml of thawing solution 2 (1.6% (w/v) NaCl) and then 5 ml of thawing solution 3 (0.9% (w/v) NaCl supplemented with 0.2% (w/v) glucose). The resulting suspension was pelleted at 600 x g for 5 min and washed with 10 ml of incomplete RPM1. Packed RBC pellets were then cultured in accordance with sec. 3.2.3.

3.3 Binding platelets to glass micro beads

Binding platelets to glass micro beads (4.2μm diameter) required modification of procedure as described previously (Buttrum, Hatton, and Nash, 1993) for binding platelets to glass microslides. so although the majority of the procedure was relevant (in particular the method for extracting platelets from fresh blood and washing in preparation for exposure to glass which activates the platelets to bind to surface) there was issues with trying to get the platelets to bind to the beads and then fix them allowing the use of the platelet coated beads for up to a month instead of 24 hour expiry date.

3.3.1 Acid washing silica beads

Firstly, the glass (silica) beads were acid washed. Briefly, $10\,ml$ solution of $70\%\,v/v$ Nitric acid in water was placed in glass $50\,ml$ universal bottle placed in fume hood. 5μg of glass beads $4.86 \pm 0.47\mu$m diameter (Bangs Beads, USA) was added and allowed to settle through solution overnight. The next day the majority of the acid solution was removed using plastic pipette being careful not to disturb settled beads. Approximately $40\,ml$ of distilled water was then added, beads resuspended into solution and placed into $50\,ml$ falcon tube. Solution was centrifuged at 3200 rpm for 5 min to settle beads, supernatant removed and distilled water added. Wash was repeated 3 more times. The beads were then kept in distilled water at 4^oC until use.

3.3.2 Pre-coating silica beads with APES

Acid washed glass beads in distilled water were placed in polypropylene plastic tubes. Beads were pelleted using centrifugation (600 ×g for 5 minutes) and supernatent removed. Sufficient anhydrous acetone (greater than 99% purity) was added to cover the beads fully. Sonication was used to get beads into solution and then tube was placed on roller for 5min. This process was repeated twice more. Acetone was removed using centrifugation to pellet the beads (600 × g for 5 minutes) and a freshly prepared solution of APES (4% v/v in anhydrous acetone) was added to pelleted beads. Beads were placed on roller for 5 minutes. Process was repeated twice more with a freshly made solution of APES each time. APES solution was removed and beads washed twice with acetone. The beads were again pelleted, excess acetone removed and then beads were washed with distilled water twice. The beads were kept in distilled water at 4^oC until required.

3.3.3 Coating platelets to acid washed silica beads

Platelets were extracted from fresh blood and washed in accordance to the Standard Operating: Procedures *Plasmodium falciparum* Culture manual. The final stage before incubation step requires the platelets to be resuspended in Tyrodes buffer with $1\,mM$ $CaCl_2$. The $CaCl_2$ is added to induce platelet activation. Although platelets will activate in the presence of glass, the $CaCl_2$ increases activation. Unfortunately, issues arose with the addition of the calcium. Initially, $1\,mM$ $CaCl_2$ was added with Tyrodes buffer and beads/platelet mixture incubated at 37^oC for 1 hour on rotating spinner. It was evident after the hour incubation that the platelets had clumped together. The issue with the platelet/beads aggregating together is that they can thereafter not be solubilised evenly and consequently obtaining a single bead within the chamber to do adhesion assay with is extremely difficult. The mixture was sheared through 23G needle as well as vortexed, however, the aggregations were not able to be broken and so were not useable. In order to investigate whether the aggregation was due to the presence of calcium the procedure was repeated for $1\,mM$, $0.1\,mM$ and $0\,mM$ $CaCl_2$. As expected without the calcium no clumping was observed however IFA indicated low/negligible presence of CD36 and adhesion studies showed no adhesion. The incubation process was then investigated to develop a gentler way to rock the samples. Procedure was repeated with the various concentrations of calcium however the incubation stage was carried out at both RT and 37^oC but with a gentle rocker. After the hour no aggregation was

observed and micropipette experiment at this point showed adhesion to occur which was backed up by IFA studies.

3.3.4 Fixation

However it is required to fix the platelets to ensure they are viable for up to a month. The process to fix the beads requires the beads to be centrifuged for a minute at 2000xg to wash them with PBS. The beads are then centrifuged again and $1\% \, w/v$ of formalin in PBS added. The fixed platelet coated beads are then stored at 4^oC until use.

The issue with this method is that as soon as the beads were centrifuged they again clumped together and were un-useable. In order to circumvent this issue the beads that are incubated in 1ml Tyrodes in a microcentrifuge tube were placed into a 10ml falcon tube and then 9ml of the $1\% \, w/v$ formalin in PBS added without the wash stage. This circumvented the aggregation issue however the concentration of bead was unreasonable and so mixture was stored at 4^oC overnight and then the next day $9 \, ml$ of solution was removed and the settled beads re-suspended in the remaining $1 \, ml$ of solution. Although this resulted in solution being a reasonable concentration there was a further issue. By fixing solution in presence of the calcium and Tyrodes the calcium forms a salt and segments. This means when you add solution to chamber you get a significant amount of salts that settle to bottom of chamber decreasing the clarity of video. However, not fixing the solution is un-viable as is not adding the calcium the last method was deemed the most suitable and thus was the procedure employed throughout the length of study.

3.4 Indirect immunoflorescence assay

Indirect immunofluorescence assays were performed on thin smears of bead solution that had been air-dried and fixed with ice-cold acetone/methanol (9:1). Smears were incubated with appropriate anti-body (VM58) diluted in 3% (w/v) BSA in 1X PBS for either 1 hr at RT or O/N at 4^oC. Slides were then washed three times with 1X PBS for 15 min. After washes, slides were incubated with appropriate secondary antibodies for 1 hr at RT. Slides were then washed three times using 1X PBS for 15 min and visualised using fluorescence microscope.

3.5   Adhesion cell assay

3.5.1   Adhesion cell assay using dual micropipettes

A well described technique using glass micropipettes was modified extensively from the setup previously described by Nash et al. (1989), Nash et al. (1992), and Glenister et al. (2002). Development of the modified methodology is described in detail in chapter 4.

3.5.2   Adhesion cell assay using optical tweezers

Optical tweezers were also used to investigate adhesion properties of iRBCs. The general setup, components and calibration methods of optical tweezers are well described (refer to (Molloy and Padgett, 2002; Sarshar, Wong, and Anvari, 2014; Baek, Hwang, and Lee, 2007)). A detailed description of the actual setup used to measure adhesive properties as well as calibration methods used is described in chapter 5.

Chapter 4

Micropipette analysis of abnormal adhesive properties of *Plasmodium falciparum* infected red blood cells

4.1 Introduction

During the RBC stage the *P. falciparum* parasite exports proteins that assist in important modifications that are integral for parasitic survival. However, these modifications can have a detrimental effect on the human host (Maier et al., 2009; Cooke, Stuart, and Nash, 2014). In particular, the iRBCs ability to adhere to the blood vessel wall, and hence avoid splenic clearance, is of critical importance as it circumvents the body's inbuilt defense mechanisms and leads to severe clinical complications (Buffet et al., 2011). However, there is still a substantial gap in our knowledge of the strength of these bonds, the kinetic mechanism, and factors that affect these properties. This chapter focuses on the use of micropipettes for studying adhesion between *P. falciparum* iRBCs and CD36. Furthermore, the effect certain parameters have on the probability of adhesion and the force of the obtained adhesive bonds is explored. For more background on *P. falciparum* and modifications that occur see section 2.4.

Micropipettes have been used previously to study the 2D kinetics of adhesion, however to this authors knowledge, the kinetics of iRBC adhesion to CD36 using this method has not been explored. Further, the method has been expanded to determine forces associated with adhesion, and explore the factors that affect bond force and the probability of adhesion. These factors include the time of contact and the compressive force, as well as the deformability of the cell being

investigated.

This chapter is structured as follows. Section 4.2 contains an overview of the setup and a detailed explanation of each component in the setup and implementation of the micropipette adhesion experiment. Section 4.3 details how micropipettes were used to obtain the elastic modulus of each cell under investigation which gives a measure of the cells deformability and presents the results obtained using this micropipette aspiration technique. Section 4.4 discusses the results of the adhesion experiment and looks in detail at the factors affecting the probability of adhesion and the forces associated with the obtained adhesion. Section 4.5 concludes this chapter.

4.2 Materials and methods

A broad overview of the experimental setup is given, with greater details of the different components to be given in the following sub-sections.

4.2.1 Experimental setup

The RBCs and the glass beads are prepared as detailed in section 4.2.5. A cell chamber, approximately 2mm deep (section 4.2.3), was filled with 2% bovine serum albumin (BSA) in phosphate buffer solution (PBS) for ten minutes to reduce the likelihood of nonspecific binding. The chamber was then filled with a mixture containing 1000 μL BSA in complete RPMI media solution, $10\,\mu L$ of culture containing iRBCs, and $10\,\mu L$ of the ligand coated bead solution. The glass chamber with the solution was then placed on the stage of an inverted light microscope (Leica DMIRB).

Glass micropipettes with an approximately 8mm long taper and a internal diameter between 1.1-1.8 μm were fabricated (section 4.2.4), filled with $1\times$ PBS solution and mounted on hydraulic micro-manipulators (Narishige, Japan) which allow precision movement.

The pipettes are connected to a hydrostatic pressure system consisting of syringes and chambers full of microfiltered water which can be manipulated to change hydraulic pressure through the pipettes, by either changing position of the water level in the chambers by raising or lowering the platform they are situated on or by manipulating the syringe. The resolution of the hydrostatic pressure system is 0.01 mm H_2O. Pipettes in the chamber were visualized using a $\times 63$ objective lens with a numerical aperture of 0.7.
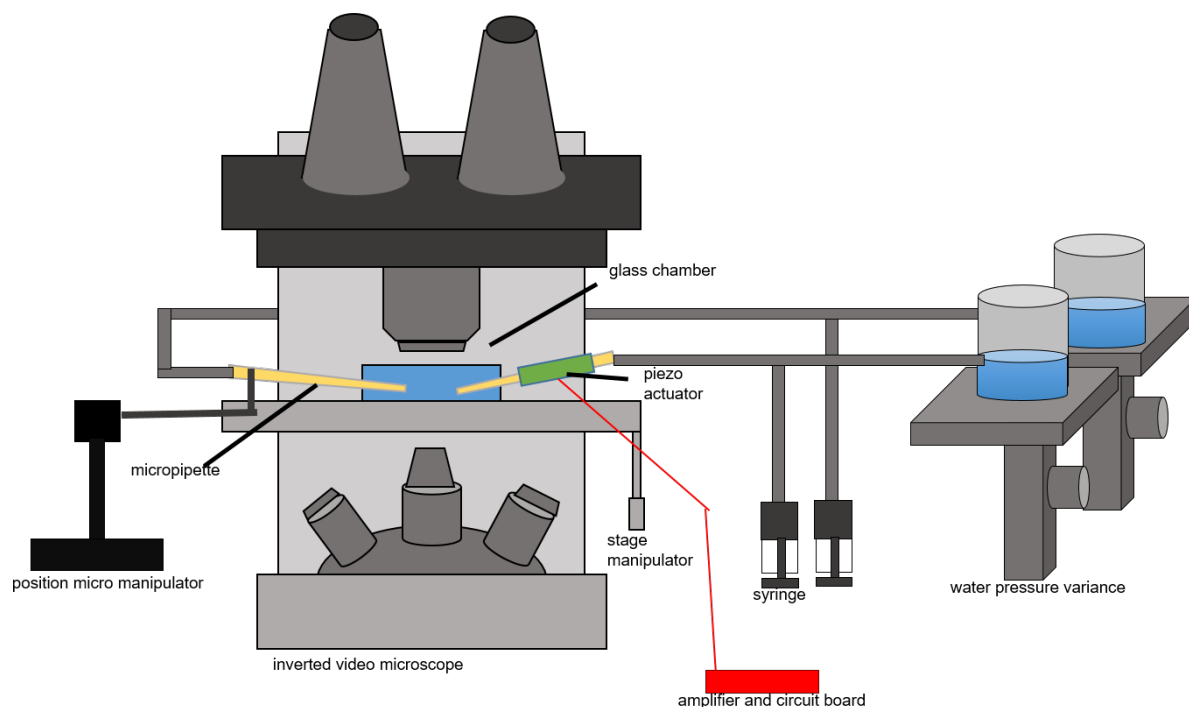
FIGURE 4.1: **Schematic diagram of dual micropipette setup.** RBCs and glass beads are contained in the chamber and are caught using micropipettes mounted to micromanipulators which allow precision movement. The pipettes are connected to a hydraulic pressure system consisting of syringes and water chambers which are manipulated to change hydraulic pressure through the pipettes. The chamber was located on inverted light microscope, magnified by a $\times 63$ lens and viewed through a mounted high speed digital camera (not shown).

Micropipette aspiration was viewed and analysed on a high resolution monitor using customized digital image capture and analysis software (Total Turnkey Solutions, Australia). Adhesion experiments were captured using a high speed 14MP USB 2.0 microscope digital camera (Omax, USA). The Omax ToupView software was used for capturing and analysis of the video data.

4.2.2 Micropipette construction

Micropipettes were constructed using a micropipette puller machine (Sutter instrument Co. Model P-97 Flaming/Brown). Glass capillaries were cut to $11\,\mathrm{cm}$ using a diamond headed stylus. The cut capillaries were inserted into the pipette puller, heated in the center and then stretched until failure.

There are two methods to obtain the required pipette end diameter, between 1.2 and $1.8\,\mu$m.
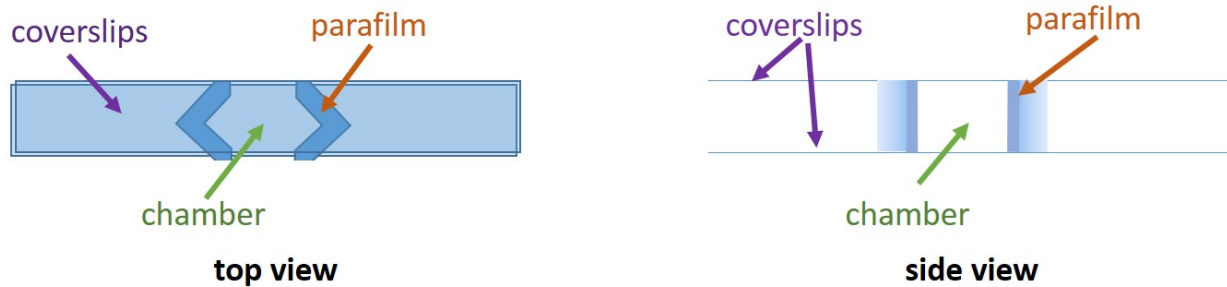
FIGURE 4.2: **Schematic of the top and side view of the chamber design for adhesion assays using micropipette manipulation.** Design reduced exposed surface area of liquid within chamber whilst increasing the volume of fluid able to be contained within the chamber. Parafilm was used to form the chamber between two coverslips.

A heated glass bead (70°C) can be used to cut the capillary to the correct diameter. However, this method can cause the pipette end to bend due to the heat from the glass bead, resulting in difficulties catching RBCs or beads. A second method involves placing the uncut pipettes onto yellow tac (UHU) and using a scalpel to exert pressure upon the tip, approximately 12 mm from pinch point, resulting in a clean cut pipette of the correct diameter.

4.2.3 Building the cell chamber

The cell chamber required significant modifications in order to develop an optimized design. There were two main requirements. Firstly, the pipettes had to be able to enter from opposing sides whilst still being able to reach the center and bottom of the chamber. This put restrictions on the width of the chamber, as well as the design of the chamber. A further requirement was that evaporation of the solution had to be reasonably slow ($< 10\mu$l/hr) to ensure that the RBCs remained healthy in an isotonic solution.

The basic design has two glass coverslips, ($50 \times 22 \times 0.2$mm^2 sourced from Merck, USA), with parafilm in between to form the chamber. The arrangement is heated to melt the parafilm and a chamber is formed (depth $\approx$2mm). The original design was for deformability measurements where only one opening was required.

The chamber design further needed to minimize the evaporation rate while ensuring that the capillary forces were sufficient to retain the solution in the chamber. This was achieved through a chevron design in which two chevrons were used to form a chamber in the shape of an opened diamond. A schematic of the chamber design is shown in Fig. 4.2. The simplest design of two

parallel lines of parafilm was considered, however the original width of the coverslips was too large. The coverslips were then halved, however although the width was ideal, the surface area to volume ratio was too high resulting in an unacceptable rate of evaporation. Doubling the depth of the chamber fixes the evaporation issue, however capillary forces were then not strong enough to retain the solution in the chamber. The final chevron design was settled on as being optimal. Oil was considered as a seal to reduce the evaporation rate, however due to its higher viscosity it detrimentally affected the pipette movement which was unacceptable.

4.2.4 Setup of the piezoelectric actuator

To obtain cytoadhesion probabilities with specific contact times, consistent velocities, and displacements, it was necessary to automate the adhesion assay process with a piezoelectric actuator (piezo translator). Piezo translators operate using the piezoelectric properties of crystals, which when placed under a strong electrical field change width proportional to the applied field.

A fast prototyping board (Arduino Uno, USA) was used to generate the required signal for the piezo translator. The board outputs a signal using pulsed-width modulation (PWM), where it generates a square wave that is time averaged to produce an analogue signal. This is achieved by using a simple first-order low-pass filter, consisting of three resistors varying from $1 - 10\,k\Omega$ and a grounded capacitor, 220μF. The Arduino Uno can be programmed to ramp up the duty cycle to the desired level, hold for the specified time, and then ramp down to the initial duty cycle.

This program enabled the piezo translator to move the RBC, at a constant velocity, into contact with the bead for a set length of time and then move back to the original position, again at constant velocity. This can be repeated consistently as many times as necessary to obtain statistically significant data. The parameters are defined by the operator prior to compiling and uploading.

The circuit diagram used to generate an analogue signal with the Arduino Uno is shown in Fig.4.3. A push button (left) is used to begin the cycle, and the LED (centre) is used to show the change in duty cycle. The piezo translator was mounted inline on the micropipette boom arm, which was machined to accommodate it. An amplifier (Thorlabs 3-axis piezo controller model MDT693) was used to amplify the analogue output from the Arduino. The amplifier increases the voltage supplied by a factor of 15 and limits the current to $60\,$mA. The maximum voltage obtained using the Adruino Uno is 5 V. Incorporating the amplifier increases the maximum voltage output
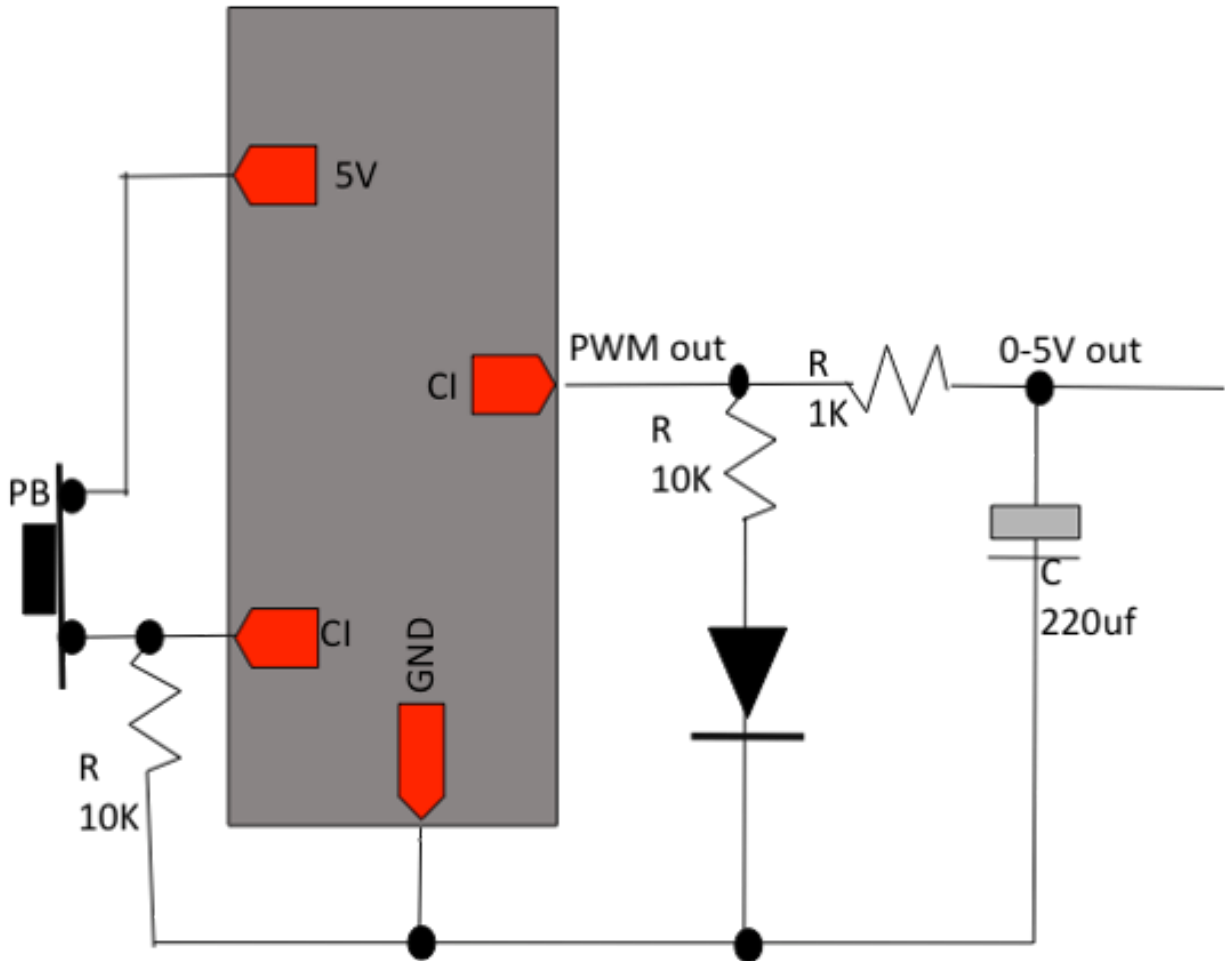
FIGURE 4.3: **Circuit diagram used to generate triangular signal.** Push button (PB) is used to start/stop the electric signal to the actuator. 5V is applied to the circuit, a simple first-order low-pass filter consisting of resistors (R) and a grounded capacitor (C) which generates a time-averaged square wave with voltage ranging from 0 to 5 V. An LED (∇) is used to visually show the change in voltage output. Cl indicates connection to the computer and system is grounded (GND).

to 75 V, which corresponds to a displacement of $8\,\mu$m. The Arduino Uno program is detailed in appendix A.1.

4.2.5   iRBC and bead preparation

The *P. falciparum* parasites were cultivated as described in section 3.2.3. Parasites were selected for knobs by the gelatin floatation method (see section 3.2.5) two days prior to experiment. The culture was then synchronised using sorbitol (see section 3.2.5) the day before the experiment and assessed for a parasitemia (see section 3.2.4) of greater than 4% ring stage. On the day of the experiment the culture was again assessed to ensure there was a parasitemia of greater than 4% in
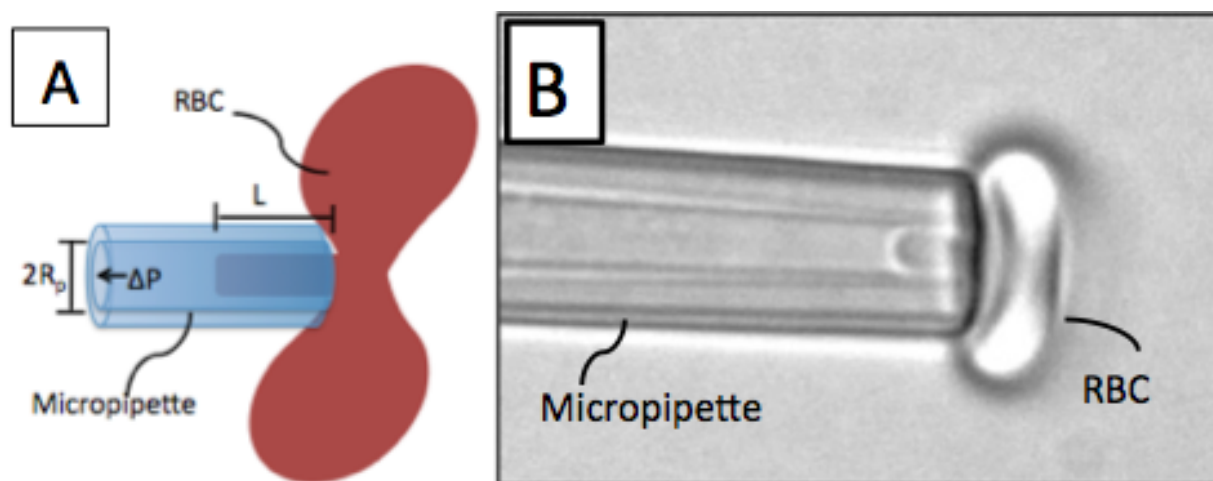
FIGURE 4.4: **Micropipette aspiration of RBC using glass micropipette.** Schematic representation (**A**) of a micropipette aspirated RBC where L is the length of tongue pulled into micropipette of radius R_p by a hydrostatic pressure ΔP. The length of tongue is related to the hydrostatic pressure as detailed in equation 4.1. **B**: An image of a micropipette aspirated RBC (modified from (Lee and Lim, 2007)).

the trophozoite stage. 5 ml of the culture was then centrifuged down, the supernatant removed, fresh media added and then placed in a 50ml falcon tube, gassed and kept at 37^oC until required.

Recombinant human CD36 (R&D systems, USA) was coated onto acid washed glass (silica) beads (Bangs Beads, USA) 4.86±0.47 μm diameter. 10 μl of the glass beads (0.5% w/v), 10 μl sterile water (Baxter Healthcare) and 2 μl of CD36 (100 μg/ml) was added to the micro centrifuge tube and incubated for 1 hr at room temperature. During incubation the tube was gently mixed 5 times every 10 minutes to achieve an even coverage of CD36 on the glass beads. After 1 hr had elapsed, 1000 μl of sterile water was added and the solution was placed into microcentrifuge tubes in 4μl aliquots which were stored in the -18°C freezer until use (for a maximum of 1 month).

4.3 Measuring the shear elastic modulus of iRBCs

The adhesion force of an iRBC to CD36 can be measured directly by the amount the RBC is deformed, due to presence of the bond, if the RBC stiffness is known. The shear elastic modulus (μ) is representative of a cells 'stiffness'. The ability to measure the cell stiffness of the same iRBC that is getting measured for adhesion is an advantage of the micropipette procedure. Cell stiffness can be measured using a micropipette aspiration technique (Hochmuth, 2000; Nash, Johnson, and Meiselman, 1984; Evans and La Celle, 1975; Lee and Lim, 2007). A schematic (A) and optical image (B) of an aspirated erythrocyte are shown in Fig. 4.4.

Micropipette aspiration was carried out as previously described (Black et al., 2008). Briefly, the iRBC having previously been caught by the micropipette, with radius R_p, to carry out adhesion assay is held at equilibrium, i.e. with the pressure being such that the RBC is neither pushed away from nor pulled into the pipette. The position of the 'tongue' is recorded. The hydrostatic pressure is then increased incrementally, ΔP, and each time the new tongue position, ΔL_p is recorded (refer to schematic in Fig. 4.4).

The elastic shear modulus (μ), was calculated using equation 4.1 (Hochmuth, 2000).

$$\frac{\Delta L_p}{R_p} = \frac{1}{2.45} \frac{\Delta P R_p}{\mu} \tag{4.1}$$

where L_p is cell elongation (length of tongue) in μm, R_p is micropipette inner radius in μm, 2.45 is constant dependent on mechanical model used, ΔP is the suction pressure exerted in pN /μm^2 and μ is the shear elastic modulus, pN/μm.

Fig. 4.5 shows experimentally obtained data for a single iRBC. Linear regression was carried out to obtain a linear line passing through the origin. Linearity was checked by the R^2 value which was between 0.992 to 0.995 across the iRBCs measured, indicating data had a good fit and was linear over the strains to which the iRBC was exposed. The gradient of this slope can then be converted, via eq. 4.1, to obtain the shear elastic modulus. For iRBCs the elastic modulus values obtained ranged from 17 to 28 pN/μm, whereas for uninfected RBCs the shear elastic modulus ranged from 2 to 5 pN/μm. This is comparable to values reported in the literature (Suwanarusk et al., 2004; Glenister et al., 2002; Glenister et al., 2009).

To determine whether the RBC elastic modulus remained constant over the range of stresses subjected to the RBCs during the adhesion experiment, the force exerted on RBC as it is aspirated into pipette, F_p was plotted versus the length of the RBC aspirated, L_p (Fig. 4.6). The force experienced by the RBC during micropipette aspiration was determined by the product of the hydraulic pressure, ΔP exerted on the RBC and the cross sectional area (a function of the micropipette radius, R_p) over which the pressure was applied (eq. 4.2).

$$F_p = \pi R_p^2 \Delta P \tag{4.2}$$
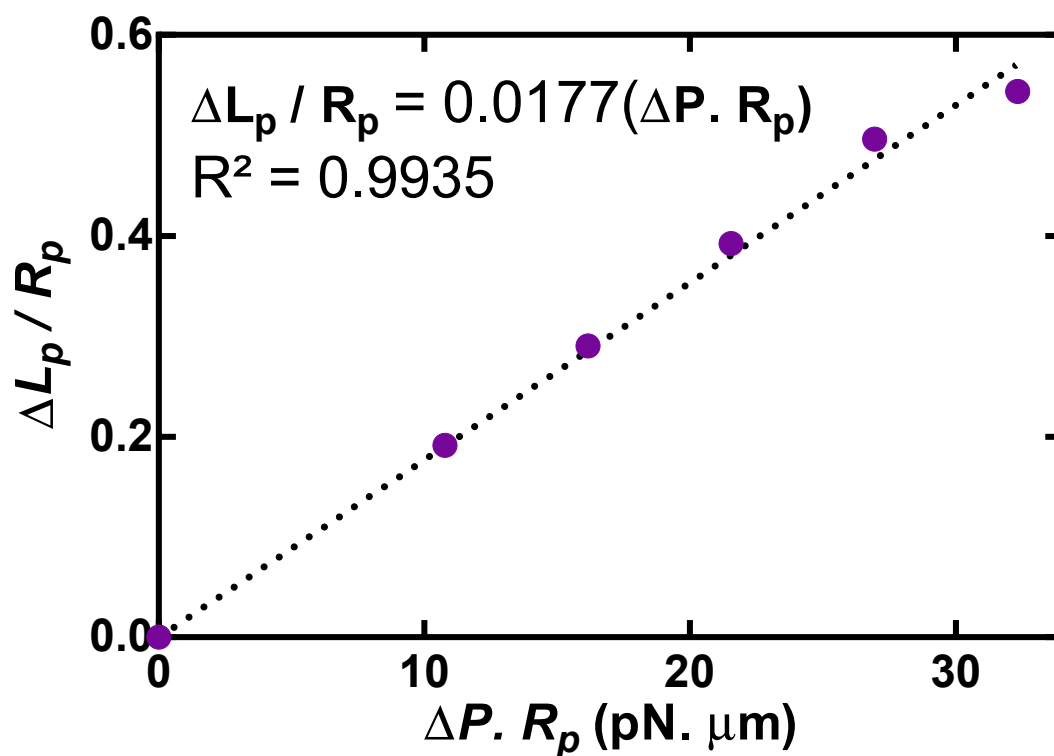
FIGURE 4.5: **Micropipette aspiration results for a single iRBC showing tongue length as a function of applied hydrostatic pressure.**The tongue length ΔL_p in μm of a RBC aspirated into a micropipette divided by the radius of the pipette R_p in μm was plotted against the hydraulic pressure ΔP (pN/μm) exerted on the cell multiplied by the pipette radius. Linear regression was carried out on data to obtain the gradient. The elastic modulus, μ (pN/μm) was determined from the inverse of gradient multiplied by a mechanical model factor 0.4, as detailed in eq. 4.1. The goodness of fit to the linear regression was measured by an R^2 value (R^2 was between 0.992 - 0.995).
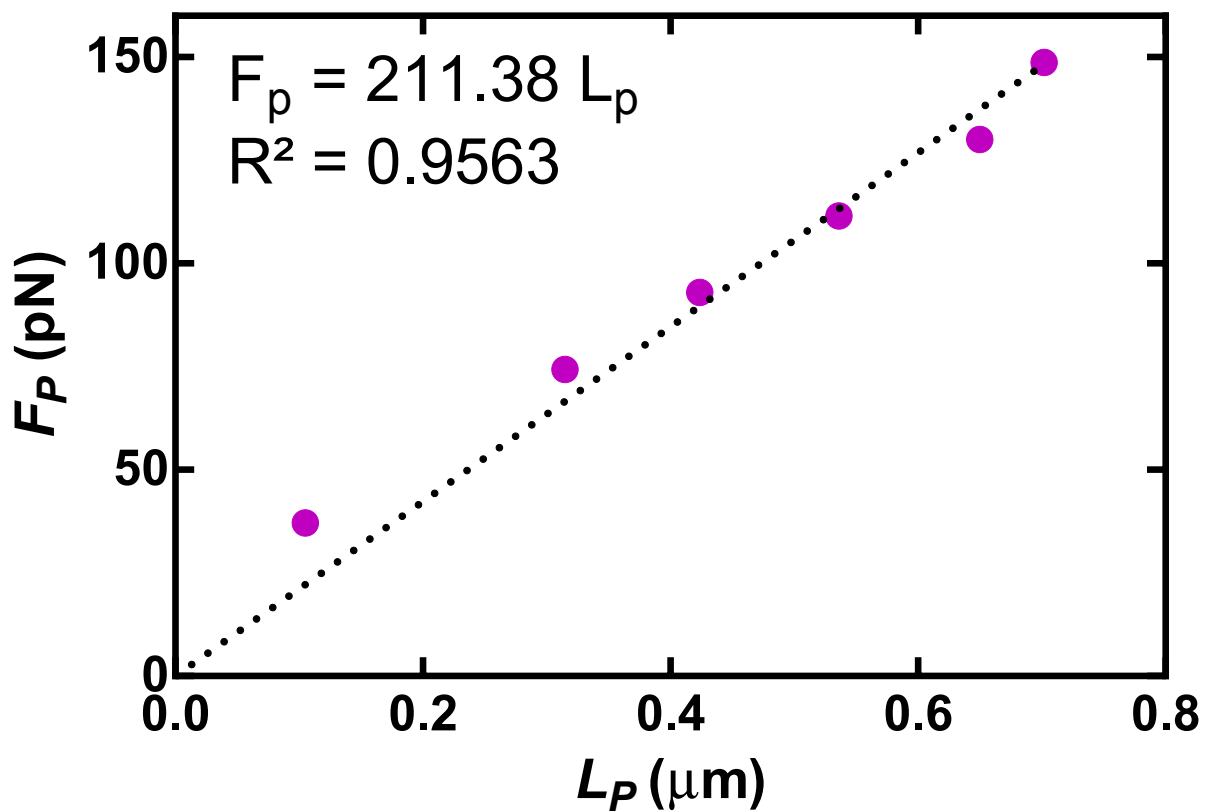
FIGURE 4.6: **Force exerted on RBC during aspiration versus length drawn into pipette for a single iRBC.** The force F_p exerted on a RBC during aspiration is linear over the length L_p the cell is pulled into the pipette. The elastic modulus, μ, is constant over force ranging between 0 and 150pN and an R^2 values ranging from 0.94 to 0.98.
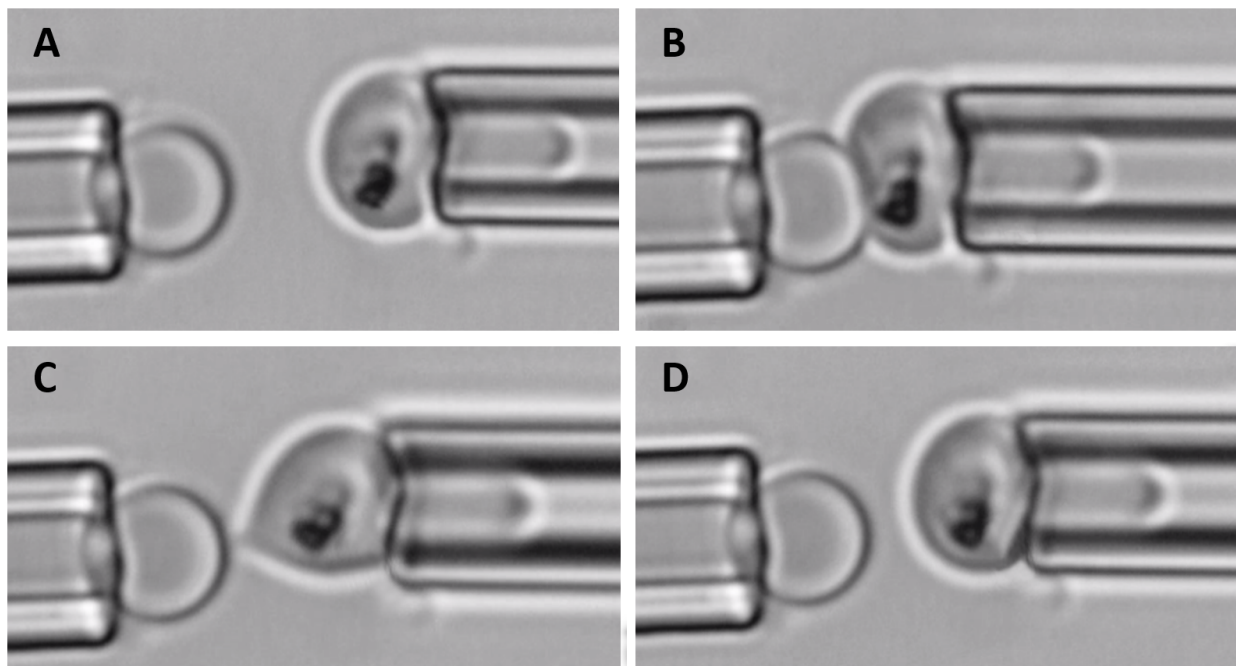
FIGURE 4.7: **Sequence of steps in adhesion experiment**. (A) An iRBC and a CD36 coated bead are securely trapped by opposing pipettes and held at rest for specified time. (B) The iRBC is moved at constant velocity until it is brought into contact with the bead, the compressive force of this contact can then be found. Contact is held for a predefined time. The RBC is then moved away at a constant velocity and adhesion (C) or no adhesion (D) is visually observed. The cycle is repeated as required.

4.4 Results and Discussion

A CD36 coated glass bead was held securely in the left hand side pipette whilst an iRBC was held in the right hand side pipette (Fig. 4.7 -A). They are brought into contact (Fig. 4.7 -B) for a specified time. The right hand side pipette was then slowly drawn back and adhesion was either observed (Fig. 4.7 -C) or not observed (Fig. 4.7 -D).

4.4.1 Probability of adhesion of *P. falciparum* infected red blood cells to CD36

The probability of adhesion, P_A, was determined via visual confirmation in the form of elongation of the RBC. The total number of adhesions was divided by the total number of contacts in the cycle (minimum of 50 contacts per cycle). To ensure the adhesions counted in the probability analysis were due solely to specific PfEMP1-CD36 adhesions and not non-specific interactions, negative controls were examined.

Three factors were analysed with respect to RBC preparation to determine whether they significantly affected adhesion. RBCs obtained directly from blood donors were analysed for adhesion
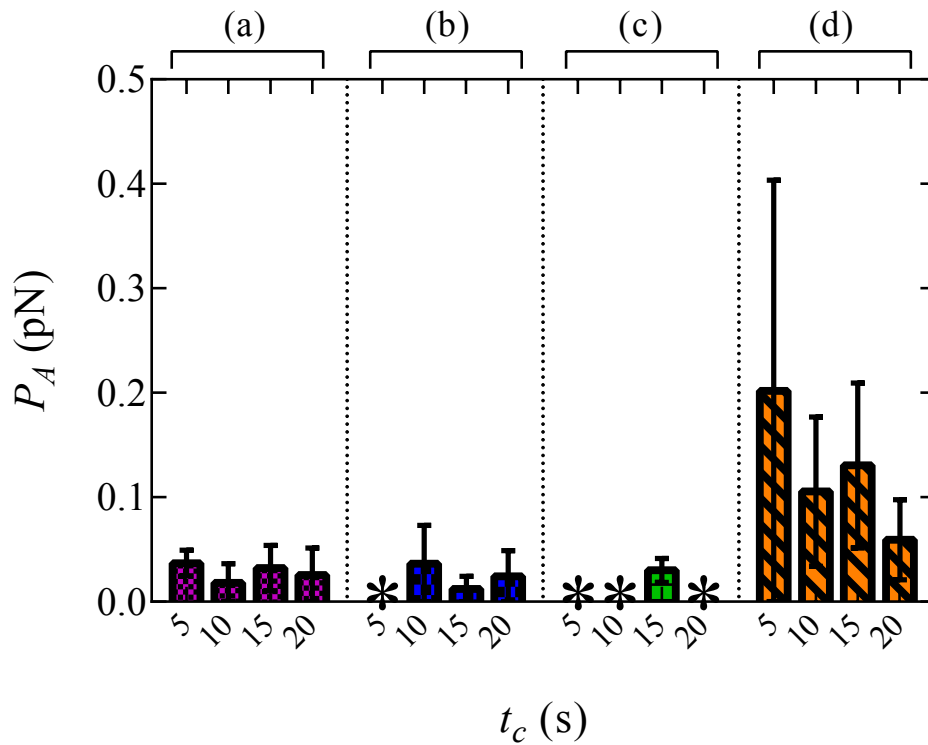
FIGURE 4.8: **Probability of adhesion,P_A, for various contact times, t_c(s) of healthy RBCs vs CD36.** The probability of adhesion P_A of RBC (blood sourced direct from donors and which had never come into contact with *P. falciparum*) was brought into contact with CD36 coated glass beads for various contact times, t_c(s) (a). P values obtained from ANOVA test across contact times indicate no statistically significance (P>0.05). The experiment was carried out again but with the donor blood was washed by centrifugation (b). There was no statistical significant variance of P_A across contact time or between washed and unwashed RBC (P>0.05). Uninfected blood was taken from culture that had been exposed to parasite for 48hr (c). Exposure to culture showed no statistically significant effect on adhesion probability for contact time or compared to RBC that had not been exposed to culture (P>0.05). Stressing the RBC membrane (d) had a statistically significant effect on the adhesion probability (P=0.036). A cell was considered stressed when greater than 50% of the cell volume had been pulled into pipette. Error bars show ± standard error of the mean (n=6). Significance was determined by One way ANOVA test of the mean value. * indicate mean and error was zero.

with CD36 coated glass beads to compare whether washing the RBCs affected adhesion. RBCs were washed as described in section 3.2.2. Secondly, the effect of RBCs being exposed to *P. falciparum* in culture was compared by using uninfected RBCs that had been in culture for a period of 48hr. Finally, the effect of excessive stress on the RBC was analysed by sucking the RBC into the pipette until the ratio of RBC volume free to in the pipette was less than 2:1 and then the adhesion assay was conducted.

The results are shown in Fig 4.8. The mean values were taken from the probability of adhesion for 100 contacts per RBC for 3 different RBCs per day, on two different days for contact times 5s, 10s, 15s and 20s. The error bars shown are standard error of the mean. For empty columns no adhesion was observed. Washing or not washing, and exposure to culture had no statistically significant (P>0.05) effect on the probability of adhesion that was observed. Further, increasing contact time had no effect on adhesion probability. However, stressing of the RBC so that over 50% of the RBC volume was pulled into the pipette did show a potentially different probability of adhesion. As such, when conducting the adhesion experiment care was taken to ensure that at least 75% of the RBC remained outside of pipette.

To determine the binding specificity, the probability of adhesion of iRBCs with CD36 coated glass beads (Fig: 4.9-column 1) was compared to that of iRBCs with un-coated glass beads (Fig: 4.9-column 2) for the same contact times and apparent contact area (6 μm^2). The uncoated glass beads were prepared in an analogous method to that described in section 4.2.5 without the CD36 being added. Adhesion was dramatically decreased when CD36 was not present on the bead. Moreover, the probability of adhesion of un-infected RBCs with CD36 coated glass beads (Fig: 4.9-column 3) and un-infected RBCs with un-coated glass beads (Fig: 4.9-column 4) showed a statistically significant decrease in the probability of adhesion (P < 0.0039). The time of contact did not have a statistically significant effect on the probability of adhesion.

The dependence of P_A on t_c was systematically measured and the results shown in Fig. 4.10. The probability of adhesion was measured for each experiment, and the mean and standard error was taken across all experiments carried out at a constant contact time. To ensure 50 contacts was sufficient to get an accurate probability, the total number of adhesions were divided by the total number of contacts for each contact time. The values were accurate within the error bars, and consequently all further analysis was carried out only for the overall probabilities at each contact
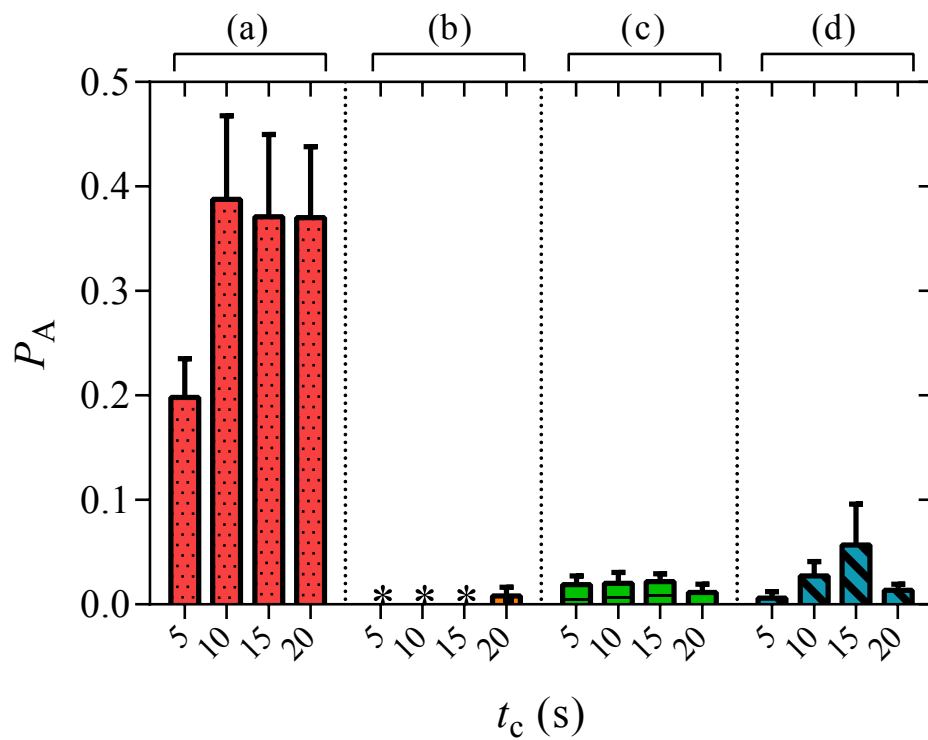
FIGURE 4.9: **Demonstration of binding specificity.** Each grouped data set shows probability of adhesion for contact times 5s, 10s, 15s and 20s. 3D7 iRBCs with CD36 coated glass beads (a), 3D7 iRBC with uncoated glass bead (b), healthy RBC with CD36 coated glass bead (c) and healthy RBC with uncoated glass bead (d). * indicates the mean and error are 0.
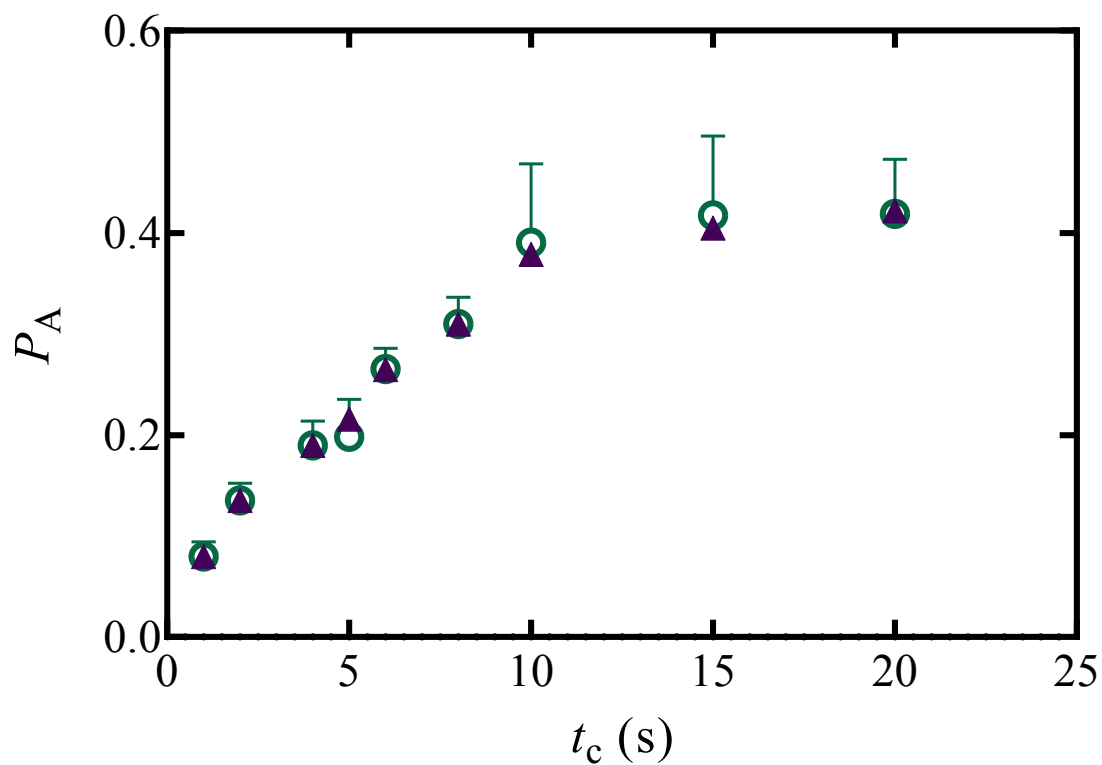
FIGURE 4.10: **Probability of adhesion (P_A) versus contact time (t_c) of iRBCs to CD36.** A single iRBC and bead were selected and for each contact time 50 cycles were conducted and the probability of adhesion obtained. The mean of different iRBC-bead pairs (green circle) was obtained. Error bars represent (+) standard error of the mean (n=4). For each contact time the overall probability (purple triangle) was obtained by dividing total number of adhesions by the total number of contact cycles. As this is an overall value across all iRBC pairs there is no mean or error bars.

time. As expected, the probability of adhesion increased with increasing the contact time, reaching a plateau at contact times greater than 10s. Information about the kinetic rates is contained within the initial transient phase, whereas the equilibrium association constant can be derived from the steady state phase.

As described in detail in sec. 2.6.5, the master equation can be solved for the probability of zero bonds occurring at a specified contact time, $p_0(t)$. As $p_A(t)=1-p_0(t)$, the measured and predicted dependence of adhesion probability on contact time can be plotted and evaluated to find the kinetic rates and equilibrium adhesion constant of PfEMP1-CD36 interaction. Briefly, the kinetic mechanism used for these calculations assumes a first order dissociation rate and an overall second order in association (first order for both CD36 and PfEMP1). The master equation can be simplified by approximations if densities of one or more components can be approximated to be constant. A binomial approximation (eq. 4.3) can be used if one density is significantly greater than the other, meaning the comparatively large density of either receptor or ligand can be approximated to remain constant.

$$p_A(t) = 1 - [1 - q(t)]^{-A_c m_{min}} \tag{4.3}$$

where:

$$q(t) = \frac{1 - \exp(-k_r t_c)}{1 + m_{max} K_A^o} \tag{4.4}$$

A Poisson distribution (eq. 4.5) can be used if the number of bonds is significantly lower than the densities of both receptors and ligands, receptor and ligand density can be assumed to remain constant.

$$p_A(t) = 1 - \exp\left\{-A_c m_r m_l K_A^o \left[1 - \exp(-k_r t_c)\right]\right\} \tag{4.5}$$

where:

p_A = probability of adhesion, A_c = area of contact (μm^2), m_{min} = density of the species (either receptor or ligand) that has the lower density (molecules/μm^{-2}), m_{max} = density of the species (either receptor or ligand) that has the higher density (molecules/μm^{-2}), m_r = receptor density (molecules/μm^{-2}), m_l = ligand density (molecules/μm^{-2}), K_A^o = equilibrium adhesion constant (μm^2), t_c = contact time (s) and k_r = reverse rate constant (s^{-1}).

To determine the most accurate approximation, the experimental data (p_A versus t_c) was curve

fitted using the two models (binomial and Poisson) and the goodness of fit (R^2) compared. The Poisson distribution is actually a limiting case of a binomial distribution when the number of trials, n, is large and p_A, the probability of success (adhesion), is small.

In order to evaluate the models initial values and constants need to be defined. The area of contact was kept constant for both models, at a value $A_c = 7.33\ \mu m^2$ corresponding to the mean contact area across all experiments (contact area is discussed in greater detail in sec. 4.4.2). However, the densities of *Pf*EMP1 (ligand) and CD36 (receptor) are unknown in this case.

Chesla, Selvaraj, and Zhu (1998) explored the interaction between CD16A receptor expressed on Chinese hamster ovary cell transfectants and immunogobulin G (IgG) coated on human erythrocytes using an analogous micropipette method and analysis. The densities of receptor and ligand were able to be determined and consequently the equilibrium adhesion constant, K_A^o for this interaction was found unambiguously. However due to basic fundamental problems concerning the determination of *Pf*EMP1 and Cd36 densities these are unknowns.

*Pf*EMP1 is a highly variant antigenically diverse malarial protein of 200–350 kDa. Consequently, it is very difficult to make an antibody, to which it binds, to obtain information about the density of *Pf*EMP1 on the surface of the iRBCs. A further complication is the presence of knobs and the effect they have on density distribution and activity of *Pf*EMP1. Knobs are a requirement for cells to adhere under flow conditions (Crabb et al., 1997) and the density of knobs, ρ_k, on iRBCs can be measured (Quadt et al., 2012; Subramani et al., 2015). However, *Pf*EMP1 expression is not restricted to the knob surface (Rug et al., 2006) since the *Pf*EMP1 molecules remain organized in clusters whether knobs are present or not. Further, the *Pf*EMP1 variant expressed will actually affect the resulting knob density (Subramani et al., 2015). To further complicate matters the actually density of protein varies in the presence of knobs with protein density being sparse on the knobs apart from the apex of the knob where a high density of protein is found (Watermeyer et al., 2016).

A simple assumption is that *Pf*EMP1 density is related to the knob density (Subramani et al., 2015). A range of *Pf*EMP1 densities can be approximated if knob density is known. A minimum *Pf*EMP1 density $m_{l,min}$ could be assumed to correspond to one *Pf*EMP1 per knob ($m_l = \rho_k$). Maximum *Pf*EMP1 density $m_{l,max}$ corresponds to the maximum number of *Pf*EMP1 that could physically fit onto a knob (Subramani et al., 2015). Values of published knob density and consequently a range of *Pf*EMP1 density are shown in table 4.1. These values in connection with CD36

densities were used as initial values to fit the Poisson and binomial distributions.

The density of CD36 coated on glass beads is another unknown. Antibodies to recombinant CD36 are accessible. However, to determine the exact density of CD36 on the glass beads, concentration standards on similar sized glass beads would also be required which could not be obtained. Estimates of CD36 density were taken from published articles and used as initial values for analysis (table 4.1).

Non-linear regression was carried out on the overall probability of adhesion data as a function of contact time. Fourteen combinations of *Pf*EMP1 and CD36 densities were examined, and the kinetic rate of dissociation, equilibrium association obtained and the R^2 values (goodness of fit) were analysed. Evaluation of the time variant probability of adhesion for PfEMP1-CD36 interaction gave a kinetic rate of dissociation k_r of $0.113 \pm 0.0153 \text{s}^{-1}$. The dissociation rate is higher than the k_r of 0.0707s^{-1} reported in Xu et al. (2013) which used atomic force microscopy (AFM) and flow experiments to determine kinetic rate. There was no statistical difference between the Poisson and binomial models for any of the combinations analysed with a constant R^2 of 0.9806. Table 4.1 lists the results of the analysis. The fitting method used was least squares.

An overall combined equilibrium constant of association $m_r m_l K_A$ of 0.091 ± 0.007 was found using the Poisson model. The equilibrium constant of association was found for the 14 combinations of receptor and ligand densities (table. 4.1). Due to the variation in densities, the value of K_A varied from $(2.3 \pm 0.17) \times 10^{-4}$ to $(1.1 \pm 0.088) \times 10^{-7}$.

4.4.2   Adhesive force between iRBCs to CD36

Determining the adhesive and compressive forces

The forces associated with adhesion can be calculated by the magnitude of the stretch or compression of the RBC given the deformability of the cell. An advantage of this micropipette technique is the ability to accurately measure the deformability of each individual cell being investigated. The simplest model relating amount deformed to force exerted is the linear spring model (eq. 4.6).

$$F = \mu \Delta x \tag{4.6}$$

The deformation, Δx, was found by measuring the resting diameter compared to the maximum extended diameter due to adhesion, or minimum diameter due to compression (Fig. 4.12). The

TABLE 4.1: Derived values and goodness of fit from master equation approximations of binomial and Poisson distributions. * Density of CD36 and PfEMP1 are given in molecules/μm^2

Density*		Binomial distribution			Poisson distribution		
*Pf*EMP1	CD36	K_A ($\times 10^5$) (M)	k_r(s^{-1})	R^2	K_A ($\times 10^5$) (M)	k_r (s^{-1})	R^2
20	20	23 ± 1.7	0.113 ± 0.015	0.9806	23 ± 1.7	0.113 ± 0.015	0.9806
35	20	13 ± 0.98	0.113 ± 0.015	0.9806	13 ± 0.98	0.113 ± 0.015	0.9806
50	20	9.4 ± 0.69	0.113 ± 0.015	0.9806	9.4 ± 0.69	0.113 ± 0.015	0.9806
8000	20	0.057 ± 0.0044	0.113 ± 0.015	0.9806	0.057 ± 0.0044	0.113 ± 0.015	0.9806
5	50	36 ± 2.8	0.113 ± 0.015	0.9806	36 ± 2.8	0.113 ± 0.015	0.9806
20	50	9.1 ± 0.70	0.113 ± 0.015	0.9806	9.1 ± 0.70	0.113 ± 0.015	0.9806
35	50	5.2 ± 0.41	0.113 ± 0.015	0.9806	5.2 ± 0.41	0.113 ± 0.015	0.9806
50	50	3.6 ± 0.28	0.113 ± 0.015	0.9806	3.6 ± 0.28	0.113 ± 0.015	0.9806
8000	50	0.023 ± 0.0018	0.113 ± 0.015	0.9806	0.023 ± 0.0018	0.113 ± 0.015	0.9806
5	100	18 ± 1.4	0.113 ± 0.015	0.9806	18 ± 1.4	0.113 ± 0.015	0.9806
20	100	4.6 ± 0.35	0.113 ± 0.015	0.9806	4.6 ± 0.35	0.113 ± 0.015	0.9806
35	100	2.6 ± 0.20	0.113 ± 0.015	0.9806	2.6 ± 0.20	0.113 ± 0.015	0.9806
50	100	1.8 ± 0.14	0.113 ± 0.015	0.9806	1.8 ± 0.14	0.113 ± 0.015	0.9806
8000	100	0.011 ± 0.00088	0.113 ± 0.015	0.9806	0.011 ± 0.00088	0.113 ± 0.015	0.9806
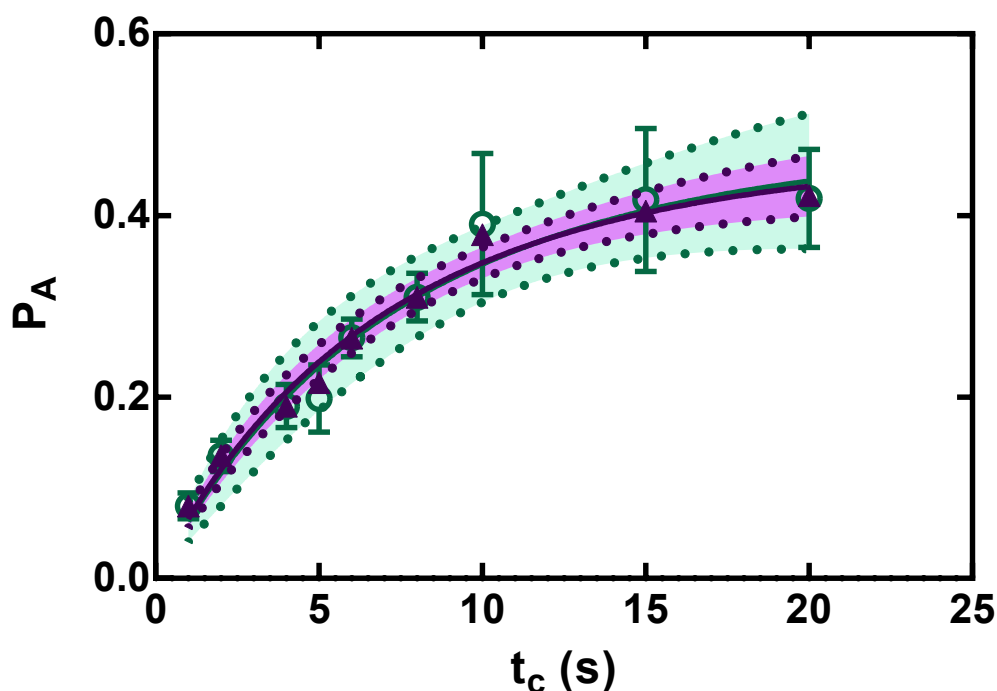
FIGURE 4.11: **Probability of adhesion (P_A) versus contact time (t_c) for the interaction of iRBCs with CD36.** A nonlinear equation 4.5 was fit to the mean and overall data (solid lines) with 95% confidence interval (dotted lines). The fit was used to obtain the on and off rates for PfEMP1 and CD36 interaction. The fitting method used was least squares and no constraints or weighting was used.
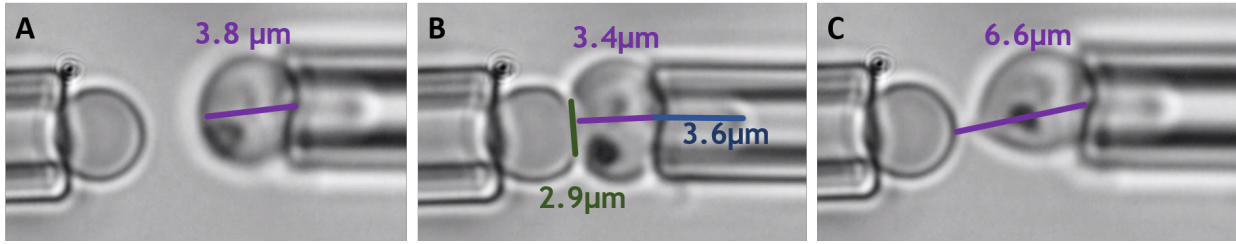
FIGURE 4.12: **RBC deformation measured using point to point difference.** The point to point distance was measured at resting state (A) from the pipette edge to the edge of the iRBC membrane to obtain iRBC diameter. The iRBC is then brought into contact with bead (B) and the new compressed diameter is measured. During compression (B) the contact distance $(2r)$ and the length of the iRBC that is sucked into the pipette (L_p) are also measured. The iRBC is moved away from the bead and if adhesion occurs the maximum extension of the iRBC membrane is recorded.

high speed digital camera was calibrated using a micro ruler to convert the units from pixels to μm. The RBC stiffness, μ, in pN/μm, is the elastic shear modulus measured using the micropipette aspiration technique for each RBC, as detailed in sec. 4.3.

Determining area of contact

The area of contact, A_c, was calculated to determine what, if any, effect it had on the resulting adhesive force. Area of contact can be approximated by visual measurement of the RBCs length of contact, $2r$, with the glass bead (Fig. 4.12-B). The simplest assumption is that the contact area is circular (eq. 4.7):

$$A_c = \pi \left(\frac{2r}{2} \right)^2 \tag{4.7}$$

where r is the contact radius as indicated on schematic in Fig. 4.13

RBCs are not spheres, they are bioconcave disks with a flattend center. The contact area between two spheres is a circle. Therefore once the contact length surpasses that of the minimum diameter of the RBC the contact area may not be circular (Fig. 4.14). Nevertheless a circular contact area can still be used as a first approximation. Further, as the parasite matures the RBC becomes more sphere-like thus increasing $D_{minimum}$ progressively.

To determine what, if any, relationship exists between the observed contact area and the compressive force felt by the RBC these values were plotted as shown in Fig. 4.15. The mean contact area for compressive forces varying from 10 to 50 pN was found to increase as compressive force
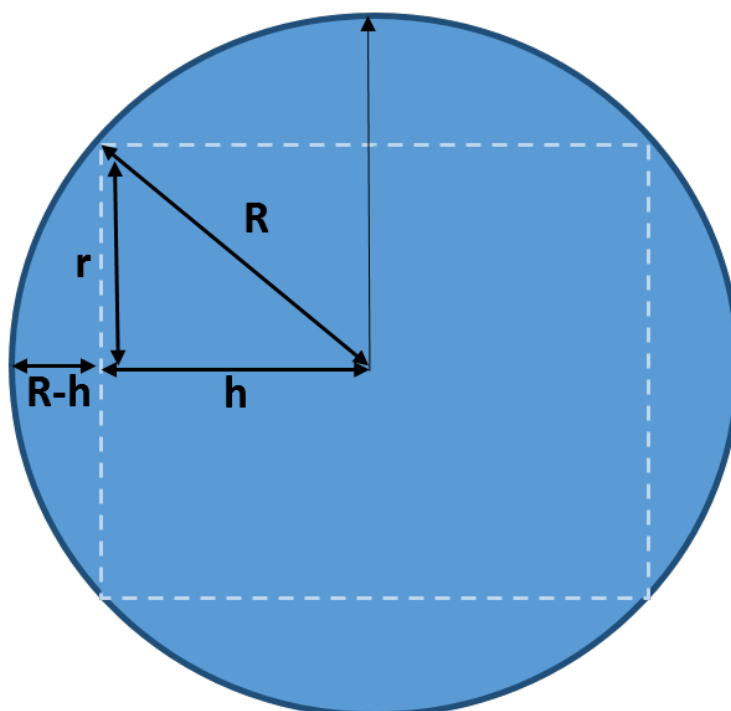
FIGURE 4.13: **Schematic of circle defining radius and compression length.** If cell can be assumed to be circular in the 2D view the radius, R and compression length, $(R - h)$ are related by Pythagoras theorem to the contact radius, r which is used to find the contact area, A_c. This method can only be used if shape is circular and not oval.
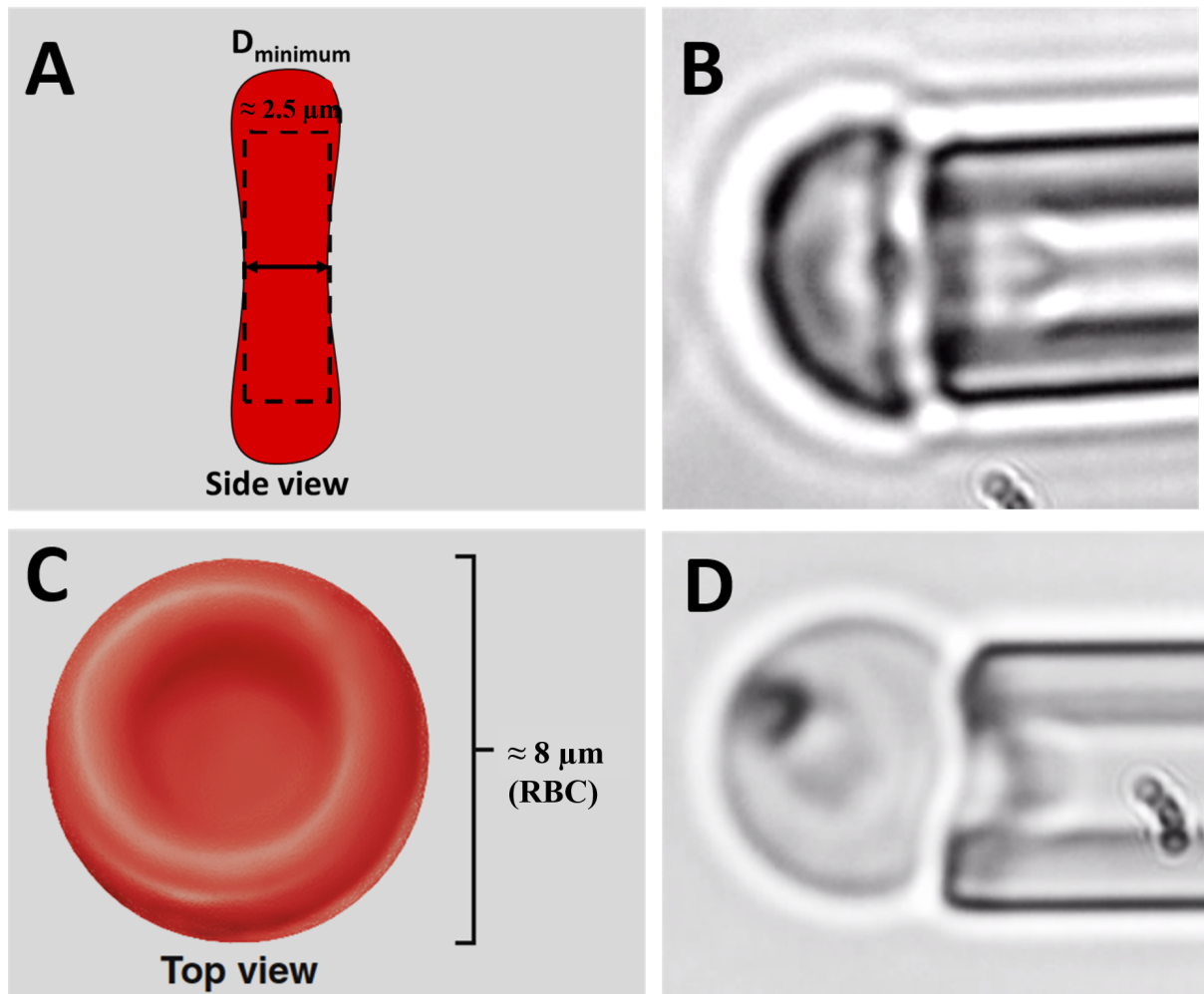
FIGURE 4.14: **RBCs are shaped as a biconcave disk with a flattened center.**
Schematic (**A**) of the side view of a RBC, indicating the minimum diameter
($D_{minimum}$) in the x direction. Shape is approximately a rectangle and as such, since
diameter is not constant, eq. 4.8 is not valid. This situation occurs when cell is
caught in pipette as shown in (**B**). (**C**) shows a schematic where cell can be approxi-
mated as circular and hence eq. 4.8 may be valid. (**D**) shows a situation where iRBC
is caught such that 2D view can be approximated as circular.
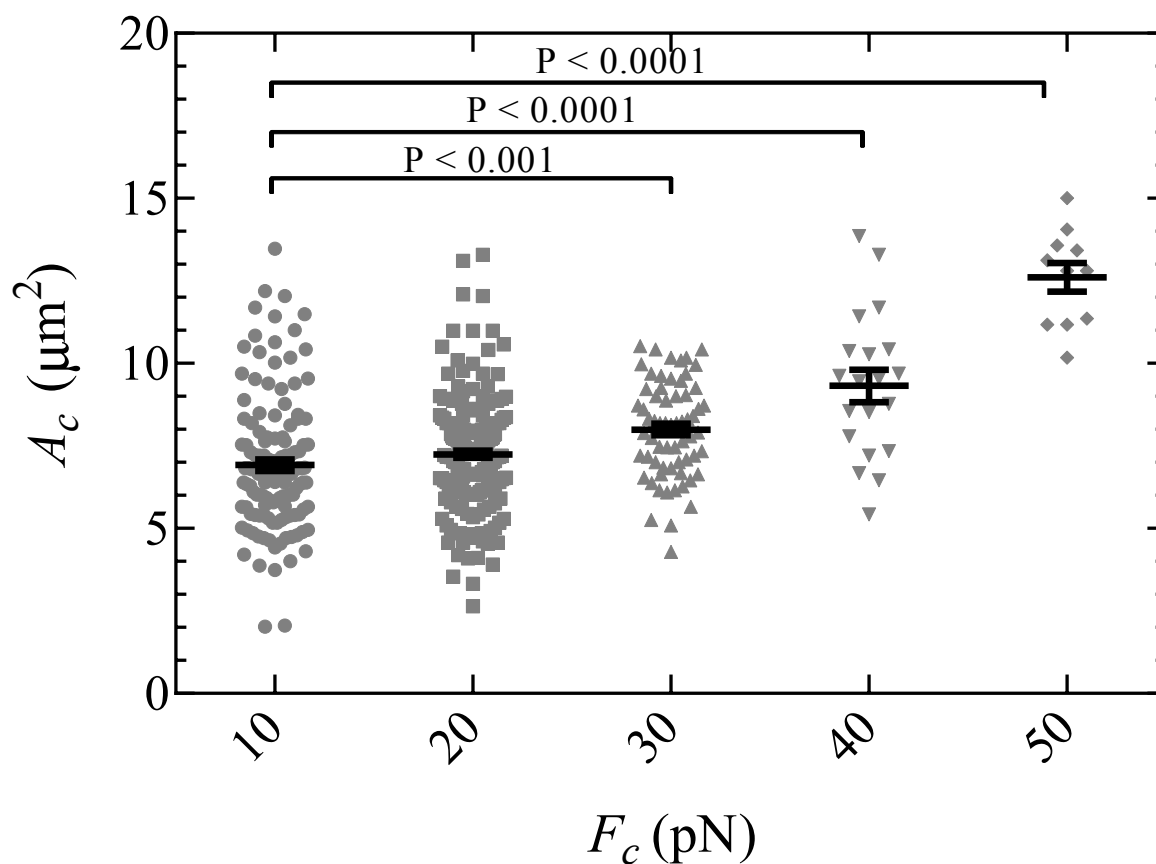
FIGURE 4.15: **Measurements of contact area, A_c of iRBCs in contact with CD36 coated glass beads with varying forces of compression, F_c.** Individual values of A_c are shown in gray whilst the mean and standard error are shown in black. The mean contact area increases with increased compressive force. Significance was calculated using one way ANOVA and is shown for increasing F_c. Significant difference between the means, $F(4,436)=33.72$, $P<0.0001$.

was increased. The mean contact area between 10 to 20 pN was found to be statistically insignificant ($P>0.05$). However the mean contact area for a compressive force of greater than 30pN compared to that of 10pN was found to be statistically significant ($F(4,436)=33.72$, $P<0.0001$). To further investigate the relationship between contact area and compressive force, an analytical approach was taken to determine how compressive force relates to contact area.

Relation between contact area and compressive force

The contact area can be found as a function of the compression length. The radius of contact, r, can be calculated:

$$r = \sqrt{R^2 - h^2}$$
$$= R\sqrt{1 - \left(\frac{h}{R}\right)^2} \qquad (4.8)$$

where $(R - h)$ is equivalent to the compression length, R is the radius of the RBC at rest, h is radius of RBC at compression and r is the radius of the circle formed at contact. These parameters are indicated in Fig. 4.13 . The derived contact radius, r, can be used to determine the contact area using eq. 4.7:

However, this relation between the contact area and the compressive force can be written only if the following is true:

1. The RBC can be approximated as a circle with a constant radius at any angle.

2. The compressive length is less than the minimum diameter of RBC.

These requirements restrict the cells suitable for this analysis. As shown in Fig. 4.14-(A,B), if the cell is caught in the flattened center it can not be approximated as a circle and thus eq. 4.8 is not applicable in this case. However if the cell is caught on the edge as shown in Fig. 4.14-(C,D), the radius can be approximated to be constant and thus eq. 4.8 can be used. Consequently, the contact area was determined visually as detailed in section 4.4.2, and not by the compressive length, for the remainder of this chapter.

Determining magnitude of non-specific adhesion forces

To determine the magnitude of non-specific adhesion, various negative controls were investigated and compared to the forces obtained during specific adhesion (Fig. 4.16). The mean force of adhesion of iRBCs with CD36 coated beads at various contact times was ≈ 40pN. This adhesion force is significantly larger than that obtained from non-specific bonds.

Out of over 200 contacts only one adhesion event occurred between iRBC and non-coated glass beads which had an adhesive force of 20pN, significantly lower than the mean force values obtained when CD36 was present. Further, when healthy RBC were put into contact with CD36
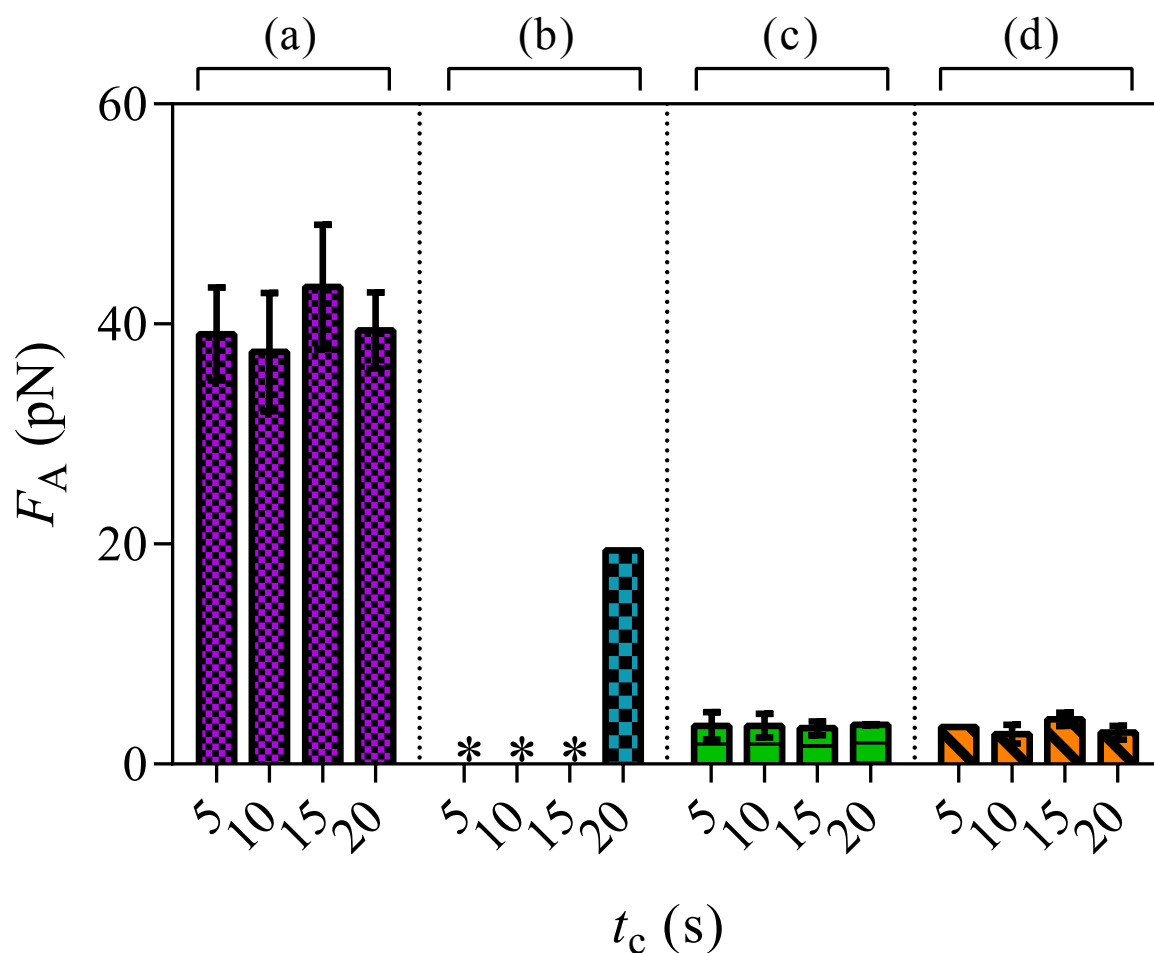
FIGURE 4.16: **Force of adhesion of *P. falciparum* with CD36 compared to negative controls.** The mean adhesion force for 3D7 infected RBCs with CD36 coated glass beads (a) is shown for various contact times (5s, 10s, 15s and 20s). The mean force is significantly greater than that of the negative controls ($F_A \approx 40$pN for iRBCS with CD36 coated glass beads). Healthy RBCs in contact with CD36 coated glass beads (b) and uncoated glass bead (c) had significantly smaller forces of adhesion (≈ 4pN).iRBC with uncoated glass bead (d) had no adhesion events for contact times 5, 10 and 15s. One adhesion event occurred at contact time 20s with a force of adhesion 19pN. Significance was determined statistically using one way ANOVA test (P<0.001).

coated and uncoated glass beads respectively, although adhesion events were more prevalent than with iRBC and uncoated glass bead, the mean adhesions forces were around 4 pN. These non-specific adhesion forces were therefore approximately a factor of 10 smaller than those associated with specific adhesion.

There was no statistically significant difference between the mean adhesion force for varying contact times for healthy RBC with either CD36 coated or un-coated glass beads. As there was only one adhesion event with iRBC and uncoated glass bead which occurred during the 20s contact time the mean adhesion force at this time could not be compared to other contact times, as there were no adhesion events and therefore no adhesion forces.

The mean adhesion force when an adhesion event occurred between iRBC and CD36 coated beads did not appear to be a function of contact time. However, these mean values were obtained by correlating data across all iRBCs investigated for varying contact area's, compressive forces and cell stiffness. As such, these parameters will now be further investigated to determine their contribution, if any, on the obtained adhesion forces.

Competitive factors that affect adhesion bond force

The changes that result as the parasite matures in the iRBC and the consequent effect these changes have on adhesion is complex due to a variety of factors. Two opposing factors that may contribute to adhesion during the trophozoite stage, and alter as the iRBC matures, are ligand density and cell rigidity.

The increase in adhesion from ring to trophozoite stage correlates with the appearance of *Pf*EMP1 at the erythrocyte surface (approximately 16 h after merozoite invasion) which corresponds to the transitioning period between ring and trophozoite stage (Pouvelle et al., 2000). However, as the cell matures it also becomes increasingly stiffer, resulting in which results in a decrease in contact area which has been suggested to contribute to a decrease in adhesion (Gallant, Michael, and García, 2005).

Fig. 4.17 displays the relation between contact area and cell stiffness for various compression forces. The area of contact was measured, from experimental visualization, between iRBC and CD36 coated glass beads that were observed for four compression forces: 10pN (pink circle), 20pN (dark blue square), 30pN (light blue triangle) and 40pN (green inversed triangle). As the cell stiffness increases at constant compressive force, the area of contact decreases. This indicates that
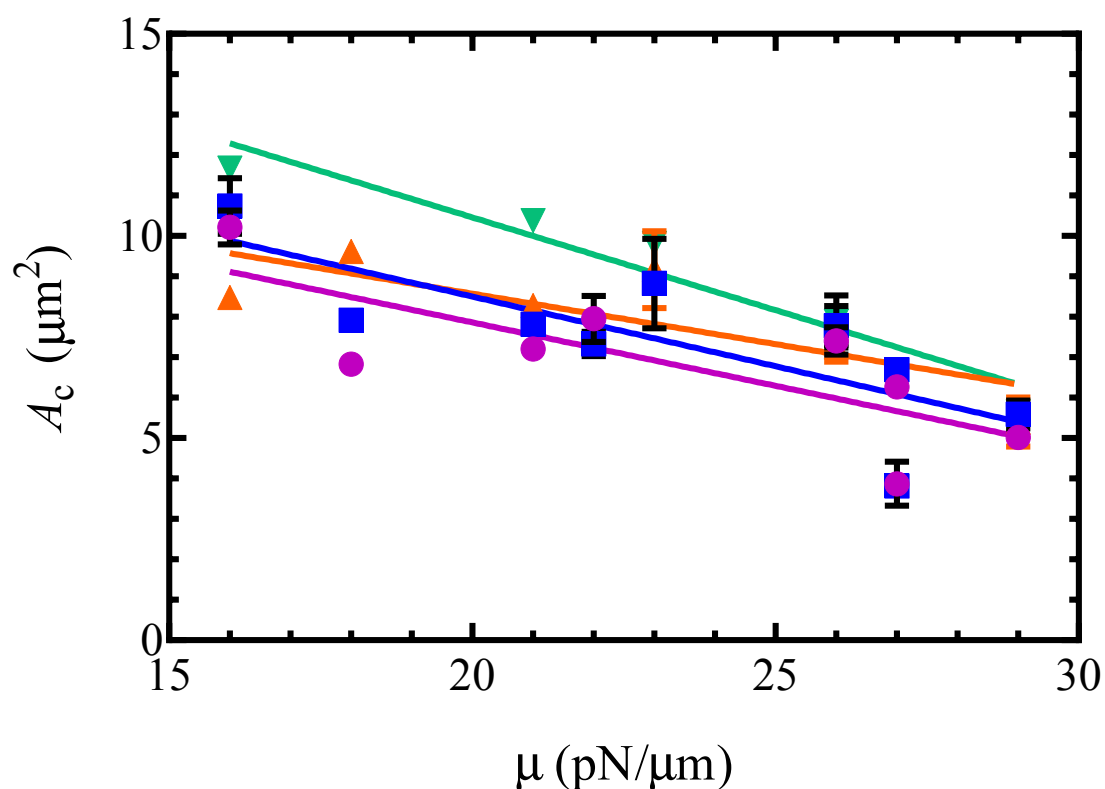
FIGURE 4.17: **Relationship between contact area and cell stiffness for various compression forces.** The area of contact between iRBC and CD36 coated glass beads were observed for four compression forces: 10pN (•), 20pN (■), 30pN (▲) and 40pN (▼). As cell stiffness increases at constant compressive force, the area of contact decreases. Linear correlation lines are shown in the analogous colours (R^2 values vary from 0.60 to 0.93 and all slopes were found to be significantly non-zero with P<0.05). The standard error of the mean are shown as black lines.
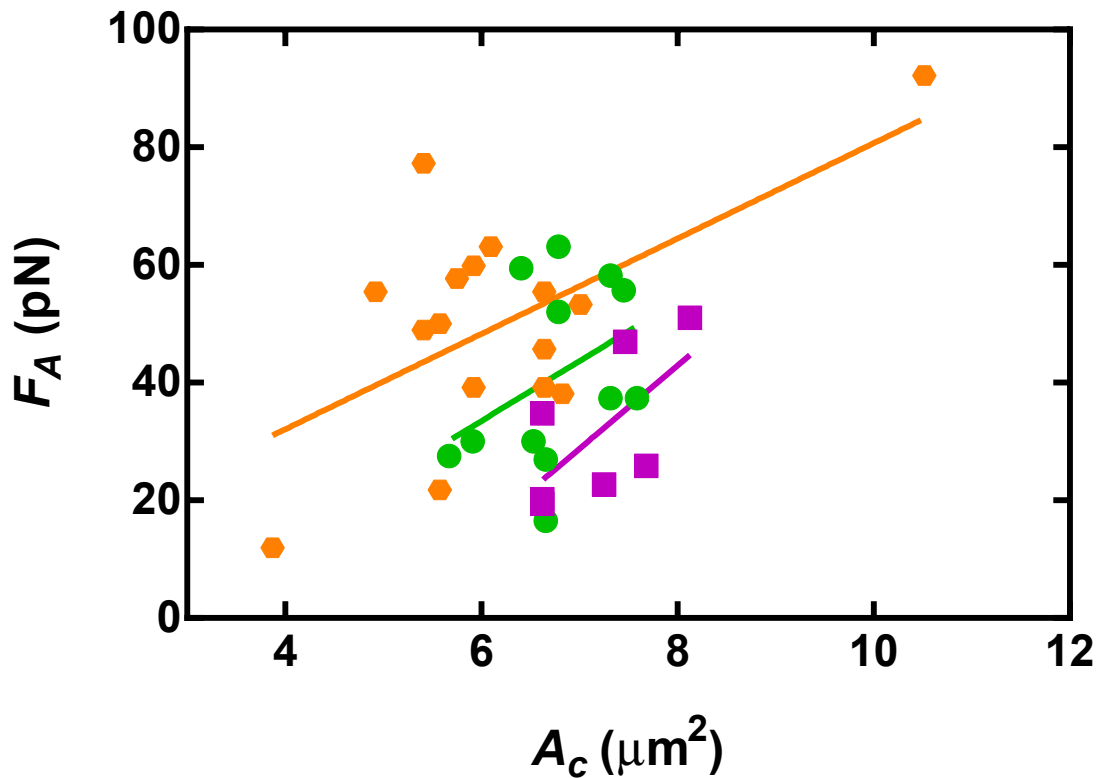
FIGURE 4.18: **Correlation between contact area and adhesion force for individual iRBCs.** Contact area, A_c (μm) is plotted against obtained adhesion force, F_A (pN) for three different cells of varying elastic modulus, μ (■ =18 pN/μm, ● =22 pN/μm, ● =27 pN/μm). Linear regression was carried out for the individual cells. Positive slopes which were found to be significantly non-zero (P<0.05) indicates that as contact area increases the force of adhesion increases for individual cells. Data is shown for contact time 5s.

there may be competing factors for adhesion force as a cell matures. The expression of PfEMP1 changes as the cell matures, which could increase adhesion strength due to more ligands being present per contact area. Conversely, the resulting increased stiffness may have a degradative effect on adhesion in that it results in a decreased contact area reducing amount of ligands that come into contact with the receptors on the opposing surface.

Fig. 4.17 also indicates an overall trend of increased contact area as compressive force increases for any cell stiffness. This trend was assessed using linear correlation and corresponding lines are shown in the analogous colours indicating respective compression forces. R^2 values vary from 0.60 to 0.93 and all slopes were found to be significantly non-zero (P<0.05). The standard error of the mean are shown as black lines.

Fig. 4.18 shows the correlation between contact area and adhesion force for individual cells.

Contact area, A_c (μm^2) varying from 4-10 μm^2 is plotted against the obtained adhesion force, F_A (pN) for three different cells of varying elastic modulus, μ (pink squares =18 pN/μm, green circle =22 pN/μm, orange hexagon =27 pN/μm). Linear regression was carried out for the individual cells. Positive slopes which were found to be significantly non-zero (P<0.05) indicated that as the contact area increased the force of adhesion also increased for individual cells. Data is shown for a contact time of 5 seconds. As the elastic modulus, μ (pN/μm), increases the force of adhesion is stronger for any given contact area. This supports the notion that, for any given contact area, as the rigidity increases the force of adhesion also increases due to the increased maturity of the cell.

Finally, the effect compressive force has on the adhesive force is plotted for cells of varying stiffness. iRBC were brought into contact with CD36 coated beads with varying compressive forces F_c and the corresponding adhesion force, F_A, was plotted in Fig. 4.19. Forces are shown in pN and the contact time was 15s. Three cells of various cell stiffness are shown: μ=18 (dark purple circle), μ=26 (light purple square), μ=29 (purple inverted triangle). The mean adhesion force is indicated by respective coloured lines for each cell investigated. Linear regression indicated no significant slope. Although the compression force is related to contact area, contact area was not kept constant which could contribute to the resulting lack of correlation between compressive force and adhesive force.

Cell stiffness is known to decrease the contact area (Fig. 4.17) for any given compression. However, it has also been shown to result in an increased adhesive force for increased cell stiffness if the contact area is kept constant (Fig. 4.18). Interestingly, the plot of adhesion force for various compressive forces (Fig. 4.19) for three cells of varying cell stiffness (18, 26 and 29 pN/ μm) did not show a clear correlation between increasing cell stiffness and respective adhesion forces obtained. A significant (P<0.05) increase in adhesion force occurred between the most deformable cell (stiffness 18 pN/ μm) and the cell with intermediate stiffness (26 pN /μm). Conversely as stiffness is increased from intermediate stiffness (26 pN /μm) to the most rigid (29 pN /μm) the adhesion force, for any given compressive force, actually decreased indicating that there could be competitive properties that occur as a cell becomes more rigid. Fig. 4.17 indicates that the contact area decreases with increased cell stiffness and Fig. 4.18 adhesion force increased with increased contact area. Consequently, an increase in cell stiffness should result in a decreased adhesion force due to the decreased contact area. However, this is not taking into account that *Pf*EMP1 expression on the RBC surface can vary, especially as the cell matures and an increased
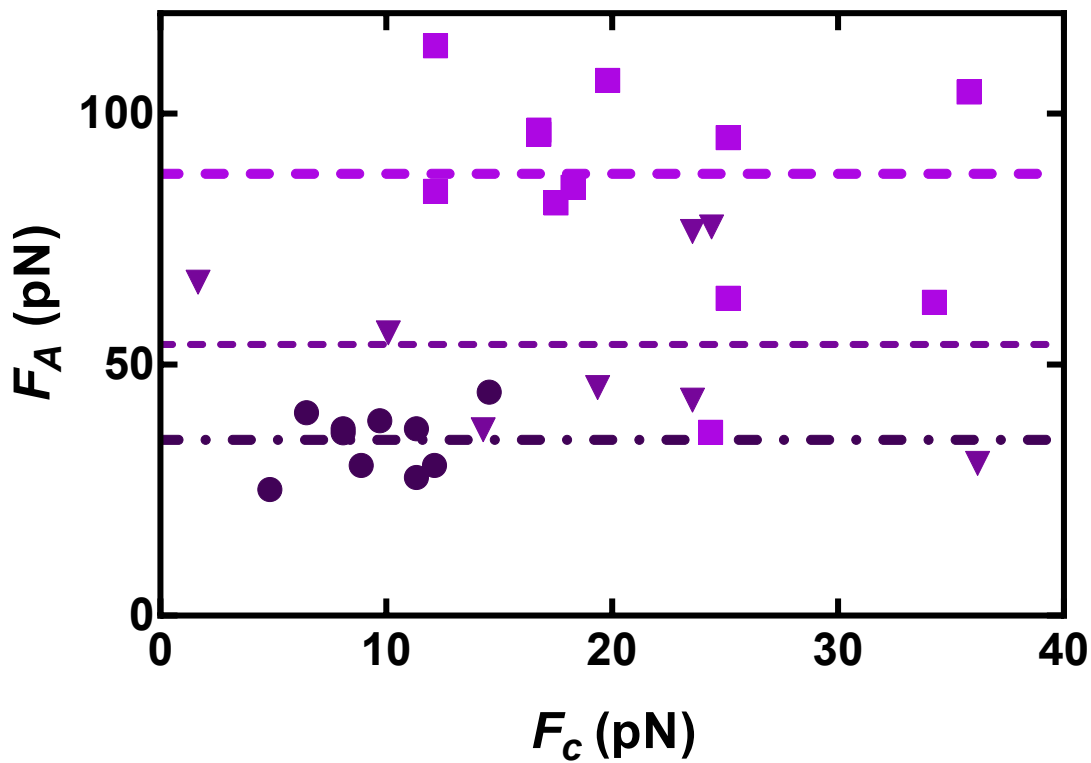
FIGURE 4.19: **Effect of compression force on adhesion force for individual cells** iRBC were brought into contact with CD36 coated beads with varying compressive forces F_c and the corresponding adhesion force, F_A, plotted. Forces are shown in pN and contact time was 15s. Three cells of various cell stiffness are shown; $\mu=18$ (dark purple circle), $\mu=26$ (light purple square), $\mu=29$ (purple inverted triangle). Mean adhesion force is indicated by respective coloured lines for each cell investigated, linear regression carried out indicated no significant slope.

cell stiffness could be representative of a more mature cell as RBC rigidity increases as the parasite matures.

The presence of two competing factors as the cell matures, namely increased *Pf*EMP1 expression on surface of iRBC leading to increased adhesion, and decreased contact area due to increased cell rigidity leading to decreased adhesion, may account for the increased adhesion force between the most deformable iRBC and the more rigid iRBC but also the decrease in adhesion between the most rigid cell and the cell of intermediate rigidity.

The contribution of various parameters such as contact area, cell maturity and contact time result in a complex relationship to determine the adhesion force of iRBC and CD36 coated glass beads. Fig. 4.20 displays the mean adhesion force for five different cells of varying rigidity (μ from 16 to 29 pN /μm) for contact times varying from 5s to 20s. At constant contact time, the mean adhesive force varied for each cell investigated. Generally, adhesive force increased as cell stiffness increased. However, at contact times 5, 10 and 15s the adhesion force decreased between cell 4 (μ= 27 pN /μm) to the most rigid cell (μ= 29 pN /μm). Interestingly, the mean adhesion force for the majority of cells (μ= 21,27 and 29 pN/μm) increased as the contact time increased from 5s to 15s for the individual cells, then started to decrease as contact time increased to 20s. However, the cell with stiffness 22 pN/μm did not show a specific trend of the mean: the mean adhesion force increased as contact time increased from 5s to 10s, then dropped at 15s, and then increased at 20s contact time.

Rare adhesion events

A typical adhesion event for determining mean adhesion force was defined as having only one visible tether point that broke before the maximum displacement of the pipette was reached. However events did occur where there was visually more than one tether point. This event occurred in less than 5% of adhesion events and was not observed in any non-specific adhesion event when looking at negative controls. In the majority of cases (>80%) cases, where multiple tethers occurred, the tethers broke apart first one tether then the next. Generally, the final tether broke less than two seconds after the first tether broke, although on one occasion there was a four seconds interlude between the first tether breaking and the final tether breaking (Fig, 4.21).

Another rare event (<0.05% of adhesion events) occurred when the adhesion did not break even after the maximum displacement between the bead and iRBC was reached. In these rare
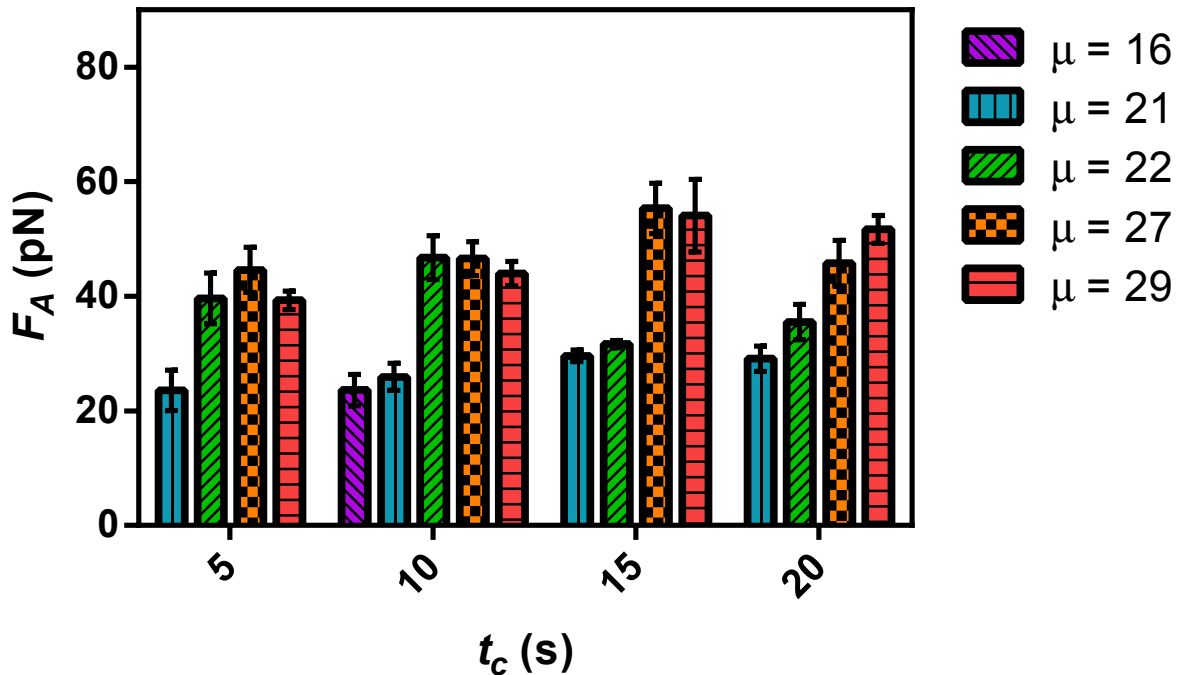
FIGURE 4.20: **Force of adhesion to CD36 for individual iRBCs.** At each contact time (t_c) the force of adhesion F_A varies depending on the cell stifness (μ in pN/μm). Each bar indicates the mean adhesive force for an individual iRBCs. The error bars indicate the standard error of the mean.
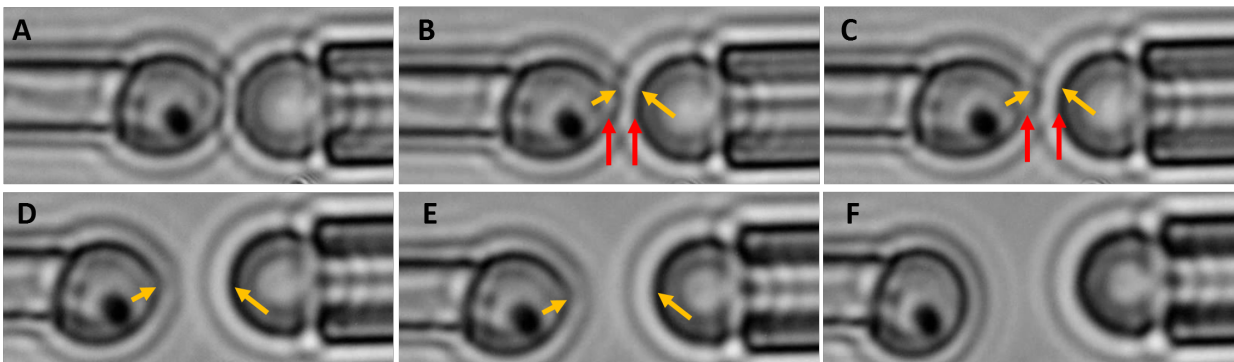
FIGURE 4.21: **Timelapse of an adhesion event with two distinct tether points that broke consecutively.** The iRBC (held on the left) and a CD36 coated glass bead (held on the right) are brought into contact and then the iRBC is moved at a constant velocity (1μm/s) away from the bead (A). An adhesion event is observed as the cell is moved away (B). As the cell is continuously moved away it becomes evident that there are two tether events (C). The first tether breaks between timelapse C and D, however a second tether is still present. The iRBC is still moved back (E) until the second tether breaks (F) and there is no longer any bonds connecting the iRBC to the bead. Red arrows indicate the first tether which breaks 4s before the second/final tether breaks (indicated with orange arrows).
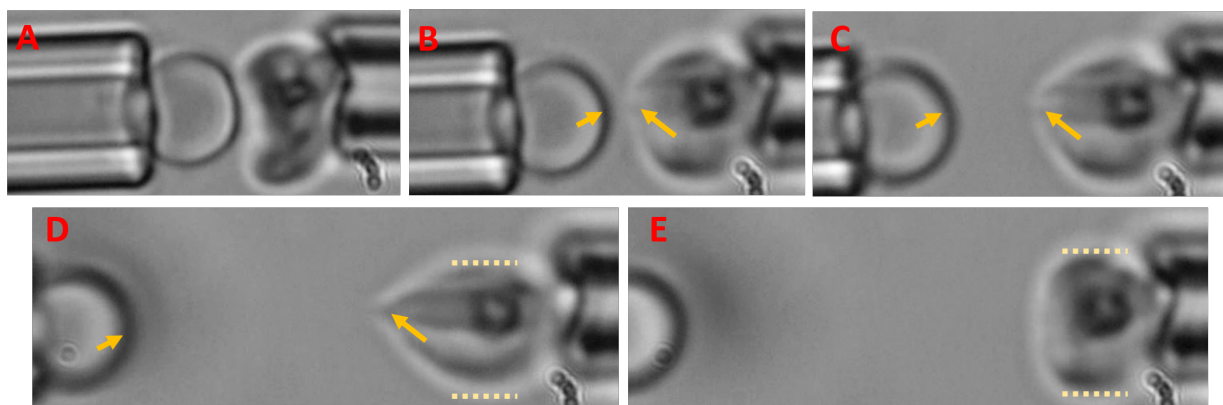
FIGURE 4.22: **Image sequence of a strong adhesion event.** An iRBC and CD36 coated glass bead are brought into contact (A) and then the bead (held in left pipette) is slowly (1μm/s) moved away and an adhesion event is observed (B). Even after the bead has displaced to its designated distance (5μm) the adhesion bond is still present (C). The cycle is stopped and the bead is manually displaced until the maximum deformation is reached (D) before the bond breaks (E). Adheshion tether is indicated with yellow arrows. In cases where the whole length of the connecting tether is not visible (C,D) the presence of adhesion is determined by visible deformation of iRBC in both the horizontal direction (elongation) and vertical direction (compression, highlighted by green dashed line).

cases the cycle was stopped and the bead moved away from the iRBC until the adhesion tether broke and the displacement was then measured. The length the cell deformed in these cases was significantly larger than what the cell was subjected to during the elastic modulus measurements. Therefore, one cannot assume linearity at these excessive deformations and so the events were not included in mean force calculations. Fig. 4.22 shows time lapse images of one such event.

At these extreme deformations the membrane along the tether can appear non-visible at the magnifications used in this experiment. The presence of adhesion is therefore observed from the visible deformation of the iRBC being pulled and the distinct recoil when the bond breaks. These large deformations due to strong bonding only occurred between iRBCS with CD36 coated beads and were not observed in any of the negative control cases.

4.5 Conclusions

Adhesion of iRBC expressing PfEMP1 with CD36 coated glass beads was investigated using an micropipette method. This method allowed not only the probability of adhesion but also the strength of the obtained bonds to be investigated on the individual cell level. The cell stiffness was able to be measured for each cell investigated, allowing information about how the cell rigidity

affects the probability and the strength of adhesion.

Investigation with negative controls showed that non-specific bonds did occur when the receptors and/or ligands were not present. However, the frequency and strength of these non specific bonds were significantly lower than what occurred when receptors and ligand was present (specific adhesion).

The cell stiffness of iRBC varied from 16 to 29 pN/μm and was shown to be linear over the force range investigated for the majority of adhesion events that occurred, although rare events did occur (<0.05% of adhesive events) where extremely large adhesive forces were measured (F_A>200pN).

Adhesion probability as a function of contact time was measured and an analtyical expression for a simplified master equation was fitted to obtain a kinetic rate of dissociation of 0.11$\pm$0.02 s^{-1}. Increased compression force between iRBC and bead was shown to result in an increased contact area. However, increased cell stiffness at a constant compressive force was shown to decrease the observed contact area. It was further shown for individual cells that as the area of contact increased the force of adhesion also increased and that at a constant contact area the adhesion force increased as cell stiffness increased. However, no significant correlation was found between compressive force and adhesive force for cells of varying stiffness, nor did adhesion force always increase as contact time increased.

For any given contact time the mean adhesion force observed differed depending on the cell investigated. It is evident that various factors, such as contact area, contact time and cell stiffness contribute to the force of adhesion between specific bonds formed between iRBC and CD36 coated beads. It should be kept in mind that the individual cells surface expression and density of PfEMP1 was unable to be measured which may have an important contribution to the variation in adhesion force and probability. An important future direction would be to develop a method that would allow measurement of surface densities of the receptors and ligands so individual cells could be investigated to determine the effect surface density has on the adhesion force observed. Further, the master equation could be fitted to curves of adhesion probability versus contact time for varying surface densities allowing the equilibrium constant of association to be determined for PfEMP1 and CD36 bond.

One limitation of this method is that the iRBC are deformed and stressed when held in the micropipette which could effect adhesion properties. Optical tweezers offer a method to study

adhesion properties of iRBCs in a non-invasive way. This method and results will be discussed in chapter 5.

Chapter 5

Optical tweezer analysis of abnormal adhesive properties of *Plasmodium falciparum* infected red bloods

5.1   Introduction

Adhesion of *P. falciparum* infected red blood cells (iRBCs) to microvascular endothelial cells in the human hosts circulatory system is believed to be one of the main causes of lethal complications associated with malaria infection (Xu et al., 2013; Sherman, Eda, and Winograd, 2003). Existing experimental data indicates that iRBC cytoadhesion is mediated by the ligand *Plasmodium falciparum* erythrocyte membrane protein 1 (PfEMP1) with various receptors including CD36 which is present on endothelial cells in the microvasculature (Cooke et al., 1994; Ochola et al., 2011). For more details on *P. falciparum* adhesion see Sec. 2.7.5.

Experiments conducted previously have begun to explore iRBC adhesion and their kinetics on a molecular level (Cooke, Coppel, and Wahlgren, 2000), a single cell level (Li et al., 2013) and as a population of cells (Joergensen et al., 2010). Although all perspectives are important, when trying to understand cell adhesion an advantage of looking at individual cells is that properties can be attributed to the individual cell, instead of overall population values where information can be lost. Single molecule force spectroscopy using AFM (Atomic force microscope) have been used to obtain kinetic parameters however this method is invasive. Further, there is still gaps in our knowledge of iRBC adhesion on a single cell level in particular the affect important factors such as contact area and contact time have on adhesion which cannot be taken into account when

looking at just a molecular level (Zhu, Bao, and Wang, 2000).

This chapter will focus on the potential use of optical tweezers to investigate iRBC adhesion. A non invasive technique is used that does not require any modification of the iRBC. A focused laser is used to trap and manipulate the iRBC without the requirement of external beads to be attached to the cell. This method allows us to explore the probability of adhesion and the forces involved in iRBC adhering to a platelet coated bead. By looking at different contact times, information about the kinetics of a PfEMP1-CD36 bond can be obtained. Further, the strength of the bond can be investigated by exploring the magnitude of the force required to break the bond. Another advantage of this technique is that parameters such as velocity towards and away from contact, compressive force of contact, and contact time can be defined and manipulated to determine the affect these parameters have on iRBC adhesion.

The structure of this chapter is as follows: In section 5.2 the experimental method using optical tweezers to investigate iRBC adhesion with platelet coated glass beads is described. This section includes the specific preparation method of the iRBCs and the platelet coated glass beads, details of the optical tweezer setup and the procedure used to explore iRBC adhesion. In section 5.3 the results of the adhesion assays using optical tweezers is presented and discussed. Adhesion probabilities were investigated as a function of contact time and the simplified master equations were fitted to determine kinetic parameters. Parameters, such as contact area, displacement force and contact time, that could affect the adhesion force were also explored. The results were also compared to those obtained using the micropipette method. Section 5.4 concludes this chapter.

5.2   Materials and Methods

5.2.1   iRBC and bead coating procedures

The buffer used in the optical tweezer experiments was a PBS (1X) solution with 2%wt of bovine serum albumin (BSA) (pH = 7.4). Buffer was prepared, filter sterilized (0.22μm filter), placed in 10ml aliquots and stored at -20°C until use. The solution was warmed to 37°C before use.

Silica glass beads (Bangs Beads, USA) 4.86 $\pm$0.47 μm diameter were acid washed prior to binding of platelets (refer to Section 3.3.1). Human platelets were used to coat the microspheres to study adhesion of iRBCs to CD36. Platelets were harvested and prepared as detailed in Section

3.3.3. After incubation the platelets were fixed to the silica beads using formalin (see Section 3.3.4). Fixed platelet covered silica beads were stored at 4^oC, for a maximum of one month, until use.

There are some advantages of using a platelet monolayer instead of purified CD36 or recombinant CD36. As platelets are cells and therefore exhibit membrane properties, unlike recombinanant CD36 bound to rigid surfaces, the platelets are therefore better able to reflect the situation in-vivo. Further, platelets do not require flow to produce confluent monolayers unlike human umbilical vein endothelial cells (HUVEC). Finally, platelets adhere to and spread to near-confluence under static conditions within 30 min when activated by silica glass so the procedure to coat silica beads can be achieved within 1-2 hr. There are however disadvantages of using platelets; the density of receptor is difficult to determine, and there can be issues when fixing the platelets to the microspheres (see Section 3.3.4).

P. falciparum iRBCs were cultivated as detailed in section 3.2.3. Positive selection for knobs and synchronization of culture was achieved using gelatin flotation method (see section 3.2.5. Gelatin flotation was carried out weekly. On the day of experiment, mature stage iRBCs were selected and concentrated using the magnet purification technique (for details refer to Section 3.2.5). Concentration of mature iRBCs was required to ensure that iRBCs could be found in solution within a reasonable time frame (<5 min) however the concentration of cells also needed to be kept low to minimise interference of iRBCs or RBCs getting drawn towards and into traps as the experiment was being conducted.

The sample was prepared by addition of 100μl of iRBCs from magnet purification and $2\,\mu$l of platelet covered beads to 5ml of buffer.

Detection of CD36

To detect the presence of CD36 immobilised on microspheres an indirect fluorescence assay (IFA) was used (refer section 3.4). Further, the IFA was used to determine the optimal preparation method of the silica beads prior to coating the platelets. Two preparation methods were analysed; acid washing the silica beads and pre-coating with 3-hydroxy amino-propyl tri-ethoxy silane (APES), a covalent modifying agent. The pre-coating procedure is detailed in Section 3.3.2. Figure 5.1 shows sample IFA images generated for the various preparation methods that were trialed. It is evident from these images that the platelets were able to bind onto the silica glass beads and thus able to express CD36 regardless of the preparation method used.
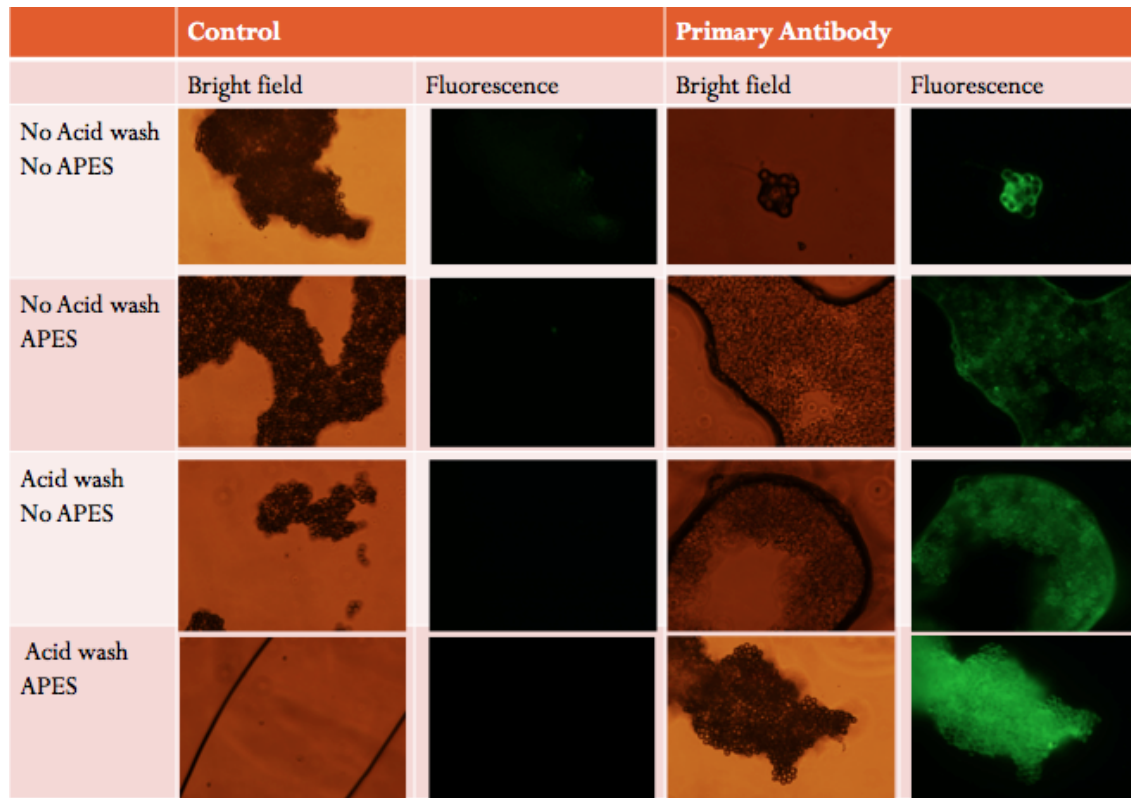
FIGURE 5.1: **IFA to determine presence of CD36 on silica bead** 4.87 μm diameter silica glass beads were prepared prior to platelet addition using different methods. First row silica beads that had not been acid washed nor pre-coated with APES prior to exposure to platelets. Second row the beads were not acid washed however were precoated with APES. Third and fourth row the beads were acid washed and without/with APES precoating prior to platelet addition. Control had no primary antibody added. Fluorescence was observed regardless of bead preparation method used.
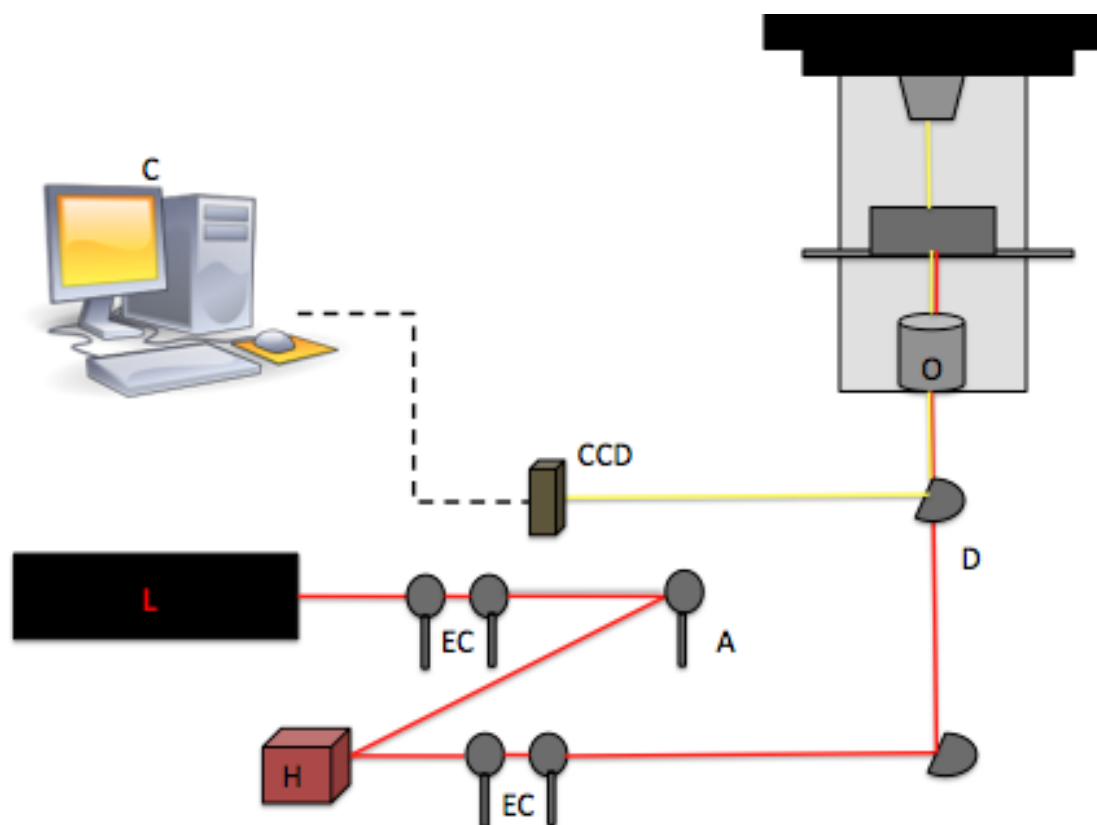
FIGURE 5.2: **Schematic representation of the optical tweezer setup** A light beam with Guassian intensity (TEM$_{00}$) is emitted from a 4W infrared (λ=1064nm) laser (L). Expanders and collimators (E C A) are used to expand, focus, and align the beam. A spatial light modulator (H) allows two or more traps to be formed from the one laser source. A dichroic mirror (D) allows the infrared beams to pass through and reflects the illuminating beam into a charge coupled device (CCD) camera which relays the images to a computer screen and to quandrant photo diodes for position detection. A (o) high numerical aperture objective (60-100X, N.A. =1.3) focused the beam into the sample to form the trap. Sample is illuminated by an LED beam.

5.2.2 Design of optical tweezers

A schematic of the optical tweezer design for the adhesion assay is shown in Figure 5.2. The OT apparatus consists of a 4 W Nd:YAG infrared laser λ =1064 nm (Coherent, USA) and a Nikon DIAPHOT 300 inverted microscope equipped with a 100 $\times$ (NA =1.3) oil-immersion objective lens isolated on an air-cushioned optical table. Expansion lenses are used to expand the beam to illuminate the 16$\times$ 12 mm^2 area of a programmable liquid crystal spatial light modulator (Hamamatsu phototonics, Japan model: LCOS-SLMx10468) designed to work at IR. The spatial light modulator (SLM) was used to modify the incoming wavefront so that multiple optical traps can be formed with the one laser source.

A dichroic mirror allows infrared light ($\lambda > 810\,\text{nm}$) to pass through, however reflects the illuminating blue LED light ($\lambda = 470$ nm, model HLV2-22BL-3W CCS, Japan) into a charge coupled device (CCD) camera. The CCD (model: MC1362 Mikrotron, Germany) is a CMOS monochrome full HD high speed camera which relays the images to a computer screen.

Placement of the microscope stage was controlled by a servo-motor to within $\pm 0.1 \mu$m and a quadrant photodiode sensor (S4349 Hamamatsu, Japan) detects particle position with a resolution of 15 nm at a 1 kHZ sampling rate. Labview and a PCI-6014 data acquisition card (National Instruments, USA) were used to record and analyse data. The location of the trapped bead and the force it feels from the trap is determined by analysis of bead positions and force displacement calibration.

5.2.3 Adhesion assay

The laser was warmed up for 5 minutes prior to the start of the experiment. The sample was then placed into the sample chamber (60mm $\times$ 10mm $\times$ 10mm). The rectangular sample chamber was made of teflon with a metal frame and a glass viewing section in the bottom and top of the chamber (thickness 0.10 mm). The chamber was sealed to reduce the rate of evaporation of the buffer solution. The chamber was moved using a servo-motor until a bead was located and a stable trap formed. The movement of the bead in the stationary trap was measured for 5 minutes to calibrate the trap and obtain the trap stiffness measurement (refer to section 5.2.4 for more detail on trap calibration).

A iRBC was then securely trapped in a second trap (designated moving trap). Using Labview software the SLM was programmed to move the moving trap a certain distance (d_m) in a specified amount of time (t_m) until it is in contact with the trapped bead. This position was then held for a defined contact time (t_c) and then the iRBC in the trap was moved away, and adhesion was either observed or not (timeshot images of a cycle are shown in Fig. 5.3). This cycle was then repeated. Ideally the cycle was repeated 50 times and then t_c was varied and the experiment repeated. However, the total number of contacts could be cut short if other RBCs or beads jumped into the traps or if a strong adhesion occurred and could not be broken apart.

The platelet covered beads were kept in the stationary trap as the iRBCs are not smooth, inflexible spheres and consequently it was difficult to get accurate power spectrum readings for the iRBCs. Therefore the iRBCs were incrementally moved towards and then away from the platelet
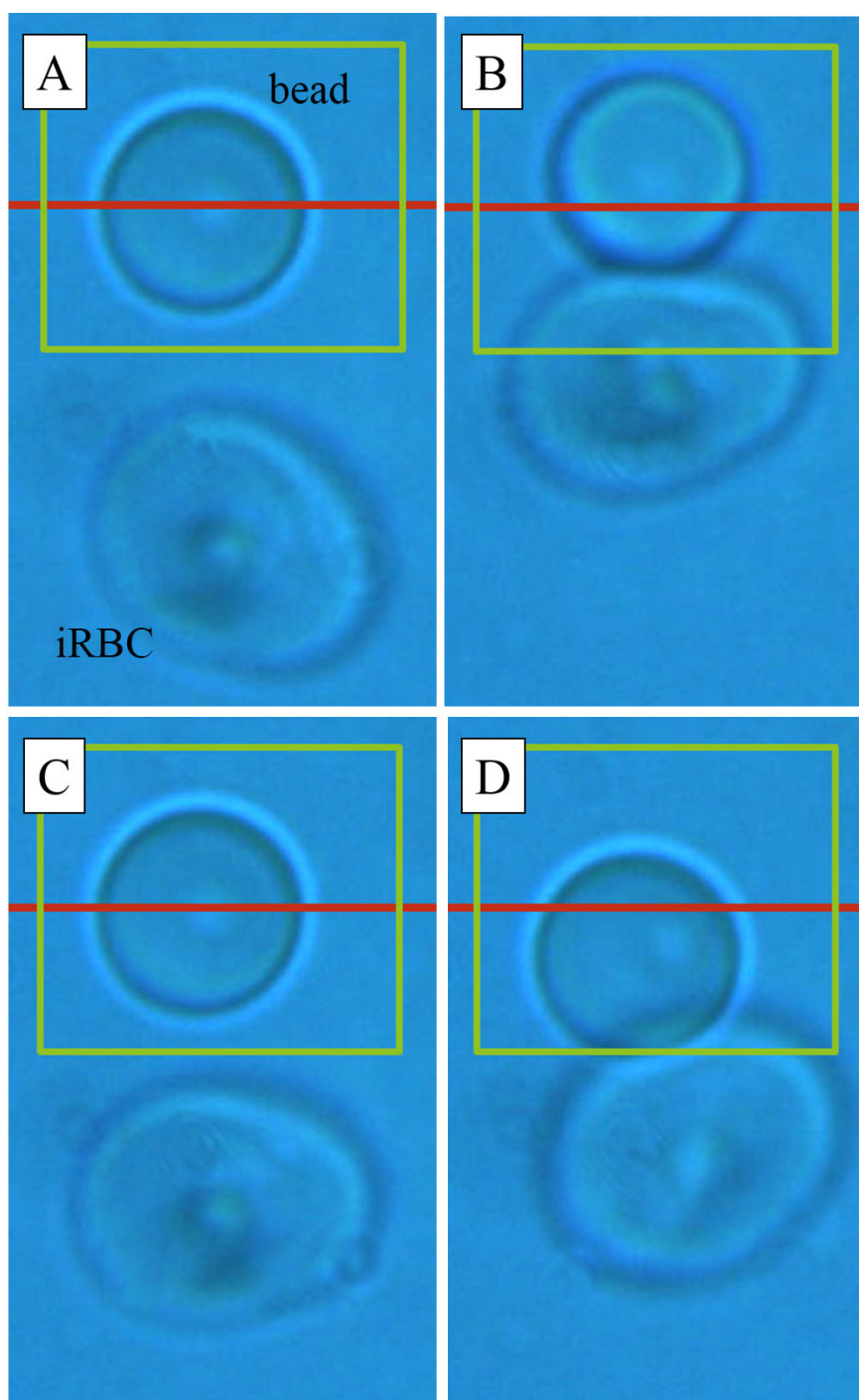
FIGURE 5.3: **Sequence images of adhesion assay using optical tweezer apparatus**
(A) platelet covered bead is held in a stationary trap and an iRBC is held in a trap
below the bead. The area the QPD can 'read' is illustrated by the green box around
the bead. The lowest energy position of the bead in the y-direction is indicated by
the red line. The iRBC was then brought into contact with the bead (B) causing the
bead to be pushed into a higher energy position for a defined contact time. iRBC
was then moved away from the bead and either no adhesion occurred, so the bead
returned to its lowest energy position (C) or an adhesion occurred resulting in the
bead being drawn into a higher energy position due to its attachment to the iRBC
(D).

covered glass bead held in the stationary trap whilst constant power spectrum density (PSD) readings of the platelet covered bead position were measured and later converted to force.

5.2.4   Calibration

QPD

The quadrant photodiode (QPD) was used to measure the trapped bead position within the trap, specifically the distance away from the trap center. This distance was then used to determine the force the trap exerted on the bead as the force increases linearly with distance from the trap's center. The photodiode allows finer spatial resolution and much higher frequencies to be recorded compared to the use of video to determine spatial position of the bead over time.

The QPD outputs allow x and y position calculation. Within a certain range of light intensities, the output voltage of a photodiode scales linearly with the intensity of light incident upon the diode. The light incident upon each quadrant in the QPD generates a tiny current which is then converted into voltage by passing known resistors. The analog circuitry then outputs a voltage V_x and V_y, which are proportional to the actual x and y position of the incident beam. As the light scatters in a predictable way off of the spherical beads, this information can be used to recover the actual bead position within a narrow range around the center of the trap. This placed a restriction on the experimental method as the light scatter was more difficult to predict for the iRBC and consequently it was harder to calibrate the trap for the iRBC. Therefore, only the bead trap was calibrated.

When the laser beam was tightly focused, the trapped bead was in the center of the trap and was aligned to the center of the QPD, giving V_x and V_y signals of zero. When a trapped bead was then moved slightly away from the center of the trap, the bead imageg moves on the QPD, causing V_x and V_y to vary accordingly. To calibrate the QPD to convert voltage signal to displacements first the magnification factor was calculated using a particle of known size. The particle was tightly trapped and the image size on QPD was measured, the ratio of known particle size to the measured image size was the magnification factor.

The conversion factor to convert voltage data to displacement data was obtained using a calibration program (Labview, National Instruments Australia). Briefly, a particle of known size was trapped tightly and kept in place. The QPD detector was then moved in increments (generally 0.1 μm). After each move the detector was kept in place for 1 s and voltage readings taken at a

frequency of 500 Hz to give an average voltage at that displacement. The QPD was moved until the output difference between two consecutive moves was less than the pre-set value (normally 0.1 V).

The trap stiffness was calibrated for every bead held in the optical trap. The calibration method used was the equipartition theorem method (for more information about this method refer to Molloy and Padgett, 2002; Sarshar, Wong, and Anvari, 2014; Baek, Hwang, and Lee, 2007). The obtained trap stiffness constants for the x and y direction were then used to convert the displacement data to force data as detailed in section 5.2.4. The programs used for calibration of QPD can be found in appendix B.

Analysis of QPD data

To analyse the QPD data a QPD reading program (using C programming language) was developed (for the full code please see appendix B.3). Briefly, the program was broken up into 3 sections. Section 1 contained all the inputs and definitions it also read the raw QPD data file and converted the displacement data into force data and normalised the data to ensure the averaged rest position was at $(x, y) = (0, 0)$.

Section 2 in the QPD reading program undertakes analysis of the normalised force data. It separates the data into cycles (rest - moving - contact - moving). For each cycle the program obtains information about the averaged contact force, contact time, and the maximum force of adhesion.

Section 3 of the program concentrated on analysing the cycle data and outputs the results to a text file that can be used for further analysis. The output file contains information about adhesion forces and compressive forces. The mean force of compression and adhesion over the whole time set is calculated from the summed average compressive force and maximum adhesion force in each cycle, respectively, over the total number of cycles. It also analysis the adhesion forces in terms of how many standard deviations they are away from the mean resting force.

Details of the program is as follows. Trap strength in the x and y direction (k_x and k_y, respectively) was inputted into the QPD reading program as well as a number key which was used to define the position of the moving trap in order to read where in the cycle the trap was for each x and y value of the stationary trapped bead. The number key worked as follows; 3 = resting state, -1 = moving and 1 = contact.

The QPD data file was then read by the program. The QPD data file consisted of three columns; column 1 and 2 contain data on the x-position and y-position of the bead, respectively, and column 3 has the number key which relates the position of the moving trap at that x and y position of the bead. The position of the moving trap is defined as either at rest (a distance, d, away from the bead), moving (either towards or away from bead) and in contact with the bead. The row number corresponded to time. The number of rows varied as it is a factor of the total amount of time data was recorded (generally 30 minutes) and the frequency the data is recorded (ν =1000 Hz).

The adhesion force can be grouped into various bins. Firstly, it should be reiterated that one limitation of this method is that there was a maximum force that could be recorded and any force larger than that could not be measured. A maximum on the recordable adhesion occurs due to finite size of QPD analysis square. As soon as the bead was drawn past this maximum distance the QPD could not do any further measurements and so the true bead displacement and thus adhesion force was not known, only a minimum was known. Consequently, the adhesion could be separated into 3 main groups. Group 1 was for any adhesion that was less than the maximum recordable adhesion. Group 2 contained any adhesion where a maximum recordable adhesion was reached however it broke before the iRBC moved again. Group 3 contained adhesions where the maximum recordable adhesion was reached and the bond did not break for at least one full cycle.

In order to determine what constitutes an adhesion, a measure based on the standard deviation was used. To determine whether it should be considered an adhesive event, or whether it was just normal recoil as the bead returned to its resting state, the mean and standard deviation of the force values of the bead in its resting state was analysed. If the maximum force during the cycle was within three standard deviations of the overall resting value was considered to be normal recoil. However, if the maximum force recorded in a single cycle was greater than four standard deviations from the mean resting force it was considered a specific adhesion. This was confirmed visually using the video recordings.

To further analyse the number and probability of adhesions, the maximum force in each cycle was grouped according to the number of standard deviations greater than the overall mean force the bead felt at rest. The mean and variance of the adhesion forces per data set were also analysed overall and placed in bins designated by the number of standard deviations away from the mean

of the adhesion force per cycle.

Statistical analysis

All statistical analysis of the data reported in section 5.3 below was obtained using GraphPad Prism 6.01. P values were used to interpret whether results were statistically significant (for more details on the statistical anaylsis see Motulsky, 2014). Statistical comparision between two different models was obtained using Akaike Information Criterion (for more details see Sakamoto, Ishiguro, and Kitagawa, 1986 and Motulsky, 2014).

5.3 Results and Discussion

Experiments were carried out for varying contact times (t_c=3-20s). CCD recorded video was analysed in parallel with the obtained QPD data. By analysing the two data sources in synergy greater accuracy and confidence was obtained. The video was able to easily show the 'strong' adhesion events however it can be difficult to distinguish the 'weaker' adhesion events and further, no quantitative data can be obtained from the videos in terms of bond force. Conversely, the QPD data allows quantitative force data to be obtained as well as being able to pick up those 'weaker' events. However, 'false' readings from the QPD can be obtained in cases where other objects interfere by jumping into the optical trap or if the trapped object was pushed out of the trap. These scenarios are easily observed in the CCD video.

The analysis was carried out to look at two distinct results; A: whether adhesion occurred or not (the probability of adhesion), and B: If adhesion occurred what force was required to break the bond. The following sections will look in detail into the two areas.

5.3.1 Adhesion probability of PfEMP1 expressing iRBCs to CD36

A combination of QPD data and video was used to obtain the adhesion probability, p_A, of PfEMP1 expressing iRBCs brought into contact with CD36-expressing platelet covered beads using OT.

A running average of adhesion occurrences was plotted with respect to the test cycle (Fig. 5.4) until adhesion reached stability (> 40 cycles). Running frequency of the binary adhesion scores (one if adhesion results, and zero if not) for sequential adhesion tests are plotted against the test cycle count. The binding specificity is indicated in Fig. 5.4 by the significantly lower adhesion
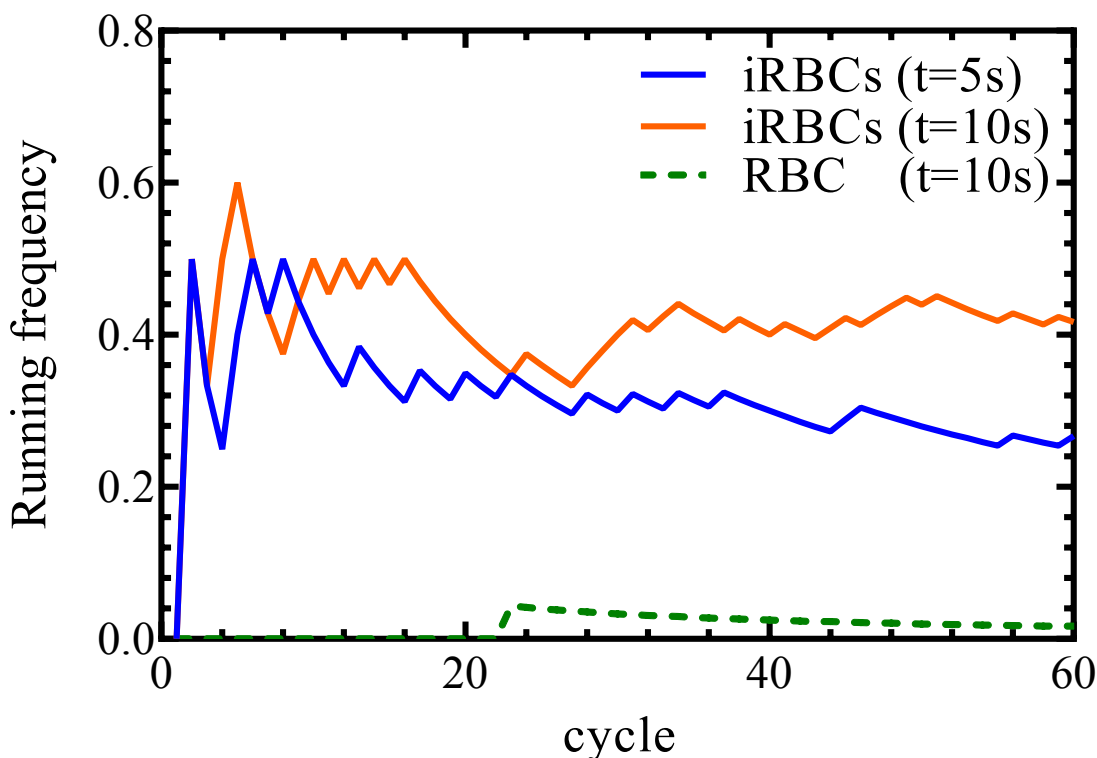
FIGURE 5.4: **Measurement of adhesion probability per contact.** The running averages of adhesion probability versus test cycle counts of three sequences of 60 adhesion cycles each. Each sequence was performed in a single bead-cell pair of a CD36-expressing platelet covered bead interacting with either a iRBC (solid line) or healthy RBC (dashed line). The fraction adhered is plotted as a running frequency for sequential adhesion tests against the test cycle count. The apparent contact area was kept constant (4 μm^2) for all tests. The contact duration were t=10s for the healthy RBC (nonspecific) and for one of the iRBC test series (orange) and t=5s for the iRBC series (blue). Adhesion specificity is indicated by the dependence of the magnitude of adhesion probability on the presence of 3D7 expressed on iRBC.

probability of a healthy RBC in contact with platelet covered bead to that for iRBCs. Further, the dependence of contact time, t_c (s), on the adhesion probability is also indicated giving credence to the importance of looking at the kinetics of iRBC adhesion.

The running frequencies were used to determine the probability of adhesion for iRBCs brought into contact with platelet covered beads using OT for various contact times. At each contact time the total number of adhesion events over all cells and days was divided by the total number of contacts to determine an overall probability of adhesion at the specific contact time. This was compared to the individual iRBC-bead sequences where probability of adhesion was determined
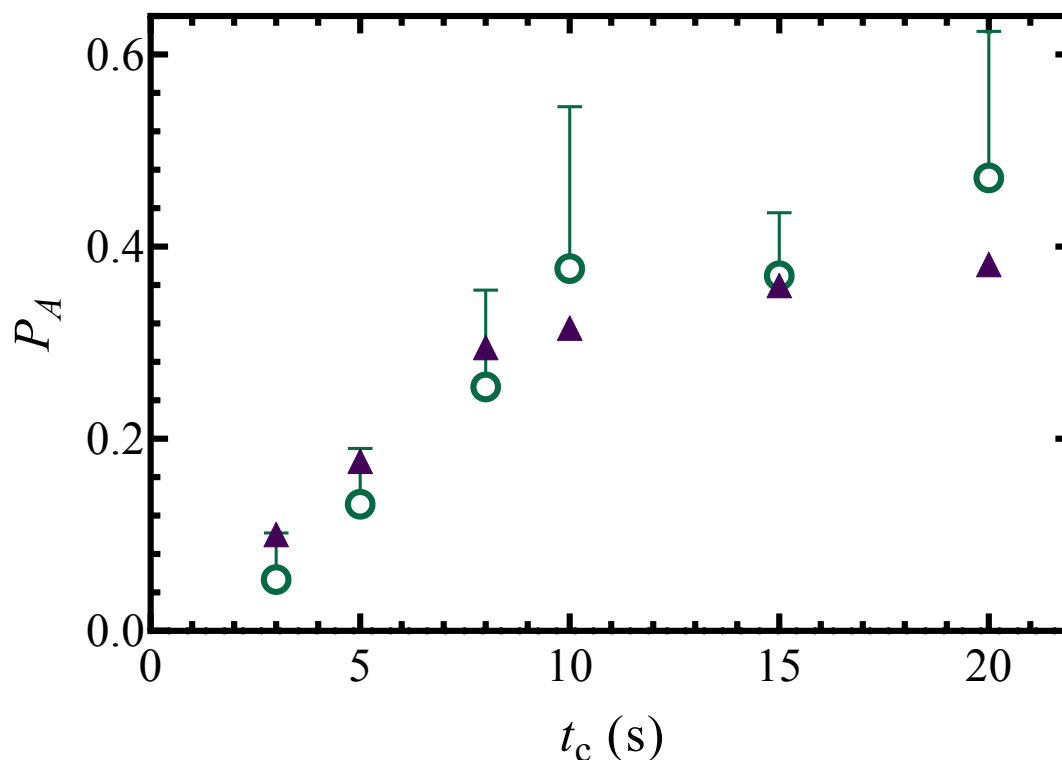
FIGURE 5.5: **Adhesion probability as a function of contact time as assessed using OT.** An iRBC was trapped and brought into contact with a platelet covered bead. As contact time, t_c, increased the probability of adhesion, p_A also increased. The mean of the probability across different iRBC-platelet coated bead pairs (o) was obtained (total number of contacts > 40). Error bars are (+) standard error of mean (n=3). The overall contact time (▲) was obtained by dividing the total number of adhesion's by the total number of contact cycles for each contact time (overall value has no mean or error bars).

(cycles > 40) and the mean and standard error of the probabilities were determined for each contact time (Fig. 5.5). Both the overall and mean probability of adhesion increased as contact time increased until around 10 s where the probability remained approximately constant at around 40% iRBCs adhered.

The probability of adhesion (p_A) as a function of contact time (t_c) was compared between the two methods, optical tweezer (OT) and micropipette (MP), as shown in Fig. 5.6. A similar trend can be observed from both methods with the probability increasing up until a contact time of around 10s after which the probability is observed to stabilise at a value of around 40% adhesion. However, it does appear that the OT method resulted in a lower adhesion probability for any given contact time. This could be attributed to the different source of receptor used.

In the MP method the CD36 receptor was sourced as recombinant CD36 coated onto glass beads whilst the OT method used platelets coated on beads which express the CD36 receptor. This may have resulted in different concentrations of the receptor on the bead surface, affecting the adhesion probability. Further, the error bars for the OT method were larger than that of the MP method, indicating a larger variance in adhesion probability at any given contact time. This could be attributed to the lower number of sequences that could be used, as it was difficult to get a high number of contacts (>60). This was due to the instability of iRBCs in the trap as well as the likelihood of contamination from other cells and beads jumping into the trap whilst the experiment was underway, resulting in the sequence having to be stopped early. Further, if a strong adhesion occurred, that could not be pulled apart, the sequence had to be stopped prematurely. Another reason for the greater variance with the OT method could be due to the ability of the cell to move in the trap. Unlike in the MP method, where the cell and bead are held relatively fixed and hence the same surfaces come into contact each cycle, in the OT method the iRBC and bead can move around in the trap so different surfaces may come into contact each cycle.

Similar to the MP results, the simplified master equations can be fitted to the probability of adhesion data for various contact times obtained using the OT method (for details on master equation see sec. 2.6.5). The kinetic mechanism was assumed to be second order for association and first order for dissociation. The master equation was simplified in two different ways, giving either a binomial or Poisson distribution. The binomial simplification (see eq. 4.3 in Ch. 4) can be used when the density of either the receptor or ligand is significantly greater than the other, allowing the larger one to be assumed to remain constant. The Poisson distribution (see eq. 4.5 in Ch. 4) is a special case of the binomial simplification where both the receptors and ligands can be considered non vanishing (densities remain constant). This occurs when the number of bonds being formed is significantly lower than the initial receptor and ligand densities.

The two models were fitted to the experimental results (Fig. 5.7) and compared using both sum of squares F-test and Akaike Information Criterion (AIC). The F-test (Motulsky and Christopoulos, 2004) can be used as models are nested, the suitability of the model is assessed by the degrees of freedom (DF) and the sum-of-squares for each fit. However, the DF are the same for the two models and the F-test cannot choose between the two models if that is the case. AIC (Sakamoto, Ishiguro, and Kitagawa, 1986) can be used to compare and select between the two models even if DF is the same. The AIC takes into account the complexity of the model and the precision of
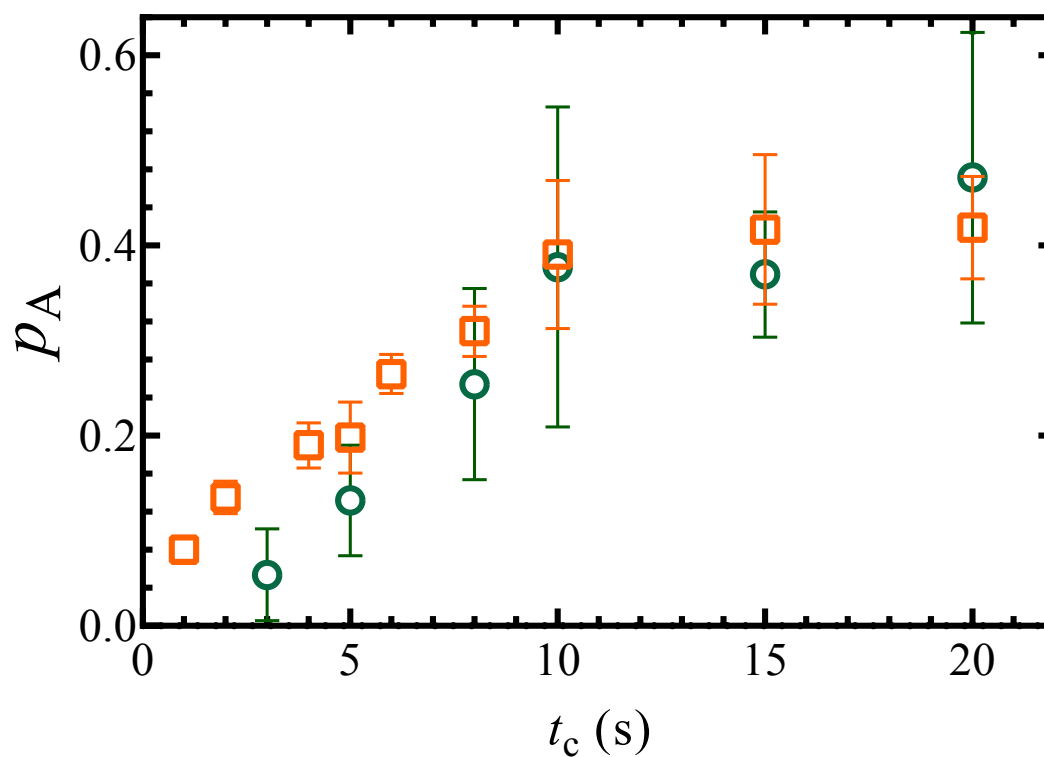
FIGURE 5.6: **Comparing the probability of adhesion as a function of contact time with the OT and MP method.** The probability of adhesion, (p_A), increases as contact time (t_c in s) increases until $t_c = 10$s at which time adhesion remains stable at around 40% adhesion. The mean probability of adhesion and standard error of the mean are shown for the two methods, OT method (o, n=3) and MP method (□, n=4).
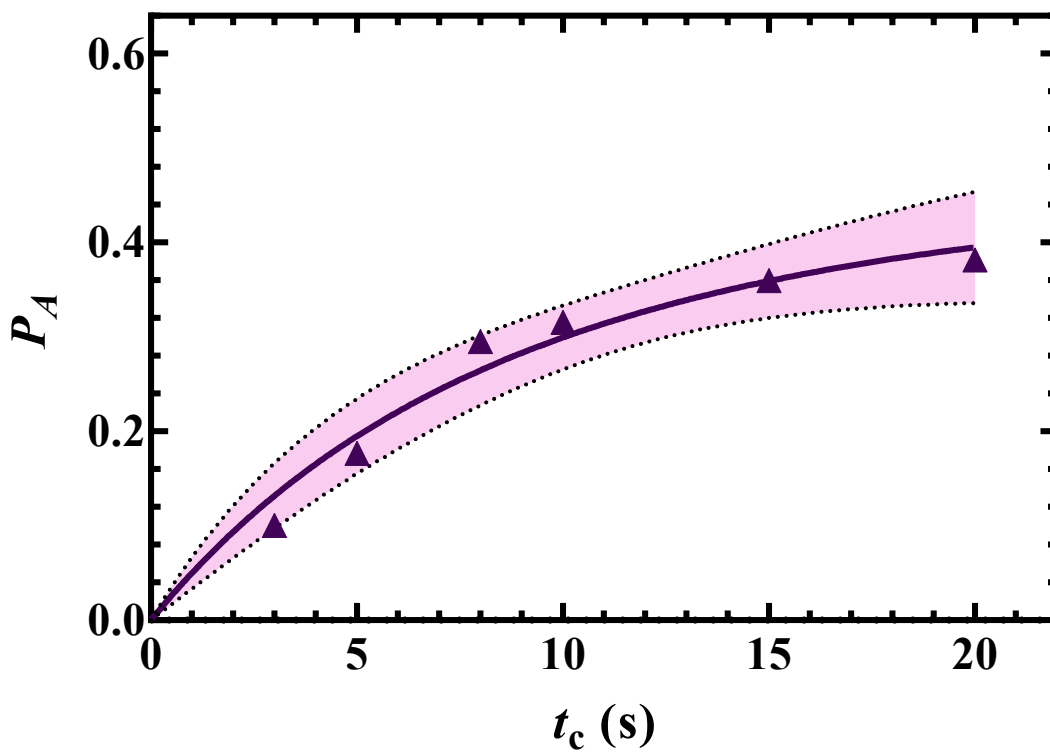
FIGURE 5.7: **Adhesion probability as a function of contact time using OT with the master equations fitted.** The simplified master equations (eq. 4.3 and eq. 4.5) were fitted to the overall probability of adhesion (p_A) versus contact time (t_c) data. A non-linear equation was fitted using least squares fit with no constraints or weighting. The two master equations were compared using sum of squares F test (fit was comparable). 95% confidence interval is shown (shaded area) and R^2 value was 0.9559.

TABLE 5.1: Comparison of fitted parameters from data obtained by two different experimental methods for iRBC adhesion to CD36.

	$m_r m_l K_A^o$	k_r (s^{-1})	R^2
MP	0.091 ± 0.007	0.113 ± 0.015	0.981
OT	0.086 ± 0.014	0.089 ± 0.025	0.956

that given model to represent a process. The binomial model had a 50.13% probability it is correct compared to Poisson's 49.87% with a AIC difference of -0.01043. The results indicate that either model can be used. Due to technical limitations, receptor and ligand density were unable to be determined and therefore only a grouped adhesion equilibrium constant ($m_r m_l K_A^o$). A future objective is to be able to accurately calculate receptor and ligand densities for CD36 expressing platelets and iRBCs, and use these values to infer the equilibrium constant K_A^o.

The results of the Poisson model fitting for both the MP and OT experiments are shown in table 5.1. Although the mean values for $m_r m_l K_A^o$ and k_r are lower for the OT method than that of the MP the values obtained from either experimental method are within error range of the other. The error margins are higher for the OT method and it has a lower R^2.

5.3.2 Forces of adhesion

Determining forces

The force felt on the bead can be considered to be proportional to the distance the center of the bead has been displaced from the center focus of the trap. The force on the bead can be determined by

$$F = kx \tag{5.1}$$

where k was the trap stiffness and x is the distance between the center of the bead and the focus of the laser.

When an iRBC was brought into contact with the bead it displaces the bead and the bead therefore feels a displacement force (F_d in pN):

$$F_d = kx \tag{5.2}$$

where the trap stiffness, k, was found for every new bead trapped and then the adhesion assay was carried out on that bead. Trap stiffness was measured using the equipartition method (refer to section 5.2.4). The bead displacement from the trap center was recorded using a QPD which produces a voltage signal that is converted to a displacement (refer to section 5.2.4).

Adhesion force (F_A in pN) was calculated using an analogous method. The displacement (x in μm) was a result of adhesion to the iRBC which then was moved away by the moving trap. The bead was pulled away from the center of its trap until the bond to the iRBC broke at which time the bead returned to its trap center.

Contact area

The contact length $2r$ between the bead and an iRBC was determined visually from optical images. The contact area (A_c in μm^2) was estimated by assuming the contact to be circular:

$$A_c = \pi \left[\frac{(2r)^2}{4} \right]$$

(5.3)

The displacement force was plotted for individual iRBCs and the corresponding contact area (Fig. 5.8). No correlation was found between the amount the bead was displaced due to contact with the iRBC and the corresponding contact area for the individual iRBCs.

At any given displacement force the area of contact varied for different iRBCs. This could have been due to varying iRBC membrane stiffness however the iRBC maturity also affects the positioning of the iRBC in the optical trap and consequently the contact area. This is displayed in Fig. 5.9. As the iRBCs could move within trap, when it was brought into contact with the bead the contact area and the surface of contact varied each cycle for the same iRBC-bead combination.

Factors that affect adhesion force

A contact that was deemed to result in an adhesion was defined as follows. The mean and standard deviation of the force felt on the bead in its resting state was calculated for each sequence of cycles. An adhesion was considered to occur if the force felt on the bead was greater than four standard deviations from the mean resting value. However, a limitation of the optical tweezer method is that the QPD can only record displacement, and consequently forces for a finite distance. Once the bead goes past this point only a lower bound for the force felt by the bead can be
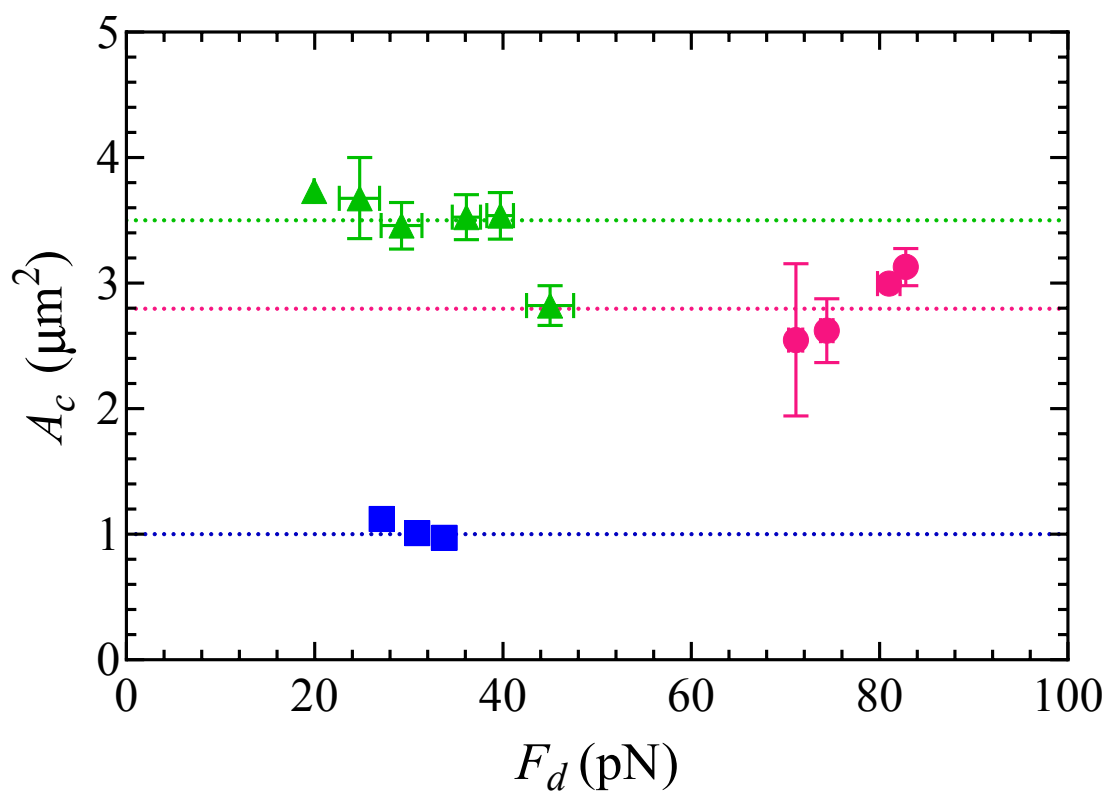
FIGURE 5.8: **Displacement force and contact area of iRBC with platelet coated bead.** Apparent area of contact (A_c in μm^2) appears to have no statistical dependence on the force the bead felt being displaced in the optical trap due to contact with an iRBC (F_d in pN). Three cells are shown. Contact time was 5s. Error bars are standard error of the mean (N > 3)
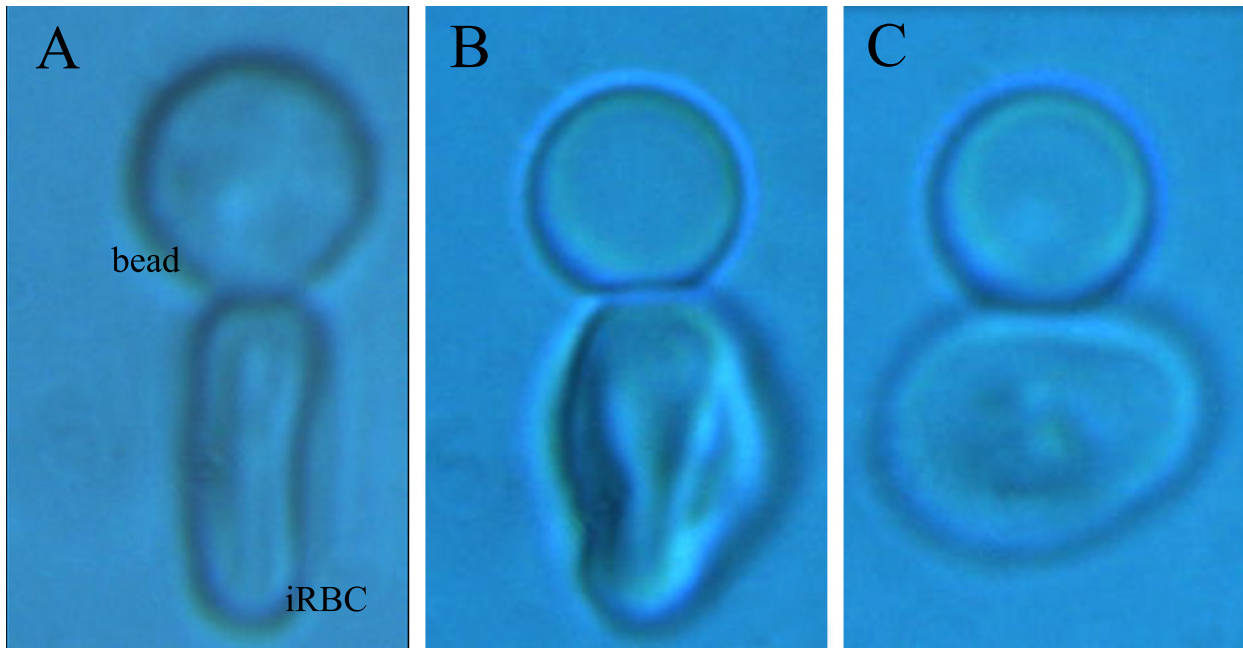
FIGURE 5.9: **Area of contact between iRBC and bead.** The area of contact between an iRBC and bead is dependant on the parasite maturity. Healthy RBCs and early stage iRBCs orientate in OT as shown in (A). However as the parasite matures the shape of the iRBC changes (B) and the orientation of the iRBC in the optical trap varies. An example of this is shown in (C).

determined. Further there is a maximum force the trap can impose on the bead. Consequently, if the bond force is greater than this value the bond will not be broken and the bead will remain attached to the iRBC. In these cases, the adhesion force is not used in analysis as the actual adhesion force is not known.

The effect the displacement force has on the resulting adhesion force when an adhesion occurs was investigated (Fig. 5.10). There was no apparent correlation between the adhesion force and the displacement force. However, for any given displacement force the resulting adhesion force was a function of the cell being investigated. This correlates with the results obtained (shown in Fig. 5.8) that indicates area of contact is not a function of the displacement force applied. Theoretically, adhesion force is directly correlated to the contact area. Therefore, if contact area is not a function of displacement force, the adhesion force observed will not vary with the displacement force, if contact area and contact time are kept constant, for the individual iRBCs.

The relationship between the contact area and the resulting adhesion force obtained was explored (Fig. 5.11). At a constant contact time, as the area of contact increased the resulting adhesion force observed also increased. At any given contact area the adhesive force was a function of the iRBC-bead pair being investigated. Interestingly, two of the cells investigated had a similar
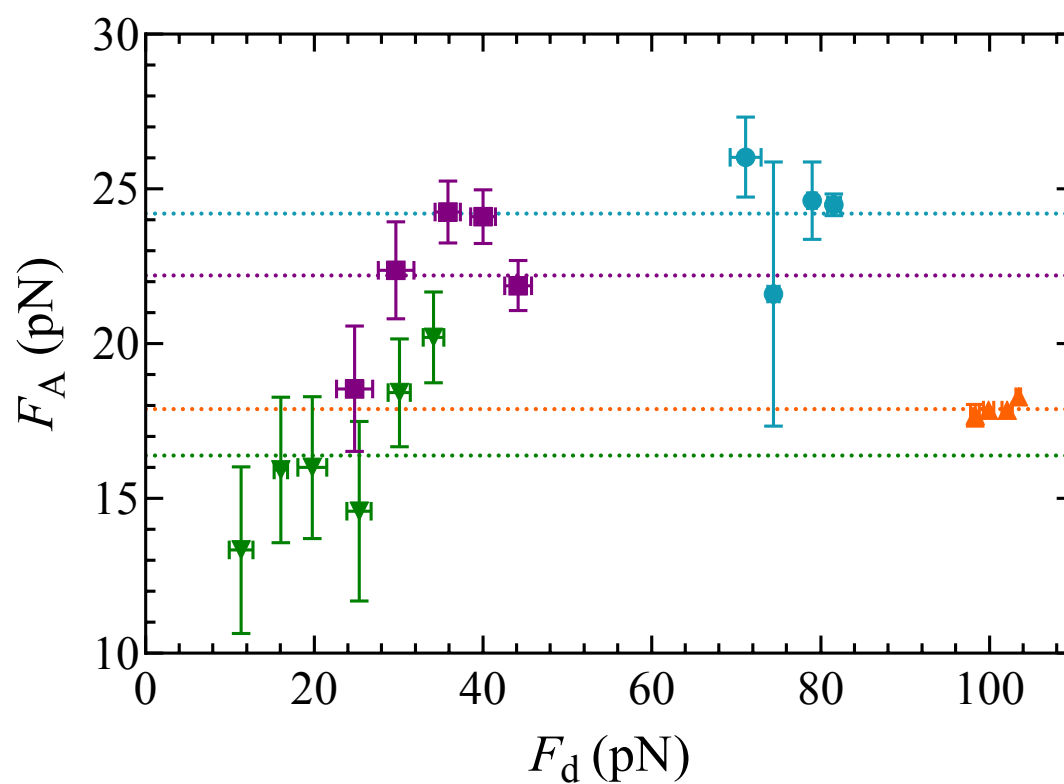
FIGURE 5.10: **Dependence of adhesion force on the magnitude of bead displacement in OT upon contact with iRBC.** The force (pN) corresponding to the bead being displaced in the OT due to contact with iRBC, F_d, showed no affect on the corresponding adhesion forces obtained. Four different cells are plotted with contact time maintained at 5s. Vertical and horizontal error bars correspond to standard error of the mean (N>2).

relationship between contact area and adhesive force over the contact areas investigated.

Adhesive forces as a function of contact area: comparison between MP and OT experiments

The adhesion forces obtained for a given contact area were compared from data obtained, using the MP and the OT methods, analysing iRBC adhesion to CD36. Fig. 5.12 shows the adhesion forces obtained for three cells using the MP method where the cell stiffness of the iRBCs was known and three cells using the OT method. It is evident that by the nature of the OT experiment only a smaller contact area can be achieved, compared to that of MP experiments, as the bead is not held fixed. Contact areas achieved using MP varied from 4 to 8 μm^2 whereas for OT experiments contact areas were between 1 to 4 μm^2. The MP method was able to detect and measure stronger adhesion forces. The OT method had a restriction on the maximum measurable adhesion force. Interestingly, the MP method seemed to require a larger contact area to obtain a similar adhesion force, when the adhesion force was between 20 to 30 pN.

Effect of contact time on adhesion force

The averaged adhesion force for each iRBC-pair at a defined contact time was determined and values shown in box and whisker plots in Fig. 5.13. The contact times were between 5 to 20 s in increments of 5 s. Although the mean adhesion force increased as contact time was increased at any contact time the spread of values did not change significantly.

Fig. 5.14 compares the results of adhesion force versus contact time for the MP and OT methods. It is evident that at any given contact time the median adhesion force was higher using MP method than that obtained using OT method. This could be due to limitation in the OT method in obtaining force information when bond was sufficiently strong as to either not break within the cycle or strong enough to pull bead past the QPD registering area. However, there were also rare events during MP experiments where the bond did not break. As such the bead was drawn away resulting in a very long tether and was not included in calculations of averaged adhesion force. Finally, it should be noted that although the adhesion forces obtained in the MP method are greater than those obtained in the OT method the contact area was also greater in the MP method (Fig. 5.12).
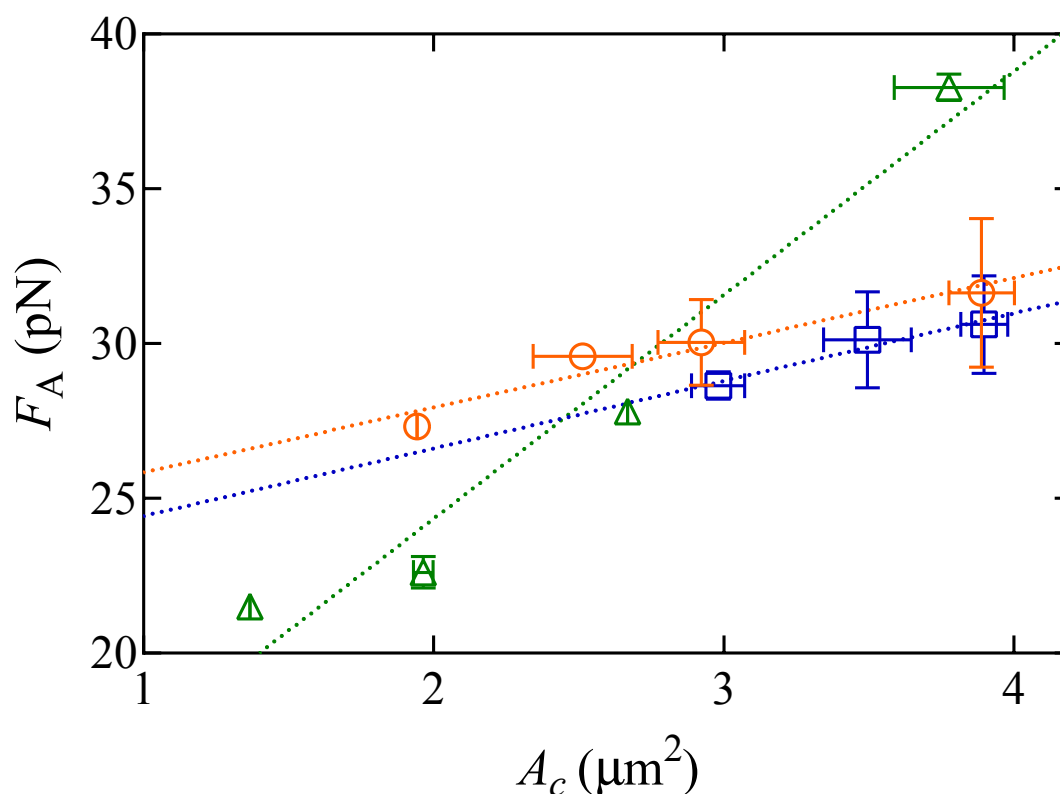
FIGURE 5.11: **Force of adhesion between iRBC and CD36 as a function of contact area.** As contact area (A_c) in μm^2 increases the resulting adhesion force (F_A in pN) between iRBC and CD36 also increases. Contact time was 5s. Three different iRBC-bead pairs were investigated: pair 1 ($\triangle$), pair 2 ($\square$) and pair 3 (o) with mean and standard error of mean (n=4) shown. Linear regression was carried out on the data for pair 1, 2 and 3 with a goodness of fit (R^2 value) of 0.9532, 0.9551 and 0.9303, respectively. At any given area of contact the force of adhesion was a function of the iRBC-bead pair. The slopes were statistically assessed to determine whether they were significantly non-zero. The slope for pair 1 and 3 was statistically significant ($F_{1,2} = 26.69, p = 0.0355$ and $F_{1,2} = 40.69, p = 0.0237$). The slope for pair 2 was not statistically significant ($F_{1,1} = 21.30, p = 0.1359$).
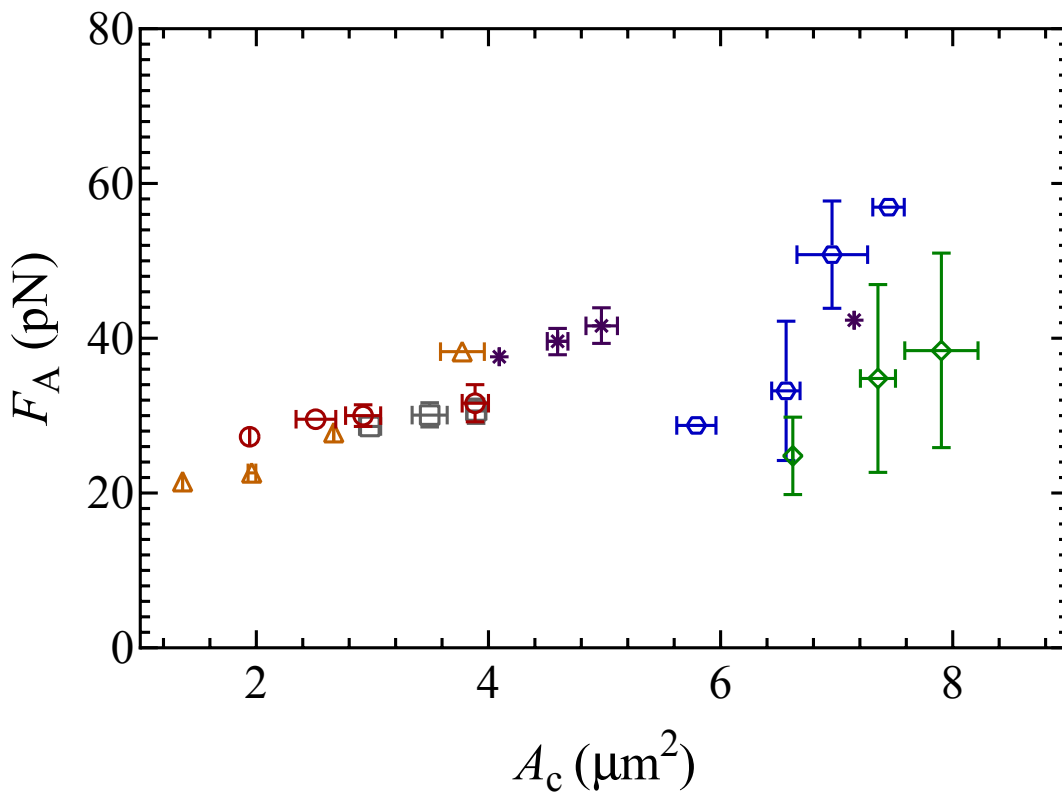
FIGURE 5.12: **Comparison of adhesion forces obtained for varying contact areas using OT and MP methods.** Increasing contact area (A_c in μm^2) resulted in an increase in the force of adhesion (F_A in pN) observed for both experimental methods. Three iRBCs-bead pairs are shown that used the OT method: pair 1 ($\triangle$), pair 2 (o) and pair 3 ($\square$). Three iRBCs-bead pairs of known cell stiffness that used the MP method are also shown: pair 4 with iRBC μ =29 pN/μm ($*$), pair 5 with iRBC μ =22 pN/μm (o) and pair 6 with iRBC μ =18 pN/μm ($\diamond$).
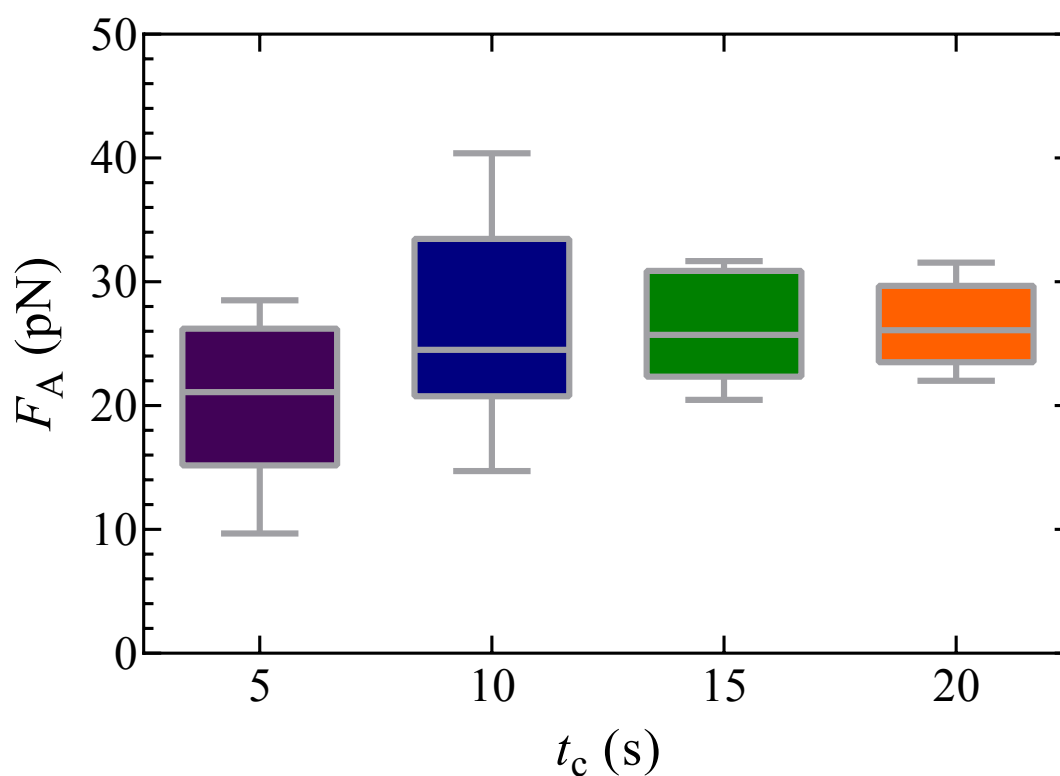
FIGURE 5.13: **Adhesion force as a function of contact time using OT** Adhesion forces (F_A in pN) obtained using OT experiment are shown for specific contact times (t_c) between 5 to 20 s in 5 s increments. The box ranges from the first to third quartile with line indicating median. The whiskers display the minimum and maximum adhesion force at that contact time. Adhesion forces plotted were the average adhesion forces for individual iRBC-bead pairs at specified contact time.
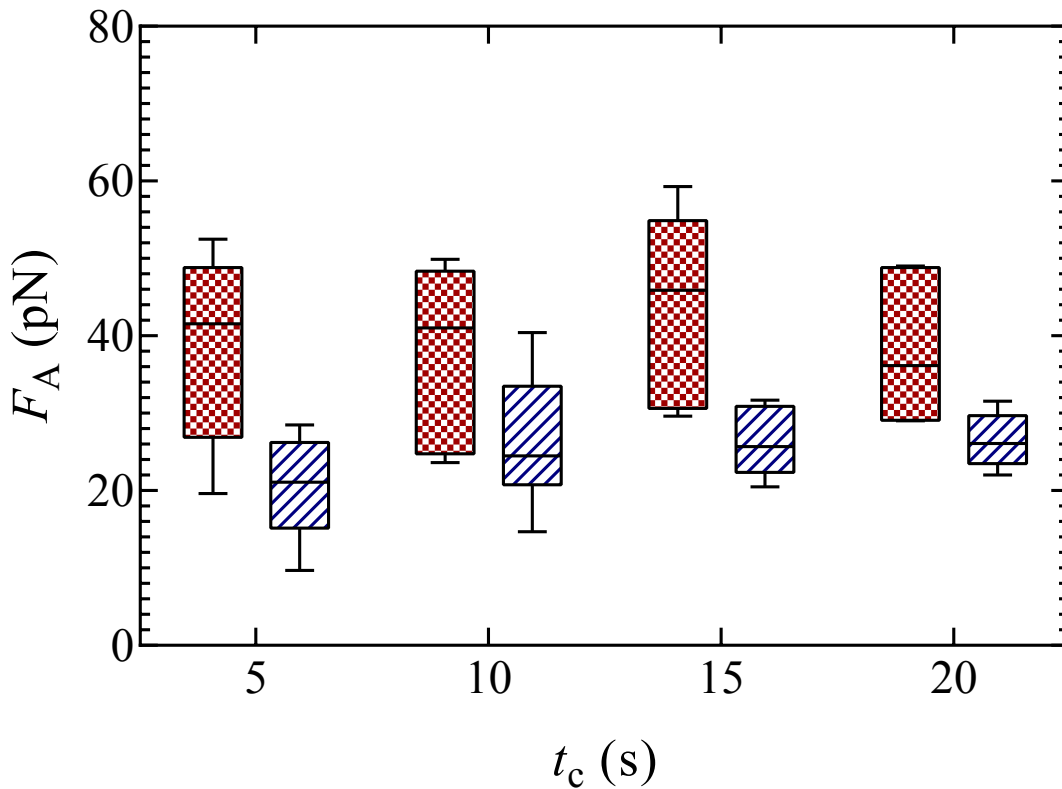
FIGURE 5.14: **Comparison of MP and OT methods to obtain adhesion force as a function of contact time.** The spread of the averaged adhesion forces (F_A in pN) obtained between iRBCs to CD36 at varying contact time (t_c in s) is shown for both OT (blue strip) and MP (red checkered) methods. Box indicates the first to third quartile of the averaged adhesion force per sequence. The whiskers display the minimum and maximum averaged adhesion force per sequence at that contact time. Six sequences were analysed at each contact time for each experiment (n=6).

5.4 Conclusion and future work

Adhesion between iRBC and CD36 expressed on platelets was investigated using the OT method. The optical tweezer method has the advantage of being non-invasive and the forces on the bead can be determined from the displacement of the bead in the trap and the trap stiffness. This method analysed the probability of adhesion occurring for various contact times varying between 3 and 20 s. As contact time increased to 10s the probability of adhesion also increased. At contact times greater than 10 s the adhesion probability reached a stable value of approximately 40% adhesion. This trend mirrors that which was observed using the MP method. The adhesion probabilities were within error margins between the two methods although the mean adhesion probability at low contact times was lower in the OT method than that for the MP method.

The simplified master equations were fitted to the adhesion probability versus contact time data. A comparison between the binomial distribution and Poisson distribution simplifications was undertaken using AIC. The AIC indicated that either model could be used. From the fitted data, the reverse kinetic rate was found to be 0.089 ± 0.025 s^{-1} and the grouped adhesion constant $(m_r m_l K_A^o)$ was found to be 0.086 ± 0.014 . A comparison between the MP and OT method indicated the values were within error bars of each other.

The forces involved in the adhesion between iRBC and CD36 using OT method were also investigated. The displacement force was found to have no correlation with the resulting contact area between the iRBC and bead. However, the contact area for any giving displacement force was a factor of the iRBC under investigation. As the iRBC is not held fixed in the optical trap the contact area can vary during the sequence. Further, depending on the maturity of the parasite within the iRBC, and consequently the shape of the iRBC, the optical trap holds the iRBC in different positions which can effect the contact area.

It was further shown that an increase in contact area does result in an increase in observed adhesion force as expected. However, the displacement force was found to have no correlation to the corresponding adhesion force when adhesion occurs. This is not surprising as displacement force does not affect contact area. Overall the contact areas achieved in the OT method were smaller than those obtained using the MP method as a direct result of the bead not being held fixed.

As contact time was increased the median value of the averaged adhesion force per sequence

also increased. Overall, the adhesion forces measured in the OT method were lower than those measured using MP method for any given contact time. However, this could be contributed to the lower average area of contact which occurred when using the oT method.

The OT method has the advantage of being non-invasive to the iRBC and thus reduces the likelihood of external parameters affecting the adhesion. Such external parameters include the use of micropipettes that could adversly affect the iRBC due to deforming the membrane. However, there are limitations with the OT method. As the objects are not held in a fixed position they can move around in the trap and therefore it cannot be guaranteed that the same surfaces contact each cycle.

There is also a limit on the strength of the OT trap and as such if a bond was stronger than this force, the iRBC and bead could not be pulled apart. Further, equipment limitations exist with the QPD that it can only measure a certain displacement from the trap center and if the bead is pulled further than this distance the actual force felt by the bead cannot be determined. Finally, in both the MP and OT methods a experimental limitation is the unknown densities of the receptors and ligands being investigated. If, in the future, a method can found to determine these densities more information could be obtained about the kinetic parameters involved in these adhesion events, in particular the overall equilibrium constant could be obtained.

Chapter 6

Equilibrium binding energies from fluctuation theorems and force spectroscopy simulations

6.1 Introduction

The energy of attachment/detachment of a cell-cell complex can be characterised by the change in the equilibrium free energy. This is traditionally measured using calorimetric methods that measure at a molecular level, where populations of bound and unbound receptors and ligands are monitored (Charych et al., 1993). Technically, the free energy for a cell-cell complex can be related to the work of single detachment events as explored in force spectroscopy (such as the experiments detailed in chapter 5), but only if the detachment event or path is traversed so slowly that the cell/membrane is at equilibrium at every point along the detachment path. In force spectroscopy measurements, the work can depend upon the speed of the "pulling" or detachment path. Friction or energy dissipation increases with speed and requires more work to achieve detachment. Moreover, if the rate of pulling is comparable or larger than the relaxation rate of the bound cell and membrane, then the work will depend critically upon the rate.

The present chapter details a theoretical study of model tweezer experiments and their quantitative analysis, and a procedure for biasing the work measured along de-binding events, irrespective of the speed at which the events are sampled, to obtain a free energy of binding. Such an experiment (as detailed in chapter 5) usually involves two objects, one of which is the cell under investigation, while the other can be a cell, or a ligand-coated bead/ substrate. At least one of the

objects is trapped within a tweezer potential. The optical tweezer is then moved through space, and as a consequence, the trapped object is pulled at a finite rate, and work is applied to the system. The objective was to demonstrate that in the presence of weak interactions, the determination of the adhesion free energy is possible, by taking advantage of modern tools of statistical mechanics, i.e., the recently developed non-equilibrium work theorems (Evans and Searles, 2002; Seifert, 2012), most notably the Jarzynski theorem (Jarzynski, 1997b; Jarzynski, 1997a), and the Crooks' fluctuation theorem (Crooks, 1998; Crooks, 1999; Crooks, 2000), which have been used with great success to interpret data from both computer simulations and experiments (Sandberg et al., 2015; Gapsys et al., 2015; Carberry et al., 2004; Bustamante, 2005; Gao et al., 2012; Wang et al., 2002).

In the presence of thermal fluctuations, the particle trajectories are stochastic, and hence the non-equilibrium work becomes a random variable, the distribution of which is the central object of the theorems. The optical tweezer experiments involve moving the locus of at least one tweezer potential minimum through space, and hence they are by their very nature intrinsically far from equilibrium. The main goal of the present theoretical and numerical study was therefore to find out whether an application of the work theorems to such experiments would be feasible under typical (but weak-binding) conditions in practice. In this context, it should be noted that the theorems involve an average over (in principle infinitely many) non-equilibrium processes, where, however, larger and larger sample sizes are needed the stronger the system is driven (Jarzynski, 1997b; Jarzynski, 1997a). It is clear that this behavior puts strong limits on the practical applicability of the theory.

It is worth noting that fluctuation theorems have already been used to computationally calculate binding free energies in drug-receptor systems (Sandberg et al., 2015; Gapsys et al., 2015). These computations involve *deterministic* nonequilibrium molecular dynamics of ligand-receptor pairs whose molecular properties, such as Lennard-Jones parameters and force fields are known. In this chapter, the analysis of single cell detachment events will be described and the usefulness of fluctuation theorems demonstrated, using data generated by *stochastic* simulation of a model cell and substrate. As a first explorative step a detailed realistic system was not studied, but rather a highly simplified model that however does capture the most salient features. In particular, parameters were chosen, like the interaction ranges and the driving protocol, in such a way that they

(very roughly) mimick the experimental situation under weak-binding conditions. As will be outlined in more detail below, the simulation studies the one-dimensional motion of a single particle (the bead), which is modeled as a point particle moving under the influence of a time-dependent external potential, and thermal fluctuations. The cell is replaced by a fixed point particle that exerts a force on the bead, such that the total potential is the static cell (or "membrane") potential, plus the harmonic tweezer potential, the position of whose minimum is time-dependent.

The remainder of the chapter is organised in the following manner: First, details of the Langevin simulation will be presented, including code validation. Second, the Jarzynski and Crooks fluctuation theorems are shown to be valid for this two state system. As a result, non-equilibrium work trajectories, calculated for the different trap velocities, can be used to obtain the equilibrium free energy of binding of the cell to the membrane. Thirdly, limitations of the fluctuation theorems will be discussed and illustrated with the use of cumulants. Finally, umbrella sampling will be used to derive equilibrium values such as probability of detachment or adhesion for a variety of different trap potentials.

6.2 Problem formulation

6.2.1 Fluctuation theorems

The adhesive free energy is defined as the difference in the free energies of two equilibrium states; the state where the bead and cell are bound together, and the state where they are unbound and independent of each other. If the process of unbinding the cell and bead is carried out isothermally and infinitesimally slowly, then the free energy difference ΔF is equal to the work W performed in carrying out the separation of bead and cell. On the other hand, if the unbinding experiment is carried out at a finite rate over a period of time t_{D}, the work performed will not be unique. Rather, an ensemble of such unbinding experiments will lead to a distribution of work values, $P_{\mathrm{F}}(W)$ (where the subscript 'F' indicates the experiment is carried out in the *forward* direction, from the cell and bead being bound together to being unbound). Note that in this scenario, it is possible that at the end of the experiment, the bead remains attached to the cell, even though work has been performed. The quasi-static process corresponds to the limit $t_{\mathrm{D}} \to \infty$, and $P_{\mathrm{F}}(W) \to$

$\delta(W - \Delta F)$. For finite rates of detachment, however,

$$\langle W \rangle = \int dW \, W \, P_{\text{F}}(W) \geq \Delta F \qquad (6.1)$$

The great advance that has been made with the recently developed fluctuation theorems is that, contrary to the suggestion of Eqn. (6.1), a knowledge of the non-equilibrium work distribution is sufficient to determine the equilibrium free energy ΔF exactly.

The two fluctuation theorems that are primarily used in this work are the Crooks' fluctuation theorem (Crooks, 1998; Crooks, 1999; Crooks, 2000), and the Jarzynski equality (Jarzynski, 1997b; Jarzynski, 1997a). Both these theorems are based on the following set of assumptions. The system, whose dynamics are stochastic and Markovian, is driven by an external perturbation from an initial equilibrium state, to a final state that is not necessarily at equilibrium. The external parameter driving the perturbation at a finite rate from the initial to the final state is usually denoted by λ, with values λ_0 in the initial equilibrium state, and λ_{f} in the final state.

The Crooks fluctuation theorem states that (Crooks, 1998; Crooks, 1999; Crooks, 2000),

$$\frac{P_{\text{F}}(W)}{P_{\text{R}}(-W)} = \exp\left[W - \Delta F\right] \qquad (6.2)$$

where both the work and the free energy have been non-dimensionalised with the energy scale $k_B T$. The distribution $P_{\text{F}}(W)$ is the probability that the work of magnitude W is performed in perturbing the system from an initial equilibrium state with $\lambda = \lambda_0$ to a final state with $\lambda = \lambda_{\text{f}}$ in a finite time t_{D}, while $P_{\text{R}}(-W)$ is the probability that work of the same magnitude but opposite sign will be performed on perturbing the system in the reverse path, from an equilibrium state with $\lambda = \lambda_{\text{f}}$ to a state with $\lambda = \lambda_0$, over the same length of time.

Equation 6.2 clearly suggests that the value of work W^* at which $P_{\text{F}}(W^*) = P_{\text{R}}(-W^*)$, is nothing but the equilibrium free energy difference between the initial and final states. We use this result subsequently in order to estimate the free energy of binding.

The Jarzynski equality in its original form (Jarzynski, 1997b; Jarzynski, 1997a) only considers perturbations from λ_0 to λ_{f}, and states that,

$$\langle e^{-W} \rangle_{\text{F}} = e^{-\Delta F} \qquad (6.3)$$

where the subscript 'F' on the ensemble average on the left hand side indicates an average over forward trajectories. While the ensemble average of the nonequilibrium work is always greater than the equilibrium free energy for finite rates of system perturbation, Jarzynski's equality states that an ensemble average of the exponential of $(-W)$ can be used to directly evaluate the equilibrium free energy. As will be seen subsequently, however, driving the system from λ_0 to λ_f at increasingly rapid rates leads to a widening of the distribution P_F, and consequently requires larger and larger ensembles to obtain an accurate estimate of ΔF.

In the next few sections, we introduce the model unbinding experiment, define precisely the initial and final states, identify the values of the external driving parameter λ corresponding to these states, and discuss the determination of the stochastic trajectory of the bead between these two states.

6.2.2   The model unbinding experiment

A truncated one-dimensional harmonic potential is used to describe both the membrane and optical trap potentials, as shown in Figs. 6.1 (a) and (b). They are defined by the following expressions,

$$U_{\mathrm{M}}(x) = \begin{cases} \dfrac{1}{2} k_{\mathrm{M}}\, x^2 - \epsilon_{\mathrm{M}} & \text{for} \quad x < x_{\mathrm{M}}^{\mathrm{ub}} \equiv \sqrt{2(\epsilon_{\mathrm{M}}/k_{\mathrm{M}})} \\ 0 & \text{for} \quad x \geq x_{\mathrm{M}}^{\mathrm{ub}} \end{cases} \tag{6.4}$$

and,

$$U_{\mathrm{OT}}(x) = \begin{cases} 0 & \text{for} \quad x < x_{\mathrm{OT}}^{\mathrm{lb}} \equiv x_{\mathrm{OT}} - \sqrt{2(\epsilon_{\mathrm{OT}}/k_{\mathrm{OT}})} \\ \dfrac{1}{2} k_{\mathrm{OT}}\, (x - x_{\mathrm{OT}})^2 - \epsilon_{\mathrm{OT}} & \text{for} \quad x \geq x_{\mathrm{OT}}^{\mathrm{lb}} \end{cases} \tag{6.5}$$

where, U_{M} and U_{OT} are the non-dimensional membrane and optical trap potential energies, respectively, with the energy scale $k_B T$ used for non-dimensionalisation. The distance x, measured from the fixed location of the minimum of the membrane potential, is non-dimensionalised by a length scale $\sqrt{k_B T/k_{\mathrm{s}}}$, where k_{s} is a spring constant. For typical optical trap strengths of $\mathcal{O}(\mathrm{fN/nm})$, displacements would be of $\mathcal{O}(\mathrm{nm})$. The spring constants k_{M} and k_{OT} (non-dimensionalised by k_{s}), determine the strength of the membrane and optical trap potentials. The location of the minimum of the optical trap potential is given by x_{OT}, while ϵ_{M} and ϵ_{OT} describe the depths of the membrane and optical trap potentials, respectively.
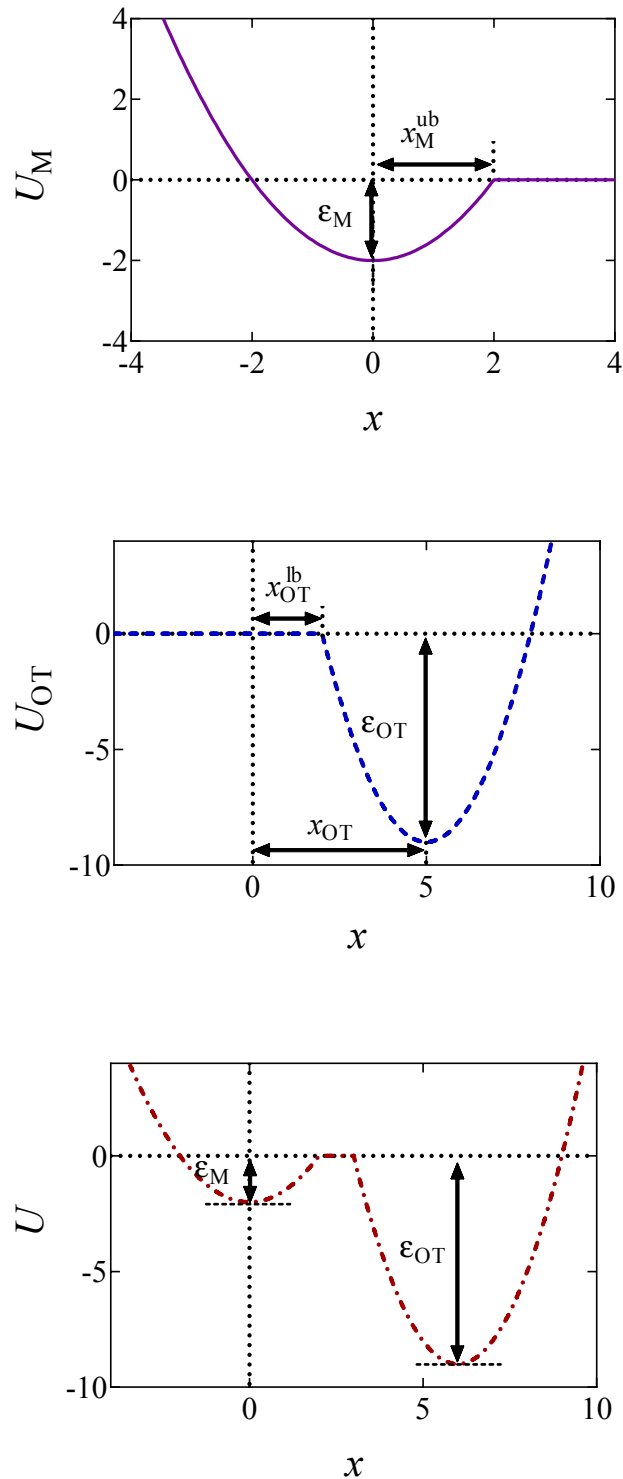
FIGURE 6.1: (Color online) Schematic of the potentials. (a) The membrane potential (held stationary at all times). (b) The optical trap potential. The minimum, x_{OT}, changes linearly with time as the optical trap is moved at a constant speed v_{OT} to a final position, $x_{OT}^{final} = 2\sqrt{2(\epsilon_{OT}/k_{OT})}$. (c) The 'summed' potential, $U = U_M + U_{OT}$, experienced by the bead at some time $t > 0$. In order to detach from the membrane the bead needs an energy greater than ϵ_M, while in order for the bead to go from being unattached to attached, it would require an energy of order ϵ_{OT} or greater.

The repulsive segment of the membrane potential ($-\infty < x \leq 0$) accounts for the impenetrability of the membrane to the bead, while the attractive segment ($0 < x \leq x_\mathrm{M}^\mathrm{ub}$) represents the adhesive force exerted by the membrane on the bead (Fig. 6.1(a)). Beyond this distance, the bead detaches from the membrane and the influence on the bead by the membrane potential becomes negligible. Note that the minimum of the potential is held fixed at the origin ($x = 0$) for all time. Traditionally optical tweezer potentials are represented by harmonic wells (Carberry et al., 2004; Wang et al., 2002). However, we wish to model scenarios where the optical trap fails to detach the bead from the membrane. In other words, the bead escapes the trap and remains on the membrane. The optical trap potential is consequently truncated on the side nearest the membrane at $x = x_\mathrm{OT}^\mathrm{lb}$ (Fig. 6.1(b)). The summed potential, $U(x) = U_\mathrm{M}(x) + U_\mathrm{OT}(x)$, at some time $t > 0$, is shown schematically in Fig. 6.1(c).

The optical trap potential minimum is located at the origin at time $t = 0$, i.e., $x_\mathrm{OT}(t = 0) = 0$. At later times, the optical trap is translated horizontally linearly with time, at varying speeds v_OT (i.e., $x_\mathrm{OT}(t) = v_\mathrm{OT}\, t$), in order to simulate the process of bead detachment by the optical trap. The final position of the trap minimum is always maintained at a fixed location, $x_\mathrm{OT}^\mathrm{final} = 2\sqrt{2(\epsilon_\mathrm{OT}/k_\mathrm{OT})}$, regardless of the value of v_OT. The summed potential U is time dependent because of the time dependence of the optical potential. For the purpose of illustration, the shapes of the membrane and optical trap potentials, along with the summed potential, during the course of the simulation, at three different locations of the optical trap minimum are shown in Figs. 6.2.

The relative ease of attachment and detachment is controlled by the magnitudes of the barrier heights for the membrane (ϵ_M), and the optical tweezer (ϵ_OT) potentials, and strengths k_M and k_OT, respectively. In order to model different adhesive interactions between the bead and the membrane, the barrier heights and spring constants can be changed appropriately. In the present work, we choose three different sets of values for these parameters (given in Table 6.1), allowing different scenarios to be tested, as illustrated in Figs. 6.3. In Figs. 6.3 (a), the membrane potential is weaker than the optical trap in both strength and depth. In Figs. 6.3 (b), both the potentials have the same strength and depth, with the dimensional depth being of order $10\, k_\mathrm{B}T$, while in Figs. 6.3 (c), their dimensional depths are of order $1\, k_\mathrm{B}T$. As will be seen subsequently, these three different scenarios lead to considerably different adhesive behaviour.
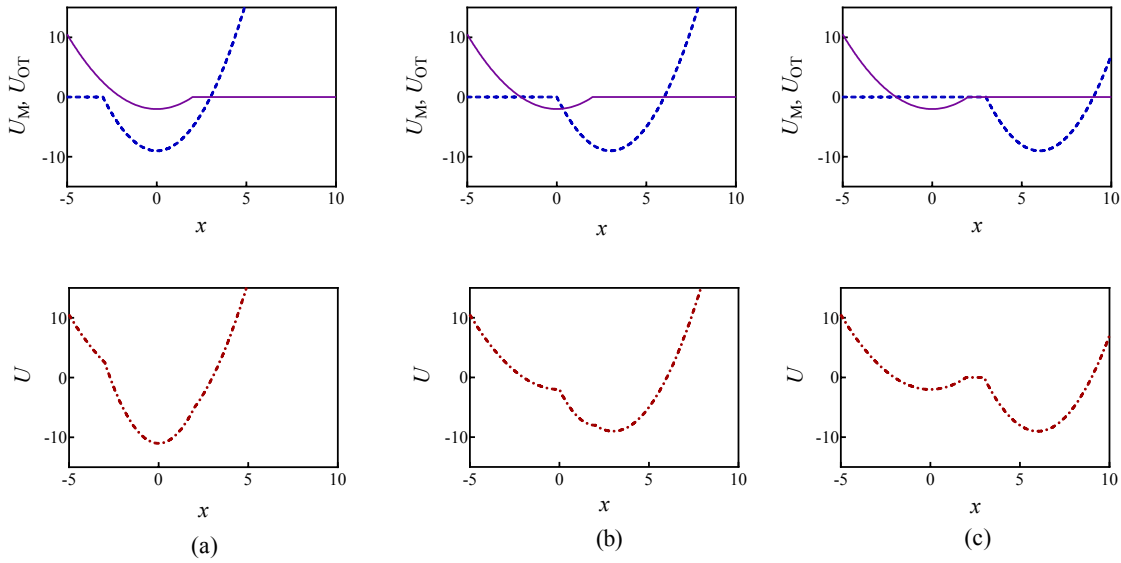
FIGURE 6.2: Potential snapshots at three different locations of the optical trap minimum corresponding to parameter set 1 in Table 6.1. The first row shows the membrane (purple solid line) and optical trap (blue dashed line) potentials separately, whilst row two shows the summed potential (red dashed-dot line). Potential shapes at: (a) $x_{\mathrm{OT}} = 0$, (b) $x_{\mathrm{OT}} = 0.5\, x_{\mathrm{OT}}^{\mathrm{final}}$, and (c) $x_{\mathrm{OT}} = x_{\mathrm{OT}}^{\mathrm{final}}$.

TABLE 6.1: Various non-dimensional parameter values chosen to provide membrane and optical trap potentials with different depths and strengths.

	Parameter sets		
	1	2	3
k_{M}	1	2	1
k_{OT}	2	2	1
ϵ_{M}	2	9	2
ϵ_{OT}	9	9	2

6.2.3 Analytical evaluation of the binding free energy

The external perturbation parameter λ driving the unbinding of the bead and cell in the model experiment described in the previous section is the location of the minimum of the optical trap potential x_{OT}, with $x_{\mathrm{OT}} = 0$ corresponding to the initial state of the system $\lambda = \lambda_0$, and $x_{\mathrm{OT}} = x_{\mathrm{OT}}^{\mathrm{final}}$ corresponding to the final state $\lambda = \lambda_{\mathrm{f}}$. In order to apply the fluctuation theorems to this model experiment, it is necessary to calculate the work performed in driving the system from its initial to its final state. The steps involved in calculating the work are described in the next section. However, for the simple scenario considered here, the free energy difference between the initial and final states can be evaluated analytically exactly.
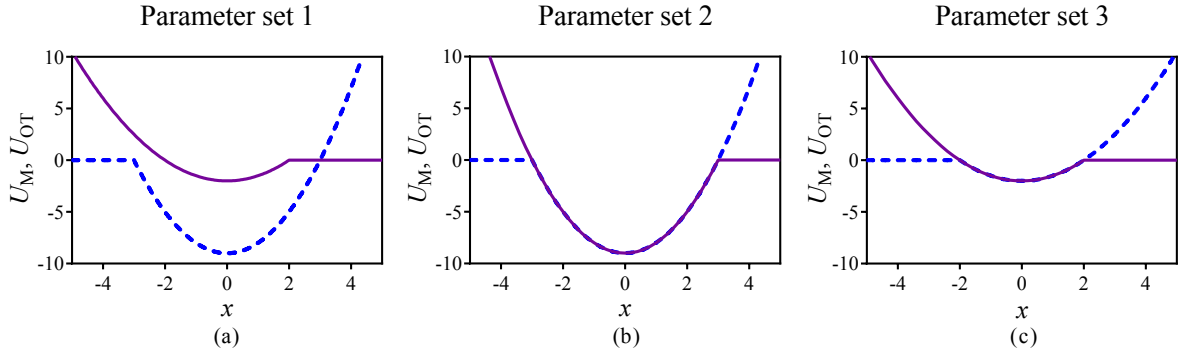
FIGURE 6.3: (Color online) Snapshots of the membrane (purple solid line) and optical tweezer (blue dashed line) potentials at time $t = 0$, at three different non-dimensional values of well depths, and membrane and trap strengths, as given in Table 6.1.

The difference in the free energies of the initial and final states is given by,

$$\Delta F_{\text{anal}} = F_{\lambda_f} - F_{\lambda_0} = -\ln \frac{Z(x_{\text{OT}} = x_{\text{OT}}^{\text{final}})}{Z(x_{\text{OT}} = 0)} \tag{6.6}$$

where the respective partition functions are given by the expressions,

$$
\begin{aligned}
Z(x_{\text{OT}} = 0) = \int_{-\infty}^{\infty} dx\, e^{-U_{\lambda_0}(x)} &= \int_{-\infty}^{x_{\text{OT}}^{\text{lb}}} dx \exp\left[-\left(\frac{1}{2}\,k_{\text{M}}\,x^2 - \epsilon_{\text{M}}\right)\right] \\
&+ \int_{x_{\text{OT}}^{\text{lb}}}^{x_{\text{M}}^{\text{ub}}} dx \exp\left[-\left(\frac{1}{2}\,k_{\text{M}}\,x^2 - \epsilon_{\text{M}} + \frac{1}{2}\,k_{\text{OT}}\,x^2 - \epsilon_{\text{OT}}\right)\right] \\
&+ \int_{x_{\text{M}}^{\text{ub}}}^{\infty} dx \exp\left[-\left(\frac{1}{2}\,k_{\text{OT}}\,x^2 - \epsilon_{\text{OT}}\right)\right]
\end{aligned} \tag{6.7}
$$

$$
\begin{aligned}
Z(x_{\text{OT}} = x_{\text{OT}}^{\text{final}}) = \int_{-\infty}^{\infty} dx\, e^{-U_{\lambda_f}(x)} &= \int_{-\infty}^{x_{\text{M}}^{\text{ub}}} dx \exp\left[-\left(\frac{1}{2}\,k_{\text{M}}\,x^2 - \epsilon_{\text{M}}\right)\right] + \int_{x_{\text{M}}^{\text{ub}}}^{x_{\text{OT}}^{\text{lb}}} dx \exp\left(-0\right) \\
&+ \int_{x_{\text{OT}}^{\text{lb}}}^{\infty} dx \exp\left[-\left(\frac{1}{2}\,k_{\text{OT}}\,(x - x_{\text{OT}}^{\text{final}})^2 - \epsilon_{\text{OT}}\right)\right]
\end{aligned} \tag{6.8}
$$

The bounds on the integrals in the expressions above can be understood from the schematic representations of the potentials in Figs. 6.1 and 6.2.

These integrals can be evaluated analytically, and give rise to the following expressions for the partition functions of the initial and final states, respectively (see appendix C.2 for more details),

$$
\begin{aligned}
Z(x_{\mathrm{OT}} = 0) = {} & \frac{\sqrt{\pi/2}}{\sqrt{k_{\mathrm{M}}}} \exp\left(\epsilon_{\mathrm{M}}\right) \left[\mathrm{erf}\left(\frac{x_{\mathrm{OT}}^{\mathrm{lb}} \sqrt{k_{\mathrm{M}}}}{\sqrt{2}} \right) + 1 \right] \\
& + \frac{\sqrt{\pi/2}}{\sqrt{k_{\mathrm{M}} + k_{\mathrm{OT}}}} \exp\left(\epsilon_{\mathrm{M}} + \epsilon_{\mathrm{OT}}\right) \left[\mathrm{erf}\left(\frac{x_{\mathrm{M}}^{\mathrm{ub}} \sqrt{k_{\mathrm{M}} + k_{\mathrm{OT}}}}{\sqrt{2}} \right) - \mathrm{erf}\left(\frac{x_{\mathrm{OT}}^{\mathrm{lb}} \sqrt{k_{\mathrm{M}} + k_{\mathrm{OT}}}}{\sqrt{2}} \right) + 1 \right] \\
& + \frac{\sqrt{\pi/2}}{\sqrt{k_{\mathrm{OT}}}} \exp\left(\epsilon_{\mathrm{OT}}\right) \left[\mathrm{erfc}\left(\frac{x_{\mathrm{M}}^{\mathrm{ub}} \sqrt{k_{\mathrm{OT}}}}{\sqrt{2}} \right) \right] \quad (6.9)
\end{aligned}
$$

$$
\begin{aligned}
Z(x_{\mathrm{OT}} = x_{\mathrm{OT}}^{\mathrm{final}}) = {} & \frac{\sqrt{\pi/2}}{\sqrt{k_{\mathrm{M}}}} \exp\left(\epsilon_{\mathrm{M}}\right) \left[\mathrm{erf}\left(\frac{x_{\mathrm{M}}^{\mathrm{ub}} \sqrt{k_{\mathrm{M}}}}{\sqrt{2}} \right) + 1 \right] + \left(x_{\mathrm{OT}}^{\mathrm{lb}} - x_{\mathrm{M}}^{\mathrm{ub}} \right) \\
& + \frac{\sqrt{\pi/2}}{\sqrt{k_{\mathrm{OT}}}} \exp\left(\epsilon_{\mathrm{OT}}\right) \left[\mathrm{erfc}\left(\frac{(x_{\mathrm{OT}}^{\mathrm{lb}} - x_{\mathrm{OT}}^{\mathrm{final}}) \sqrt{k_{\mathrm{OT}}}}{\sqrt{2}} \right) \right] \quad (6.10)
\end{aligned}
$$

Equations (6.9) and (6.10) can be used along with Eqn. (6.6) to obtain the exact value of the free energy difference between the initial and final state for any choice of parameter values in the potentials $U_{\mathrm{M}}(x)$ and $U_{\mathrm{OT}}(x)$. Free energy differences for the particular choice of values listed in Table 6.1 as parameter sets 1, 2 and 3, are given in Table 6.2. They are used to evaluate the accuracy of the free energy differences predicted by the Crooks and Jarzynski fluctuation theorems.

6.2.4   Nonequilibrium work

The application of the fluctuation theorems requires the determination of the distribution of work $P_{\mathrm{F}}(W)$ when the system is driven from λ_0 to λ_{f} in the forward path, and the distribution $P_{\mathrm{R}}(W)$ when the path is reversed. Following the arguments of Jazynski (Jarzynski, 1997a), we introduce the function $H_\lambda(x)$, as the energy of the system for any fixed value of λ, where $x(t)$ is the stochastic phase-space trajectory that describes the time evolution of the system, which depends on the time dependence of the external parameter λ. The total work performed on the system, when it evolves from $\lambda = \lambda_0$ to $\lambda = \lambda_{\mathrm{f}}$, in a time period t_{D}, is (Jarzynski, 1997a)

$$
W = \int_0^{t_{\mathrm{D}}} dt'\, \dot{\lambda} \frac{\partial H_\lambda}{\partial \lambda}\left(x(t')\right) \quad (6.11)
$$

where $\dot{\lambda} = d\lambda/dt$. The stochastic phase-space trajectory $x(t)$ of the bead is determined here by solving a Langevin equation, as described in the next section. In the model system considered here, the only component of the system's energy that depends on the external driving parameter $\lambda \, (= x_{\mathrm{OT}})$, is the potential energy of the trap, U_{OT}. As a result, $\partial H_\lambda/\partial \lambda = \partial U_{\mathrm{OT}}/\partial x_{\mathrm{OT}}$, and $\dot{\lambda} = dx_{\mathrm{OT}}(t)/dt = v_{\mathrm{OT}}$. From Eqn. (6.5), for $x \geq x_{\mathrm{OT}}^{\mathrm{lb}}$, since

$$F_{\mathrm{OT}}(x) = -\frac{\partial U_{\mathrm{OT}}}{\partial x} = \frac{\partial U_{\mathrm{OT}}}{\partial x_{\mathrm{OT}}} = -k_{\mathrm{OT}}\,(x - x_{\mathrm{OT}}) \tag{6.12}$$

it follows that (for derivation see appendix C.2),

$$W = \int_0^{t_{\mathrm{D}}} dt' \, v_{\mathrm{OT}} \, F_{\mathrm{OT}}\left(x(t')\right) \tag{6.13}$$

Equations (6.12) and (6.13) are used here to calculate the work done on the bead when the optical trap is translated from $x_{\mathrm{OT}} = 0$ to $x_{\mathrm{OT}} = x_{\mathrm{OT}}^{\mathrm{final}}$, at all times t at which the bead's location satisfies, $x(t) \geq x_{\mathrm{OT}}^{\mathrm{lb}}$. At other times, when the force of the optical trap on the bead is zero, the contribution to the work is zero.

6.2.5 The Langevin equation

In the absence of inertia, the time evolution of the particle's position $x(t)$, subject to an external force due to the presence of the membrane and optical potentials, and subject to thermal fluctuations, is described by a non-dimensional Langevin equation

$$\frac{dx}{dt} = F_{\mathrm{ext}} + F_{\mathrm{rand}} \tag{6.14}$$

where time is non-dimensionalised by ζ/k_{s}, with ζ being the friction coefficient of the particle, F_{ext} is the external force due to the combined potential, given by $F_{\mathrm{ext}} = -\partial U/\partial x$, and F_{rand} is the random force, which has the following mean and variance,

$$\langle F_{\mathrm{rand}} \rangle = 0$$

$$\langle F_{\mathrm{rand}}(t) F_{\mathrm{rand}}(t') \rangle = 2\,\delta(t - t') \tag{6.15}$$

We use an Euler algorithm,

$$x_{n+1} = x_n + F_{\text{ext}}\,\Delta t + \sqrt{2\,\Delta t}\,r$$

to numerically integrate the Langevin equation, where $\langle r \rangle = 0$, and $\langle r^2 \rangle = 1$. Using a random number generator that produces random numbers u uniformly between zero and one, the conditions on r are satisfied by choosing $r = \sqrt{12}\,(u - 0.5)$.

Details of time step sizes and the number of trajectories used in the simulations are given in the context of the various results discussed below.

6.3   Results and Discussion

6.3.1   Code validation

In order to validate the predictions of the current algorithm, comparisons were carried out with the results of two earlier studies which demonstrated the Evans-Searles fluctuation theorems using experiments and simulations involving an optical trap (Wang et al., 2002; Carberry et al., 2004). The *transient fluctuation theorem* (TFT) of Evans and Searles (Evans and Searles, 1994; Evans and Searles, 2002) states that,

$$\frac{P(\Sigma_t = A)}{P(\Sigma_t = -A)} = \exp(A) \tag{6.16}$$

while the *integrated form* of the transient fluctuation theorem (ITFT) states that,

$$\frac{P(\Sigma_t < 0)}{P(\Sigma_t > 0)} = \langle \exp(-\Sigma_t) \rangle_{\Sigma_t > 0} \tag{6.17}$$

Here, Σ_t is the dissipation function, which is a dimensionless measure of the total entropy production that occurs along the system's trajectory, over time t. It assumes different forms depending on the system under consideration. The TFT relates the probability of observing a trajectory with entropy *production*, $\Sigma_t = A$, to the probability of observing a trajectory with the *consumption* of the same magnitude of entropy, $\Sigma_t = -A$. On the other hand, the integrated version of the theorem specifies a relationship between the frequency of entropy-consuming trajectories to that of entropy-producing trajectories, with the average on the right hand side of Eqn. (6.17) carried out over only entropy-producing trajectories.

In the first study considered here, Wang et al. (2002) examined the trajectory of a colloidal particle captured in an optical trap translated at a uniform velocity relative to the surrounding medium. They experimentally demonstrated the validity of the ITFT, and also carried out molecular dynamics simulations to show that the predictions of both the TFT and the ITFT were correct. In the second study, Carberry et al. (2004) observed the time-dependent relaxation of a colloidal particle subjected to a step change in the strength of a stationary optical trap. In this case, they were able to experimentally demonstrate the validity of both the TFT and the ITFT.

We have carried out Langevin simulations of these two previously studied applications of the Evans-Searles fluctuation theorems in order to ensure that our algorithm was implemented correctly. In both these examples, only a single optical trap is involved. As a consequence, the external force (in Eqn. (6.14)) on the colloidal particle due to the optical trap is given by,

$$F_{\text{ext}}(t) = -k_{\text{OT}}\left(x(t) - x_{\text{OT}}(t)\right) \tag{6.18}$$

where k_{OT} and $x_{\text{OT}}(t)$ assume different expressions in the two studies. As mentioned earlier, the dissipation function Σ_t is also different in the two cases. The relevant expressions are listed below.

Study 1 (Wang et al. (2002)):

$$k_{\text{OT}} = \text{constant}$$

$$x_{\text{OT}}(t) = x_{\text{OT}}(0) + v_{\text{OT}}\,t$$

$$\Sigma_t = \int_0^t dt'\, v_{\text{OT}}\, F_{\text{OT}}\left(x(t')\right)$$

where $F_{\text{OT}}(x)$ is given by Eqn. (6.12).

Study 2 (Carberry et al. (2004)):

$$k_{\text{OT}} = k_0 + (k_1 - k_0)H(t)$$

$$x_{\text{OT}}(t) = \text{constant} = 0, \text{ for all } t$$

$$\Sigma_t = \frac{k_0 - k_1}{2}\left[x^2(t) - x^2(0)\right]$$

where $H(t)$ is the Heaviside step function, and k_0 and k_1 are constants equal to the optical trap strength before and after the step change, respectively.
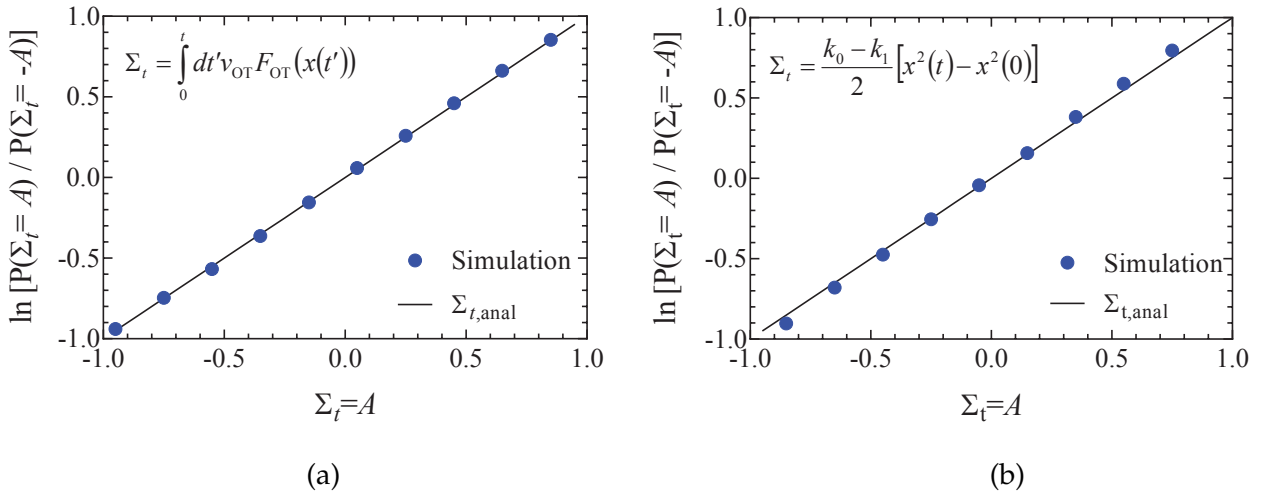
FIGURE 6.4: Validation of code through demonstration of the Evans-Searles transient fluctuation theorem. Natural log of the number ratio of trajectories with entropy production Σ_t to those with entropy production $-\Sigma_t$ versus Σ_t (filled circles), found from 2×10^6 trajectories. Lines are drawn with slope of 1 as predicted by the TFT (indicated as $\Sigma_{t,\text{anal}}$ in the figure legend). (a) Study 1 (Wang et al. (2002)). A line of best fit through simulation data has a slope 1.007 ± 0.004. (b) Study 2 (Carberry et al. (2004)). A line of best fit through simulation data has a slope 1.058 ± 0.002.

The Langevin simulation of both these cases was carried out with 2×10^6 trajectories, using a time step of 10^{-4}. In both cases, after an initial equilibration time of 10^4 time steps, the distribution of particle positions was checked to see if the respective equilibrium distribution functions were obeyed. In Study 1, after equilibration, the optical trap was translated with a constant velocity $v_{\text{OT}} = 0.5$, from time $t = 0$ to $t = 10$, with a constant trap strength $k_{\text{OT}} = 1$. In Study 2, after equilibration, the optical trap strength was changed discontinuously from $k_0 = 1$ to $k_1 = 2$ at time $t = 0$, and the simulation continued until $t = 10$. The position of the colloidal particle at time $t = 0$ is taken to be $x(0)$. Figures 6.4 and 6.5 summarise the results of the validation studies.

In order to demonstrate the TFT a histogram of the values of the dissipation function Σ_t at the end of the simulation was constructed over the 2×10^6 trajectories. If N_i is the number of trajectories with dissipation function between $\Sigma_{t,i} \pm \Delta/2$ (where $\Delta = 0.1$ is the size of the histogram bin, and $\Sigma_{t,i} = i\,\Delta$), then the ratio of probabilities on the left hand side of Eqn. (6.16) can be evaluated from (N_i/N_{-i}). Figures 6.4(a) and 6.4(b) show the natural log of the ratio of the probabilities obtained in this manner for both the studies, plotted against the value of Σ_t. Also shown in the figures is a line of slope unity, which represents the prediction of the TFT.

The ITFT is demonstrated for the two studies in Figs. 6.5(a) and 6.5(b), respectively, by plotting the ratio of the number of entropy consuming trajectories ($\Sigma_t < 0$) to the number of entropy
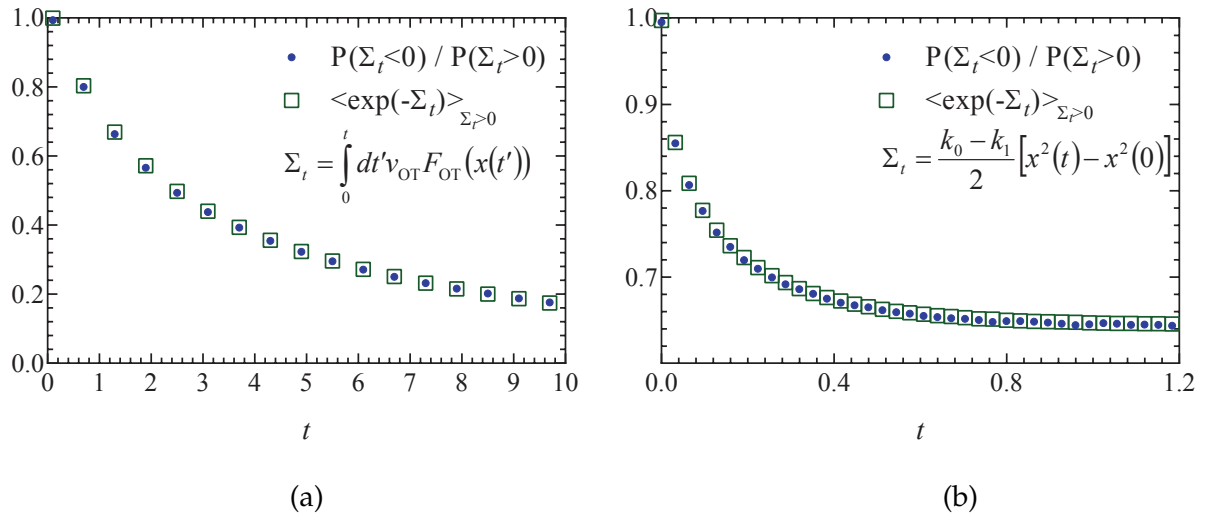
FIGURE 6.5: Validation of code through demonstration of the Evans-Searles integrated fluctuation theorem. The number ratio of entropy consuming ($\Sigma_t < 0$) trajectories to entropy producing ($\Sigma_t > 0$) trajectories (filled circles), and the entropy production averaged over entropy producing trajectories, $\langle \exp(-\Sigma_t) \rangle_{\Sigma_t > 0}$ (empty squares), versus time, found from 2×10^6 trajectories. (a) Study 1 (Wang et al. (2002)). (b) Study 2 (Carberry et al. (2004)).

producing ($\Sigma_t > 0$) trajectories as a function of time, along with the time dependence of the entropy production averaged over the subset of 2×10^6 trajectories in which entropy is produced. The exponential decrease in the number of entropy consuming trajectories with time is evident in both cases.

In the subsequent sections, the validated Langevin simulation algorithm is used to establish the usefulness of the Crooks fluctuation theorem and the Jarzynski equality in finding the equilibrium binding energy in the model unbinding experiment (refer to appendix D.1 for details on Langevin program).

6.3.2 Crooks fluctuation theorem

The usefulness of the Crooks fluctuation theorem to determine the equilibrium binding free energy was examined by carrying out simulations with the three sets of values listed in Table 6.1 for the membrane and optical trap potential parameters. Each simulation was carried out with a time step size $\Delta t = 10^{-3}$. Rather than running the simulations for an initial equilibration period, the positions of the bead at time $t = 0$ were chosen such that they satisfied the known initial equilibrium distribution functions. Two kinds of simulations were carried out. The first kind, that generated *forward* trajectories, started at time $t = 0$ with the optical trap minimum at $x_{\text{OT}} = 0$,
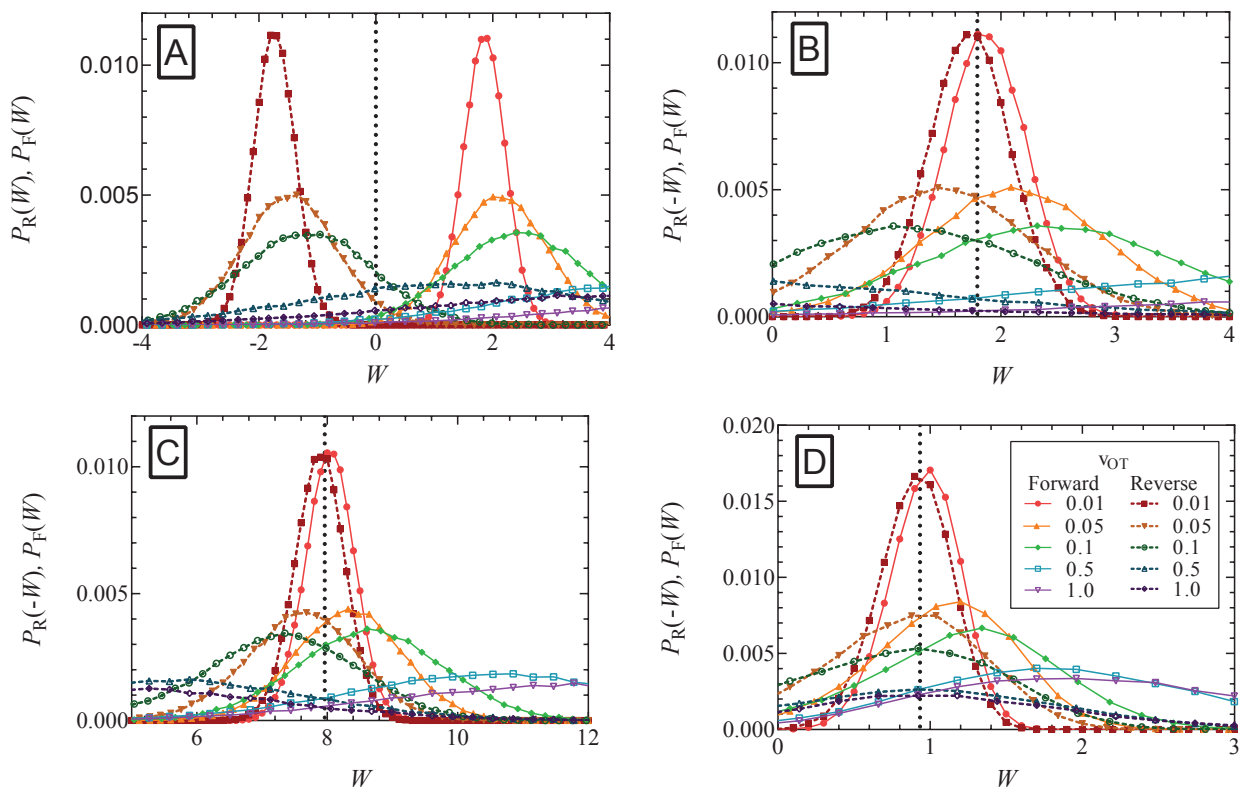
FIGURE 6.6: Evaluation of the equilibrium binding free energy using the Crooks fluctuation theorem for the three sets of potential parameter values listed in Table 6.1. In panel A, the probability of work W being performed in the *forward* path ($P_F(W)$) is plotted alongside the distribution of work values in the *reverse* path ($P_R(W)$) for parameter set 1, for the trap velocities $v_{OT} = \{0.01, 0.05, 0.1, 0.5, 1\}$. In panels B (parameter set 1), C (parameter set 2), and D (parameter set 3), $P_F(W)$ is plotted alongside $P_R(-W)$. Note that the equilibrium free energy $\Delta F = W^*$, where, W^* is the value of work at which $P_F(W^*) = P_R(-W^*)$ (indicated by the dotted vertical lines).

followed by the trap minimum being translated with a uniform velocity v_{OT} until it was located at $x_{\mathrm{OT}}^{\mathrm{final}}$ at time $t = t_{\mathrm{D}}$. The set of optical trap velocities $v_{\mathrm{OT}} = \{0.01, 0.05, 0.1, 0.5, 1\}$ was used. Note that t_{D} depends on the value of v_{OT} since the location $x_{\mathrm{OT}}^{\mathrm{final}}$ is fixed and the same for all simulations. The second set of simulations, which generated *reverse* trajectories, started at time $t = 0$ with the optical trap minimum at $x_{\mathrm{OT}} = x_{\mathrm{OT}}^{\mathrm{final}}$, followed by the trap minimum being translated with the same set of velocities (but with opposite sign), until the minimum was located at $x_{\mathrm{OT}} = 0$ at time $t = t_{\mathrm{D}}$. Each simulation in the forward and reverse direction consisted of 10^5 trajectories. Ten such simulations were carried out in each case. The work values obtained after each trajectory in both sets of forward and reverse simulations (calculated using Eqn. (6.13)), were sorted into bins of width equal to 0.01. The distributions of work values obtained in this manner are plotted in Figs. 6.6 for the various cases.

Panel A in Figs. 6.6 plots the probability of work W being performed in the forward path ($P_{\mathrm{F}}(W)$) alongside the distribution of work values in the reverse path ($P_{\mathrm{R}}(W)$) for the various trap velocities v_{OT} indicated in the figure legend. While the work is predominantly positive in the forward trajectories (with a positive mean value), the work is predominantly negative in the reverse trajectories (with a negative mean value). The widening of the distributions with increasing trap velocities is also apparent. As noted previously, in the limit of a quasistatic process ($v_{\mathrm{OT}} \to 0$), $P_{\mathrm{F}}(W) \to \delta(W - \Delta F)$, and $\langle W \rangle_{\mathrm{F}} = \Delta F$. However, for increasing values of v_{OT}, the mean value shifts towards the right with a wider range of work values, and with $\langle W \rangle_{\mathrm{F}} \geq \Delta F$.

The usefulness of Crooks fluctuation theorem is best appreciated when $P_{\mathrm{F}}(W)$ is plotted alongside $P_{\mathrm{R}}(-W)$ as shown in panels B, C and D of Figs. 6.6. These three figure panels correspond to the three potential parameter sets listed in Table 6.1, respectively. As noted before, according to Eqn. (6.2), the value of work W^* at which $P_{\mathrm{F}}(W^*) = P_{\mathrm{R}}(-W^*)$ is nothing but the equilibrium binding free energy. Consequently, ΔF is estimated from Figs. 6.6 by finding the point of intersection of the forward and reverse probability curves for each of the trap velocities, for the three sets of parameter values. The values of ΔF obtained in this way are listed in Table 6.2. The percentage relative error in the free energy predicted by the Crooks fluctuation theorem, defined by the expression,

$$\mathrm{Error} = \left| \frac{\Delta F - \Delta F_{\mathrm{anal}}}{\Delta F_{\mathrm{anal}}} \right| \times 100 \tag{6.19}$$

TABLE 6.2: Comparison of equilibrium binding free energies calculated with the Crooks fluctuation theorem, the Jarzynski equality, and from a sum over the first six terms of the cumulant expansion, with exact analytical values, for the various trap velocities. The three sets of values for the membrane and optical trap potential parameters are given in Table 6.1.

Parameter set 1: $\Delta F_{\text{anal}} = 1.796$						
v_{OT}	Crooks		Jarzynski (forward)		Cumulants	
	ΔF	% error	ΔF	% error	ΔF_6	% error
0.01	1.796	$\sim 10^{-2}$	1.7955 ± 0.0002	$\sim 10^{-2}$	1.796	$\sim 10^{-2}$
0.05	1.796	$\sim 10^{-2}$	1.796 ± 0.001	$\sim 10^{-2}$	1.799	0.1
0.1	1.805	0.5	1.796 ± 0.002	$\sim 10^{-2}$	1.797	0.1
0.5	1.764	1.8	1.808 ± 0.016	0.7	1.823	1.5
1	1.814	1.0	1.834 ± 0.044	2.1	1.746	2.8

Parameter set 2: $\Delta F_{\text{anal}} = 7.960$						
v_{OT}	Crooks		Jarzynski (forward)		Cumulants	
	ΔF	% error	ΔF	% error	ΔF_6	% error
0.01	7.959	$\sim 10^{-2}$	7.9600 ± 0.0005	$\sim 10^{-3}$	7.961	$\sim 10^{-2}$
0.05	7.956	$\sim 10^{-2}$	7.960 ± 0.001	$\sim 10^{-2}$	7.964	0.1
0.1	7.959	$\sim 10^{-2}$	7.962 ± 0.002	$\sim 10^{-2}$	7.951	0.1
0.5	7.878	1.0	7.974 ± 0.023	0.2	8.019	0.7
1	7.960	$\sim 10^{-2}$	8.165 ± 0.035	2.6	8.213	3.2

Parameter set 3: $\Delta F_{\text{anal}} = 0.934$						
v_{OT}	Crooks		Jarzynski (forward)		Cumulants	
	ΔF	% error	ΔF	% error	ΔF_6	% error
0.01	0.941	0.7	0.9333 ± 0.0002	0.1	0.933	0.1
0.05	0.937	0.3	0.934 ± 0.001	$\sim 10^{-2}$	0.937	0.3
0.1	0.933	0.1	0.933 ± 0.001	0.1	0.933	0.1
0.5	0.934	$\sim 10^{-2}$	0.936 ± 0.012	0.2	0.955	2.2
1	0.937	0.3	0.933 ± 0.020	0.6	1.063	13.9

is also listed in Table 6.2. Remarkably, for each parameter set, the intersection of the forward and reverse probability curves occurs at nearly identical values, with the error in the estimated free energy being at most 1.8% even for large trap velocities.

The increase in error with increasing trap velocity can be understood by considering panel B in Fig. 6.6. As the velocity increases, it causes the mean value of work to shift away from the free energy value, with a simultaneous increase in the standard derivation of the distribution. As a

result, the crossover occurs at the tails of the distributions, where errors are high and therefore require much larger populations to ensure adequate statistics. Figure 6.6 indicates that the velocities at which this could become an issue is sensitive to the choice of potential parameters. Parameter set 1 (panel B), where the optical trap strength was double that of the membrane, and the barrier height for detachment was much lower than that of re-attachment (see Figs. 6.3a), seems to have the most movement of the mean away from the exact free energy value. On the other hand parameter set 3 (panel D), where barrier heights are of $\mathcal{O}(k_B T)$ (see Figs. 6.3c), seems to be the least affected by increased velocity.

6.3.3 Jarzynski equality

The original form of the Jarzynski equality, as given by Eqn. (6.3), corresponds to switching the system from an initial equilibrium state with $\lambda = \lambda_0$ to a final state with $\lambda = \lambda_\mathrm{f}$. However, it is also possible to derive a form of the Jarzynski equality when the system is switched from an initial equilibrium state with $\lambda = \lambda_\mathrm{f}$ to a final state with $\lambda = \lambda_0$ (Hummer, 2001),

$$\langle e^{-W} \rangle_\mathrm{R} = e^{\Delta F} \tag{6.20}$$

where the subscript 'R' on the ensemble average on the left hand side indicates an average over reverse trajectories, and the change in free energy is still defined by $\Delta F = F_{\lambda_\mathrm{f}} - F_{\lambda_0}$.

The sets of forward and reverse simulations carried out to demonstrate the Crooks fluctuation theorem can also be used to examine the usefulness of the Jarzynski equality. The ensemble averages on the left hand sides of Eqns. (6.3) and (6.20) were calculated using the values of work accumulated at the end of each of the 10^5 trajectories corresponding to a particular simulation. Since each of the forward and reverse simulations was repeated ten times, we obtain ten estimates for the equilibrium free energy in each case. The mean of these 10 values, and the standard error in these mean values are displayed in Figs. 6.7 for all the cases considered here. Parameter sets 1, 2, and 3 are shown in rows 1, 2, and 3 respectively, with the left hand column showing results for the forward trajectories whilst the right hand column shows results for reverse trajectories. The mean value of ΔF and the standard error in the mean are also compared with exact analytical values in Table 6.2 for simulations carried out in the forward direction. Note that the percentage relative error reported in the Table is calculated using Eqn. (6.19) with the mean value of ΔF.
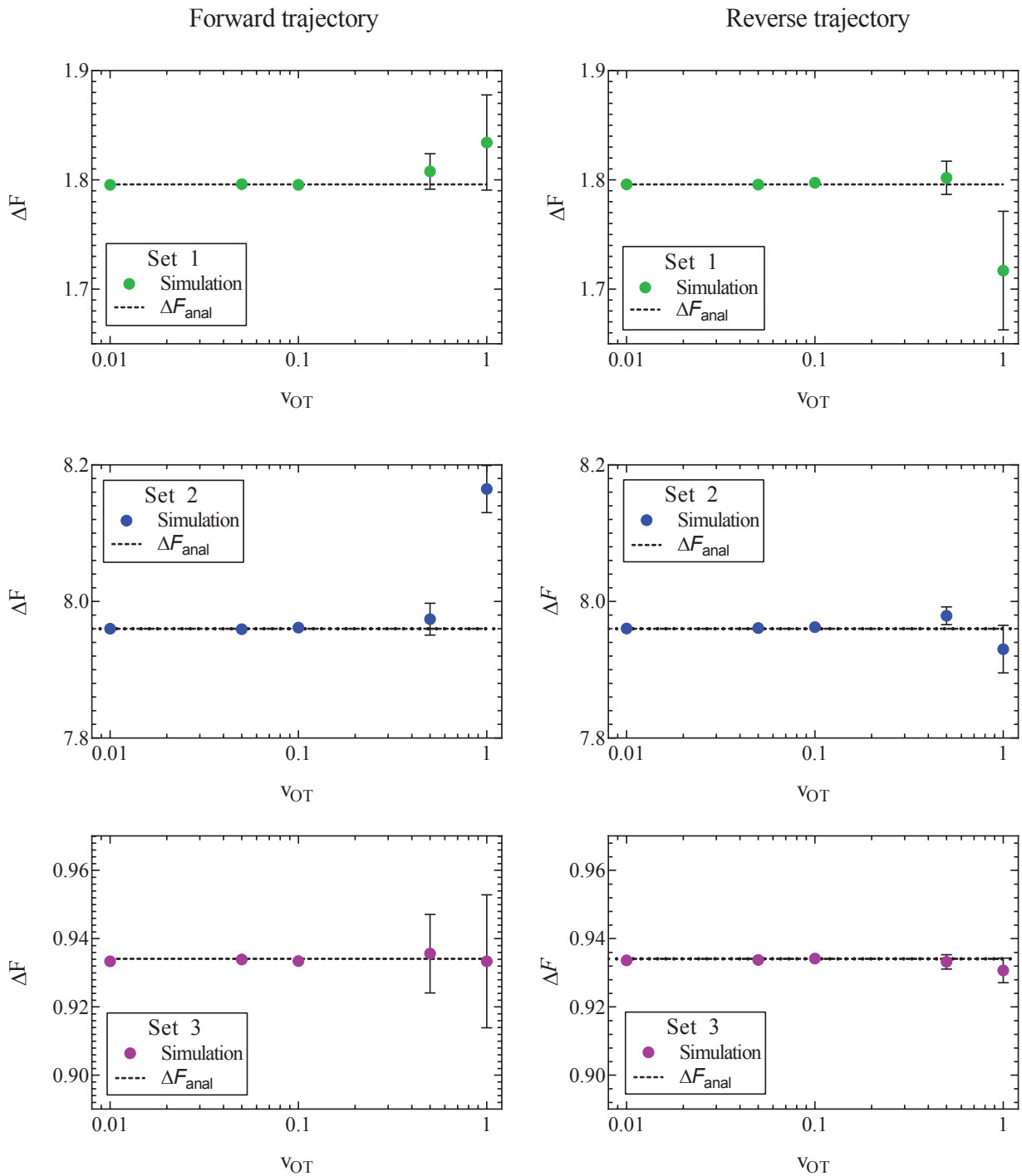
FIGURE 6.7: Free energy values estimated using Jarzynski's equality as a function of trap velocity v_{OT}. Symbols are results of simulations, while the dashed lines indicate the exact analytical value of the free energy, for parameter sets 1 (row 1), 2 (row 2) and 3 (row 3). Results for the forward trajectories are displayed in column one, whilst reverse trajectories are displayed in column two. Error bars indicate the standard error in the estimated mean free energy values obtained from ten repeated simulations.

TABLE 6.3: Accuracy of the Gaussian approximation at various trap velocities in the forward and reverse paths, for the membrane and optical trap potential parameters corresponding to Set 1 in Table 6.1.

Forward trajectories					
v_{OT}	ΔF_{anal}	$\langle W \rangle_{\mathrm{F}}$	σ_{F}^2	$\langle W_d \rangle_{\mathrm{F}}$	E_{F}
0.01		1.860	0.128	0.064	0.000
0.05		2.116	0.632	0.320	0.003
0.1	1.796	2.428	1.262	0.632	0.001
0.5		4.842	5.922	3.046	0.085
1		7.535	10.604	5.739	0.437

Reverse trajectories					
v_{OT}	ΔF_{anal}	$\langle W \rangle_{\mathrm{R}}$	σ_{R}^2	$\langle W_d \rangle_{\mathrm{R}}$	E_{R}
0.01		-1.732	0.128	0.064	0.000
0.05		-1.481	0.633	0.315	0.001
0.1	1.796	-1.159	1.281	0.637	0.003
0.5		1.320	6.337	3.116	0.052
1		4.258	12.552	6.054	0.222

A feature of all approaches for determining free energy differences using ensemble averages, of which the Jarzynski equality is no exception, is their limitation due to sample size. As argued by Jarzynski (Jarzynski, 1997a), for systems where the spread in the distributions $P_{\mathrm{F}}(W)$ and $P_{\mathrm{R}}(W)$ is large, the function $\exp(-W)$ varies significantly over many standard deviations about the mean value of work. As a result, the numerically determined average $\langle \exp(-W) \rangle$ can be dominated by work values that are by their very nature statistically rare. Therefore an unreasonable number of measurements of the work would be required to get an accurate result. This results in a practical restriction on the rates at which the system can be switched between λ_0 and λ_{f}. As can be seen from Figs. 6.7 and Table 6.2, the accuracy in the estimation of the free energy decreases with the trap velocity in all cases.

A comparison of the relative errors in the free energies predicted by the Crooks fluctuation theorem and the Jarzynski equality (in the case of forward trajectories) in Table 6.2 shows that they are roughly similar in magnitude for the various cases. As noted earlier, there is a reduction in accuracy with increasing trap velocity, which appears to be magnified when either one or both the potential well depths are high compared to $k_{\mathrm{B}}T$, which is the case for parameter sets 1 and 2 (displayed in Figs. 6.3). The dependence of the error on well depth is studied shortly below.

For slow rates of switching between λ_0 and λ_f, the distributions $P_F(W)$ and $P_R(W)$ are expected to be approximately Gaussian (Hummer, 2001). In this case, retaining only the first two terms in the cumulant expansion for $\langle \exp(-W) \rangle$ (which is discussed in greater detail in the section below), one can write (Hummer, 2001),

$$\Delta F_F = F_{\lambda_f} - F_{\lambda_0} \approx \langle W \rangle_F - \frac{\sigma_F^2}{2}$$

$$\Delta F_R = F_{\lambda_0} - F_{\lambda_f} \approx \langle W \rangle_R - \frac{\sigma_R^2}{2}$$

where σ_F^2 and σ_R^2 are the variances of the work distributions $P_F(W)$ and $P_R(W)$, respectively. Defining the mean dissipated work $\langle W_d \rangle$ as the difference between the mean actual work of the process and the reversible work (which is equal to the equilibrium free energy), we can estimate the departure from the Gaussian approximation by evaluating the error estimates E_F and E_R defined by,

$$E_F = \left[\langle W \rangle_F - \frac{\sigma_F^2}{2} \right] - \Delta F_{\text{anal}} = \langle W_d \rangle_F - \frac{\sigma_F^2}{2} \tag{6.21}$$

$$E_R = \left[\langle W \rangle_R - \frac{\sigma_R^2}{2} \right] - (-\Delta F_{\text{anal}}) = \langle W_d \rangle_R - \frac{\sigma_R^2}{2} \tag{6.22}$$

The values of mean actual work, variances, mean dissipated work and error estimates, for membrane and optical trap potential parameters corresponding to Set 1, are displayed in Table 6.3 for both the forward and reverse paths. Clearly, the Gaussian approximation leads to an error of less than 5% up to trap velocities $v_{\text{OT}} = 0.5$. Interestingly, the variances of $P_F(W)$ and $P_R(W)$ and the mean dissipated work in the forward and reverse paths are roughly equal in magnitude for identical velocities in the forward and reverse paths.

For distributions that are not Gaussian, the exponential average in Jarzynski's equality can be expanded in terms of cumulants (Hummer, 2001), and the convergence of ΔF can be studied as a function of the various potential parameters, as discussed in the section below. It is worth noting that it is also possible to obtain estimates for the free energy that are accurate to a higher order in the cumulant expansion than the Gaussian approximation by suitably combining the mean work and variance in the forward and reverse paths (Hummer, 2001).
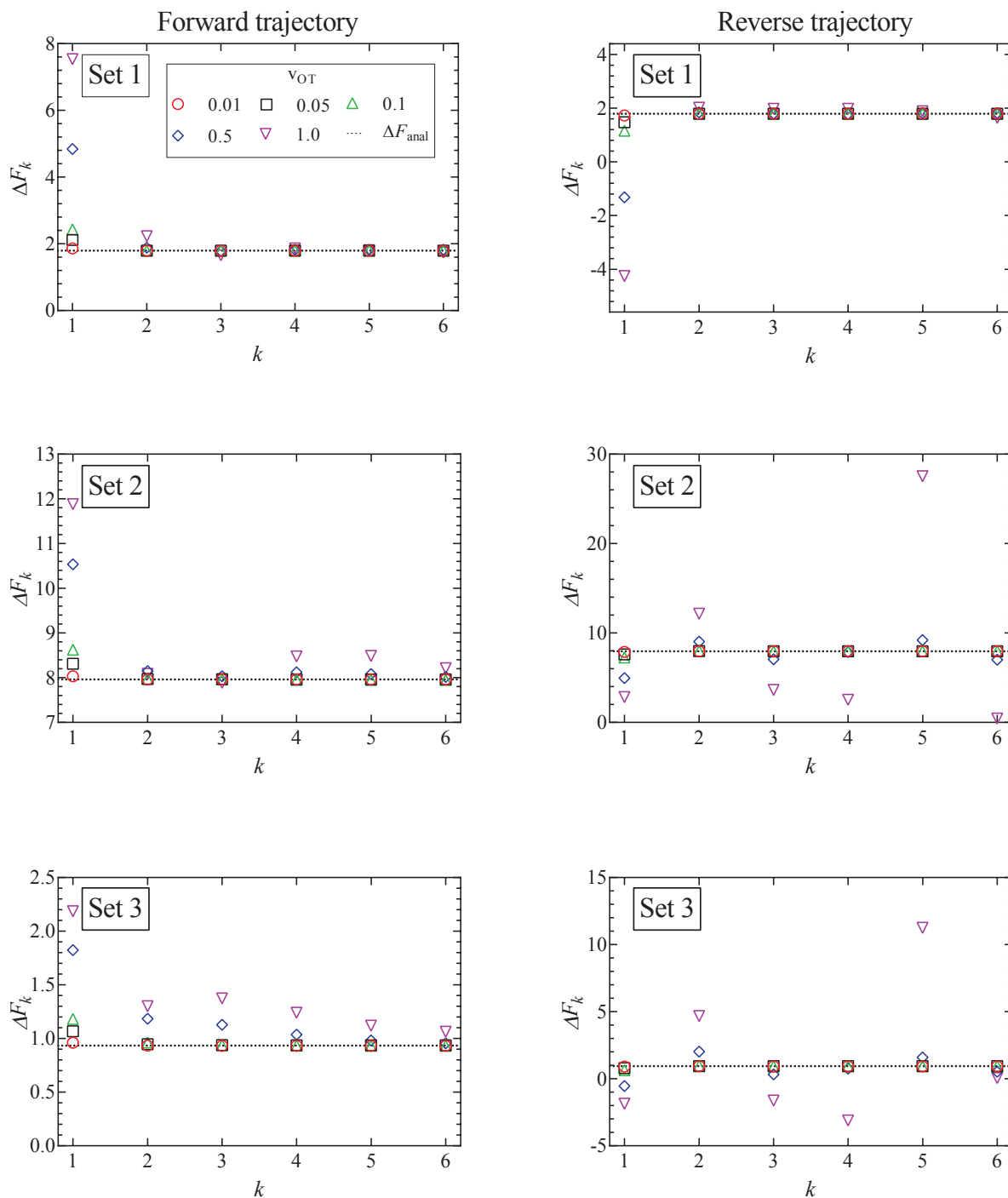
FIGURE 6.8: Approximate estimate of the free energy change from a cumulant expansion for the average of the exponential of work, at various values of trap velocity v_{OT}. ΔF_k is the approximate value obtained from a sum over k terms in the expansion. Symbols are results of simulations, while the dashed lines indicate the exact analytical value of the free energy, for parameter sets 1 (row 1), 2 (row 2) and 3 (row 3). Results for the forward trajectories are displayed in column one, whilst reverse trajectories are displayed in column two.

6.3.4   Cumulant expansion for the free energy of binding

The average of the exponential of work on the left hand sides of Eqns. (6.3) and (6.20) in Jarzynski's equality can be expanded in terms of cumulants (Hummer, 2001). In the case of forward paths, this leads to the following expression for the free energy change,

$$\Delta F = \lim_{k \to \infty} \Delta F_k \tag{6.23}$$

where,

$$\Delta F_k = \sum_{n=1}^{k} (-1)^{n+1} \frac{C_n}{n!} \tag{6.24}$$

Here, the cumulants C_n are defined by the following expressions,

$$C_1 = \langle W \rangle_{\mathrm{F}}$$

$$C_2 = \mu_2 = \sigma_{\mathrm{F}}^2$$

$$C_3 = \mu_3$$

$$C_4 = \mu_4 - 3\,\mu_2^2$$

$$C_5 = \mu_5 - 10\,\mu_2\,\mu_3$$

$$C_6 = \mu_6 - 15\,\mu_2\,\mu_4 - 10\,\mu_3^2 + 30\,\mu_2^3$$

$$\vdots$$

$$C_n = \mu_n - \sum_{j=1}^{n-2} \binom{n-1}{j} \mu_j\,C_{n-j}; \quad n \geq 2 \tag{6.25}$$

with μ_n being the central moments of $P_{\mathrm{F}}(W)$,

$$\mu_n = \big\langle\, [W - \langle W \rangle_{\mathrm{F}}]^n \,\big\rangle_{\mathrm{F}} \tag{6.26}$$

The recursive relationship between the cumulants and central moments in Eqn. (6.25) has been given by Smith (1995). In the case of reverse paths, the cumulant expansion on the right hand side of Eqn. (6.24) leads to the free energy change $-\Delta F = F_{\lambda_0} - F_{\lambda_f}$, with μ_n in the expressions for C_n being the central moments of $P_{\mathrm{R}}(W)$.

An analysis of the simulation results for the forward and reverse paths in terms of the cumulant expansion is displayed in Figs. 6.8, where the values of ΔF_k (which represent the approximate estimate of the free energy change given by k terms of the cumulant expansion), are plotted against k (up to $k = 6$), and compared with the analytical value ΔF_{anal}. Additionally, the particular values obtained for ΔF_6 in the case of forward trajectories, and the relative error compared to the exact values are listed in Table 6.2. Details of cumulant analysis program can be found in appendix D.2. As expected, at low trap velocities where the system approaches a quasistatic process, the work distribution approaches a Gaussian, and convergence occurs quickly within 2 cumulants. However as the trap velocity increases, higher cumulant numbers are required until, for $v_{\text{OT}} = 1$, even at cumulant numbers of 6 the system has still not converged. While the numerical reliability decreases with the order of the cumulant, the results of the cumulant analysis agree with the observations made earlier in the case of Crooks fluctuation theorem and the Jarzynski equality.

The cumulant expansion can also be used to examine the influence of well depth. In order to do so, simulations in the forward direction were carried out for 1,000,000 trajectories with time step $\Delta t = 10^{-4}$, for trap velocities $v_{\text{OT}} = \{0.01, 0.05, 0.1, 0.5, 1, 3\}$. In all cases, the final location of the trap potential minimum was $x_{\text{OT}}^{\text{final}} = 6$. The membrane potential depth was held fixed at $\epsilon_{\text{M}} = 4$, whilst a parameter sweep from 1 to 8 was carried out for the optical trap potential depth, ϵ_{OT}. The trap strengths k_{M} and k_{OT} for both the membrane and the optical trap potentials were held constant at a value of two. Results of the cumulant analysis are plotted in Figs. 6.9 for the relative percentage error in ΔF_k (calculated from the known analytical values of the free energy), as a function of k, at the various trap velocities, with each subfigure representing a different value of ϵ_{OT}. The relative percentage error was used rather than ΔF_k, since the exact analytical value ΔF_{anal} was different for each value of trap well depth (as indicated in the caption to Figs. 6.9).

The cumulant analysis suggests that convergence occurs quickly at the low velocities and diverges at higher velocities. It is also evident that increasing optical trap well depth significantly increases the error in the estimate of the free energy for a given value of the number of terms k in the cumulant expansion.
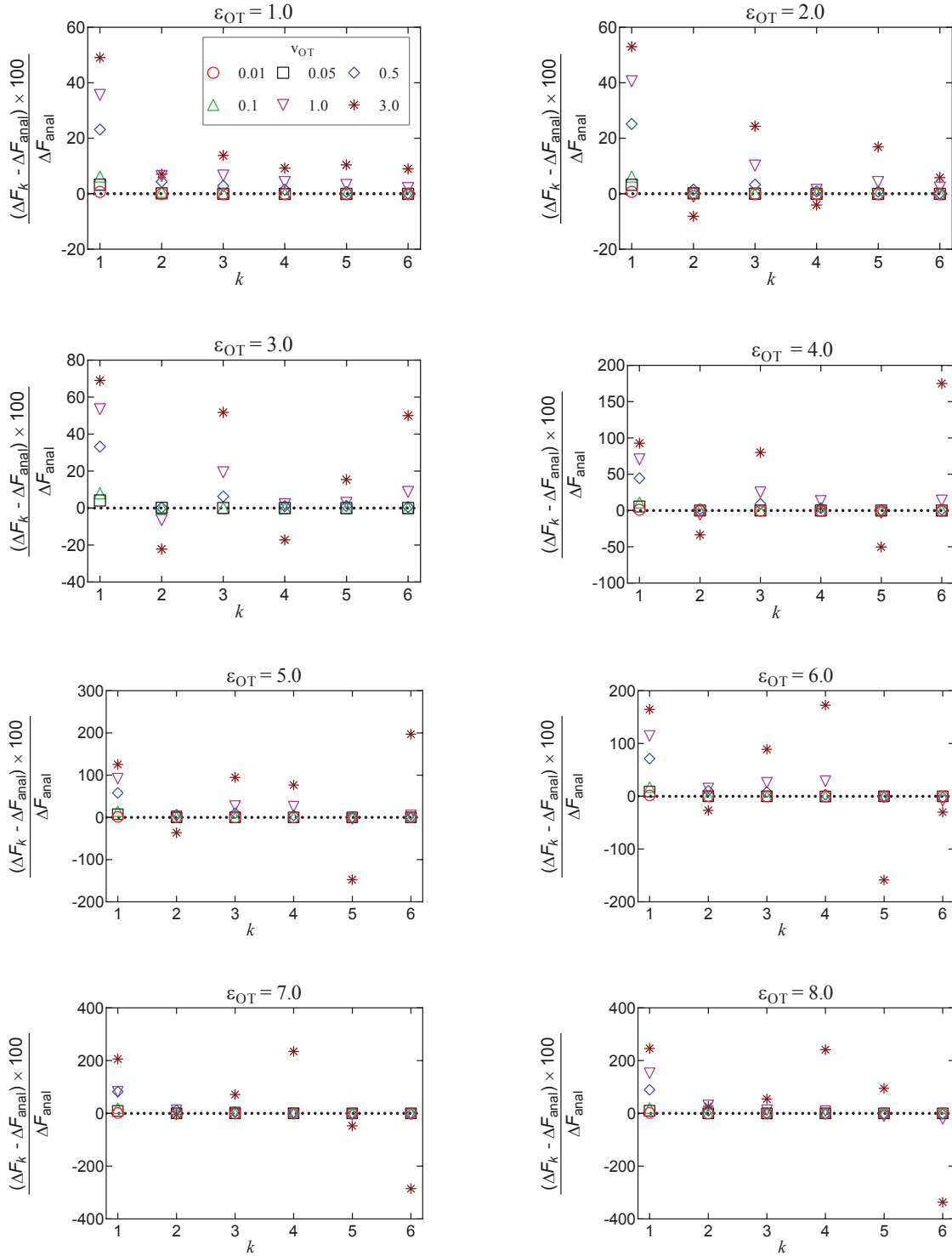
FIGURE 6.9: Relative percentage error in the free energy from a cumulant expansion for different optical trap well depths, at various values of trap velocity $v_{OT} = \{0.01, 0.05, 0.1, 0.5, 1, 3\}$. A parametric sweep was carried out from $\epsilon_{OT} = 1$ (top left) to 8 (bottom right), whilst keeping all other potential parameters constant ($\epsilon_M = 4$, $k_M = 2$ and $k_{OT} = 2$). The exact analytical values of the free energy for each of the optical trap depths were, $(\epsilon_{OT}, \Delta F_{anal})$: $(1.0, 0.599574)$, $(2.0, 1.509950)$, $(3.0, 2.327020)$, $(4.0, 2.952370)$, $(5.0, 3.336500)$, $(6.0, 3.525130)$, $(7.0, 3.604400)$, $(8.0, 3.635160)$.

6.3.5 Probabilities of attachment and detachment via umbrella sampling

An important quantity that is frequently the focus of experiments on cell adhesion is the probability of adhesion. Measurements of the adhesion probability are often used to determine the kinetics of the adhesion process through the calculation of on and off-rates of binding etc. The experiments, which typically monitor whether a binding event occurs or not when ligand and receptor bearing surfaces are brought into contact, are by their very nature carried out at finite rates. As a result, a true measure of the equilibrium probability of binding is difficult to obtain. In this context, the method of non-equilibrium umbrella sampling (Crooks, 2000; Williams, Evans, and Searles, 2011; Williams and Evans, 2010; Gao et al., 2012) provides a means of determining the equilibrium binding probability from non-equilibrium measurements. Here, we demonstrate how non-equilibrium umbrella sampling can be used to find, at the end of the unbinding experiment, the probability of either the bead being attached to the cell, or being detached from it and held in the optical trap.

The bead is considered still *attached* to the cell (membrane) at the end of the experiment, if at time t_D, when the optical trap minimum is located at x_{OT}^{final}, the position of the bead lies in the interval, $-\infty < x(t_D) \leq x_M^{ub}$. On the other hand, it is considered *detached* if $x_{OT}^{lb} \leq x(t_D) < \infty$ (see Figs. 6.1). It is useful to introduce the indicator functions χ_A and χ_D in order to define the probabilities of attachment and detachment,

$$\chi_A = 1 - H\left(x(t_D) - x_M^{ub}\right) = \begin{cases} 1 & \text{if } -\infty < x(t_D) \leq x_M^{ub}, \\ 0 & \text{if } x_M^{ub} < x(t_D) < \infty. \end{cases} \tag{6.27}$$

$$\chi_D = H\left(x(t_D) - x_{OT}^{lb}\right) = \begin{cases} 0 & \text{if } -\infty < x(t_D) < x_{OT}^{lb}, \\ 1 & \text{if } x_{OT}^{lb} \leq x(t_D) < \infty. \end{cases} \tag{6.28}$$

where, $H(x)$ is the Heaviside function.

Consider the situation where the unbinding simulations have been carried out at a finite rate for a total of N_T times, of which the number of times the bead remains attached is N_A, while the number of times it is detached is N_D. If $p_{neq}^{\lambda_f}(x(t_D))$ is the *non-equilibrium* distribution of bead positions at time t_D after switching the system from an initial equilibrium state with $\lambda = \lambda_0$ to a final non-equilibrium state with $\lambda = \lambda_f$, then the non-equilibrium probabilities of attachment and

detachment, defined by the following expressions, are easily determined by simulations from the ratios N_A/N_T and N_D/N_T, respectively,

$$p_A^{\text{neq}} = \int_{-\infty}^{x_M^{\text{ub}}} dx \, p_{\text{neq}}^{\lambda_f}(x) = \int_{-\infty}^{\infty} dx \, \chi_A \, p_{\text{neq}}^{\lambda_f}(x) = \langle \chi_A \rangle_{\text{neq}}^{\lambda_f} = \frac{N_A}{N_T} \qquad (6.29)$$

$$p_D^{\text{neq}} = \int_{x_{\text{OT}}^{\text{lb}}}^{\infty} dx \, p_{\text{neq}}^{\lambda_f}(x) = \int_{-\infty}^{\infty} dx \, \chi_D \, p_{\text{neq}}^{\lambda_f}(x) = \langle \chi_D \rangle_{\text{neq}}^{\lambda_f} = \frac{N_D}{N_T} \qquad (6.30)$$

The true goal of the experiments however, is to determine the *equilibrium* probabilities of attachment and detachment, p_A and p_D. If $p_{\text{eq}}^{\lambda_f}(x(t_D))$ is the equilibrium distribution of bead positions at t_D, then p_A and p_D are given by the expressions,

$$p_A = \int_{-\infty}^{\infty} dx \, \chi_A \, p_{\text{eq}}^{\lambda_f}(x) = \langle \chi_A \rangle_{\text{eq}}^{\lambda_f} \qquad (6.31)$$

$$p_D = \int_{-\infty}^{\infty} dx \, \chi_D \, p_{\text{eq}}^{\lambda_f}(x) = \langle \chi_D \rangle_{\text{eq}}^{\lambda_f} \qquad (6.32)$$

For the choice of potentials in the present work, it is straightforward to determine the equilibrium probabilities of attachment and detachment analytically. Using arguments along the lines of those in section 6.2.3 for the analytical determination of free energy differences, we can show that,

$$p_A^{\text{anal}} = \frac{1}{Z(x_{\text{OT}} = x_{\text{OT}}^{\text{final}})} \int_{-\infty}^{x_M^{\text{ub}}} dx \, \exp\left[-\left(\frac{1}{2} k_M x^2 - \epsilon_M\right)\right] = \frac{Z_A}{Z(x_{\text{OT}} = x_{\text{OT}}^{\text{final}})} \qquad (6.33)$$

$$p_D^{\text{anal}} = \frac{1}{Z(x_{\text{OT}} = x_{\text{OT}}^{\text{final}})} \int_{x_{\text{OT}}^{\text{lb}}}^{\infty} dx \, \exp\left[-\left(\frac{1}{2} k_{\text{OT}} (x - x_{\text{OT}})^2 - \epsilon_{\text{OT}}\right)\right] = \frac{Z_D}{Z(x_{\text{OT}} = x_{\text{OT}}^{\text{final}})} \qquad (6.34)$$

where the quantities Z_A and Z_D defined in the equations above are given by,

$$Z_A = \frac{\sqrt{\pi/2}}{\sqrt{k_M}} \exp(\epsilon_M) \left[\text{erf}\left(\frac{x_M^{\text{ub}} \sqrt{k_M}}{\sqrt{2}}\right) + 1\right] \qquad (6.35)$$

$$Z_D = \frac{\sqrt{\pi/2}}{\sqrt{k_{\text{OT}}}} \exp(\epsilon_{\text{OT}}) \left[\text{erfc}\left(\frac{(x_{\text{OT}}^{\text{lb}} - x_{\text{OT}}^{\text{final}})\sqrt{k_{\text{OT}}}}{\sqrt{2}}\right)\right] \qquad (6.36)$$

These expressions are useful to evaluate the success or otherwise of the non-equilibrium umbrella sampling technique in determining the equilibrium probabilities p_A and p_D from non-equilibrium measurements p_A^{neq} and p_D^{neq}. Analytical derivation is detailed in appendix C.3

In situations where a system property B assumes a large value when the equilibrium probability distribution assumes a small value, or vice versa, the average $\langle B \rangle_{\text{eq}}$ is likely to be dominated by
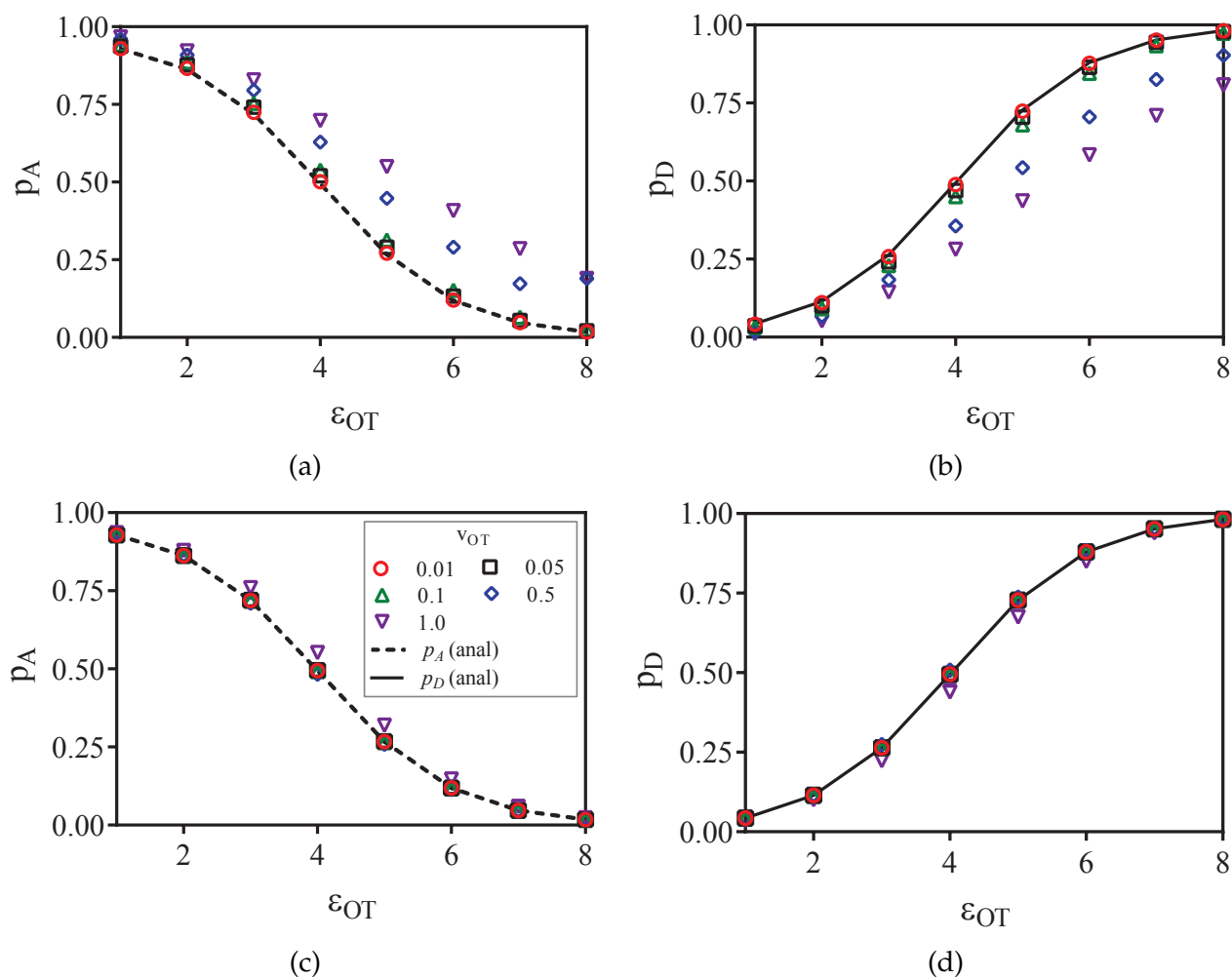
FIGURE 6.10: Probabilities of attachment and detachment as a function of optical trap well depth, at various values of trap velocity $v_{OT} = \{0.01, 0.05, 0.1, 0.5, 1\}$. The optical trap well depth ϵ_{OT} was varied from 1 to 8, whilst keeping all other potential parameters constant ($\epsilon_M = 4$, $k_M = 2$ and $k_{OT} = 2$). The symbols in (a) and (b) are the non-equilibrium probabilities of attachment and detachment p_A^{neq} and p_D^{neq}, while the symbols in (c) and (d) represent the equilibrium probabilities p_A and p_D obtained from non-equilibrium umbrella sampling. The curves in (a) to (d) are the analytical equilibrium probabilities p_A^{anal} and p_D^{anal} (as appropriate).

rare events, leading to slow convergence of numerical simulations for the average. The technique of equilibrium umbrella sampling has been developed to overcome such sampling problems (Torrie and Valleau, 1974). Essentially, a weighting function is used such that events that are rare end up being sampled much more frequently. The use of the quantity e^{-W} as the weight function has been shown to lead to the dynamic analogue of this approach, i.e., equilibrium averages can be obtained by appropriately analysing data from a system that has not reached true equilibrium (Jarzynski, 1997b; Crooks, 2000; Williams and Evans, 2010). In terms of the notation used in the present work, the method of non-equilibrium umbrella sampling takes the form of the expression,

$$\langle B \rangle_{\text{eq}}^{\lambda_{\text{f}}} = \frac{\langle B e^{-\beta W} \rangle_{\text{F}}}{\langle e^{-\beta W} \rangle_{\text{F}}} \tag{6.37}$$

It follows from Eqns (6.31) and (6.32) that the equilibrium probabilities of attachment and detachment can be obtained from non-equilibrium simulation data by evaluating the ensemble averages on the right hand sides of the expressions below,

$$p_{\text{A}} = \frac{\langle \chi_{\text{A}} \, e^{-\beta W} \rangle_{\text{F}}}{\langle e^{-\beta W} \rangle_{\text{F}}} \tag{6.38}$$

$$p_{\text{D}} = \frac{\langle \chi_{\text{D}} \, e^{-\beta W} \rangle_{\text{F}}}{\langle e^{-\beta W} \rangle_{\text{F}}} \tag{6.39}$$

Simulation data generated previously for examining the influence of well depth in section 6.3.4 has been used here for evaluating the usefulness of non-equilibrium umbrella sampling, for trap velocities $v_{\text{OT}} = \{0.01, 0.05, 0.1, 0.5, 1\}$. The potential parameters used in the simulations are as given in the caption to Figs. 6.9, along with $x_{\text{OT}}^{\text{final}} = 6$.

The symbols in Figs. 6.10 (a) and (b) are the non-equilibrium probabilities of attachment and detachment $p_{\text{A}}^{\text{neq}}$ and $p_{\text{D}}^{\text{neq}}$, determined from Eqns. (6.29) and (6.30) for various trap velocities, while the symbols in Figs. 6.10 (c) and (d) are the equilibrium probabilities p_{A} and p_{D}, determined by applying the umbrella sampling procedure as expressed in Eqns. (6.38) and (6.39). Error bars estimated from the ten repeated simulations are smaller than the symbol size in Figs. 6.10 (c) and (d). The curves in the subfigures of Fig. 6.10 represent the analytical equilibrium probabilities $p_{\text{A}}^{\text{anal}}$ and $p_{\text{D}}^{\text{anal}}$ (as appropriate), calculated from Eqns. (6.33) and (6.34), respectively,.

As expected, Figs. 6.10 (a) and (b) indicate that the non-equilibrium distribution functions are nearly identical to the equilibrium distribution functions at low trap velocities, and diverge with

increasing trap velocity. Interestingly, the greatest departure occurs for membrane and optical trap potential well depths that are roughly equal in magnitude. Not surprisingly, the probability of detachment is greatest for the largest optical trap well depth, while the likelihood of remaining in the membrane potential is high at low trap well depths. For nearly all the trap velocities, except perhaps at $v_{OT} = 1$ (for roughly equal trap strengths), application of umbrella sampling recovers the equilibrium distribution functions p_A and p_D, from a simulation estimate of $P_F(W)$.

6.4 Conclusions

A simple model for the detachment of a ligand coated bead with the help of an optical tweezer, from receptors on the surface of a cell to which it is bound, has been used to examine if fluctuation theorems are useful in determining equilibrium binding free energies. By using truncated harmonic potentials to represent the stationary cell membrane and the moving optical trap, and a Langevin equation to model the stochastic motion of the bead in these potentials, the distribution of work performed in driving the system from an initial equilibrium state to a final non-equilibrium state (at various finite rates) has been calculated by carrying out repeated simulations of the Langevin equation in the forward and reverse directions. The former corresponds to the membrane and trap potentials being superposed at time $t = 0$, followed by the optical trap being translated uniformly until the two potentials are sufficiently apart at the final time $t = t_D$. The latter refers to the opposite situation.

The calculation of work distributions enables the determination of the equilibrium free energy change between the initial and final states of the system, using both the Crooks fluctuation theorem and the Jarzynsky equality. The simplicity of the model also permits a straight forward determination of the exact free energy change by analytical means. It is found that both fluctuation theorems lead to excellent predictions provided the rate of switching from the initial to the final state is sufficiently slow. For relatively rapid rates of trap translation, sampling problems (for the given sample size) lead to a decrease in accuracy. The reduction is accuracy is discussed both in terms of a Gaussian approximation for the work distributions, and a cumulant expansion for the average of the exponential of work.

The method of non-equilibrium umbrella sampling has been used to determine the equilibrium probability that, after translating the trap from its initial to its final location, the bead and

cell are still attached (i.e, the bead lies only within the range of influence of the membrane po-
tential), and the equilibrium probability that the bead and cell have been detached (the bead lies
only within the range of influence of the optical trap potential), for a range of different values of
the optical trap well depth. It is seen that by appropriately analysing the non-equilibrium simu-
lation data, accurate estimates of the equilibrium probabilities of attachment and detachment can
be found for all but the highest rates of trap translation.

Chapter 7

Conclusions and future work

7.1 Conclusions

The broad objective of this work was to understand the behavior of adhesion between *P. falciparum* iRBCs and CD36 using a variety of experimental methods. The work focused on experimental techniques using optical tweezers and micropipettes to analyse the probability and force of iRBC to CD36 adhesion. This was further expanded to look at the potential use of fluctuation theorems with respect to cell adhesion to obtain equilibrium free energies of binding. This was achieved by using a Langevin equation to numerically model a cell being detached from a membrane by an optical tweezer potential.

   In particular, the following is a brief list of the key aspects of this thesis:

1. The probability of adhesion between an iRBC to CD36 steadily increased as contact time increased up until a contact time of ten seconds. At which point the probability of adhesion remained stable at approximately forty percent as contact time increased up until twenty seconds. A two dimensional kinetic model was fitted to the obtained data and an off rate of $0.11 \pm 0.02 \text{s}^{-1}$ was obtained. As the receptor and ligand densities were unable to be measured, a grouped equilibrium association constant ($m_r m_l K_A^o$) was obtained and found to be 0.091 ± 0.007. Further, the kinetic model was of the form of a simplified master equation and both the Poisson and binomial distributions were assessed and found to give equivalent results.

2. Micropipette aspiration was used to assess the membrane rigidity of the iRBCs under investigation. The iRBCs assessed had elastic sheer modulus of 16 to 29 pN/μm. As the iRBC membrane rigidity increased, for a constant compression force, the contact area decreased.

Further, the contact area was shown to be proportional to the obtained adhesion force, as contact area increased so did the adhesion force. However, although increased rigidity resulted in decreased contact area this did not correlate directly to a decreased adhesion force as may have been expected due to potential change in density of the receptors as the cell matures. This can be seen when the contact area was kept constant the adhesion force did increase with increasing cell rigidity.

3. The micropipette and optical tweezer method was compared. With respect to the adhesion probability experimental data and subsequent fitting of the two dimensional model the experiments obtained similar results. The adhesion forces measured by the micropipette data were consistently larger than those measured by optical tweezers however this could be attributed to the contact area being larger with the micropipette method as the bead is held fixed, allowing greater contact area to be achieved. Both the optical tweezer and micropipette methods have advantages and limitations. The OT method is non-invasive however there were limitations on the maximum adhesion force that this method can measure. The MP method on the other hand was invasive and adhesion could be affected when the iRBC was over stressed, however the membrane rigidity could be easily measured. A further advantage of this method was its ability to measure a larger range of adhesive forces than the OT method.

4. Numerical simulations of a Langivan equation were used to model the detachment of a particle from a substrate to which it was bound. The Jarzynski Equality and the Crooks Fluctuation Theorem were applied to obtain equilibrium free energy at bindings from the non-equilibrium work trajectories. Further, umbrella sampling was used to obtain equilibrium probability of detachment for a variety of different optical trap potentials.

7.2 Future work

The studies conducted in this thesis highlight opportunities for further research into important questions.

The experimental techniques discussed within this thesis allowed data to be obtained in regards to adhesion probability and subsequent fitting of this data to kinetic models. A limitation in

the analysis was that the receptor and ligand densities were unknown so only a grouped equilibrium association constant could be obtained. In the future it would useful to be able to determine these densities to not only be able to determine the equilibrium association constant but also confirm the kinetic mechanism.

The optical tweezer method was explored however an apparent limitation was identified with respect to the maximum force the optical tweezers could impart to separate adhered iRBCs to CD36. During the scope of this work only the CD36 receptor was investigated, however different receptors may have different adhesion strengths and consequently may be more appropriate to study via the optical tweezer method.

This thesis has explored the use of micropipette and optical tweezer methods to assess adhesion of iRBC with CD36. The probabilities and forces of adhesion to different receptors such as VCAM1, ICAM1, and CSA should be explored in the future. An interesting expansion to current acquired knowledge would be to obtain information on the kinetics of different iRBC to receptor bonds and use that information in concert with known flow characteristics to produce a flow state diagram for *falciparum* adhesion.

Finally it would be beneficial to further explore the potential of fluctuation theorems to be used with experimental data for cellular adhesion to obtain equilibrium values that are independent of the work you impose on the system by the experimental technique.

Appendix A

Programs developed for micropipette assay

A.1 Arduino program to move piezoelectric actuator

A program was written to drive the micropipette by use of a piezo actuator. The program provides an analog signal to the piezo actuator by the use of pulse width modulation (PWM). A microcontroller board (Arduino uno) is programmed to deliver a smooth ramp up, hold for a certain time, smooth ramp down and hold for certain time. The program is shown in section A.2

A.2 Program for driving piezo-actuator

PWM Ramper.
Unit creates a changing PWM signal which is then converted to an Analog Voltage (simple resistor cap —10k—220uf) to drive a micro-pipette.
Author - Emma Hodges 23/04/2015

Basic requirements:
Output zero
Wait for trigger (start button)
Loop over ITERATIONS (number of repeat cycles) "300-1000"
Increase PWM duty from 0% to MAXPWM (MAX PWM user selectable via code constant " 3v3")
over RAMPUPSEC seconds.
Hold PWM for pwmDwelHI seconds "5-10secs"
Decrease PWM duty from MAXPWM to 0% over RAMPDWNSEC seconds
Hold PWM at 0% duty for pwmDwelLO seconds
Repeat
 NOTE: PWM freq is dependent on the Arduino in question. 490HZ or 980HZ

// Initialise pins

```
    int PinPWM1 = 3; // PWM output connected to digital pin 3
    int pinStrt = 2; //our start switch
 //Program constants

    int maxPWM = 255; // Maximum analog voltage output
    int minPWM=0; //Zero output
 //                    USER Modifiers

// Number of cycles to perform
    int cycles=50; // run for 10 iterations
// values for ramp and dwell times set here
    int pwmDwellHI=4000; //dwell HIGH for 2 seconds
    int pwmDwellLO=2000; //dwell low for 5 seconds
    int rampUPsec=5000; //ramp up takes 5 seconds
    int rampDWNsec=5000; //ramp down takes 6 seconds


//Program variables
    int runexp=LOW; //used to stop/start exp


//ramp up routine
    void rampUP()
// Ramp up PWM from min to max over user set seconds:
    int rampI = rampUPsec/(maxPWM-minPWM); // Calculate ramp increments
for(int pwmVal = minPWM ; pwmVal <= maxPWM; pwmVal +=1) {
// sets the pwm Duty (range from min to max):
    analogWrite(PinPWM1, pwmVal);
// wait for rampI milliseconds before updating PWM
    delay(rampI);
//ramp down routine
    void rampDWN(){
// Ramp up PWM from min to max over user set seconds:
    int rampI = rampDWNsec/(maxPWM-minPWM); // Calculate ramp increments
for ( int pwmVal = maxPWM ; pwmVal >= minPWM; pwmVal -=1) {
// sets the PWM duty (range from min to max):
    analogWrite(PinPWM1, pwmVal);
// wait for rampI milliseconds before updating PWM
    delay(rampI);
    }
}
// Run pwm ramp for so many cycles
void runExp(){
    runexp=LOW; //this tells the code to stop the execution of experiment code on exit.
    for (int i=0; i <=cycles ;i++){
        rampUP();
        delay(pwmDwellHI);
        rampDWN();
        delay(pwmDwellLO);
```

```
    }
}
void setup() {
    pinMode(pinStrt,INPUT); //setup pin as an input.
    analogWrite(PinPWM1, minPWM); //ensure output starts at zero
}


//MAIN loop starts here
void loop() {
    if (runexp == HIGH) //if start pin is high run
        {
          runExp();
        }
    else
        {
          runexp=digitalRead(pinStrt); //read condition of start pin
        }
    analogWrite(PinPWM1, minPWM); //ensure we stop at zero output.

}
```

Appendix B

Programs used to analyse QPD data obtained during adhesion experiments with optical tweezers

B.1 Program developed to analyse QPD voltage data from optical tweezer experiment

A fortran program was used to convert the voltage data obtained from QPD during adhesion experiments using optical tweezers to displacement data in the x and y direction.

B.2 Program to determine optical trap stiffness (k)

The following program written in Fortran 77 was used to obtain the optical trap stiffness using equipartition theorem. An input file (labeled camera equip.in) contains information about the calibration files that are to be read to obtain trap stiffness in the x (k_x) and y (k_y) direction.

```
program camera_equip

implicit none

integer i, j, numlines, numfiles, start_offset

character*60 filein, temp

character*60 files(10000)

double precision volt(12000000), volt2(12000000)
```

```fortran
double precision disp(12000000), disp2(12000000)
double precision sum, sum2, xbar, ybar, conv, conv2
double precision x0, x1, x2, x3, x4, x5
double precision y0, y1, y2, y3, y4, y5
double precision sample_rate, sample_time
filein = 'camera_equip.in'
open(unit = 12, file = filein, status = 'unknown')
open(unit=19, file = 'avdist.txt', status='unknown')
open(unit=20, file = 'results.txt', status='unknown')
write(*,*) filein,' opened successfully'
read(12,*) numfiles, start_offset
read(12,*) sample_rate, sample_time, x0, y0
numlines=int(sample_rate*sample_time)
c Gets the names of all files to process
do j=1, numfiles,1
read(12,*) files(j)
open(unit = 13, file = files(j), status = 'unknown')
c — — — — — — — — — — — — — — — — — — — — — — — — —
sum=0.0
sum2=0.0
read(13,*)
do i=1, start_offset
read(13,*)
enddo
do i = 1, numlines, 1
```

```fortran
read (13,*) volt(i), volt2(i)

disp(i) = volt(i)*x0

disp2(i) = volt2(i)*y0

sum=sum+disp(i)

sum2=sum2+disp2(i)

enddo

write (*,*) 'File ',j, '',numfiles,' read, processing.....'

xbar = sum/dble(numlines)

ybar = sum2/dble(numlines)

sum = 0.0

sum2 = 0.0

do i = 1, numlines, 1

disp(i) = disp(i) - xbar

disp2(i) = disp2(i) - ybar

disp(i) = disp(i)**2

disp2(i) = disp2(i)**2

sum = sum + disp(i)

sum2 = sum2 + disp2(i)

enddo

sum = sum/dble(numlines)

sum2 = sum2/dble(numlines)

write (19,*) files(j), sum, sum2, char(13)

conv = 4.14d-3 / sum

conv2 = 4.14d-3/ sum2

write (20,*) files(j), conv, conv2, xbar, ybar, char(13)
```

```
close(13)

c  -- -- -- -- -- -- -- -- -- -- -- -- -- -- -- -- -- -- -- -- -- -- --

-- -- -- --

enddo

close(12)

close(19)

close(20)

stop

end
```

B.3 C program to convert displacement data to force data and analysis of the force data

```c
/*
  Code to analyse OT QPD data.
 */

/*
 * File:    main.c
 * Author: Emma Hodges
 *Created on 4 January 2016, 8:36 PM
 *Modified on 8 Feb  2016,
 */

#include <stdio.h>
#include <stdlib.h>
#include <math.h>
#include <string.h>

#define KX 14.6904508
#define KY 14.5715295

typedef enum
{
    RESTING = 3,
    MOVING = -1,
    CONTACT = 1,

} BALL_STATE;
```

```c
typedef enum
{
    NOAD,
    TYPE1,
    TYPE2,
    TYPE3,
    TYPE23,


}ADHESION_TYPE;

/*
 * Main Program
 */
int main(int argc, char** argv)
{

    int i;
    double average_resting = 0.;
    double cycle_max = 0.;
    double average = 0.;
    double average_contact = 0.;
    int average_contact_count = 0;
    int num_lines = 0;
    double ny_displace = 0.;
    double ave_contact = 0.;
    double lbound = 0.;
    double ubound = 0.;
    double shift = 0.;
    int nt = 0;
    int nadt = 0;
    int nad1 = 0;
    int nad2 = 0;
    int nad3 = 0;
    int nad23 =0;
    double probadt=0.;
    double probad1=0.;
    double probad2=0.;
    double probad3=0.;
    double probad23 = 0.;
    char strain [10]= "3D7";
    char stage [20]= "troph";
    int contact_time = 8;
    int pause_time = 8;
    int tforward = 3;
    int tback = 3;
    double distance = 3.4;
    double vforward = 0.;
    double vback = 0.;
```

```cpp
double ave_cycle_max = 0.;
double stddev_max = 0.;
double ave_adhesiont = 0.;
double ave_adhesion1 = 0.;
double ave_adhesion2 = 0.;
double ave_adhesion3 = 0.;
double ave_adhesion23 = 0.;
double ave_compresst = 0.;
double ave_compress1 = 0.;
double ave_compress2 = 0.;
double ave_compress3 = 0.;
double ave_compress23 = 0.;
double adhesiont = 0.;
double adhesion1 = 0.;
double adhesion2 = 0.;
double adhesion3 = 0.;
double adhesion23 = 0.;
double compresst = 0.;
double compress1 = 0.;
double compress2 = 0.;
double compress3 = 0.;
double compress23 = 0.;
double compresss1 = 0.;
double compresss2 = 0.;
double compresss3 = 0.;
double compresss4 = 0.;
double compresss5 = 0.;
double compresss6 = 0.;
double adhesions1 = 0.;
double adhesions2 = 0.;
double adhesions3 = 0.;
double adhesions4 = 0.;
double adhesions5 = 0.;
double adhesions6 = 0.;
double compresssm1 = 0.;
double adhesionsm1 = 0.;
double compresssm2 = 0.;
double adhesionsm2 = 0.;
double compresssm3 = 0.;
double adhesionsm3 = 0.;
double compresssm4 = 0.;
double adhesionsm4 = 0.;
double compresssm5 = 0.;
double adhesionsm5 = 0.;

double ave_compresss1 = 0.;
double ave_compresss2 = 0.;
double ave_compresss3 = 0.;
double ave_compresss4 = 0.;
double ave_compresss5 = 0.;
```

```c
double ave_compresss6 = 0.;
double ave_adhesions1 = 0.;
double ave_adhesions2 = 0.;
double ave_adhesions3 = 0.;
double ave_adhesions4 = 0.;
double ave_adhesions5 = 0.;
double ave_adhesions6 = 0.;
int ns1 =0;
int ns2 =0;
int ns3 =0;
int ns4 =0;
int ns5 =0;
int ns6 =0;
double probads1 =0.;
double probads2 =0.;
double probads3 =0.;
double probads4 =0.;
double probads5 =0.;
double probads6 =0.;

double pcycle_max = 0.;
double pave_contact = 0.;
double cutoff = -45.;
double s1cutoff = 0.;
double s2cutoff = 0.;
double s3cutoff = 0.;
double s4cutoff = 0.;
double s5cutoff = 0.;

ADHESION_TYPE previous = NOAD;


FILE * file = fopen("inputfile", "r");
if (file == NULL)
{
    fprintf(stderr, "cant_open_input_file\n");
}

FILE * fnif = fopen("fnif.txt", "w");
FILE * afp = fopen("average.txt", "w");
FILE * nyf = fopen("norm_y_force.txt", "w");
FILE * aqpd = fopen("analysed.txt", "w");
FILE * ad;
FILE * result;
printf("28\n");
char newline[256];

double xdisp, ydisp, position;
double x_displace, y_displace;
int optical_position;
```

```c
while (fgets(newline, sizeof (newline), file))
{
    sscanf(newline, "%lf\t%lf\t%lf\n", &xdisp, &ydisp, &position);

    x_displace = xdisp * KX;
    y_displace = ydisp * KY;
    optical_position = round(position);
    BALL_STATE current_state = round(position);

    switch (current_state)
    {
        case RESTING:
          if (y_displace>cutoff)
            {
                average_resting = average_resting + y_displace;
                num_lines++;
                fprintf(afp, "%lf_%lf_%d\n", y_displace, average_resting,
    num_lines);
            }
          break;

        case MOVING:
        case CONTACT:
            break;

        default: printf("Invalid_state!\n");
            break;
    }
    fprintf(fnif, "%f\t%f\t%d\n", x_displace, y_displace,
    optical_position);

}

fclose(fnif);
fclose(afp);

fnif = fopen("fnif.txt", "r");

average = average_resting / num_lines;
printf("Average_=_%f\n", average);
char newline2[256];
double stddev = 0.;
double stddevadd = 0.;

while (fgets(newline2, sizeof (newline2), fnif))
{
    sscanf(newline2, "%lf\t%lf\t%d\n", &x_displace, &y_displace,
    &optical_position);
    BALL_STATE current_state = optical_position;
```

```
        switch (current_state)
        {
            case RESTING:
              if (y_displace>cutoff)
                {
                    stddevadd = stddevadd + (y_displace − average)∗
        (y_displace − average);
                }
              break;

            case MOVING:
            case CONTACT:
                break;

            default: printf("Invalid_state!\n");
                break;
        }
        shift = 0 − average;

        double ny_displace = shift + y_displace;

        fprintf(nyf, "%lf_%d\n", ny_displace, optical_position);
    }
    double inv_num_lines = 1 / ((double) num_lines);
    stddev = sqrt(inv_num_lines ∗ stddevadd);
    printf("stddevadd_%lf\n", stddevadd);
    printf("num_lines_%d\n", num_lines);
    printf("inv_num_lines_%lf\n", inv_num_lines);
    printf("stddev_%lf\n", stddev);
    fclose(file);
    fclose(fnif);
    fclose(afp);
    fclose(nyf);

    //Part B: Analyse the normalised force data of
    //x−displacement QPD data.
    nyf = fopen("norm_y_force.txt", "r");
    BALL_STATE previous_state = CONTACT;
    BALL_STATE current_state = MOVING;
    int n_cycle = 0;

    while (fgets(newline2, sizeof (newline2), nyf))
    {
        sscanf(newline2, "%lf_%d\n", &ny_displace, &optical_position);
        // average contact
        current_state = optical_position;
        if (previous_state == MOVING && current_state == CONTACT)
        {
            ave_contact = average_contact / average_contact_count;
            fprintf(aqpd, "%d_%d_%lf_%lf\n", n_cycle,
```

```
                average_contact_count, ave_contact, cycle_max);
                n_cycle++;
                printf("average_contact_=_%lf\n", ave_contact);
                printf("contact_time_=_%d\n", average_contact_count);
                cycle_max = 0.;
                average_contact = 0;
                average_contact_count = 1;
        }
        else
        {
            if (ny_displace < cycle_max)
            {
                cycle_max = ny_displace;
            }
            // average contact force for this cycle
            if (current_state == CONTACT)
            {
                average_contact += ny_displace;
                average_contact_count++;
            }
        }

        previous_state = current_state;
    }

    fclose(nyf);
    fclose(aqpd);

    /* Part C: analyse the cycles to get adhesion probabilities
    and forces etc.
     */
    aqpd = fopen("analysed.txt", "r");
    ad = fopen("adhesion.txt", "w");
    fprintf(ad, "_contact_force___adhesion_force_max__\n");
    int ntm =0;
    char newline3[256];
    while (fgets(newline3, sizeof(newline3), aqpd))
      {
        sscanf(newline3, "%d_%d_%lf_%lf\n", &n_cycle,
    &average_contact_count, &ave_contact, &cycle_max);
        ave_cycle_max += cycle_max;
        printf("%lf_%d\n",ave_cycle_max, ntm);
        ntm++;
      }
    printf("%lf_%d\n",ave_cycle_max,ntm);
    ave_cycle_max = ave_cycle_max/(double)ntm;
    printf("%lf_%d\n",ave_cycle_max,ntm);
    ntm =0;
    fclose(aqpd);
    aqpd = fopen("analysed.txt", "r");
```

```c
    while (fgets(newline2, sizeof (newline2), aqpd))
      {
        sscanf(newline2, "%d_%d_%lf_%lf\n", &n_cycle,
    &average_contact_count, &ave_contact, &cycle_max);
        stddev_max = stddev_max + (cycle_max - ave_cycle_max)*
    (cycle_max - ave_cycle_max);
        ntm++;
        printf("%lf_%d\n",stddev_max, ntm);
      }
    printf("%lf_%d\n",stddev_max, ntm);
    stddev_max = stddev_max/(double)ntm;
    printf("%lf_%d\n",stddev_max,ntm);
    ntm=0;
    fclose(aqpd);
    aqpd = fopen("analysed.txt", "r");

    while (fgets(newline2, sizeof (newline2), aqpd))
      {
        sscanf(newline2, "%d_%d_%lf_%lf\n", &n_cycle,
        &average_contact_count, &ave_contact, &cycle_max);

        s1cutoff = -1 * stddev_max;
        s2cutoff = -2 * stddev_max;
        s3cutoff = -3 * stddev_max;
        s4cutoff = -4 * stddev_max;
        s5cutoff = -5 * stddev_max;

        ntm ++;

        if(cycle_max>s1cutoff)
          {
            ns1++;
            adhesionsm1 += cycle_max;
            compresssm1 += ave_contact;
          }

        if(cycle_max<=s1cutoff && cycle_max>s2cutoff)
          {
            ns2++;
            adhesionsm2 += cycle_max;
            compresssm2 += ave_contact;
          }
        if(cycle_max<=s2cutoff && cycle_max>s3cutoff)
          {
            ns3++;
            adhesionsm3 += cycle_max;
            compresssm3 += ave_contact;
          }
        if(cycle_max<=s3cutoff && cycle_max>s4cutoff)
```

```
              {
                 if(ave_contact!=ave_contact)
                   {
                      ave_contact=0;
                   }
                 ns4++;
                 adhesionsm4 += cycle_max;
                 compresssm4 += ave_contact;
              }
            if(cycle_max<=s4cutoff && cycle_max>s5cutoff)
              {
                 ns5++;
                 adhesionsm5 += cycle_max;
                 compresssm5 += ave_contact;
              }
       }

   adhesionsm1 = adhesionsm1/ns1;
   compresssm1 = compresssm1 / ns1;
   adhesionsm2 = adhesionsm2/ns2;
   compresssm2 = compresssm2 / ns2;
   adhesionsm3 = adhesionsm3/ns3;
   compresssm3 = compresssm3 / ns3;
   adhesionsm4 = adhesionsm4/ns4;
   compresssm4 = compresssm4 / ns4;
   adhesionsm5 = adhesionsm5/ns5;
   compresssm5 = compresssm5 / ns5;
   printf("%d_%d_%d_%d_%d_%d\n",ntm, ns1, ns2, ns3, ns4, ns5);
   double probadsm1 = (double)ns1/ (double)ntm;
   double probadsm2 = (double)ns2/ (double)ntm;
   double probadsm3 = (double)ns3/ (double)ntm;
   double probadsm4 = (double)ns4/ (double)ntm;
   double probadsm5 = (double)ns5/ (double)ntm;

   ns1 = 0;
   ns2 = 0;
   ns3 = 0;
   ns4 = 0;
   ns5 = 0;
   ntm = 0;

   ubound = -3*stddev;
   lbound = -54+shift;

   s1cutoff = -1 * stddev;
   s2cutoff = -2 * stddev;
   s3cutoff = -3 * stddev;
   s4cutoff = -4 * stddev;
   s5cutoff = -5 * stddev;
```

```
      printf("%lf %lf %lf %lf %lf %lf %lf\n",
ubound,lbound,stddev,s1cutoff,s2cutoff,s3cutoff,s4cutoff);
fclose(aqpd);
aqpd = fopen("analysed.txt", "r");

while (fgets(newline2, sizeof (newline2), aqpd))
  {
     sscanf(newline2, "%d %d %lf %lf\n", &n_cycle,
     &average_contact_count, &ave_contact, &cycle_max);
     nt ++;

     if(cycle_max>s1cutoff)
       {
         ns1++;
         adhesions1 += cycle_max;
         compresss1 += ave_contact;
       }

     if(cycle_max<=s1cutoff && cycle_max>s2cutoff)
       {
         ns2++;
         adhesions2 += cycle_max;
         compresss2 += ave_contact;
       }
     if(cycle_max<=s2cutoff && cycle_max>s3cutoff)
       {
         ns3++;
         adhesions3 += cycle_max;
         compresss3 += ave_contact;
       }
     if(cycle_max<=s3cutoff && cycle_max>s4cutoff)
       {
         if(ave_contact!=ave_contact)
           {
             ave_contact=0;
           }
         ns4++;
         adhesions4 += cycle_max;
         compresss4 += ave_contact;
         printf("%lf %lf\n",ave_contact, compresss4);
       }
     if(cycle_max<=s4cutoff && cycle_max>s5cutoff)
       {
         ns5++;
         adhesions5 += cycle_max;
         compresss5 += ave_contact;
       }
     if (cycle_max <= s5cutoff)
       {
         ns6++;
```

```c
          adhesions6 += cycle_max ;
          compresss6 += ave_contact ;
      }

   if (cycle_max<ubound)
   {

     fprintf(ad, "%d_%lf_%lf\n", n_cycle , ave_contact , cycle_max );
        nadt++;
        adhesiont += cycle_max ;
        compresst += ave_contact ;


        if (cycle_max>lbound)
        {
            nad1++;
            adhesion1 += cycle_max ;
            compress1 += ave_contact ;
            previous = TYPE1;
        }
        else
        {
            nad23++;
            adhesion23 += cycle_max ;
            compress23 += ave_contact ;
            if(previous == TYPE2)
            {
            nad3++;
            nad2−=1;
            adhesion2 −= pcycle_max ;
            compress2 −= pave_contact ;
            adhesion3 += pcycle_max ;
            compress3 += pave_contact ;
            previous = TYPE3;
            }
            if (previous ==TYPE3)
            {
            nad3++;
            adhesion3 += cycle_max ;
            compress3 += ave_contact ;
            previous = TYPE3;
            }
            else
            {
            nad2++;
            adhesion2 += cycle_max ;
            compress2 += ave_contact ;
            previous = TYPE2;
            }
```

```
            }

        }
        else
        {
            previous = NOAD;
        }
    pcycle_max = cycle_max;
    pave_contact=ave_contact;

}
fclose(ad);

ave_adhesiont = adhesiont/(double)nadt;
ave_adhesion1 = adhesion1/nad1;
ave_adhesion2 = adhesion2/nad2;
ave_adhesion3 = adhesion3/nad3;
ave_adhesion23 = adhesion23/nad23;
ave_compresst = compresst / nadt;
ave_compress1 = compress1 / nad1;
ave_compress2 = compress2 / nad2;
ave_compress3 = compress3 / nad3;
ave_compress23 = compress23 / nad23;
ave_adhesions1 = adhesions1/ns1;
ave_compresss1 = compresss1 / ns1;
ave_adhesions2 = adhesions2/ns2;
ave_compresss2 = compresss2 / ns2;
ave_adhesions3 = adhesions3/ns3;
ave_compresss3 = compresss3 / ns3;
ave_adhesions4 = adhesions4/ns4;
printf("%lf_%d\n",compresss4,ns4);
ave_compresss4 = compresss4 / ns4;
ave_adhesions5 = adhesions5/ns5;
ave_compresss5 = compresss5 / ns5;
ave_adhesions6 = adhesions6/ns6;
ave_compresss6 = compresss6 / ns6;

probadt = (double)nadt/ (double)nt;
probad1 = (double)nad1/ (double)nt;
probad2 = (double)nad2/ (double)nt;
probad3 = (double)nad3/ (double)nt;
probad23 = (double)nad23/ (double)nt;
probads1 = (double)ns1/ (double)nt;
probads2 = (double)ns2/ (double)nt;
probads3 = (double)ns3/ (double)nt;
probads4 = (double)ns4/ (double)nt;
probads5 = (double)ns5/ (double)nt;
probads6 = (double)ns6/ (double)nt;
```

```
vforward = distance/tforward;
vback = distance/tback;
result = fopen("result.txt", "w");
fprintf(result,"file_name_%s\n",filename);
fprintf(result,"strain_%s\n",strain);
fprintf(result,"stage_%s\n",stage);
fprintf(result,"contact_time_%d\n",contact_time);
fprintf(result,"pause_time_%d\n",pause_time);
fprintf(result,"time_forward_%d\n",tforward);
fprintf(result,"time_back_%d\n",tback);
fprintf(result,"distance_%lf\n",distance);
fprintf(result,"velocity_forward_%lf\n",vforward);
fprintf(result,"velocity_back_%lf\n",vback);
fprintf(result,"total_contacts_%d\n",nt);
fprintf(result,"std_deviation_%lf\n",stddev);
fprintf(result,"std_deviation_max_%lf\n",stddev_max);
fprintf(result,"average_cycle_max_%lf\n",ave_cycle_max);
fprintf(result,"lower_bound_%lf\n",lbound);
fprintf(result,"upper_bound_%lf\n",ubound);

fprintf(result,"parameter_total_set1_set2_set3_set23\n_");
fprintf(result,"ave_adhesion_%lf_%lf_%lf_%lf_%lf\n", ave_adhesiont,
ave_adhesion1,ave_adhesion2,ave_adhesion3,ave_adhesion23);
fprintf(result,"ave_compress_%lf_%lf_%lf_%lf_%lf\n",
ave_compresst,ave_compress1,ave_compress2,ave_compress3,ave_compress23);
fprintf(result,"number_adhesion_%d_%d_%d_%d_%d\n",nadt,
nad1, nad2, nad3, nad23);
fprintf(result,"probability_adhesion_%lf_%lf_%lf_%lf_%lf\n",
probadt, probad1, probad2, probad3, probad23);

fprintf(result,"parameter_max_sigma1_sigma2_sigma3_sigma4_sigma5\n_");
fprintf(result,"ave_adhesion_%lf_%lf_%lf_%lf_%lf\n",adhesionsm1,
adhesionsm2, adhesionsm3, adhesionsm4, adhesionsm5);
fprintf(result,"ave_compress_%lf_%lf_%lf_%lf_%lf\n",
compresssm1,compresssm2,compresssm3,compresssm4,compresssm5);
fprintf(result,"probability_adhesion_%lf_%lf_%lf_%lf_%lf\n",
probadsm1, probadsm2, probadsm3, probadsm4, probadsm5);


fprintf(result,"parameter_sigma1_sigma2_sigma3_sigma4_sigma5_sigma6
_____\n_");
fprintf(result,"ave_adhesion_%lf_%lf_%lf_%lf_%lf_%lf\n",ave_adhesions1,
ave_adhesions2,ave_adhesions3, ave_adhesions4, ave_adhesions5,
ave_adhesions6);
fprintf(result,"ave_compress_%lf_%lf_%lf_%lf_%lf_%lf\n",
ave_compresss1,ave_compresss2,ave_compresss3,ave_compresss4,
ave_compresss5, ave_compresss6);
fprintf(result,"number_adhesion_%d_%d_%d_%d_%d_%d\n",
ns1, ns2, ns3, ns4, ns5, ns6);
```

```
        fprintf(result,"probability adhesion %lf %lf %lf %lf %lf %lf\n",
        probads1, probads2, probads3, probads4, probads5, probads6);


        fclose(result);

    return (EXIT_SUCCESS);
}
```

Appendix C

Analytical derivations

C.1   Derivation of deterministic work of detachment

The work relation used in our theoretical model can be derived from first principles as follows:

A force on a particle with mass m subjected to an acceleration a over a time t can be defined:

$$F = ma = m\frac{dv}{dt} = m\dot{v}$$

where the velocity v is defined as the change in the particles position x over time.

$$v = \frac{dx}{dt} = \dot{x}$$

The momentum p of the particle is the product of the mass and velocity of the particle,

$$p = mv = m\dot{x}$$

The change in the momentum over time $\dot{p}$ is therefore,

$$\dot{p} = m\ddot{x} = m\dot{v}$$

Re-arranging the above equations we get that the force is equal to the change in the particles momentum over time,

$$\dot{x} = \frac{p}{m}; \quad \dot{v} = \frac{\dot{p}}{m}; \quad F = \dot{p}$$

The kinetic energy of the particle $\mathcal{K}$ can be defined as follows,

$$\mathcal{K} = \frac{1}{2}mv^2 = \frac{1}{2}m\dot{x}^2 = \frac{1}{2}\frac{(mv)^2}{m} = \frac{1}{2}\frac{p^2}{m}$$

and consequently the change in the kinetic energy can be found to be the momentum of the particle,

$$\frac{\partial\mathcal{K}}{\partial\dot{x}} = \frac{1}{2}m \cdot 2\dot{x} = m\dot{x} = p$$

The potential energy on the particle ϕ is a function of the beads position and the force felt by the bead is equal to the change in the potential energy as a function of bead position,

$$\phi = \phi(x); \quad F = -\frac{\partial\phi}{\partial x}$$

The Hamiltonian is the sum of the kinetic and potential energies of the bead and is a function of the bead position and momentum,

$$\mathcal{H} = \mathcal{K} + \phi = \frac{1}{2m}p^2 + \phi(x)$$

The partial derivative of the Hamiltonian with respect to bead position and momentum can be written (eq. C.1 and eq. C.2, respectively).

$$\frac{\partial\mathcal{H}}{\partial x} = \frac{\partial\phi}{\partial x} = -F = -\dot{p} \tag{C.1}$$

$$\frac{\partial\mathcal{H}}{\partial p} = \frac{1}{2m} \cdot 2p = \frac{p}{m} = \dot{x} \tag{C.2}$$

The potential energy is the sum of the contributions of the membrane and optical tweezer potentials. The membrane potential as a function of bead position, $\phi_{\mathrm{M}}(x)$, is a function of the membrane strength k_{M} and bead position relative to the location of the membrane minimum, x_{M}. The membrane minimum is independent of time.

$$\phi_{\mathrm{M}}(x) = \frac{1}{2}k_{\mathrm{M}}\left(x - x_{\mathrm{M}}\right)^2$$

The optical tweezer potential, $\phi_{\mathrm{OT}}(x)$, is a function of the strength of the optical trap, k_{OT}, and

the bead position relative to the location of the optical trap minimum x_{OT}. The location of the OT trap minimum is dependent on time.

$$\phi_{OT}(x) = \frac{1}{2}k_{OT}\left(x - x_{OT}\right)^2$$

The location of the OT trap minimum can be expressed,

$$x_{OT}(t) = x_{OT}^0 + v_{OT}t;$$

where x_{OT}^0 is x_{OT} at $t = 0$ and v_{OT} is the velocity of the optical trap.

The total potential energy felt by the bead is therefore,

$$\phi = \phi_M + \phi_{OT}$$

The work is defined as the change in the hamiltonian going from state 1 to state 2, where state 1 is defined as the intial state at $t = 0$ and state 2 is at the final time where $t > 0$.

$$w = \mathcal{H}_2 - \mathcal{H}_1 = \mathcal{K}_2 - \mathcal{K}_1 + \phi_2 - \phi_1$$

The work can therefore be defined as the sum of the contributions of the kinetic and potential energies at the initial and the final state. The kinetic energy contribution comes from the momentum of the particle and the potential energies are due to both the membrane and optical trap contributions.

$$w = \frac{1}{2m}\left[p_2^2 - p_1^2\right] + \phi_{OT,2} - \phi_{OT,1} + \phi_{M,2} - \phi_{M,1}$$

since $F = -\frac{\partial \phi}{\partial x}$, the force felt by the bead can be written the change in the sum of the potential energies contributed by the membrane and optical trap,

$$F = -\frac{\partial}{\partial x}\{\phi_M + \phi_{OT}\} = -\frac{\partial}{\partial x}\left[\frac{1}{2}k_M\left(x - x_M\right)^2 + \frac{1}{2}k_{OT}\left(x - x_{OT}\right)^2\right]$$

hence,

$$F = -k_M\left(x - x_M\right) - k_{OT}\left(x - x_{OT}\right)$$

and since $F = \dot{p}$,

$$\dot{p} = -\left[k_{\mathrm{M}}(x - x_{\mathrm{M}}) + k_{\mathrm{OT}}(x - x_{\mathrm{OT}})\right]$$

now,

$$\dot{w} = \frac{1}{2m}\left(p_2\dot{p}_2 + \dot{p}_2 p_2 - p_1\dot{p}_1 - \dot{p}_1 p_1\right) + \dot{\phi}_{\mathrm{OT},2} - \dot{\phi}_{\mathrm{OT},1} + \dot{\phi}_{\mathrm{M},2} - \dot{\phi}_{\mathrm{M},1}$$

which can be simplified,

$$\dot{w} = \frac{1}{m}\left(p_2\dot{p}_2 - p_1\dot{p}_1\right) + \dot{\phi}_{\mathrm{OT},2} - \dot{\phi}_{\mathrm{OT},1} + \dot{\phi}_{\mathrm{M},2} - \dot{\phi}_{\mathrm{M},1}$$

now the potential energy due to the optical trap,

$$\phi_{\mathrm{OT}} = \frac{1}{2}k_{\mathrm{OT}}(x - x_{\mathrm{OT}})^2 = \frac{1}{2}k_{\mathrm{OT}}\left(x - x_{\mathrm{OT}}^o - \mathrm{v}_{\mathrm{OT}}t\right)^2$$

therefore the change in the potential energy as a function of time is,

$$\frac{d\phi_{\mathrm{OT}}}{dt} = \dot{\phi}_{\mathrm{OT}} = k_{\mathrm{OT}}\left(x - x_{\mathrm{OT}}^o - \mathrm{v}_{\mathrm{OT}}t\right) \times \left(\dot{x}(t) - \mathrm{v}_{\mathrm{OT}}\right)$$

and, $\dot{x}(t) = p/m$

$$\dot{\phi}_{OT} = k_{OT}\left[x - x_{\mathrm{OT}}^o - \mathrm{v}_{\mathrm{OT}}t\right]\left[\frac{p}{m} - \mathrm{v}_{\mathrm{OT}}\right]$$

at t=0, when the trap is stationary,

$$\dot{\phi}_{\mathrm{OT}}(t = 0) = k_{\mathrm{OT}}\left[x(t = 0) - x_{\mathrm{OT}}^o\right] \times \left[\frac{p(t = 0)}{m}\right]$$

and at a time t where $t > 0$,

$$\dot{\phi}_{\mathrm{OT}}(t) = k_{\mathrm{OT}}\left[x(t) - x_{\mathrm{OT}}^o - \mathrm{v}_{\mathrm{OT}}t\right] \times \left[\frac{p(t)}{m} - \mathrm{v}_{\mathrm{OT}}\right]$$

also the change in the membrane potential as a function of time (due to bead position changing as a function of time),

$$\dot{\phi}_{\mathrm{M}}(t) = \frac{1}{2}k_{\mathrm{M}} \cdot 2\left[x(t) - x_{\mathrm{M}}\right]\dot{x}(t)$$
$$= k_{\mathrm{M}}\left[x(t) - x_{\mathrm{M}}\right]\frac{p(t)}{m}$$

and at initial time,

$$\dot{\phi}_{\mathrm{M}}(0) = k_{\mathrm{M}} \left[x(0) - x_{\mathrm{M}} \right] \frac{p(0)}{m}$$

so the change in the membrane potential is,

$$\dot{\phi}_{\mathrm{M}}(t) - \dot{\phi}_{\mathrm{M}}(0) = k_{\mathrm{M}} \left[x(t) - x_{\mathrm{M}} \right] \frac{p(t)}{m} - k_{\mathrm{M}} \left[x(0) - x_{\mathrm{M}} \right] \frac{p(0)}{m}$$

and the change in the optical trap potential is,

$$\dot{\phi}_{\mathrm{OT}}(t) - \dot{\phi}_{\mathrm{OT}}(0) = k_{\mathrm{OT}} \left[x(t) - x_{\mathrm{OT}}^o - \mathrm{v}_{\mathrm{OT}}t \right] \left[\frac{p(t)}{m} - \mathrm{v}_{\mathrm{OT}} \right] - k_{\mathrm{OT}} \left[x(0) - x_{\mathrm{OT}}^o \right] \frac{p(0)}{m}$$

further the momentum at initial and final time are,

$$p(t)\dot{p}(t) = -p(t) \left[k_{\mathrm{M}} \left(x(t) - x_{\mathrm{M}} \right) \right] - p(t) \left[k_{\mathrm{OT}} \left(x(t) - x_{\mathrm{OT}}^o - \mathrm{v}_{\mathrm{OT}}t \right) \right]$$

$$p(0)\dot{p}(0) = -p(0) \left[k_{\mathrm{M}} \left(x(0) - x_{\mathrm{M}} \right) \right] - p(0) \left[k_{\mathrm{OT}} \left(x(0) - x_{\mathrm{OT}}^o \right) \right]$$

it follows that the work is,

$$\dot{w} = +\frac{p(t)}{m} \left[k_{\mathrm{M}} \left(x(t) - x_{\mathrm{M}} \right) \right] \qquad \text{(from } \dot{\phi}_{\mathrm{M}})$$

$$- \frac{p(t)}{m} \left[k_{\mathrm{M}} \left(x(t) - x_{\mathrm{M}} \right) \right] \qquad \text{(from } p\dot{p}(t))$$

$$+ \left[\frac{p(t)}{m} - \mathrm{v}_{\mathrm{OT}} \right] \left[k_{\mathrm{OT}} \left(x(t) - x_{\mathrm{OT}}^o - \mathrm{v}_{\mathrm{OT}} \right) \right] \qquad \text{(from } \dot{\phi}_{\mathrm{OT}})$$

$$- \frac{p(t)}{m} \left[k_{\mathrm{OT}} \left(x(t) - x_{\mathrm{OT}}^o - \mathrm{v}_{\mathrm{OT}}t \right) \right] \qquad \text{(from } p\dot{p}(t))$$

$$- \frac{p(0)}{m} \left[k_{\mathrm{M}} \left(x(0) - x_{\mathrm{M}} \right) \right] \qquad \text{(from } \dot{\phi}_{\mathrm{M}})$$

$$+ \frac{p(0)}{m} \left[k_{\mathrm{M}} \left(x(0) - x_{\mathrm{M}} \right) \right] \qquad \text{(from } p\dot{p}(0))$$

$$- \left[\frac{p(0)}{m} \right] \left[k_{\mathrm{OT}} \left(x(0) - x_{\mathrm{OT}}^o \right) \right] \qquad \text{(from } \dot{\phi}_{\mathrm{OT}})$$

$$- \frac{p(0)}{m} \left[k_{\mathrm{OT}} \left(x(0) - x_{\mathrm{OT}}^o \right) \right] \qquad \text{(from } p\dot{p}(0))$$

therefore,

$$\dot{w} = -\mathrm{v}_{\mathrm{OT}} \left[k_{\mathrm{OT}} \left(x(t) - x_{\mathrm{OT}}^o - \mathrm{v}_{\mathrm{OT}}t \right) \right]$$

clearly as the force due to the optical trap is,

$$F_{\text{OT}} = -\frac{\partial \phi_{\text{OT}}}{\partial x} = -k_{\text{OT}}\left(x(t) - x_{\text{OT}}^o - v_{\text{OT}}t\right)$$

therefore the work is,

$$\dot{w} = F_{\text{OT}} \cdot v_{\text{OT}}$$

and,

$$w(t) = \int_0^t F_{\text{OT}} v_{\text{OT}} dt'$$

C.2   Derivation of the free energy

The equilibrium partition function, Z, is the normalisation factor for the equilibrium distribution function,

$$Z = \int dx \, \exp\left[-U(x)\right]$$

where the energy is the non-dimensionalised by $k_B T$.

The equilibrium free energy of a state is given by,

$$F = -k_{\text{B}} T \ln Z.$$

So at $t = 0, x_{\text{OT}} = 0$ (corresponding to $\lambda = \lambda_0$), and at the end of the process, at some arbitrary $t = t_{\text{d}}$, $x_{\text{OT}} = x_{\text{OT}}^{\text{final}}$ (corresponding to $\lambda = \lambda_{\text{f}}$). Now, the change in free energy is:

$$\Delta F = F(x_{\text{OT}}^{\text{final}}) - F(x_{\text{OT}} = 0) = -k_B T \ln \frac{Z(x_{\text{OT}}^{\text{final}})}{Z(x_{\text{OT}} = 0)} \tag{C.3}$$

As discussed earlier, a truncated harmonic potential is used to describe both the membrane and optical trap potentials. They are defined by equations 6.4 and 6.5. To integrate over these potentials, the bounds need to be defined. At $x_{\text{OT}} = 0$, there are three integrals, with two distinct

bounds. As defined previously, x_M^{ub} and x_{OT}^{lb} represent the upper and lower limits of the membrane and tweezer potentials. Consequently, the partition functions to evaluate are:

$$
Z(x_{OT} = 0) = \int_{-\infty}^{\infty} dx\, e^{-U_{\lambda_0}(x)} = \int_{-\infty}^{x_{OT}^{lb}} dx \exp\left[-\left(\frac{1}{2}\, k_M\, x^2 - \epsilon_M\right)\right]
$$
$$
+ \int_{x_{OT}^{lb}}^{x_M^{ub}} dx \exp\left[-\left(\frac{1}{2}\, k_M\, x^2 - \epsilon_M + \frac{1}{2}\, k_{OT}\, x^2 - \epsilon_{OT}\right)\right]
$$
$$
+ \int_{x_M^{ub}}^{\infty} dx \exp\left[-\left(\frac{1}{2}\, k_{OT}\, x^2 - \epsilon_{OT}\right)\right] \quad \text{(C.4)}
$$

$$
Z(x_{OT}^{final}) = \int_{-\infty}^{\infty} dx\, e^{-U_{\lambda_f}(x)} = \int_{-\infty}^{x_M^{ub}} dx \exp\left[-\left(\frac{1}{2}\, k_M\, x^2 - \epsilon_M\right)\right] + \int_{x_M^{ub}}^{x_{OT}^{lb}} dx \exp\left(-0\right)
$$
$$
+ \int_{x_{OT}^{lb}}^{\infty} dx \exp\left[-\left(\frac{1}{2}\, k_{OT}\, (x - x_{OT}^{final})^2 - \epsilon_{OT}\right)\right] \quad \text{(C.5)}
$$

The analytical solution of $Z(x_{OT} = 0)$ is as follows:

$$
Z(x_{OT} = 0) = \frac{\sqrt{\pi/2}}{\sqrt{k_M}} \exp\left(\epsilon_M\right) \left[\text{erf}\left(\frac{x_{OT}^{lb} \sqrt{k_M}}{\sqrt{2}}\right) + 1\right]
$$
$$
+ \frac{\sqrt{\pi/2}}{\sqrt{k_M + k_{OT}}} \exp\left(\epsilon_M + \epsilon_{OT}\right) \left[\text{erf}\left(\frac{x_M^{ub} \sqrt{k_M + k_{OT}}}{\sqrt{2}}\right) - \text{erf}\left(\frac{x_{OT}^{lb} \sqrt{k_M + k_{OT}}}{\sqrt{2}}\right) + 1\right]
$$
$$
+ \frac{\sqrt{\pi/2}}{\sqrt{k_{OT}}} \exp\left(\epsilon_{OT}\right) \left[\text{erfc}\left(\frac{x_M^{ub} \sqrt{k_{OT}}}{\sqrt{2}}\right)\right] \quad \text{(C.6)}
$$

The analytical solution of $Z(x_{OT}^{final})$ can be found directly. However, for simplicity it is best to do a change of variable. Let $y = x - x_{OT}^{final}$. Therefore the bounds of the integral will be altered. $Z(x_{OT}^{final})$ can now be written as (note that the integral which takes into account only the membrane potential remains unaltered):

$$
Z(x_{OT}^{final}) = \int_{-\infty}^{x_M^{ub}} dx \exp\left[-\left(\frac{1}{2}\, k_M\, x^2 - \epsilon_M\right)\right] + \int_{x_M^{ub}}^{x_{OT}^{lb}} dx \exp\left(-0\right)
$$
$$
+ \int_{x_{OT}^{lb} - x_{OT}^{final}}^{\infty} dy \exp\left[-\left(\frac{1}{2}\, k_{OT}\, y^2 - \epsilon_{OT}\right)\right] \quad \text{(C.7)}
$$

and the analytical solution is:

$$Z(x_{OT}^{final}) = \frac{\sqrt{\pi/2}}{\sqrt{k_M}} \exp\left(\epsilon_M\right) \left[\text{erf}\left(\frac{x_M^{ub}\sqrt{k_M}}{\sqrt{2}}\right) + 1 \right] + \left[x_{OT}^{lb} - x_M^{ub} \right]$$
$$+ \frac{\sqrt{\pi/2}}{\sqrt{k_{OT}}} \exp\left(\epsilon_{OT}\right) \left[\text{erfc}\left(\frac{(x_{OT}^{lb} - x_{OT}^{final})\sqrt{k_{OT}}}{\sqrt{2}}\right) \right] \quad \text{(C.8)}$$

Equations C.7 and C.8 can now be substituted into equation C.3 to solve for the analytically derived free energy.

C.3   Derivation of equilibrium adhesion probability

The probability of adhesion/detachment is obtained by integrating over all probabilities when the particle is in the membrane or in the trap, respectively. I.e., a particle is defined as remained attached if, at x_{OT}^{final}, the bead position is at $x \leq x_M^{ub}$ and defined as detached if bead position is at $x \geq x_{OT}^{lb}$. They are given by the following expressions at $x_{OT} = x_{OT}^{final}$,

$$p_A = \frac{Z_A}{Z(x_{OT}^{final})} \quad \text{(C.9)}$$

$$p_D = \frac{Z_D}{Z(x_{OT}^{final})} \quad \text{(C.10)}$$

where Z_A and Z_D are constrained partition functions defined by,

Membrane:
$$Z_A = \int_{-\infty}^{x_M^{ub}} dx \, \exp\left[-\left(\frac{1}{2} k_M x^2 - \epsilon_M\right) \right] \quad \text{(C.11)}$$

Optical Tweezer:
$$Z_D = \int_{x_{OT}^{lb}}^{\infty} dx \, \exp\left[-\left(\frac{1}{2} k_{OT} (x - x_{OT})^2 - \epsilon_{OT}\right) \right] \quad \text{(C.12)}$$

The expression for $Z(x_{OT}^{final})$ is given by eq. C.5.

Introducing a change of variable, $y = x - x_{OT}^{final}$, we can write,

$$Z_D = \int_{x_{OT}^{lb} - x_{OT}^{final}}^{\infty} dy \, \exp\left[-\left(\frac{1}{2} k_{OT} y^2 - \epsilon_{OT}\right) \right] \quad \text{(C.13)}$$

The analytical expression for Z_A and Z_D are,

$$Z_A = \frac{\sqrt{\pi/2}}{\sqrt{k_M}} \exp\left(\epsilon_M\right) \left[\mathrm{erf}\left(\frac{x_M^{ub} \sqrt{k_M}}{\sqrt{2}} \right) + 1 \right] \tag{C.14}$$

$$Z_D = \frac{\sqrt{\pi/2}}{\sqrt{k_{OT}}} \exp\left(\epsilon_{OT}\right) \left[\mathrm{erfc}\left(\frac{(x_{OT}^{lb} - x_{OT}^{final}) \sqrt{k_{OT}}}{\sqrt{2}} \right) \right] \tag{C.15}$$

Equations C.8, C.14 and C.15 can now be substituted into equation C.9 and equation C.10 to solve for the probabilities of attachment and detachment, respectively.

Appendix D

Programs developed to model theoretical detachment of bead from membrane

D.1 Force spectroscopy simulation program

The following program in C language was used to simulate a force spectroscopy experiment using a langevin equation. The outputs were used to calculate free energies using Crooks fluctuation theorem, Jarzynski equality and umbrella sampling. Analogous program were used for validation by TFT and ITFT.

```
/*
This c program was developed in order to analyse bead subjected to a time−varied

Trap potential is a harmonic and represented as, U = 1/2.k.r^2
where k is the trap stiffness
where r is the relative bead position compared to center of trap
x is bead position
x0 is center of trap
The force bead feels is therefore = −dU/dx = −k(x−x0)

 The bead trajectory is found using langevin equation.
 New x position is found by the old x−position + Summed Force due to external po
 In the Langevin equation inertia is assumed to be negligible and therefore set

 Written by: Emma Hodges
 Updated on: 16/12/2013


*/

#include <stdio.h>
#include <stdlib.h>
#include <math.h>
```

```c
void main()
{
  /* Declaration of parameters */

  /* Declare files both input and output */
  FILE *ifp, *ofp, *bofp, *check, *fofp, *xofp, *hofp, *oofp, *pofp, *fiofp;
  /* Declare variables that are called to external functions(i.e. not in main funct
  extern void make_exponentiation_table();
  extern void set_status();
  extern double yarn5();
  extern double force();
  extern double pot();
  extern double mem_pot();
  extern double mem_force();

  double pi = 3.14159265;

  /* Parameters for stationary (m) and moving (o) trap */
  double km = 0.;//trapping constant membrane potential
  double ko = 0.;//trapping constant ot potential
  double d2int = 0.;//x displacement of ot potential initial
  double d2final = 0.;//x displacement of ot potential final
  double ody = 0.; //y displacement of ot potential
  double v2 = 0.;// velocity of optical trap
  double d2 = 0.;//x displacement of ot potential  (minima at t= 0: x=0)
  double mdy = 0; //y displacement of membrane potential
  double sfac = 0.;
  double sigma = 0.;
  double sigmaf = 0.;
  double sigmat = 0.;
  double kbt = 0.;//Boltzmann constant
  int k = 0;
  int ntraj = 0;
  int teq = 0;
  double zeta = 0.;
  /* Parameters for random number generator */
  int iseed2 = 0;
  int iseed = 0;//seed number to produce random number
  int status[4];
  int status2[4];
  double random_number = 0.;
  double sum_force = 0.;
  /* Parameters for langevin equation */
  double x = 0.;//x position at i
  double x0 = 0.; // initial position
  double xnew = 0.;// x position at i+1
  double timestep = 0.;
  double randfac = 0.;//random number prefactor (incorporates friction coefficient
  double limit_min = 0.;//Minimum x-value
```

```c
    double limit_max = 0.; //Max x−value
    double d_step = 0.;
    int niter = 0; //number of time iterations
    int i = 0;
    int j = 0;
    int n = 0;
    double x1 =0.;
    double x2 =0.;
    double w =0.;
    double y1 =0.;
    double y2 =0.;

    /* Analysis parameters */
    double initial_pot = 0.;
    double initial_mem_pot = 0.;
    double final_pot = 0.;
    double final_x = 0.;
    double ctime = 0.;

    /* Parameters required to produce histogram */
    int hist_entries = 0;
    int hist_entriesf = 0;
    int* histogram = NULL;
    int* onehistogram = NULL;
    int* twohistogram = NULL;
    int* threehistogram = NULL;
    int* fhistogram = NULL;
    int* nhistogram = NULL;
    int* phistogram = NULL;
    double* ahistogram = NULL;
    double* onehistogramb = NULL;
    double* twohistogramb = NULL;
    double* threehistogramb = NULL;
    double* fhistogramb = NULL;
    int hist = 0;
    int ihist = 0;
    int fhist = 0;
    int rhist = 0;
    int onehist = 0;
    int twohist = 0;
    int threehist = 0;
    double histogram_factor = 0.;
    int histogram_counter = 0;
    int onehistogram_counter = 0;
    int twohistogram_counter = 0;
    int threehistogram_counter = 0;
    int rhistogram_counter = 0;
    int fhistogram_counter = 0;
    double hist_integral = 0.;
    double onehist_integral = 0.;
```

```
  double twohist_integral = 0.;
  double threehist_integral = 0.;
  double fhist_integral = 0.;


  double t = 0.;
  int itime =0;
  int thist =0;

  double* boltzmann_factor = NULL;
  double boltzmann_integral = 0.;
  double* cumulative = NULL;
  double* normcumulative = NULL;
  double* boltzmann_factorf = NULL;
  double boltzmann_integralf = 0.;
  double cum_prefac = 0.;
  double*  boltzmann0aa = NULL;
  double* boltzmann0a = NULL;
  double* boltzmann0bb =NULL;
  double* boltzmann0b = NULL;
  double* boltzmann1aa =NULL;
  double* boltzmann1a = NULL;
  double* boltzmann1bb = NULL;
  double* boltzmann1b = NULL;
  double* boltzmann1c = NULL;


  double t_factor = 0.;
  int t_entries = 0;
  double time =0.;
  double dfinal =0.;

/* Parameters to determine where bead is situated */
  double escape_pos = 0.;
  double mem_pos = 0.;
  double mem_pos2 = 0.;
  double ot_pos1 = 0.;
  double ot_pos2 = 0.;
  double bw_pos1 = 0.;
  double bw_pos2 = 0.;
  double escapeot_pos2 = 0.;

  int escape = 0;
  int descape = 0;
  int rem_mem = 0;
  int ot = 0;
  int bw = 0;
  int escape_ot = 0;

  double dworkescape = 0.;
```

```c
    double dworktotal = 0.;
    double dwork = 0.;
    double prob_escape = 0.;
    double prob_rem_mem = 0.;
    double u_final_x = 0.;
    double accdf = 0.;
    double ave_accdf = 0.;
    double memaccdf = 0.;
    double otaccdf = 0.;
    double jotaccdf = 0.;
    double sworkescape = 0.;
    double accdworktotal = 0.;
    double potaccdf = 0.;
    double bwaccdf = 0.;
    double unbias_rem = 0.;
    double unbias_escape = 0.;
    double free_energy = 0.;
    double avedworktotal = 0.;
    double aveaccdf = 0.;
    double avemaccdf = 0.;
    double aveotaccdf = 0.;
    double avejotaccdf = 0.;
    double avebwaccdf = 0.;
    double aveescapeot = 0.;

    int nif = 0;
    int sinf = 0;
    int sfin = 0;
    double sum_potential = 0.;
    double sum_pot = 0.;

    double dx = 0.;
    double temp_dt = 0.;
    int maxforce = 0;
    double random_force = 0.;
    double orem_mem = 0.;
    double oescape = 0.;
    double oaccdf = 0.;
    double omemaccdf = 0.;
    double ootaccdf = 0.;
    /*Open input file, scan input file to read values and assign
    to associated parameter, print on terminal screen the parameter
    and its assigned value
    */
    ifp = fopen("je_lang_in1.txt", "r");
    if (ifp == NULL)
      {
        fprintf(stderr, "Can't open input file je_lang_in.txt!\n");
        exit(1);
      }
```

```c
fscanf(ifp, "%lf %lf %lf %lf %lf %lf %lf\n",
&km, &ko, &d2int, &d2final, &ody, &mdy, &v2);
fscanf(ifp, "%d %lf %lf %lf\n", &ntraj, &zeta, &limit_min, &limit_max );
fscanf(ifp, "%lf %lf %d %d %d %d %d\n", &kbt, &timestep,
&hist_entries, &t_entries, &iseed, &iseed2, &maxforce);
fclose(ifp);

/*Open output files */
oofp = fopen("tft.txt", "w");

if (oofp == NULL)
  {
    fprintf(stderr, "Can't open output file overview_work2.txt!\n");
    exit(1);
  }

bofp = fopen("begin_potcr1.txt", "w");

if (bofp == NULL)
  {
    fprintf(stderr, "Can't open output file begin_pot.txt!\n");
    exit(1);
  }

fofp = fopen("final_potcr1.txt", "w");

if (fofp == NULL)
  {
    fprintf(stderr, "Can't open output file final_pot.txt!\n");
    exit(1);
  }

xofp = fopen("xint_histcr1.txt", "w");

if (xofp == NULL)
  {
    fprintf(stderr, "Can't open output file xint_hist.txt!\n");
    exit(1);
  }

hofp = fopen("xint_histboltcr1.txt", "w");

if (hofp == NULL)
  {
    fprintf(stderr, "Can't open output file xint_hist.txt!\n");
    exit(1);
  }

fiofp = fopen("works2cr1.txt", "w");
```

```c
if (fiofp == NULL)
  {
    fprintf(stderr, "Can't open output file works2.txt!\n");
    exit(1);
  }

/* Calculating langevin equation */

time = (d2final−d2int)/v2;
niter =(int)(time / timestep + 0.5);
printf("Read niter %d \n", niter);
printf("Read time %lf \n", time);
randfac = sqrt( 2. * kbt * timestep / zeta);
sfac = 1 / kbt;
t = niter * timestep;
histogram = calloc(hist_entries, sizeof(int));
nhistogram = calloc(t_entries, sizeof(int));
phistogram = calloc(t_entries, sizeof(int));
ahistogram = calloc(t_entries, sizeof(double));
fhistogram = calloc(hist_entries, sizeof(int));
histogram_factor = hist_entries / (limit_max − limit_min);
t_factor = t_entries / t;
cumulative= calloc(hist_entries, sizeof(double));
normcumulative= calloc(hist_entries, sizeof(double));
boltzmann_factor= calloc(hist_entries, sizeof(double));

for (i=0; i< hist_entries; ++i)
  {
    x = i/histogram_factor + limit_min + 0.5/histogram_factor;
    sum_pot = mem_pot(x, km, mdy) + pot(x, ko, d2int, ody);
    boltzmann_factor[i] = exp(−sum_pot);
    boltzmann_integral += boltzmann_factor[i];
  }

for (i=0; i < hist_entries; ++i)
  {
    boltzmann_factor[i] *= (histogram_factor / boltzmann_integral);
  }

printf("Boltzmann %lf \n", histogram_factor / boltzmann_integral);

// Required for boltzmann distributed x−int values
cumulative[0] = boltzmann_factor[0]*histogram_factor;
for (i=1; i < hist_entries; ++i)
  {
    cumulative[i] = cumulative[i−1]+ boltzmann_factor[i]*histogram_factor;
  }
printf("first cumulative value %lf \n", cumulative[0]);
printf("final cumulative value %lf \n", cumulative[hist_entries −1]);
```

```c
cum_prefac = 1 / cumulative[hist_entries −1];

 for (i=0; i < hist_entries; ++i)
  {
    normcumulative[i] = cumulative[i] * cum_prefac;
  }

printf("final_cumulative_value_norm_%lf_\n",
normcumulative[hist_entries −1]);

/* Requried for random number generation */
make_exponentiation_table();
set_status(&iseed, status);
make_exponentiation_table();
set_status(&iseed2, status2);

itime = niter / t_entries;
d_step = v2 * timestep;
printf("d_step_%lf\n", d_step);
nif = ntraj/5000;

for (x = −10; x < 20; ++x)
  {
    sum_force = mem_force(x, km, mdy) + force(x, ko, d2, ody);
    sum_pot = mem_pot(x, km, mdy) + pot(x, ko, d2, ody);
    fprintf(bofp, "%f_%f_%f_%f_%f_%f_%f\n", x, sum_pot,
    mem_pot(x, km, mdy), pot(x, ko, d2, ody),
    mem_force(x,km, mdy), force(x, ko, d2, ody), sum_force);
  }
escape_pos = d2final − sqrt(2*ody/ko);
mem_pos = sqrt(2*mdy/km);

/* Run code for number of trajectories you want to assess */
for (n = 0; n < ntraj; ++n)
  {
    /* Initialise all values for new trajectory */
    x = 0.;
    final_x = 0.;
    d2=d2int;
    sigma = 0.;
    sigmaf= 0.;
    sigmat = 0.;
    timestep = time / niter;
    descape = 0;

    y1=yarn5(status);
    int isearch = 1;
    while (normcumulative[isearch] < y1)
      {
         ++isearch;
```

```c
      }
   x = (y1−normcumulative[isearch−1]) / (normcumulative[isearch]
   normcumulative[isearch−1])/histogram_factor +
   (isearch−1)/histogram_factor + limit_min + 1 / histogram_factor;
   x0=x;

   fprintf(xofp, "%f\n", x0);
   double dfhist = (x0−limit_min)* histogram_factor;
   fhist = (int)dfhist;
   ++fhistogram[fhist];
   ++histogram_counter;
   if (x0 >= escape_pos)
     {
       descape = 1;
     }
/*Langevin equation to find x position as function of time*/
   for (i = 0; i < niter; ++i)
     {

       do {
         x1 = 2.0 * yarn5(status) − 1.0;
         x2 = 2.0 * yarn5(status2) − 1.0;
         w = x1 * x1 + x2 * x2;
       } while ( w >= 1.0 );

       w = sqrt( (−2.0 * log( w ) ) / w );
       y1 = x1 * w;

       timestep = time / niter;
       random_number = y1;
       random_force = random_number * sqrt( 2. * kbt * timestep / zeta);
       sum_potential = mem_pot(x, km, mdy) + pot(x, ko, d2, ody);
       sum_force = mem_force(x, km,mdy) + force(x, ko, d2, ody);
       xnew = x + sum_force * timestep/ zeta + random_force;

       sum_force = mem_force(xnew, km, mdy) + force(xnew, ko, d2, ody);
       if (fabs(sum_force) > maxforce)
         {
           timestep = timestep * 0.5;
           random_force = random_number * sqrt( 2. * kbt * timestep / zeta);
           xnew = x + sum_force * timestep/ zeta + random_force;
           sum_force = mem_force(xnew, km, mdy) + force(xnew, ko, d2, ody);
         }
       x=xnew;

       sigma += force(x, ko, d2, ody) * timestep;
       sigmat = sigma * v2 * sfac;
       double expw = exp(−sigmat);

       d2 += v2*timestep;
```

```c
      if ( i % itime == 0)
        {
          thist = i/ itime;
          if (sigmat < 0)
            {
              ++nhistogram[thist];
            }
          if (sigmat > 0)
            {
              ++phistogram[thist];
              ahistogram[thist]=ahistogram[thist]+exp(-sigmat);
            }
        }
          ++rhistogram_counter;

    }

  final_x = x;

  sigmaf = v2 * sigma * sfac;
  double esig = exp(-sigmaf);
  if (isfinite(esig))
    {
      if (esig < 200000)
        {
          if(final_x >= escape_pos)
            {
              escape = escape +1;
              otaccdf += exp(-sigmaf);
              oescape = escape +1;
              ootaccdf += exp(-sigmaf);
            }

          if(final_x <= mem_pos)
            {
              rem_mem = rem_mem + 1;
              orem_mem = orem_mem + 1;
              memaccdf += exp(-sigmaf);
              omemaccdf += exp(-sigmaf);
            }

          accdf += exp(-sigmaf);
          oaccdf +=exp(-sigmaf);
        }

      if (esig > 200000)
        {
          printf("large esig; value and traj number %f %d\n", esig, n);
        }
```

```
            if (n % 50000 == 0)
            {
                prob_rem_mem = (double) orem_mem / 50000.;
                prob_escape = (double) oescape / 50000.;
                ave_accdf = oaccdf / 50000.;
                avemaccdf = omemaccdf / 50000.;
                aveotaccdf = ootaccdf / 50000.;
                unbias_rem = avemaccdf / ave_accdf;
                unbias_escape = aveotaccdf / ave_accdf;
                free_energy = -log(ave_accdf);
                fprintf(oofp, "%d %f %f %f %f %f %f %f %f\n", n, prob_rem_mem,
        prob_escape, ave_accdf, avemaccdf, aveotaccdf, unbias_rem,
        unbias_escape, free_energy);
                orem_mem = 0.;
                oescape = 0.;
                oaccdf = 0.;
                omemaccdf = 0.;
                ootaccdf = 0.;

            }

        }

        if (isfinite(esig))
        {
            sfin = sfin + 1;
        }
        else
        {
            sinf = sinf +1;
            printf("oh no im inifinte traj: %d\n",n);

        }
        if (x>=escape_pos)
        {
            descape = 1;
        }
        fprintf(fiofp, "%f %f %f %d\n", x, sigmaf, esig, descape);

    }

  for (x = -10; x < 30; ++x)
    {
      sum_force = mem_force(x, km, mdy) + force(x, ko, d2, ody);
      sum_pot = mem_pot(x, km, mdy) + pot(x, ko, d2, ody);
      fprintf(fofp, "%f %f %f %f %f %f %f\n", x, sum_pot,
      mem_pot(x, km, mdy), pot(x, ko, d2, ody),
      mem_force(x, km, mdy), force(x, ko, d2, ody), sum_force);
```

```
        }

  for  (i=0;  i< hist_entries;  ++i)
    {
      x=i / histogram_factor + limit_min + 0.5/histogram_factor;
      double phist = histogram_factor / histogram_counter;
      fprintf(hofp, "%lf %lf %lf\n", x, phist * fhistogram[i],
      boltzmann_factor[i]);
    }

  fclose(fiofp);
  fclose(oofp);
  fclose(hofp);
  fclose(bofp);
  fclose(fofp);
  fclose(xofp);
  exit(0);
}



/* Function to calculate potential */
double mem_pot(double x, double km, double mdy)
{
  double pmem = 0.;
  double limit1 = sqrt(2*mdy/km);

  if (x <= limit1)
    {
      pmem = 0.5*km*x*x-mdy;
    }
  if (x > limit1)
    {
      pmem = 0;
    }

  return(pmem);
}

/* Function to calculate force */
double mem_force(double x, double km, double mdy)
{
  double pforce = 0.;
  double limit1 = sqrt(2*mdy/km);

  if (x <= limit1)
    {
      pforce = -km*x;
    }
  if (x > limit1)
```

```
      {
        pforce = 0;
      }

    return(pforce);
}



/*Function to calculate trap potential */
double pot(double x, double ko, double d2, double ody)
{
    double pmem = 0.;
    double limit2 = d2-sqrt(2*ody/ko);
    if (x < limit2)
      {
        pmem = 0;
      }
    if (x >= limit2)
      {
        pmem = 0.5*ko*(x-d2)*(x-d2)-ody;
      }

    return(pmem);
}

/*Function to calculate trap force */
double force(double x, double ko, double d2, double ody)
{
    double pforce = 0.;
    double limit2 = d2-sqrt(2*ody/ko);
    if (x < limit2)
      {
        pforce = 0;
      }
    if (x >= limit2)
      {
        pforce = -ko*(x-d2);
      }
    return(pforce);
}



/*Function to generate random number */
/* Implementation of the yarn5 random number generator */
/* as described in the documentation of TNRG */
/* = tina's random number generator */
/* by Heiko Bauke and Stefan Mertens */
/* University of Magdeburg */

/* 2**31 - 1 */
```

```
#define MYMAXINT        2147483647

/* inverse of that */
#define MAXINV   4.6566128752457969230960088680149056017398834 23e-10

/* 2**16 - 1 */
#define SMALLMAXINT     65535

/* 2**15 - 1 */
#define EVENSMALLERMAXINT   32767

/* 1st factor for multiple recurrence generator */
#define FACTOR1         107374182

/* 2nd factor for multiple recurrence generator */
#define FACTOR2         104480

/* base for exponentiation */
#define BASE            123567893

/* multiplicator for simple congruential generator */
#define LEHMERNUMBER    16807

/* lookup tables efficient exponentiation */
static int yarn5_exponentiation_table_part1[SMALLMAXINT];
static int yarn5_exponentiation_table_part2[EVENSMALLERMAXINT];

int moduloproduct(int number1, int number2)
  {
    /* int64_t: explicit requirement that the integer is
       represented in 64-bit mode */

    int64_t bignumber1;
    int64_t bignumber2;
    int64_t bigproduct;

    int64_t mask;
    int64_t split1;
    int64_t split2;

    int product;

    bignumber1 = (int64_t) number1;
    bignumber2 = (int64_t) number2;
    bigproduct = bignumber1 * bignumber2;

    mask = (int64_t) MYMAXINT;   /* is all ones for the lower 31 bits */

    split1 = bigproduct & mask;      /* picks the lower 31 bits */
    split2 = bigproduct >> 31;       /* picks the remaining high bits */
```

```
    /* idea: bigproduct
          = split1 + split2 * 2**31
          = split1 + split2 * (2**31 − 1) + split2
      and the middle term does not contribute to the modulo, hence
      bigproduct mod (2**31 −1) = (split1 + split2) mod (2**31 − 1) */

    bigproduct = split1 + split2;

    /* split1 and split2 are both smaller than 2**31 − 1, hence
      2**31 − 1 needs to be subtracted at most once */

    if (bigproduct >= mask)
      {
        bigproduct = bigproduct − mask;
      }

    /* final output must be converted back to standard integer */
    product = (int) bigproduct;

    return (product);

  }



int modulosum(int number1, int number2)
  {
    /* int64_t: explicit requirement that the integer is
      represented in 64−bit mode */

    int64_t bignumber1;
    int64_t bignumber2;
    int64_t bigsum;

    int64_t mask;

    int sum;

    bignumber1 = (int64_t) number1;
    bignumber2 = (int64_t) number2;
    bigsum     = bignumber1 + bignumber2;

    mask = (int64_t) MYMAXINT;

    /* each summand is smaller than 2**31 − 1, hence
      2**31 − 1 needs to be subtracted at most once */

    if (bigsum >= mask)
      {
        bigsum = bigsum − mask;
```

```
        }

    /* final output must be converted back to standard integer */
    sum = (int) bigsum;

    return(sum);

}


void yarn5_production_rule(int *status)
    {
    /* array status with five elements constitutes the
        state of the RNG */

    extern int moduloproduct();
    extern int modulosum();

    int product1;
    int product2;
    int sum;

    int factor1;
    int factor2;

    /* magic numbers by l'Ecuyer */
    factor1 = FACTOR1;
    factor2 = FACTOR2;

    product1 = status[0];
    product2 = status[4];

    product1 = moduloproduct(factor1, product1);
    product2 = moduloproduct(factor2, product2);

    sum = modulosum(product1, product2);

    status[4] = status[3];
    status[3] = status[2];
    status[2] = status[1];
    status[1] = status[0];
    status[0] = sum;

    return;
    }


void make_exponentiation_table()
    {
    /* recall: SMALLMAXINT = 2**16 - 1 */
```

```
    /*  r e c a l l :  EVENSMALLERMAXINT  =  2**15  −  1  */

    extern  int  yarn5_exponentiation_table_part1 [SMALLMAXINT];
    extern  int  yarn5_exponentiation_table_part2 [EVENSMALLERMAXINT];

    extern  int  moduloproduct ();

    int  i ;
    int  base ;

    yarn5_exponentiation_table_part1 [0]  =  1;
    yarn5_exponentiation_table_part2 [0]  =  1;

    base  =  BASE ;

    for ( i  =  1;  i  <= SMALLMAXINT;  ++i )
      {
        yarn5_exponentiation_table_part1 [ i ]  =
          moduloproduct ( yarn5_exponentiation_table_part1 [ i  −  1],
                         base );
      }

    base  =  moduloproduct ( yarn5_exponentiation_table_part1 [SMALLMAXINT] , base );
    /*  i . e .  modulo  (2**31  −  1)  we have now
        new_base  =  old_base **SMALLMAXINT  *  old_base ,  or
        new_base  =  old_base **(SMALLMAXINT+1),  or
        new_base  =  old_base **(2**16)    */

    for ( i  =  1;  i  <= EVENSMALLERMAXINT;  ++i )
      {
        yarn5_exponentiation_table_part2 [ i ]  =
          moduloproduct ( yarn5_exponentiation_table_part2 [ i  −  1],
                         base );
      }

    return ;
  }


int  delinearize ( int  number)
  {
    /*  r e c a l l :  SMALLMAXINT  =  2**16  −  1  */
    /*  r e c a l l :  EVENSMALLERMAXINT  =  2**15  −  1  */

    extern  int  yarn5_exponentiation_table_part1 [SMALLMAXINT];
    extern  int  yarn5_exponentiation_table_part2 [EVENSMALLERMAXINT];

    extern  int  moduloproduct ();

    int  output ;
```

```
    int mask;
    int split1;
    int split2;

    mask = SMALLMAXINT;            /* is all ones for the lower 16 bits */

    split1 = number & mask;        /* picks the lower 16 bits */
    split2 = number >> 16;         /* picks the remaining high bits */

    /* idea: number = split1 + 2**16 * split2 ,
       i.e. base**number = base**split1 * (base**(2**16))**split2 */

    split1 = yarn5_exponentiation_table_part1[split1];
    split2 = yarn5_exponentiation_table_part2[split2];

    output = moduloproduct(split1, split2);

    return(output);

  }


double yarn5(int *status)
  {
    /* array status with five elements constitutes the
       state of the RNG */

    extern void yarn5_production_rule();
    extern int delinearize();

    int integer_random_number;
    double float_random_number;
    double factor;

    factor = (double) MAXINV;

    yarn5_production_rule(status);
    integer_random_number = delinearize(status[0]);
    float_random_number = (double) integer_random_number * factor;

    return(float_random_number);

  }


void lehmer(int *ptr_to_iseed)
  {
    extern int moduloproduct();

    int lehmernumber;
```

```
    int integer_random_number;

    integer_random_number = *ptr_to_iseed;
    lehmernumber = LEHMERNUMBER;

    integer_random_number =
      moduloproduct(integer_random_number,lehmernumber);

    *ptr_to_iseed = integer_random_number;

    return;

  }


void set_status(int *ptr_to_iseed, int *status)
  {
    extern void lehmer();

    int i;

    for (i = 0; i < 5; ++i)
      {
        lehmer(ptr_to_iseed);
        status[i] = *ptr_to_iseed;
      }

    return;

  }
```

D.2   Program to calculate cumulants

The following program in C language was used to calculate the moments and cumulants from
the work data obtained in force spectroscopy simulation

```
#include <stdio.h>
#include <stdlib.h>
#include <math.h>

void main()

{
  FILE *fp, *ofp;
  int lines = 0;
  int i = 0;
  double dummy1, dummy2;
  int dummy3;
```

```
double *workvalues = NULL;
double meanwork = 0.;
double variance = 0.;
double standarddeviation = 0.;
double oneoverstandarddeviation = 0.;

double moment3 = 0.;
double moment4 = 0.;
double moment5 = 0.;
double moment6 = 0.;

double cumulant1 = 0.;
double cumulant2 = 1.;
double cumulant3 = 0.;
double cumulant4 = 0.;
double cumulant5 = 0.;
double cumulant6 = 0.;

double free_energy = 0.;

fp = fopen("input.dat","r");

while (EOF != (fscanf(fp,"%*[^\n]"), fscanf(fp,"%*c")))
  ++lines;
fclose(fp);
printf("number_of_lines_%d_\n",lines);

workvalues = calloc(lines, sizeof(double));

fp = fopen("input.dat","r");
ofp = fopen("output.txt","w");
for(i = 0; i < lines; ++i)
  {
    fscanf(fp,"%lf_%lf_%lf_%d\n",&dummy1,&workvalues[i],&dummy2,&dummy3);
  }
fclose(fp);

for(i = 0; i < lines; ++i)
  {
    meanwork += workvalues[i];
  }

meanwork = meanwork / ( (double) lines );
fprintf(ofp,"mean_work_=_%lf_\n",meanwork);

for(i = 0; i < lines; ++i)
  {
    workvalues[i] = workvalues[i] - meanwork;
  }
```

```
for(i = 0; i < lines; ++i)
  {
    variance += workvalues[i] * workvalues[i];
  }

variance = variance / ( (double) lines );
fprintf(ofp,"variance_=_%lf\n",variance);

standarddeviation = sqrt(variance);
fprintf(ofp,"standard_deviation_=_%lf\n",standarddeviation);

oneoverstandarddeviation = 1. / standarddeviation;

for(i = 0; i < lines; ++i)
  {
    workvalues[i] = workvalues[i] * oneoverstandarddeviation;
  }

for(i = 0; i < lines; ++i)
  {
    moment3 += workvalues[i] * workvalues[i] * workvalues[i];
    moment4 += workvalues[i] * workvalues[i] * workvalues[i]
      * workvalues[i];
    moment5 += workvalues[i] * workvalues[i] * workvalues[i]
      * workvalues[i] * workvalues[i];
    moment6 += workvalues[i] * workvalues[i] * workvalues[i]
      * workvalues[i] * workvalues[i] * workvalues[i];
  }

moment3 = moment3 / ( (double) lines );
moment4 = moment4 / ( (double) lines );
moment5 = moment5 / ( (double) lines );
moment6 = moment6 / ( (double) lines );

fprintf(ofp,"moment_3_=_%lf\n",moment3);
fprintf(ofp,"moment_4_=_%lf\n",moment4);
fprintf(ofp,"moment_5_=_%lf\n",moment5);
fprintf(ofp,"moment_6_=_%lf\n",moment6);

cumulant3 = moment3;
cumulant4 = moment4 - 3.;
cumulant5 = moment5 - 10. * moment3;
cumulant6 = moment6 - 15. * moment4 - 10. * moment3 * moment3 + 30.;

free_energy = meanwork;
fprintf(ofp,"cumulant_1_=_%lf,_free_energy_=_%lf\n",
cumulant1,free_energy);
free_energy -= (1./2.) * cumulant2 * standarddeviation *
standarddeviation;
fprintf(ofp,"cumulant_2_=_%lf,_free_energy_=_%lf\n",cumulant2,
```

```
    free_energy );
    free_energy += (1./6.) * cumulant3 * standarddeviation *
    standarddeviation * standarddeviation;
    fprintf(ofp,"cumulant_3_=_%lf,_free_energy_=_%lf\n",
    cumulant3 , free_energy );
    free_energy -= (1./24.) * cumulant4 * standarddeviation *
    standarddeviation * standarddeviation * standarddeviation;
    fprintf(ofp,"cumulant_4_=_%lf,_free_energy_=_%lf\n",
    cumulant4 , free_energy );
    free_energy += (1./120.) * cumulant5 * standarddeviation *
    standarddeviation * standarddeviation * standarddeviation *
    standarddeviation;
    fprintf(ofp,"cumulant_5_=_%lf,_free_energy_=_%lf\n",
    cumulant5 , free_energy );
    free_energy -= (1./720.) * cumulant6 * standarddeviation *
    standarddeviation * standarddeviation * standarddeviation *
    standarddeviation * standarddeviation;
    fprintf(ofp,"cumulant_6_=_%lf,_free_energy_=_%lf\n",
    cumulant6 , free_energy );
    fclose(ofp);
    exit(0);
}
```

Bibliography

Al-Yaman, F et al. (1995). "Human cerebral malaria: lack of significant association between erythrocyte resetting and disease severity". In: *Transactions of the Royal Society of Tropical Medicine and Hygiene* 89.1, pp. 55–58.

Ashkin, A. et al. (1986). "Observation of a single-beam gradient force optical trap for dielectric particles". In: *Optics letters* 11.5, pp. 288–290.

Ashley, Elizabeth A et al. (2014). "Spread of artemisinin resistance in Plasmodium falciparum malaria". In: *New England Journal of Medicine* 371.5, pp. 411–423.

Aslinia, Florence, Joseph J Mazza, and Steven H Yale (2006). "Megaloblastic anemia and other causes of macrocytosis". In: *Clinical Medicine & Research* 4.3, pp. 236–241.

Bachmann, Anna et al. (2009). "Absence of erythrocyte sequestration and lack of multicopy gene family expression in Plasmodium falciparum from a splenectomized malaria patient". In: *PLoS One* 4.10, e7459.

Baek, Jong-Ho, Sun-Uk Hwang, and Yong-Gu Lee (2007). "Trap stiffness in optical tweezers". In: *Mirror* 685, 1100nm.

Bannister, LH et al. (2000). "A brief illustrated guide to the ultrastructure of Plasmodium falciparum asexual blood stages". In: *Parasitology today* 16.10, pp. 427–433.

Bao, G., S. Suresh, et al. (2003). "Cell and molecular mechanics of biological materials". In: *Nature materials* 2.11, pp. 715–725.

Baruch, Dror I (1999). "Adhesive receptors on malaria-parasitized red cells". In: *Best Practice & Research Clinical Haematology* 12.4, pp. 747–761.

Bates, Adam H et al. (2010). "Use of magnetically purified Plasmodium falciparum parasites improves the accuracy of erythrocyte invasion assays". In: *Experimental parasitology* 126.2, pp. 278–280.

Bennett, Vann (1985). "The membrane skeleton of human erythrocytes and its implications for more complex cells". In: *Annual review of biochemistry* 54.1, pp. 273–304.

Black, C et al. (2008). *Standard Operating Procedure: Plasmodium falciparum culture*. Cooke Laboratory/ Coppel Laboratory SOP-PfCulture-301107. Monash University Department of Microbiology.

Branton, Daniel, Carl M Cohen, and Jonathan Tyler (1981). "Interaction of cytoskeletal proteins on the human erythrocyte membrane". In: *Cell* 24.1, pp. 24–32.

Bruce, MC et al. (1990). "Commitment of the malaria parasite Plasmodium falciparum to sexual and asexual development". In: *Parasitology* 100.02, pp. 191–200.

Buffet, Pierre A et al. (2011). "The pathogenesis of Plasmodium falciparum malaria in humans: insights from splenic physiology". In: *Blood* 117.2, pp. 381–392.

Bull, PC et al. (2000). "Plasmodium falciparum-infected erythrocytes: agglutination by diverse Kenyan plasma is associated with severe disease and young host age". In: *Journal of Infectious Diseases* 182.1, pp. 252–259.

Bustamante, Carlos (2005). "Unfolding single RNA molecules: bridging the gap between equilibrium and non-equilibrium statistical thermodynamics". In: *Quarterly reviews of biophysics* 38.04, pp. 291–301.

Buttrum, Stephen M, Raymond Hatton, and GB Nash (1993). "Selectin-mediated rolling of neutrophils on immobilized platelets". In: *Blood* 82.4, pp. 1165–1174.

Carberry, DM et al. (2004). "Fluctuations and irreversibility: an experimental demonstration of a second-law-like theorem using a colloidal particle held in an optical trap". In: *Physical review letters* 92.14, p. 140601.

Carlson, Johan et al. (1990). "Human cerebral malaria: association with erythrocyte rosetting and lack of anti-rosetting antibodies". In: *The lancet* 336.8729, pp. 1457–1460.

Carlson, Johan et al. (1994). "Natural protection against severe Plasmodium falciparum malaria due to impaired rosette formation". In: *Blood* 84.11, pp. 3909–3914.

Castelain, M. et al. (2012). "Single-cell adhesion probed in-situ using optical tweezers: A case study with Saccharomyces cerevisiae". In: *Journal of Applied Physics* 111.11, pp. 114701–114701.

Chan, Jo-Anne, Freya JI Fowkes, and James G Beeson (2014). "Surface antigens of Plasmodium falciparum-infected erythrocytes as immune targets and malaria vaccine candidates". In: *Cellular and Molecular Life Sciences* 71.19, pp. 3633–3657.

Charych, Deborah H et al. (1993). "Direct colorimetric detection of a receptor-ligand interaction by a polymerized bilayer assembly". In: *SCIENCE-NEW YORK THEN WASHINGTON-* 261, pp. 585–585.

Chen, Qijun, Martha Schlichtherle, and Mats Wahlgren (2000). "Molecular aspects of severe malaria". In: *Clinical microbiology reviews* 13.3, pp. 439–450.

Chesla, S E. et al. (2000). "The Membrane Anchor Influences Ligand Binding Two-dimensional Kinetic Rates and Three-dimensional Affinity of FcyRIII (CD16)". In: *Journal of Biological Chemistry* 275.14, pp. 10235–10246.

Chesla, Scott E, Periasamy Selvaraj, and Cheng Zhu (1998). "Measuring two-dimensional receptor-ligand binding kinetics by micropipette". In: *Biophysical journal* 75.3, pp. 1553–1572.

Cheung, L. S. and K. Konstantopoulos (2011). "An Analytical Model for Determining Two-Dimensional Receptor-Ligand Kinetics". In: *Biophys. J.* 100, pp. 2338–2346.

Chien, Shu (1978). "Principles and techniques for assessing erythrocyte deformability". In: *Red Cell Rheology*. Springer, pp. 71–99.

— (1987). "Red cell deformability and its relevance to blood flow". In: *Annual review of physiology* 49.1, pp. 177–192.

Chotivanich, Kesinee et al. (2004). "Platelet-induced autoagglutination of Plasmodium falciparum-infected red blood cells and disease severity in Thailand". In: *Journal of Infectious Diseases* 189.6, pp. 1052–1055.

Chua, Caroline Lin Lin et al. (2013). "Monocytes and macrophages in malaria: protection or pathology?" In: *Trends in parasitology* 29.1, pp. 26–34.

Cockburn, Ian A et al. (2004). "A human complement receptor 1 polymorphism that reduces Plasmodium falciparum rosetting confers protection against severe malaria". In: *Proceedings of the National Academy of Sciences* 101.1, pp. 272–277.

Colbert, M-J et al. (2009). "Adhesion and membrane tension of single vesicles and living cells using a micropipette-based technique". In: *The European Physical Journal E* 30.2, pp. 117–121.

Cooke, B M. et al. (2002). "Assignment of functional roles to parasite proteins in malaria-infected red blood cells by competitive flow-based adhesion assay". In: *British Journal of Haematology* 117.1.

Cooke, BM and RL Coppel (1995). "Cytoadhesion and falciparum malaria: going with the flow". In: *Parasitology Today* 11.8, pp. 282–287.

Cooke, Brian, Ross Coppel, and Mats Wahlgren (2000). "Falciparum malaria: sticking up, standing out and out-standing". In: *Parasitology Today* 16.10, pp. 416–420.

Cooke, Brian M, Narla Mohandas, and Ross L Coppel (2001). "The malaria-infected red blood cell: structural and functional changes". In: *Advances in parasitology* 50, pp. 1–86.

Cooke, Brian M and Gerard B Nash (1995). "Plasmodium falciparum: characterization of adhesion of flowing parasitized red blood cells to platelets". In: *Experimental parasitology* 80.1, pp. 116–123.

Cooke, Brian M, John Stuart, and Gerard B Nash (2014). "The cellular and molecular rheology of malaria". In: *Biorheology* 51.2-3, pp. 99–119.

Cooke, Brian M et al. (1993). "A simplified method for culture of endothelial cells and analysis of adhesion of blood cells under conditions of flow". In: *Microvascular research* 45.1, pp. 33–45.

Cooke, Brian M et al. (1994). "Rolling and stationary cytoadhesion of red blood cells parasitized by Plasmodium falciparum: separate roles for ICAM-1, CD36 and thrombospondin". In: *British journal of haematology* 87.1, pp. 162–170.

Crabb, Brendan S et al. (1997). "Targeted gene disruption shows that knobs enable malaria-infected red cells to cytoadhere under physiological shear stress". In: *Cell* 89.2, pp. 287–296.

Crooks, G E (1998). "Nonequilibrium measurements of free energy differences for microscopically reversible Markovian systems". In: *J. Stat. Phys.* 90.5-6, pp. 1481–1487.

— (2000). "Path-ensemble averages in systems driven far from equilibrium". In: *Phys. Rev. E* 61.3, p. 2631.

Crooks, Gavin E (1999). "Entropy production fluctuation theorem and the nonequilibrium work relation for free energy differences". In: *Physical Review E* 60.3, p. 2721.

Da Costa, Lydie et al. (2013). "Hereditary spherocytosis, elliptocytosis, and other red cell membrane disorders". In: *Blood reviews* 27.4, pp. 167–178.

Davis, Shevaun P et al. (2012). "Plasmodium falciparum-induced CD36 clustering rapidly strengthens cytoadherence via p130CAS-mediated actin cytoskeletal rearrangement". In: *The FASEB Journal* 26.3, pp. 1119–1130.

Diez-Silva, Monica et al. (2010). "Shape and biomechanical characteristics of human red blood cells in health and disease". In: *MRS bulletin* 35.05, pp. 382–388.

Dluzewski, AR et al. (1984). "A simple method for isolating viable mature parasites of Plasmodium falciparum from cultures". In: *Transactions of the Royal Society of Tropical Medicine and Hygiene* 78.5, pp. 622–624.

Dong, C. and X.X. Lei (2000). "Biomechanics of cell rolling: shear flow, cell-surface adhesion, and cell deformability". In: *Journal of biomechanics* 33.1, pp. 35–43.

Drelich, Jaroslaw and Kash L Mittal (2005). *Atomic Force Microscopy in Adhesion Studies*. CRC Press.

Evans, D J and D J Searles (1994). "Equilibrium microstates which generate second law violating steady states". In: *Phys. Rev. E*.

Evans, Denis J and Debra J Searles (2002). "The fluctuation theorem". In: *Advances in Physics* 51.7, pp. 1529–1585.

Evans, E (1995). "Physical actions in biological adhesion". In: *Handbook of biological Physics* 1, pp. 723–754.

Evans, E, K Ritchie, and R Merkel (1995). "Sensitive force technique to probe molecular adhesion and structural linkages at biological interfaces." In: *Biophysical journal* 68.6, p. 2580.

Evans, Evan A (1983). "Bending elastic modulus of red blood cell membrane derived from buckling instability in micropipet aspiration tests." In: *Biophysical Journal* 43.1, p. 27.

— (1989). "[1] Structure and deformation properties of red blood cells: Concepts and quantitative methods". In: *Methods in enzymology* 173, pp. 3–35.

Evans, Evan A and Paul L La Celle (1975). "Intrinsic material properties of the erythrocyte membrane indicated by mechanical analysis of deformation". In: *Blood* 45.1, pp. 29–43.

Fällman, Erik et al. (2004). "Optical tweezers based force measurement system for quantitating binding interactions: system design and application for the study of bacterial adhesion". In: *Biosensors and Bioelectronics* 19.11, pp. 1429–1437.

Frischknecht, Friedrich et al. (2004). "Imaging movement of malaria parasites during transmission by Anopheles mosquitoes". In: *Cellular microbiology* 6.7, pp. 687–694.

Fu, C et al. (2011). "Determining B2-Integrin and Intercellular Adhesion Molecule 1 Binding Kinetics in Tumor Cell Adhesion to Leukocytes and Endothelial Cells by a Gas-driven Micropipette Assay". In: *Journal of Biological Chemistry* 286.40, pp. 34777–34787.

Fung, Yuan-cheng (2013). *Biomechanics: mechanical properties of living tissues*. Springer Science & Business Media.

Gallagher, Patrick G (2005). "Red cell membrane disorders". In: *ASH Education Program Book* 2005.1, pp. 13–18.

Gallant, Nathan D, Kristin E Michael, and Andrés J García (2005). "Cell adhesion strengthening: contributions of adhesive area, integrin binding, and focal adhesion assembly". In: *Molecular biology of the cell* 16.9, pp. 4329–4340.

Gao, YX et al. (2012). "Non-equilibrium umbrella sampling applied to force spectroscopy of soft matter". In: *The Journal of chemical physics* 136.5, p. 054902.

Gapsys, Vytautas et al. (2015). "Calculation of Binding Free Energies". In: *Molecular Modeling of Proteins*. Springer, pp. 173–209.

Glenister, Fiona K et al. (2002). "Contribution of parasite proteins to altered mechanical properties of malaria-infected red blood cells". In: *Blood* 99.3, pp. 1060–1063.

Glenister, Fiona K et al. (2009). "Functional alteration of red blood cells by a megadalton protein of Plasmodium falciparum". In: *Blood* 113.4, pp. 919–928.

Goel, Suchi et al. (2015). "RIFINs are adhesins implicated in severe Plasmodium falciparum malaria". In: *Nature medicine* 21.4, pp. 314–317.

Gönnenwein, Stefanie et al. (2003). "Generic and Specific Cell Adhesion". PhD thesis. Technische Universität München.

Gou, Xue et al. (2013). "Applying combined optical tweezers and fluorescence microscopy technologies to manipulate cell adhesions for cell-to-cell interaction study". In: *IEEE Transactions on Biomedical Engineering* 60.8, pp. 2308–2315.

Grau, Georges Emile Raymond and Alister Gordon Craig (2012). "Cerebral malaria pathogenesis: revisiting parasite and host contributions". In: *Future microbiology* 7.2, pp. 291–302.

Greenwood, B.M. et al. (2008). "Malaria: Progress, perils, and prospects for eradication". In: *Journal of Clinical Investigation* 118.4, pp. 1266–1276.

Hawass, Z et al. (2010). "Ancestry and pathology in king tutankhamuns family". In: *JAMA: The Journal of the American Medical Association* 303.7, pp. 638–647.

Helm, Christiane A, Wolfgang Knoll, and Jacob N Israelachvili (1991). "Measurement of ligand-receptor interactions". In: *Proceedings of the National Academy of Sciences* 88.18, pp. 8169–8173.

Helmby, HELENA et al. (1993). "Rosetting Plasmodium falciparum-infected erythrocytes express unique strain-specific antigens on their surface." In: *Infection and immunity* 61.1, pp. 284–288.

Henon, Sylvie et al. (1999). "A new determination of the shear modulus of the human erythrocyte membrane using optical tweezers". In: *Biophysical journal* 76.2, pp. 1145–1151.

Hochmuth, RM and RE Waugh (1987). "Erythrocyte membrane elasticity and viscosity". In: *Annual review of physiology* 49.1, pp. 209–219.

Hochmuth, Robert M (2000). "Micropipette aspiration of living cells". In: *Journal of biomechanics* 33.1, pp. 15–22.

Hoffman, Stanley and Gerald M Edelman (1983). "Kinetics of homophilic binding by embryonic and adult forms of the neural cell adhesion molecule". In: *Proceedings of the National Academy of Sciences* 80.18, pp. 5762–5766.

Hogan, Brenna et al. (2015). "Characterizing Cell Adhesion by Using Micropipette Aspiration". In: *Biophysical journal* 109.2, pp. 209–219.

Huang, Jun et al. (2004). "Quantifying the effects of molecular orientation and length on two-dimensional receptor-ligand binding kinetics". In: *Journal of Biological Chemistry* 279.43, pp. 44915–44923.

Hummer, G (2001). "Fast-growth thermodynamic integration: error and efficiency analysis". In: *J. Chem. Phys.* 114.17, pp. 7330–7337.

Iolascon, A, RA Avvisati, and C Piscopo (2010). "Hereditary spherocytosis". In: *Transfusion clinique et biologique* 17.3, pp. 138–142.

Iolascon, Achille, Silverio Perrotta, and Gordon W Stewart (2003). "Red blood cell membrane defects." In: *Reviews in clinical and experimental hematology* 7.1, pp. 22–56.

Jarzynski, C (1997a). "Equilibrium free-energy differences from nonequilibrium measurements: A master-equation approach". In: *Phys. Rev. E* 56.5, p. 5018.

Jarzynski, Christopher (1997b). "Nonequilibrium equality for free energy differences". In: *Physical Review Letters* 78.14, p. 2690.

Jena, B.P. and J.K.H. Hörber (2002). *Atomic force microscopy in cell biology*. Vol. 68. Academic Pr.

Joergensen, Lars M et al. (2010). "The kinetics of antibody binding to Plasmodium falciparum VAR2CSA PfEMP1 antigen and modelling of PfEMP1 antigen packing on the membrane knobs". In: *Malaria journal* 9.1, p. 1.

Josling, Gabrielle A and Manuel Llinás (2015). "Sexual development in Plasmodium parasites: knowing when it's time to commit". In: *Nature Reviews Microbiology* 13.9, pp. 573–587.

Karl, Stephan, Timothy ME Davis, and Tim G St Pierre (2010). "Parameterization of high magnetic field gradient fractionation columns for applications with Plasmodium falciparum infected human erythrocytes". In: *Malaria journal* 9.1, p. 1.

Karlsson, Robert and Anders Fält (1997). "Experimental design for kinetic analysis of protein-protein interactions with surface plasmon resonance biosensors". In: *Journal of immunological methods* 200.1, pp. 121–133.

Kaul, DK et al. (1991). "Rosetting of Plasmodium falciparum-infected red blood cells with uninfected red blood cells enhances microvascular obstruction under flow conditions". In: *Blood* 78.3, pp. 812–819.

Kim, Youngchan, Kyoohyun Kim, and YongKeun Park (2012). *Measurement techniques for red blood cell deformability: recent advances*. INTECH Open Access Publisher.

Kinoshita, K et al. (2010). "Long-Lived, High-Strength States of ICAM-1 Bonds to b2 Integrin, II: Lifetimes of LFA-1 Bonds Under Force in Leukocyte Signaling". In: *Biophysical Journal* 98.8, pp. 1467–1475.

Kojima, N et al. (1992). "Cell adhesion in a dynamic flow system as compared to static system. Glycosphingolipid-glycosphingolipid interaction in the dynamic system predominates over lectin-or integrin-based mechanisms in adhesion of B16 melanoma cells to non-activated endothelial cells." In: *Journal of Biological Chemistry* 267.24, pp. 17264–17270.

Korn, CB and US Schwarz (2008). "Dynamic states of cells adhering in shear flow: from slipping to rolling". In: *Physical review E* 77.4, p. 041904.

Koshland, Daniel E (1995). "The key–lock theory and the induced fit theory". In: *Angewandte Chemie International Edition in English* 33.23-24, pp. 2375–2378.

Kraemer, Susan M and Joseph D Smith (2006). "A family affair: var genes, PfEMP1 binding, and malaria disease". In: *Current opinion in microbiology* 9.4, pp. 374–380.

Lacelle, Paul L, Evan A Evans, and Robert M Hochmuth (1978). "Erythrocyte membrane elasticity, fragmentation and lysis". In: *Red Cell Rheology*. Springer, pp. 331–346.

Lakey, Jeremy H and Elaine M Raggett (1998). "Measuring protein—protein interactions". In: *Current opinion in structural biology* 8.1, pp. 119–123.

Lambros, Chris and Jerome P Vanderberg (1979). "Synchronization of Plasmodium falciparum erythrocytic stages in culture". In: *The Journal of parasitology*, pp. 418–420.

Lawrence, M B. and T A. Springer (1991). "Leukocytes roll on a selectin at physiologic flow rates: Distinction from and prerequisite for adhesion through integrins". In: *Cell* 65.5, pp. 859 –873.

Lee, G. Y.H. and C. T. Lim (2007). "Biomechanics approaches to studying human diseases". In: *Trends in Biotechnology* 25.3, pp. 111–118.

Lenormand, Guillaume et al. (2001). "Direct measurement of the area expansion and shear moduli of the human red blood cell membrane skeleton". In: *Biophysical Journal* 81.1, pp. 43–56.

Li, Ang et al. (2013). "Atomic force microscopy of Plasmodium-infected red blood cells: detecting and localizing single molecular recognition events". In: *Malaria: Methods and Protocols*, pp. 299–305.

Li, Ning et al. (2015). "Mechanokinetics of receptor–ligand interactions in cell adhesion". In: *Acta Mechanica Sinica* 31.2, pp. 248–258.

Li, Q et al. (2012). "Force-dependent bond dissociation govern rolling of HL-60 cells through E-selectin". In: *Experimental Cell Research* 318.14, pp. 1649 –1658.

Liang, Shile et al. (2008). "Two-dimensional kinetics of β2-integrin and ICAM-1 bindings between neutrophils and melanoma cells in a shear flow". In: *American Journal of Physiology-Cell Physiology* 294.3, pp. C743–C753.

LIM, C.T. (2006). "Single cell mechanics study of the human disease malaria". In: *Journal of Biomechanical Science and Engineering* 1.1, pp. 82–92.

Lipowsky, Reinhard and Erich Sackmann (1995). *Structure and dynamics of membranes: I. from cells to vesicles/II. generic and specific interactions*. Vol. 1. Elsevier.

Litvinov, R. I. et al. (2002). "Binding strength and activation state of single fibrinogen-integrin pairs on living cells". In: *Proceedings of the National Academy of Sciences* 99.11, pp. 7426–7431.

Litvinov, R.I. et al. (2011). "Dissociation of Bimolecular< i> α</i> IIb< i> β</i> 3-Fibrinogen Complex under a Constant Tensile Force". In: *Biophysical journal* 100.1, pp. 165–173.

Litvinov, R.I. et al. (2012). "Resolving two-dimensional kinetics of the integrin αIIbβ3-fibrinogen interactions using Binding-Unbinding Correlation Spectroscopy". In: *Journal of Biological Chemistry*.

Lower, Steven K, Christopher J Tadanier, and Michael F Hochella (2000). "Measuring interfacial and adhesion forces between bacteria and mineral surfaces with biological force microscopy". In: *Geochimica et Cosmochimica Acta* 64.18, pp. 3133–3139.

Lyubin, E. V. et al. (2012). "Cellular viscoelasticity probed by active rheology in optical tweezers". In: *Journal of Biomedical Optics* 17.10.

Mackintosh, Claire L, James G Beeson, and Kevin Marsh (2004). "Clinical features and pathogenesis of severe malaria". In: *Trends in parasitology* 20.12, pp. 597–603.

Magistrado, Pamela et al. (2008). "VAR2CSA expression on the surface of placenta-derived Plasmodium falciparum-infected erythrocytes". In: *Journal of Infectious Diseases* 198.7, pp. 1071–1074.

Maier, Alexander G et al. (2009). "Malaria parasite proteins that remodel the host erythrocyte". In: *Nature Reviews Microbiology* 7.5, pp. 341–354.

Mallouh, Ahmad A (2012). "Red Blood Cell Membrane Disorders". In: *Textbook of Clinical Pediatrics*. Springer, pp. 2985–2993.

Mayor, Alfredo et al. (2011). "Association of severe malaria outcomes with platelet-mediated clumping and adhesion to a novel host receptor". In: *PLoS One* 6.4, e19422.

McQuarrie, Donald A (1963). "Kinetics of small systems. I". In: *The journal of chemical physics* 38.2, pp. 433–436.

Miller, Louis H et al. (2002). "The pathogenic basis of malaria". In: *Nature* 415.6872, pp. 673–679.

Mohandas, N et al. (1992). "Molecular basis for membrane rigidity of hereditary ovalocytosis. A novel mechanism involving the cytoplasmic domain of band 3." In: *Journal of Clinical Investigation* 89.2, p. 686.

Mohandas, NARLA and JA Chasis (1993). "Red blood cell deformability, membrane material properties and shape: regulation by transmembrane, skeletal and cytosolic proteins and lipids." In: *Seminars in hematology*. Vol. 30. 3, pp. 171–192.

Mohandas, Narla and Evan Evans (1994). "Mechanical properties of the red cell membrane in relation to molecular structure and genetic defects". In: *Annual review of biophysics and biomolecular structure* 23.1, pp. 787–818.

Mohandas, NARLA et al. (1980). "Analysis of factors regulating erythrocyte deformability." In: *Journal of Clinical Investigation* 66.3, p. 563.

Molloy, Justin E and Miles J Padgett (2002). "Lights, action: optical tweezers". In: *Contemporary Physics* 43.4, pp. 241–258.

Motulsky, Harvey (2014). *Intuitive biostatistics: a nonmathematical guide to statistical thinking*. Oxford University Press, USA.

Motulsky, Harvey and Arthur Christopoulos (2004). *Fitting models to biological data using linear and nonlinear regression: a practical guide to curve fitting*. OUP USA.

Moxon, C.A., G.E. Grau, and A.G. Craig (2011). "Malaria: Modification of the red blood cell and consequences in the human host". In: *British Journal of Haematology* 154.6, pp. 670–679.

Myszka, David G (1997). "Kinetic analysis of macromolecular interactions using surface plasmon resonance biosensors". In: *Current opinion in biotechnology* 8.1, pp. 50–57.

Nash, GB et al. (1989). "Abnormalities in the mechanical properties of red blood cells caused by Plasmodium falciparum". In: *Blood* 74.2, pp. 855–861.

Nash, GB et al. (1992). "Rheological analysis of the adhesive interactions of red blood cells parasitized by Plasmodium falciparum". In: *Blood* 79.3, pp. 798–807.

Nash, Gerard B, Cage S Johnson, and Herbert J Meiselman (1984). "Mechanical properties of oxygenated red blood cells in sickle cell (HbSS) disease". In: *Blood* 63.1, pp. 73–82.

Ndam, Nicaise G Tuikue et al. (2005). "High level of var2csa transcription by Plasmodium falciparum isolated from the placenta". In: *Journal of Infectious Diseases* 192.2, pp. 331–335.

Newbold, Chris et al. (1997). "Receptor-specific adhesion and clinical disease in Plasmodium falciparum." In: *The American journal of tropical medicine and hygiene* 57.4, pp. 389–398.

Ochola, Lucy B et al. (2011). "Specific receptor usage in Plasmodium falciparum cytoadherence is associated with disease outcome". In: *PloS one* 6.3, e14741.

Okegawa, Takatsugu et al. (2004). "The role of cell adhesion molecule in cancer progression and its application in cancer therapy". In: *Acta Biochimica Polonica-English Edition-* 51, pp. 445–458.

Pain, Arnab et al. (2001). "Platelet-mediated clumping of Plasmodium falciparum-infected erythrocytes is a common adhesive phenotype and is associated with severe malaria". In: *Proceedings of the National Academy of Sciences* 98.4, pp. 1805–1810.

Perrotta, Silverio, Patrick G Gallagher, and Narla Mohandas (2008). "Hereditary spherocytosis". In: *The Lancet* 372.9647, pp. 1411–1426.

Petter, Michaela and Michael F Duffy (2015). "Antigenic Variation in Plasmodium falciparum". In: *Pathogen-Host Interactions: Antigenic Variation v. Somatic Adaptations*. Springer, pp. 47–90.

Phiri, Happy et al. (2009). "Competitive endothelial adhesion between Plasmodium falciparum isolates under physiological flow conditions". In: *Malaria journal* 8.1, p. 1.

Phizicky, Eric M and Stanley Fields (1995). "Protein-protein interactions: methods for detection and analysis." In: *Microbiological reviews* 59.1, pp. 94–123.

Piper, James W, Robert A Swerlick, and Cheng Zhu (1998). "Determining force dependence of two-dimensional receptor-ligand binding affinity by centrifugation". In: *Biophysical journal* 74.1, pp. 492–513.

Pouvelle, B et al. (2000). "Cytoadhesion of Plasmodium falciparum ring-stage-infected erythrocytes". In: *Nature medicine* 6.11, pp. 1264–1268.

Qidwai, T. et al. (2013). "Assay of Glucose 6-phosphate dehydrogenase Enzyme and its Correlation with Disease Prevalence in Patients with Plasmodium falciparum Malaria". In: *American Journal of Biochemistry and Molecular Biology* 3.1, pp. 135–142.

Quadt, Katharina A et al. (2012). "The density of knobs on Plasmodium falciparum-infected erythrocytes depends on developmental age and varies among isolates". In: *PloS one* 7.9, e45658.

Quinn, D.J. et al. (2010). "Dynamic behavior of healthy and malaria infected human red blood cells". PhD thesis. Massachusetts Institute of Technology.

Reddi, A Hari (1998). "Role of morphogenetic proteins in skeletal tissue engineering and regeneration". In: *Nature biotechnology* 16.3, pp. 247–252.

Rénia, Laurent et al. (2012). "Cerebral malaria: mysteries at the blood-brain barrier". In: *Virulence* 3.2, pp. 193–201.

Rinko, Linda J, Michael B Lawrence, and William H Guilford (2004). "The molecular mechanics of P-and L-selectin lectin domains binding to PSGL-1". In: *Biophysical journal* 86.1, pp. 544–554.

Roberts, David J et al. (1992). "Rapid switching to multiple antigenic and adhesive phenotypes in malaria". In: *Nature* 357.6380, p. 689.

Roberts, David J et al. (2000). "Autoagglutination of malaria-infected red blood cells and malaria severity". In: *The Lancet* 355.9213, pp. 1427–1428.

Rowe, Alexandra et al. (1995). "Plasmodium falciparum rosetting is associated with malaria severity in Kenya." In: *Infection and immunity* 63.6, pp. 2323–2326.

Rubenstein, David, Wei Yin, and Mary D Frame (2015). *Biofluid mechanics: an introduction to fluid mechanics, macrocirculation, and microcirculation*. Academic Press.

Rug, Melanie et al. (2006). "The role of KAHRP domains in knob formation and cytoadherence of P falciparum-infected human erythrocytes". In: *Blood* 108.1, pp. 370–378.

Sackmann, Erich and Stefanie Goennenwein (2006). "Cell adhesion as dynamic interplay of lock-and-key, generic and elastic forces". In: *Progress of Theoretical Physics Supplement* 165, pp. 78–99.

Sakamoto, Yosiyuki, Makio Ishiguro, and Genshiro Kitagawa (1986). "Akaike information crite-rion statistics". In: *Dordrecht, The Netherlands: D. Reidel*.

Sandberg, Robert B et al. (2015). "Efficient nonequilibrium method for binding free energy cal-culations in molecular dynamics simulations". In: *Journal of Chemical Theory and Computation* 11.2, pp. 423–435.

Sarshar, Mohammad, Winson T Wong, and Bahman Anvari (2014). "Comparative study of meth-ods to calibrate the stiffness of a single-beam gradient-force optical tweezers over various laser trapping powers". In: *Journal of biomedical optics* 19.11, pp. 115001–115001.

Scherf, A et al. (1998). "Antigenic variation in malaria: in situ switching, relaxed and mutually exclusive transcription of var genes during intra-erythrocytic development in Plasmodium falciparum". In: *The EMBO journal* 17.18, pp. 5418–5426.

Schofield, Ann E et al. (1992). "Basis of unique red cell membrane properties in hereditary ovalo-cytosis". In: *Journal of molecular biology* 223.4, pp. 949–958.

Schreiber, Gideon (2002). "Kinetic studies of protein–protein interactions". In: *Current opinion in structural biology* 12.1, pp. 41–47.

Seifert, Udo (2012). "Stochastic thermodynamics, fluctuation theorems and molecular machines". In: *Reports on Progress in Physics* 75.12, p. 126001.

Setiawan, B. and Ministry of Health Republic of Indonesia (2010). "Current malaria management: guideline 2009." In: *Acta medica Indonesiana* 42.4, pp. 258–261.

Shankaran, Harish and Sriram Neelamegham (2001). "Nonlinear flow affects hydrodynamic forces and neutrophil adhesion rates in cone–plate viscometers". In: *Biophysical journal* 80.6, pp. 2631–2648.

Shelby, J.P. et al. (2003). "A microfluidic model for single-cell capillary obstruction by Plasmodium falciparum-infected erythrocytes". In: *Proceedings of the National Academy of Sciences* 100.25, pp. 14618–14622.

Sherman, Irwin W, Shigetoshi Eda, and Enrique Winograd (2003). "Cytoadherence and seques-tration in Plasmodium falciparum: defining the ties that bind". In: *Microbes and Infection* 5.10, pp. 897–909.

Skalak, R et al. (1973). "Strain energy function of red blood cell membranes". In: *Biophysical Journal* 13.3, p. 245.

Smith, Joseph D (2014). "The role of PfEMP1 adhesion domain classification in Plasmodium falciparum pathogenesis research". In: *Molecular and biochemical parasitology* 195.2, pp. 82–87.

Smith, M.R.J., E.L. Berg, and M.B. Lawrence (1999). "A direct comparison of selectin-mediated transient, adhesive events using high temporal resolution". In: *Biophysical journal* 77.6, pp. 3371–3383.

Smith, Peter J (1995). "A Recursive Formulation of the Old Problem of Obtaining Moments from Cumulants and Vice Versa". In: *Am. Stat.* 49.2, pp. 217–218.

Soderquist, Craig and Adam Bagg (2013). "Hereditary elliptocytosis". In: *Blood* 121.16, pp. 3066–3066.

Spadafora, Carmenza, Lucia Gerena, and Karen M Kopydlowski (2011). "Comparison of the in vitro invasive capabilities of Plasmodium falciparum schizonts isolated by Percoll gradient or using magnetic based separation". In: *Malaria journal* 10.1, pp. 1–4.

Springer, Timothy A et al. (1987). "The lymphocyte function associated LFA-1, CD2, and LFA-3 molecules: cell adhesion receptors of the immune system". In: *Annual review of immunology* 5.1, pp. 223–252.

Stuart, J and GB Nash (1990). "Red cell deformability and haematological disorders". In: *Blood reviews* 4.3, pp. 141–147.

Subramani, Ramesh et al. (2015). "Plasmodium falciparum-infected erythrocyte knob density is linked to the PfEMP1 variant expressed". In: *Mbio* 6.5, e01456–15.

Sung, K.L.P., E. Saldivar, and L. Phillips (1994). "Interleukin-1 Induces Differential Adhesiveness on Human Endothelial Cell Surfaces". In: *Biochemical and Biophysical Research Communications* 202.2, pp. 866 –872.

Suresh, S. et al. (2005). "Connections between single-cell biomechanics and human disease states: gastrointestinal cancer and malaria". In: *Acta Biomaterialia* 1.1, pp. 15–30.

Surgenor, Douglas MacN (1975). *The red blood cell*. Vol. 2. Academic Press.

Suwanarusk, Rossarin et al. (2004). "The deformability of red blood cells parasitized by Plasmodium falciparum and P. vivax". In: *Journal of Infectious Diseases* 189.2, pp. 190–194.

Svetina, Saša (2012). "Red blood cell shape and deformability in the context of the functional evolution of its membrane structure". In: *Cellular & molecular biology letters* 17.2, pp. 171–181.

Torrie, Glenn M and John P Valleau (1974). "Monte Carlo free energy estimates using non-Boltzmann sampling: Application to the sub-critical Lennard-Jones fluid". In: *Chem. Phys. Lett.* 28.4, pp. 578–581.

Trager, William and James B Jensen (1976). "Human malaria parasites in continuous culture". In: *Science* 193.4254, pp. 673–675.

Trampuz, Andrej et al. (2003). "Clinical review: Severe malaria". In: *Critical care* 7.4, p. 1.

Tse, William T and Samuel E Lux (1999). "Red blood cell membrane disorders". In: *British journal of haematology* 104.1, pp. 2–13.

Tuteja, Renu (2007). "Malaria- an overview". In: *FEBS Journal* 274.18, pp. 4670–4679.

Verdeny, I et al. (2011). "Optical trapping: a review of essential concepts". In: *Opt. Pura Apl.* 44, pp. 527–551.

Vigan-Womas, Inès et al. (2008). "An in vivo and in vitro model of Plasmodium falciparum rosetting and autoagglutination mediated by varO, a group A var gene encoding a frequent serotype". In: *Infection and immunity* 76.12, pp. 5565–5580.

Waller, Karena L et al. (1999). "Mapping the binding domains involved in the interaction between the plasmodium falciparum knob-associated histidine-rich protein (KAHRP) and the cytoadherence ligand P. FalciparumErythrocyte membrane protein 1 (PfEMP1)". In: *Journal of Biological Chemistry* 274.34, pp. 23808–23813.

Wang, GM et al. (2002). "Experimental demonstration of violations of the second law of thermodynamics for small systems and short time scales". In: *Physical Review Letters* 89.5, p. 050601.

Waterkeyn, Jacqueline G, Alan F Cowman, and Brian M Cooke (2001). "Plasmodium falciparum: gelatin enrichment selects for parasites with full-length chromosome 2. implications for cytoadhesion assays". In: *Experimental parasitology* 97.2, pp. 115–118.

Watermeyer, Jean M et al. (2016). "A spiral scaffold underlies cytoadherent knobs in Plasmodium falciparum–infected erythrocytes". In: *Blood* 127.3, pp. 343–351.

Waugh, R and EA Evans (1979). "Thermoelasticity of red blood cell membrane." In: *Biophysical journal* 26.1, p. 115.

Williams, Stephen R. and Denis J. Evans (2010). "Nonequilibrium Dynamics and Umbrella Sampling". In: *Phys. Rev. Lett.* 105 (11), p. 110601. DOI: 10.1103/PhysRevLett.105.110601. URL: http://link.aps.org/doi/10.1103/PhysRevLett.105.110601.

Williams, Stephen R, Denis J Evans, and Debra J Searles (2011). "Nonequilibrium Umbrella Sampling and the Functional Crooks Fluctuation Theorem". In: *J. Stat. Phys.* 145.4, pp. 831–840.

World Health Organization (2012). *Management of severe malaria*. World Health Organization.

— (2015). *World Malaria Report 2015*. World Health Organization.

Xu, Xiaofeng et al. (2013). "Probing the cytoadherence of malaria infected red blood cells under flow". In: *PloS one* 8.5, e64763.

Yago, T. et al. (2004). "Catch bonds govern adhesion through L-selectin at threshold shear". In: *The Journal of cell biology* 166.6, pp. 913–923.

Zhao, H. et al. (2002). "Studies on single cell adhesion probability between lymphocytes and endothelial cells with micropipette technique". In: *Microvascular research* 63.

Zhu, C. (2000a). "Kinetics and mechanics of cell adhesion". In: *J. Biomech.* 33, pp. 23–33.

Zhu, Cheng (2000b). "Kinetics and mechanics of cell adhesion". In: *Journal of biomechanics* 33.1, pp. 23–33.

Zhu, Cheng, Gang Bao, and Ning Wang (2000). "Cell mechanics: mechanical response, cell adhesion, and molecular deformation". In: *Annual review of biomedical engineering* 2.1, pp. 189–226.